Porous Copper by the Lost Carbonate Sintering - Powder Metallurgy Process Applied to Tape Casting

By

Mosalagae Mosalagae

A Thesis Submitted to the University of Sheffield for the Degree of Doctor of Philosophy

The Sheffield University

Faculty of Engineering

Materials Science and Engineering

October 2018

Abstract

The use of porous metals for heat sinks and heat exchangers is becoming more and more wide-spread in engineering and technological applications. As a result, researchers and engineers continue with the purpose of determining effective ways of producing this type of porous metal at a lower manufacturing cost. Apart from aluminium, copper is mostly used as a base metal for making heat sinks, because the properties of copper make it suitable for the purpose. Over the years several methods have been explored to improve the properties of porous metals as heat sinks. The Lost Carbonate Sintering (LCS) method offers a simple and efficient way of producing porous metals with a wider range of porosities. On the other hand, tape casting is also an efficient and low-cost method for processing powders into thin sheets.

This PhD thesis investigates the production and characterisation of porous copper heat sinks fabricated by the LCS powder metallurgy process applied to tape casting. LCS was employed to provide flexibility to control the pore parameters such as porosity and pore distribution within the component being tape cast. The effectiveness of the process was examined throughout, as well as the resulting structure. Potassium carbonate (K_2CO_3) was introduced into the matrix as a space holder. Additives such as plasticizers, binders, dispersant and solvents were added to control the properties of the green body and ease fabrication. The component was successfully debound and sintered at 450 °C and 890 °C respectively under vacuum. The potassium carbonate was removed from the sintered component via dissolution in water.

A simple assessment of porous structure was carried out by employing various techniques such Scanning Electron Microscopy (SEM), micro-CT scanning, X-ray diffraction, Raman

spectrometry, energy dispersive X-ray Spectrometry (EDS) techniques. The effectiveness of the dissolution route at removing the space holder was investigated. The mechanical properties were also assessed. To verify the porous copper samples produced in this study, their suitability for heat sink applications was investigated with simple assessments of the thermal properties under forced convection using air as a coolant. An open circuit heat transfer rig developed and designed in-house was used.

In the results, a thin double-layered sheet of thin porous copper integrated with a dense copper layer was successfully produced. The sheets had volumetric or bulk porosity ranging from 50 - 82 % within the porous layer, which increased with the addition of K_2CO_3 space holder during processing, and pore size within the sheets ranged from 30 - 790 μm. By tape casting, thicknesses ranging from 900 -1800 μm were achieved. The heat transfer performance of the porous sheets improved with increasing porosity. The sheets with the highest porosity achieved a thermal transmittance of 5.0 W/K when tested on a cylindrical heating system (CHS) under a higher Reynolds number regime (Re = 486). Similar sheets achieved thermal transmittance (*Tr*) of 1.6 W/K on a flat heating system (FHS) at Re = 1,069.

Acknowledgements

During my work on this project I have received a lot of help and advice from many different people. Hereby, it is a pleasure to thank those who made this project possible, for all the support, help, advice and guidance that I received over the past few years.

Firstly, I would like to thank my sponsor **Botswana Government** for their financial support throughout this project, covering the travel expenses to attend conferences locally and internationally. And also, would like to thank my employer Botswana International University of Science and Technology for allowing me work on this project.

Secondly, I am very thankful to my supervisor **Dr Russell Goodall** for his help, advice and supervision and for giving me the opportunity to undertake this research work and write this PhD. He manages a great knowledge with being understanding, efficient and approachable. It has been a great pleasure working under his supervision. I would like to thank him again for introducing me to Dr Robert Woolley who then introduced me to his student, Ahmed AAG Al-rubaiy.

Thirdly, I would like thank **Dr Robert Woolley** for introducing me to **Ahmed AAG Al-rubaiy** and giving access to the thermal rig for heat transfer analysis.

I would like to thank **Ahmed AAG Al-rubaiy** for his continuing support, commitment, resource and guidance throughout the heat transfer analysis.

I also would to thank **Dr Cheryl Shaw, Mr Ben Palmer, Mr Michael Bell, Mr Dean Haylock** for the assistance and technical support during the experimental work and analysis, and for keeping the equipment and machines running.

Thanks to my colleagues, **Mohammed Elbadawi, Mohammed Shbeh, Carl Magnus, Carlos M Brambila Renteria** for their help and suggestions throughout the project.

Special thanks to my girlfriend **Temogo Marble Dibonwa,** I do consider myself lucky to have a great girlfriend. I thank you for putting up with me and supporting me. The coffee machine was a very good idea.

Lastly, I offer my regards and blessings to my family and friends all of those who helped and supported me in any respect during the completion of the project.

Nomenclature

Uppercase letters

A_{CS}	Cross sectional area	m^2
A_{HT}	Heat transfer	
C_p	Specific heat	J/Kg K
D	Maximum deflection	m
D_p	Particle diameter	m
D_{pore}	Pore diameter	m
E_f	Flexural modulus	Pa
F	Applied load	N
K	Permeability	
L	Length	m
L_s	Support span	m
Q	Heat flow	W
Q_c	Heat lost	
Q_H	Heat gained	
Nu	Nusselt number	
R	Gas constant	J/K mol
Re	Reynolds number	
T_0	Initial temperature	°C, K
T_{Air}	Air temperature	°C, K
$TCart$	Cartridge temperature	°C, K
T_{In}	Temperature of air going in	°C, K
T_{Out}	Temperature of air going out	°C, K
V	Volume	m^3
V_{True}	True volume	m^3
V_{Ext}	External volume	m^3
VM	Material volume	m^3
VP	Pore volume	m^3

Lowercase letters

b	Width	m
d	Thickness	mm
$d_{measured}$	Measured diameter	m
d_{pore}	Pore diameter	m
d_w	Window diameter	m
g	Gravitational constant	$m^3/g\ s^2$
h	Convective heat transfer coefficient	$W/\ m^2\ K$
k	Thermal conductivity	W/m K
k_{cu}	Thermal conductivity of copper	W/m K
k_{In}	Thermal conductivity of the insulation material	W/m K
m_M	Material mass	g
m	Mass flow rate	
m_{Air}	Air mass flow rate	
m_{matrix}	Mass of the matrix	g
q	Heat flux	W/m^2
r	Radius	m
t	Time	s
v_{Air}	Air velocity	m/s
v_{matrix}	Volume of the matrix	m^3
x	Independent variable distance	m
y	Dependent variable distance	m

Greek Letters

γ	Surface tension	
ΔT	Temperature difference	°C, K
Δx	Distance difference	m
δi	Diffusion number	
ε	Porosity	%
ε_n	Nominal porosity	%
ε_F	Flexural strain	

π	Pi value	
σ_F	Flexural stress	Pa
ρ	Density	g/cm^3
ρ_M	Material density or true density	g/cm^3
ρ_B	Bulk density	g/cm^3

Subscripts

ave	Average
cond	Conduction
conv	Convection
crit	Critical
Cu	Copper
eff	Effective
f	Fluid
in	Inlet
inter	Intersection
K_2C0_3	Potassium carbonate
l	Low porosity
out	Outlet
part	Particle
pl	Heating plate
pore	Pore
pre	Pressure
s	Solid
t	Tensile
tot	Total

List of Figures

List of Tables

Table of Contents

CHAPTER 1: INTRODUCTION

1.1 Background

Over the past few decades, porous metals and alloys usually called metallic foams have been studied and have received growing interest from several different industries. The increasing interest is due to their unique combination of structural and functional properties such as, excellent strength to weight ratio, good surface area to volume ratio, their permeability to flowing fluids (e.g. air and water), good electrical shielding properties, damping capacity, high mechanical energy absorption efficiency etc [1]–[7]. Porous metals are now available in the market and have been explored for a wide range of engineering applications. As a result, they continue to be an area of intense current research and development, in both academia and industry.

There are several types of porous metals which are produced by different fabrication techniques[2], [8]–[11]. These types of metals are generally described by key structural features. The first key feature is the base metal. Apart from aluminium[11]–[16], copper is the most widely used material for making heat sinks, because the heat transport properties of copper make it suitable for the purpose, and its malleability makes it easy to form into the different, complex shapes that a heat sink necessitates. The research described in this thesis will concentrate on porous metals made from 99% pure copper. The other key feature is the structure of the porous metals. Porous metals are commonly classified in to two main classes: open pore and closed pore porous metals. An open pore porous metal consists of pores that are interconnected to their neighbouring pores, allowing fluids to circulate thorough them. The closed pore porous metals have pores that are enclosed with the metal matrix. This report

will be restricted to the consideration of porous copper with an open-pore structure for heat transfer applications

1.2 Motivation of the Research

In today's high-density electronics, thermal management plays a significant role. Electronic devices continue to become more compact and slimmer, and thermal aspects are becoming increasingly important to ensure device performance, reliability and durability of electronic components [17]–[19]. Reducing heat generation and removing heat from tight spaces is a constant challenge for electronics engineers designing portable electronics such as laptops, tablets, smartphones and other space-constrained gadgets. Engineers manage the heat generated in such high-density portable electronic designs by deploying optimized heat sinks [11], [20]–[24]. Open-celled porous metal with small thickness and high energy transfer capabilities could be best suited for this application. While there are many different metals that can be made in porous form [1], copper conducts heat extremely well in its solid state and so porous copper receives a lot of attention for heat sinks and heat exchangers [25].

Open-cell copper with large surface area and high permeability for fluids is a good candidate for heat sink and heat exchanger applications, especially in small electronics where high efficiency and small size are often demanded[21], [26]–[28]. However, the design of the heat sink in portable electronic devices is dependent on the physical space, cooling needs and manufacturing cost, and frequently, a thin porous sheet would be all that could be accommodated. "Versarien, a materials specialist, has found that using a micro-porous structure of copper maximizes its surface area enabling the heat sink to become more effective in dissipating heat" [29]. The porous structure is generated by employing the 'lost carbonate sintering' (LCS) technique, a space holder technique first invented by Zhao where a leachable

carbonate space-holder is applied to a powder metallurgical process to produce sintered porous copper compacts [27].

In the LCS process, metallurgists compact and sinter a mixture of pure copper powder with a carbonate space holder. This makes a network of copper matrix, with the carbonate particles sandwiched in between. Once the sintered component cools, the carbonate space holder is dissolved by water, and can then be recovered for recycling. The remaining copper matrix forms a regular and uniform porous structure, which is highly rigid and permeable to fluid and whose density per unit volume can be easily controlled by the manufacturer. Versarien PLC produced porous copper heatsinks with dimensions ranging from 10 mm × 10 mm × 2 mm to 40 mm × 40 mm × 5 mm $(l \times w \times t)$ using the LCS technique [29]. Recent studies have shown that a combination of LCS with common processes such as hot pressing are favourable, but these have limitations in terms of the thickness range and flexural strength that can be achieved**.**

On the other hand, tape casting (TP) offers an original solution for production of thin sheets of metals, in this case porous metals. This process is based on powder metallurgy and it has many good characteristics such as accurate control of thickness, high quality of laminated materials, low cost and good surface finish. It offers a low power consumption (environmental aspect) and manufacturing cost (economical aspect) as well. This process was originally developed for producing electronic ceramics and is still mainly applied for this [30]–[35]. Recently, tape casting has been applied to powder metallurgy in the production of various types of components involving powdered metals. This includes copper composites such as alumina/copper[36], copper/diamond [37] and copper/carbon [38], [39] and copper alloys [40], [41] mainly for heat sink applications where minimum thicknesses are required. It was also used for fabricating biporous copper using $C_7H_{10}N_2O_2S$ as the foaming agent [42]. Other

researchers have attempted to tape cast copper alloys from powder state, mainly for tribological applications.

LCS could be explored further to produce thin sheets of porous copper by applying it to the tape casting technique. It was believed that a combination of the two processes could offer a solution where a thin and efficient heatsink is required. Therefore, this research focuses on exploring a combined LCS and tape casting method in an attempt to produce porous copper for heatsink applications. Section 1.3 presents the objectives of this research.

1.3 Objectives of the Research

In this thesis, porous copper samples were successfully produced by a novel process combining lost carbonate sintering (LCS) and tape casting. The main objectives of the experimental work were:

- To produce open-celled porous copper by a novel process; a powder metallurgical process and lost carbonate sintering (LCS) applied to tape casting, as part of the development of an efficient material for heat sink applications.
- To create a thin porous sheet of copper integrated with a dense copper layer, to provide a superior contact to a surface where additional heat transfer is required.
- To study several basic physical parameters of porous copper, including porosity, surface roughness, density and heat transfer coefficient which are significant to evaluate the heat transfer characteristics of the porous heat sinks. It is essential to study these properties to assess the potential for the porous copper tapes to be used in advanced, compact and light weight thermal management systems.
- To investigate the suitability of porous copper tapes for heat exchanger or heat sink applications with varying porosities and pore sizes produced by different processes.

- To evaluate the mechanical behaviour of these porous copper tapes will also be assessed for their in-service target application and off-service aspects such as handling and assembling. Even though the porous copper tapes developed here are not intended for structural applications, their mechanical properties such as stiffness and yield strength, and ability to deform and conform to various shapes are still significant for use in target application, as well as for handling and assembling.

1.4 Thesis Outline

The basic concept of this PhD work is shown in the form of a flow chart in Figure 1

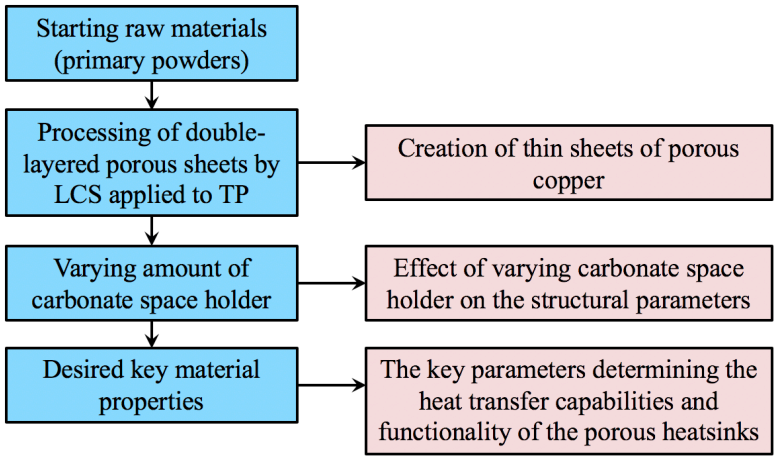

Figure 1: Basic concept of this PhD work.

The most significant contribution of this thesis is to focus on the links between the development of a novel process that combines tape casting and lost carbonate sintering processes to fabricate thin double-layered heatsinks of porous copper, and to carry out the structural analysis of the materials produced by employing different types of equipment and techniques such as scanning electron microscopy, micro CT scanners, chemical analysis equipment etc. Finally, mechanical properties and heat transfer capabilities of the porous

sheets were evaluated to examine the effects of structural parameters on heat transfer performance under forced convection.

This thesis contains seven chapters, all summarised in Table 1.

Table 1: Summary of the thesis structure.

Chapters	Contents
Chapter 1: Introduction	Provides an introduction of the thesis, highlighting the motivation and objectives of the research.
Chapter 2: Literature Review	Gives the background relevant to this research. Porous metal processing methods are introduced here. Also, the background and updates of some characterisation techniques and relevant properties.
Chapter 3: Experimental Methods	This chapter covers sample preparations, characterisation of the structure, assessment of mechanical properties and heat transfer performance. Also provides step-by-step procedures on each.
Chapter 4: Results and discussion - Processing and Structural Characterisation	This chapter focuses on all the findings and discussions from structural characterisation of the porous samples produced here.
Chapter 5: Results and Discussion – Mechanical Testing and Further Structural Characterisation	All findings and discussion from the assessment of mechanical properties are presented here
Chapter 6: Results and Discussion – Heat Transfer Measurements	Results and discussion of heat transfer measurements are covered here.
Chapter 7: Conclusions	Concludes the findings of the research
References	References

CHAPTER 2. LITERATURE REVIEW

The literature review begins with section 2.1 which provides a general overview of various methods used to produce porous metals highlighting applications for each method. The methods are divided into two groups: first, methods for producing open-cell metals (see section 2.2) and, second, methods for producing closed-cell metals (see section 4.2).

Principles of the tape casting process are also covered in section 4.3, followed by the key elements of heat transfer in porous metals or metallic foams, reviewed in section 4.4 covering the influence of mesostructure and pore parameters of the porous metal or metallic foam on the overall heat transfer properties and applications.

The mechanism of forced convection is covered in section 4.5, followed by the application of the porous metals and metallic foams as heat exchangers or heat sinks discussed in section 4.6.

2.1 Processing of Porous Metals – An introduction

In the past, several decades ago, many attempts were undertaken to produce porous metals. There are several ways of producing these porous metals and alloys based on the application. In most cases the methods of production are categorized based on the criteria followed during production. Some reviews use the state (gas, vapour liquid and solid) of the metal during the formation of pores to categorize the methods of production [1]–[4], [43]–[46]. Methods of production were categorized based on the state of the metal in this review to cover almost all the existing methods. The flow chart shown in Figure 2 below presents the methods classified according to the state of the metal during the formation of pores. The structure that is usually formed out of these fabrication methods may either be an open-cell or closed-cell pore structure depending on the intended application and the method used [1][4].

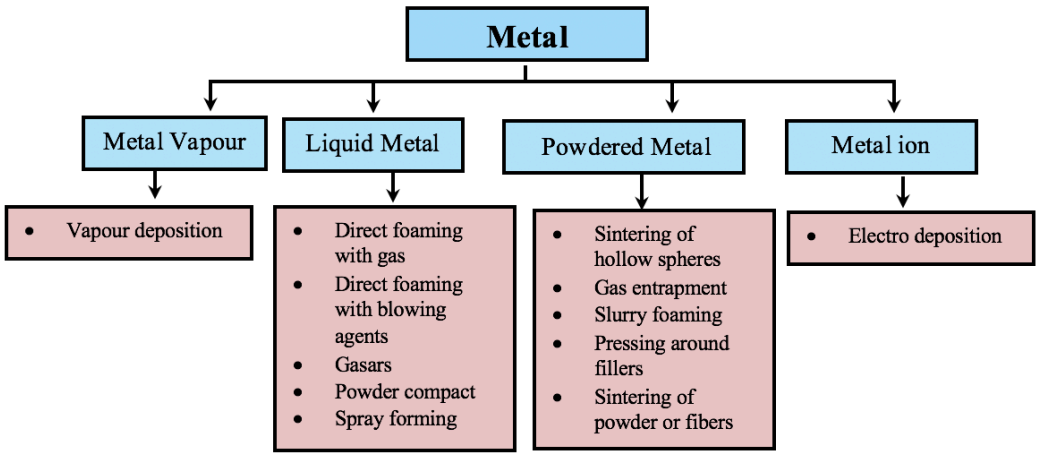

Figure 2: Methods of producing porous metals categorized by the state of metal during the formation of pores [2], [47].

The difference between the two structures is based on the way pores are arranged or distributed within a metallic structure. In a closed-pore structure, the pores are completely encompassed within the metallic structure while in an open pore structure, the pores are open

and interconnected allowing fluids to circulate through them past the metal. The open cell metals make attractive heat exchangers due to their ability to allow fluid circulation [46], [48], [49]. Figure 3 below shows examples of the open pore and closed pore structure of porous metals. It clearly indicates the pore arrangements between the two types of porous materials within the metallic foams or porous metals.

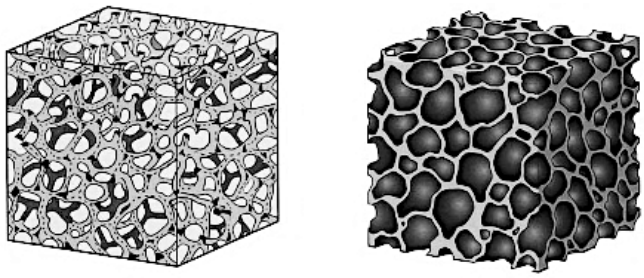

Figure 3: Schematic diagram of a) open pore and b) closed pore structure of a metal [50].

2.2 Open cell porous metals

Table 2: Methods for producing open-pore porous metals and commercial foam example [1], [45]

Method	Volume Fraction Solid	Pore size (µm)	Commercial Foam example
Investment Casting	0.05 -0.15	1,000-10,000	Duocel
Deposition onto template	0.02-0.05	1,000-10,000	INCO foam
Sintered particles	0.1-0.45	10-1,000	
Sintered Fibers	0.05-0.3	100-5,000	
Space holder Method	0.1-0.35	10-10,000	Vesarien Foam
Replication	0.1-0.35	10-10,000	Corevo Foam, Constellium
Dealloying Method	0.15-0.5	0.5-100	
Regular Lattices	0.05-0.2	1,000-10,000	
Gasar (Lotus copper heat sink)	0.4	550 (Av.)	

An open pore structure consists of interconnected pores allowing fluids to flow through them. They are specified by several geometric parameters of the foam like structures. These parameters are clearly presented in Figure 4 below, and are usually used to characterize the mesostructure of the porous metal or metallic foams being produced. The value of the physical properties of these parameters are dependent on the fabrication method implemented in producing this type of structure. Porous metals with open-pore structure may transmit heat extremely well because of the capability of allowing fluids to flow through them.

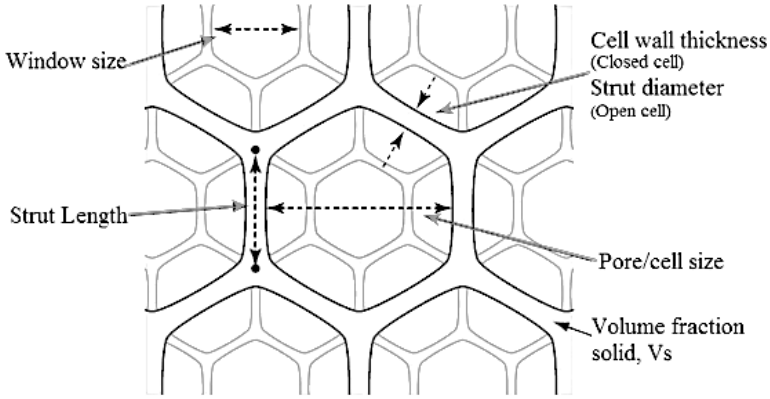

Figure 4: Schematic diagram of the geometric parameters of the mesostructure of the open pore structure [1].

Open-pore structures can further be classified based on the shape of the pores, which can fall between the extreme cases of two dimensional (2D) or channels (in honeycombs) or three-dimensional (3D) completely irregular shapes [1]–[4], [27], [51] as well as longitudinal pores [21]. Table 2 below highlights some of the common techniques employed for producing porous metals with an open-pore structure. It also highlights the commercial examples of this class of porous metals, the volume fraction solid and the pore size range [1], [45]. This class of porous metals have recently been the object of a worldwide surge of interest. As stated in [45], this is due to the appreciation of different beneficial behaviours that porosity (and particularly open porosity) can bring, including permeability, heat transport control, and maximisation of the specific binding stiffness.

Apart from porosity and permeability of the open-pore structure, a wide range of mechanical and physical properties may be adapted to multiple requirements. Section 2.2 covers the methods commonly employed in the production of porous metals or metallic foam with an open-pore structure.

4.1.1 Replication method

The replication method is well-adapted method for producing porous metals with open-pore structures. In this process, components of many shapes, including fine detail, are produced in methods where the hollow space inside a mould is replicated in the metal [52]. For foams, this process begins with making a removable porous preform, for which another foam material, such as a polymer is frequently used [52]. To make a perfect porous metal, the preform must meet the two main conditions: (i) it must be easy to remove during processing once the porous metal is formed and (ii) it must be chemically stable with the primary metal or metal matrix.

There are various forms of replication processes reported to date. The processes can be distinguished based on two basic characteristics. Firstly, the nature and processing of the perform, and secondly, the nature and processing of the materials generating the open-pore structure [52].

4.1.1.1 Investment casting

The investment casting method, also known as “lost wax casting” in some references, is one method which has been used over five centuries ago and is still used where metallic components were fabricated from moulds. It is usually selected where high precision shaping is required. This process starts by manufacturing the pattern using polymeric material (wax and stereo lithography patterns are also used). The pattern is then dipped in a ceramic slurry

mixture which is allowed to form around the pattern. After solidification is complete, the pattern is melted and/or burned out of the ceramic, which then allows it to be used as the mould for the metal. Ensuring a complete removal of the pattern is very important, to avoid contamination of the final metallic component [2]. Once the mould is ready, the molten metal is poured in, taking the shape of the pattern. The final step after complete solidification of the metal is to remove the ceramic mould around the metal. Water jets are used to wash off the ceramic leaving a final and open cell metallic component [1]–[3].

4.1.1.2 Space holder method

This is one type of replication process where the open-pore structure is generated by deliberately introducing porosity within the fabricated material by the use of a space holder. The space holders can either be dense single-phase or multi-phase mixed with powdered metal before sintering to retain pores within materials [1]. These leachable powders are added into a blend of metal powders and compressed with them to form a block, then the leachable powder is dissolved out, leaving a metal matrix with an open cell structure. Space holders are generally classified by their elimination methods after sintering as dissolution and thermal decomposition[53]. In the former group, potassium carbonate (K_2CO_3) and sodium chloride (NaCl) are commonly used, both of which can be removed by aqueous dissolution after sintering[52].

Aluminium-based sponge has been produced by several researchers by employing the space holder method using NaCl [12], [54]–[58] or carbamide[15], [16], [59], [60] as a space holder. Aluminium foams were also made using silica gel[61] or ceramic balls [62] as a space holder. Sodium chloride (NaCl) is usually a preferred leachable space holder for fabrication of open-cell porous aluminium due to its inertness when in contact with both aluminium and its alloys, low cost, and its ease of dissolution in water. During sintering, some additives such as Mg

and Sn have been used to generate supersolidus sintering[55], [57], [63]. During sintering, the oxide layer usually forms around Al or Mg particles which often results in poor boding between the particles. The problem was reportedly solved by employing spark-plasma-sintering (SPS) resulting in Al sponge with superior properties[58], [64]. Many researchers prefer to produce Al from a liquid state hence avoiding defects resulting from incomplete densification of the powdered Al.

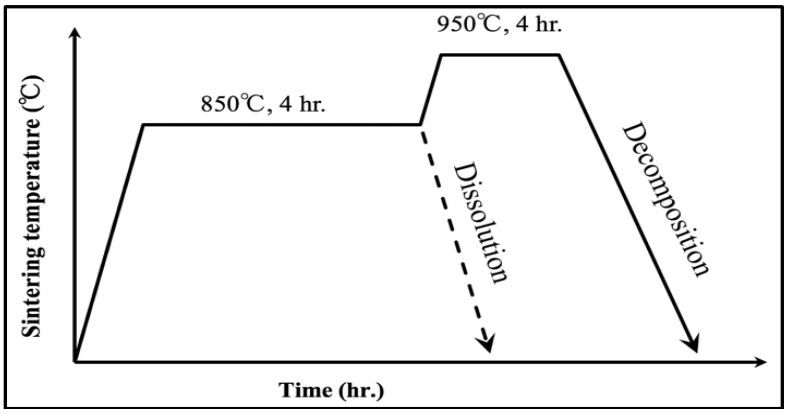

Figure 5: The schematic diagram of the sintering and carbonate removal stages of LCS [27].

However, sponge metals with higher melting temperature such as copper, titanium, stainless steel, titanium and its alloys and nickel-based alloys are usually processed following powder metallurgical routes. Porous silver and titanium were successfully produced by powder metallurgical processes using sugars as a space holder [53], [65], and porous titanium using NaCl as a space holder [66] or a KCl space holder [67]. Porous copper or copper foams are mainly processed using carbonate space holders such as sodium carbonate space holder [68] and potassium carbonate [27]. Zhao and colleagues developed a space holder technique named lost – carbonate sintering (LCS) to fabricate porous copper [27]. LCS utilises potassium carbonate (K_2CO_3) as a space holder for pore development. Though the technique was initially developed to produce porous copper, it has now been adapted to produce various porous materials such as porous aluminium[55] and porous steel [69] and titanium [70].

However, several researchers have also continued to use it for production of porous copper[27], [71][72][73]–[76]. This technique was further commercialised by *Versarien plc* to produce porous copper named *VersarienCu*^{TM} for thermal applications. Since then, this process has attracted many scientists because of its simplicity, controllability of pore parameters, low implementation cost, flexibility and the fact that it can be applied on metals with high melting points.

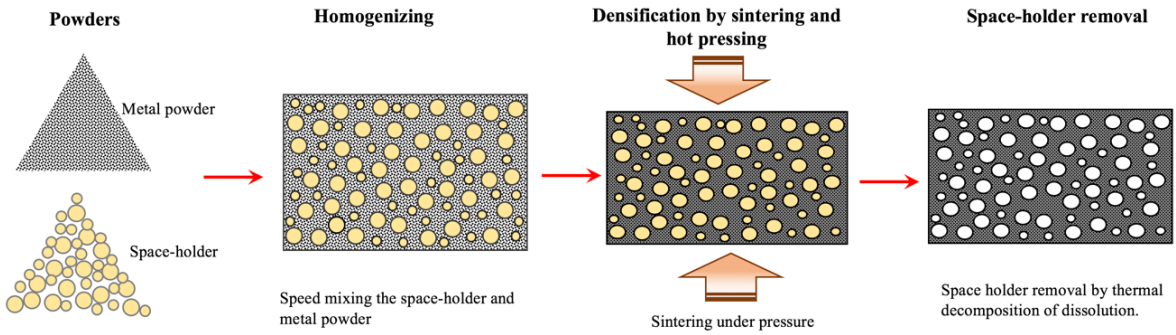

Figure 6: Schematic diagram of LCS process for production of porous metals [27].

In the study performed by Zhang and Zhao, carbonate space holder (K_2CO_3) was removed from the matrix by thermal decomposition and dissolution(see Figure 5) [69]. This usually depends on the type of space holder and metal matrix used. The melting point of the space holder and the dissolution rate play a major role in the selection of space holder required. K_2CO_3 has a solubility of 111 g per 100 g of water at 20 °C and a melting temperature of 891 °C, therefore both thermal decomposition and dissolution routes are applicable to remove K_2CO_3 from copper matrix [69].

Zhang and Zhao continued to investigate the effectiveness of K_2CO_3 loss and the characteristics of decomposition route over the dissolution route [27], [69], [71]. The outcomes of the study have shown that the particle size of K_2CO_3 plays a major role in the effectiveness of the pore generation and the removal time of the space holder. Finer particle size of K_2CO_3 is time consuming to remove and results in high shrinkage rate and also can

result in incomplete removal by both routes leaving K_2CO_3 trapped within the final product[27], [69]. Parvanian et al further investigated the structural, morphological and mechanical factors by employing advanced characterisation techniques such as X-ray computed micro tomography (XCT) to study the resulting porous copper in a 3D form [9]. The study was mainly to investigate the effectiveness of the K_2CO_3 as a space holder on the final structure of porous copper and further relate it to mechanical properties [9], [74]. It is now understood that the size of carbonate particles and overall sample (the thickness) plays a major role in the duration of the carbonate removal process by both methods; dissolution and thermal decomposition.

The decomposition reaction of potassium carbonate in the metal matrix during sintering at 950°C was confirmed by Zhang and Zhao to be [69].

$$K_2CO_3 \rightarrow K_2O + CO_2 \quad (1)$$

The melting temperature of K_2CO_3 is 891°C, therefore it is likely that melting and decomposition of K_2CO_3 particles occur at the same time during heating to 950°C. In this case, the decomposition product of gaseous CO_2 bubbles through a mixtures of undecomposed melt of K_2CO_3 and its product K_2O [69]. Zhang and Zhao [69] discussed this phenomenon at length and finally concluded that either the dissolution or decomposition route can be chosen for carbonate removal after sintering, depending on the product dimensions and carbonate particle size. It also depends on whether production time or shrinkage is the main concern [27].

In comparison, the porous metal produced by the decomposition route offers better mechanical properties. A higher tensile strength and flexural strength are achieved on samples produced by decomposition compared to the dissolution route. Production via the dissolution

route offers less shrinkage within the porous metal products, the pore shape and size reflect the K_2CO_3 particles used in the process and pores are connected by micropores and small windows in cell walls. In comparison with the dissolution route, the porous metals produced by LCS via decomposition are reported to have higher shrinkage resulting in distortion of pores from K_2CO_3 and reduction of micropores (between metal powder particles) during sintering and decomposition of K_2CO_3. Considering both carbonate removal processes, the by-products from each process may have a significant implication for the commercialisation of the LCS process, specifically, the environmental friendliness of the by-products. The by-product of LCS via the dissolution route is an aqueous solution of K_2CO_3 which may result in difficulties in recycling, as compared to K_2O which comes as solid ash which is easier to handle and recycle (provided this ash is not trapped within the sample) [69].

4.1.2 Sintered particles and fibres

Most of the current production of porous metals utilises this method of fabrication. It is used for a wide range of metals including copper and alloys, aluminium, titanium, super alloys etc. Porosity is incorporated by incomplete space filling of powders sintered together in a die. The packing densities are in the range of 40-60%, and are highly dependent on the particle shape, size and the use of vibrations. The porosities that can be achieved are nevertheless quite limited [77]. Many researchers prefer to use leachable space holders together with this method to obtain higher porosity, and thus permeability to fluids. This is due to the contribution of the micro pores from the powder metallurgy enhancing the pores introduced by using a leachable space-holder [27], [69], [72], [78]. Fabrication follows several steps which are fiber chipping/powder fractioning, mould-pressing, sintering, cooling [2][8][79].

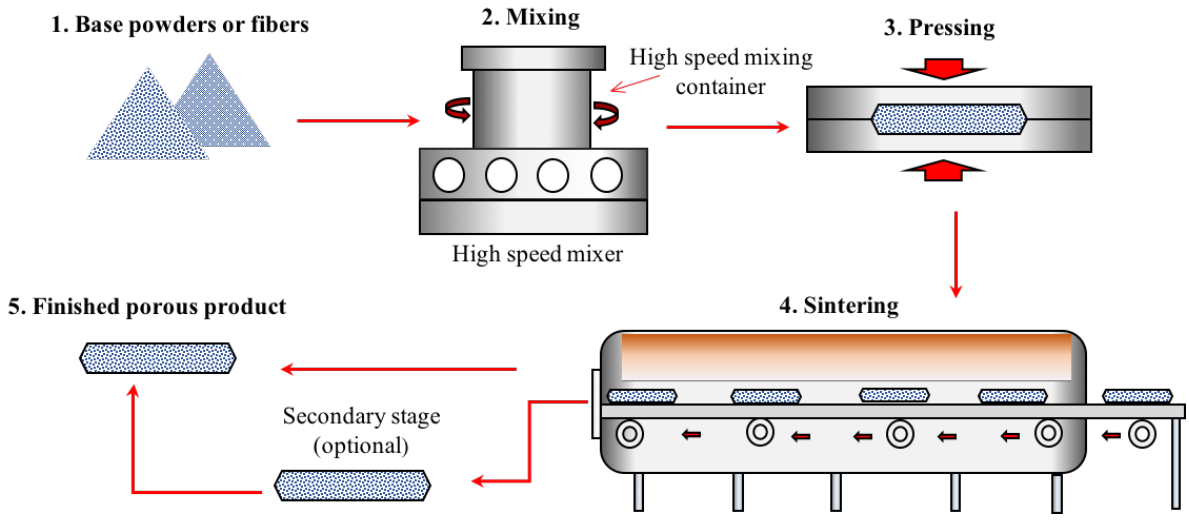

Figure 7: Convectional Powder Metallurgy (PM) process for producing porous metal [80].

In a case where fibers are the primary component, continuous fibers are chopped into short fibers usually a using multi-tooth tool. On the other hand, powder fractioning is the first step if powder is used. The second step, which applies to both powder or fibers is that they are then mixed together then pressed between two rams within the chamber. The compacted product is then sintered and then cooled [79].

4.1.3 Additive Layer Manufacturing

Additive Layer Manufacturing (ALM) a subset of additive manufacturing (AM), is the opposite of subtractive manufacturing where the product is produced by removing material. In this process, the desired shape of the product is achieved by adding layer after layer of the materials which are available in fine powder form. The addition of layers is guided by a 3D design model. First, ALM 3D parts are designed in a computer-controlled programme (3D Computer-Aided Design (CAD)). The CAD model is then cut into slices using a machine operating software; the thickness of the slices depends on the type of the material used (e.g. 0. 1 mm for polymers and 0.03mm for metals).

Table 3: A summary of categories of ALM, processes and materials

Categories	Process/Technique	Materials
Powder Bed Fusion	Electron Beam Melting (EBM), Selective Laser Melting (SLM), Selective Laser Sintering (SLS)	Polymers, Metals: titanium alloys, stainless steel 316, nickel-based superalloys, chrome-cobalt, aluminium AlSi10Mg
Materials Extrusion	Fused Deposition Modelling (FDM)	Thermoplastic filament
Sheet Lamination	Paper Lamination Technology (PLT), Ultrasonic Additive Manufacturing (UAM), Laminated Object Manufacturing (LOM)	Plastic Sheet material, Metal tapes and foils, adhesive-coated papers
Materials Deposition	Binder jetting, material jetting	Wax-like materials, photopolymers
Directed Energy Deposition	Direct Metal Deposition (DMD), Blown Powder, Laser Cladding, Laser Engineered Lens	Aluminium and its alloys, Nickel-based alloys

Addition of layers follows the CAD model produced. Although the term "3D printing' is usually used as a synonym for all additive manufacturing processes, there are several individual processes which differ in the way individual layers are added. These categories include: material extrusion, powder bed fusion, direct energy deposition, material deposition, sheet lamination, and vat photopolymerization (See Table 3). There are several examples of porous copper fabricated by ALM, for example Ramirez et al [81] fabricated Cu reticulated mesh with densities in the range of 0.73 g/cm^3 to 6.67 g/cm^3 with the potential for multi-functional electrical and thermal management systems. Lodes et al [82] also successfully produced 99.94% pure copper via selective electron beam melting (SEBM), which offered freedom in design. Sriraman et al successfully produced 150µm thick copper foil by very high power ultrasonic additive manufacturing [83].

Selective laser sintering is one of the techniques commonly used for addition of layers following the CAD model generated. Figure 8 is the schematic diagram of selective laser sintering of powder during fabrication of metallic foam. A moving rake or a blade sweeps an even layer of the powder above the work piece within the chamber. The laser beam scans back and forth over the powder layer surface following the shape of the CAD model. The work surface then drops by the thickness of the layer by movement of the Z-Stage (see Figure 8) before another layer is swept over. This continues until the shape of the CAD model is complete.

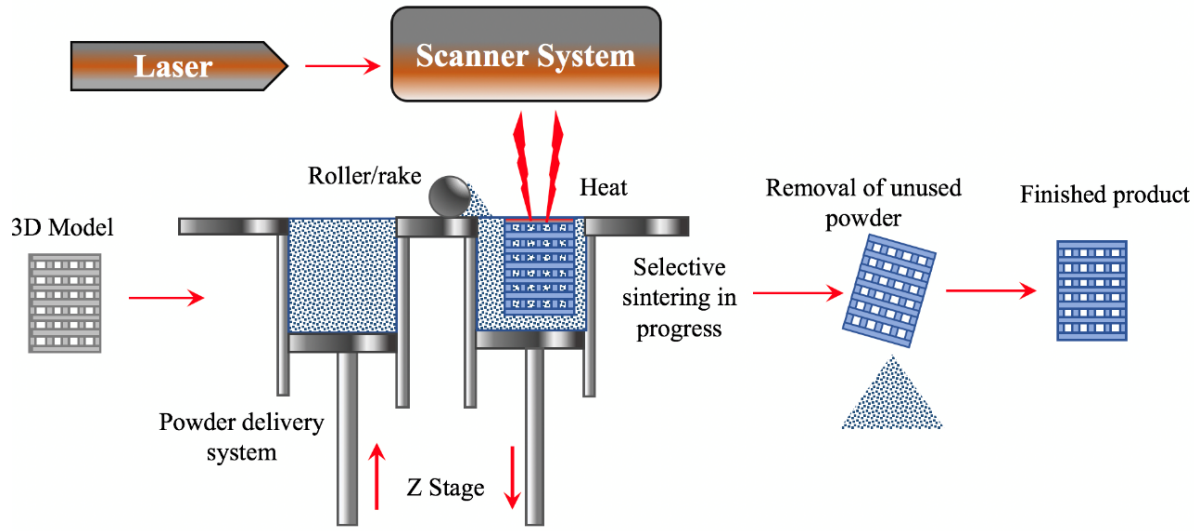

Figure 8: Fabrication of metallic foam by Additive Later Manufacturing technique; Selective laser sintering of powdered metal [5].

4.1.3.1 Dealloying method

Dealloying is one of the historical techniques which has been used since the last century to fabricate nanoporous metals such as Raney Nickel from Aluminum – Nickel alloys, but the understanding of their performance and microstructure is still not adequate [84]. The dealloying or selective leaching is basically an electrochemical reaction in which one element or phase constituting an alloy is separated and removed from the alloy into the electrolyte leaving pores (or pits) in the remaining metal or alloy. In this process the more active

components are removed from the alloy when exposed to a corrosive environment, and this component can be either an element from single phase solid solution alloys or a phase in multiphase alloys [85]. The basic principles of this method are not new, but they have now been developed and used in production of metallic cellular materials. Nanoporous copper metals have been fabricated by dealloying Al-Cu[85], Ti-Cu[86], and TiCuNi [87].

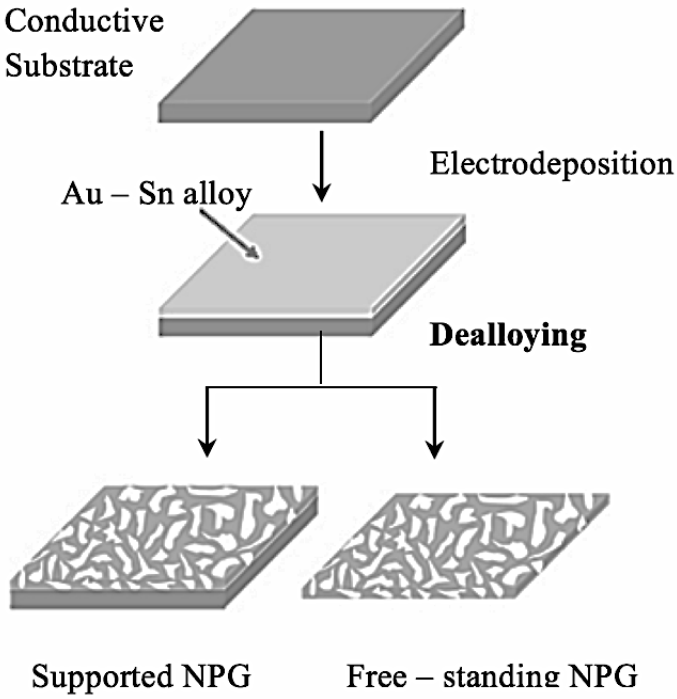

Figure 9: Fabrication of Nanoporous metal by dealloying [88].

The pore size, porosity and pore distribution/morphology can be controlled by changing the grain morphology, composition (of the starting alloy) and the corrosion parameters. According to the study performed by Ref. [89] nanoporous copper ribbons with average pore size ranging from 325-520nm were fabricated by differentiating corrosion times of $Mn_{70}Cu_{30}$ in 6wt% HCl solution. Again, nanoporous copper was fabricated in a recent study by Ref. [86] where the less noble titanium was dealloyed from amorphous binary Ti-Cu alloys depending on alloy composition, treatment time and solution concentration. This technique mainly concentrates on controlling the chemistry of the process, temperature and changing the composition of the alloy to control the pore size and porosity of the nanoporous metal

fabricated [1]. Heat treatment and solidification processes are normally used to control the phase or element distribution within the microstructure of the metal before dealloying and this will determine the final structure of the porous metal.

4.2 Closed-cell porous metals

In a closed-pore structure, the pores are completely enclosed within the metallic matrix. Various reviews shows that this type of porous metal or metallic foam can be manufactured in many different ways[1]–[3], [43]. These metals are usually used in structural applications where good strength to weight ratio and large part sizes are required. Table 4 below shows examples of the common methods used for producing this type of porous metal or metallic foam, as well as the commercial examples. This type of porous metal is usually processed from a liquid state, which involves the usage of blowing agents or injection of the gas [1], [43]. The research of this thesis is mainly centered around the fabrication of the open-cell porous metals, and therefore this section will be brief.

Table 4: Methods for producing closed-cell porous metals and the commercial examples [45].

Method	Volume Fraction Solid	Pore size (μm)	Commercial Foam example
Metal sheet foaming	0.05 -0.15	1,000-10,000	Duocel
Direct foaming	0.02-0.05	1,000-10,000	INCO foam
Bonded hollow spheres	0.1-0.45	10-1,000	
Additive manufacturing technology	0.05-0.3	100-5,000	
Sacrificial filters	0.1-0.35	10-10,000	
Incomplete sintering	0.1-0.35	10-10,000	Corevo Foam, Constellium
Phase separation	0.15-0.5	0.5-100	

4.2.1 Gas injection into the melt

This process involves directly introducing air bubbles into the metal melt using a tube assisted by specially designed impeller to enhance distribution. The metal is then allowed to solidify with the air bubbles still trapped in the melt. The morphology of the foam structure is dependent mainly on the factors influenced by the foaming process such as the nucleation of the bubbles. The bubbles created grow into spheres where the internal pressure is in equilibrium with hydrostatic pressure untill the melt solidifies. Stability of the foam depends on the temperature and pressure in the gas-liquid system, as well as its physical – chemical properties, surface tension, viscosity, gas solubility, and presence of surfactants.

Though it is easy to generate the bubbles into the melt, maintaining the pores within the melt at the same size and well distributed across the melt was a challenge for the researchers who developed these techniques. There was also insufficient time to keep the bubbles in the melt before solidification because the bubbles generated exit from the melt quickly. However, stabilizers such as ceramic powders (e.g. Al_3O_2 and SiC) are usually added to stop the bubbles from rupturing or merging by increasing the viscosity of the melt during bubbling. 5% of 70 nm SiC particles was added and homogenously dispersed ultrasonically and proved to be sufficient to stabilise aluminium foams [90]–[92]. On the other hand, particles formed *in-situ* by chemical reaction have also been used, for example 4 wt.% of TiC particles formed *in-situ* in an aluminium melt, and aluminium was successfully foamed as a result [91], [92].

Recently, the research and development of this method has been centred around understanding the foaming and stabilisation of the melt as well as developing new foaming agents and reducing the manufacturing cost by optimising the process. There are several challenges to understanding the complexities, and most of the research conducted has focused

on this. This method is now used commercially, especially for producing aluminium foams. Liaoning Rontec Advanced Material Technology Co.,Ltd based in China, CYMAT technologies Ltd based in Canada and MRSK HYDRO ASA based in the USA are commercially producing aluminium foams from this method.

4.2.2 Gas releasing agent by decomposition

In the process, gas releasing agents are introduced in to the melt. The agent is then decomposed while still in the melt to produce air bubbles. Ceramic powder is usually also added to the melt to modify its viscosity, being followed by the foaming agent. To promote homogeneity of the pores across the aluminium foam, the melt is usually mixed using impellers. Several researchers attempted to use various gas releasing agents to produce foams[93].

The most commonly used gas releasing agent is TiH_2. Aluminium foam has been produced by mixing aluminium powder or melt with a TiH_2 blowing agent[94]–[97]. Alporas aluminium foam (Alporas, USA) is one typical example of foam produced by this method[98]. A detailed explanation of this process is fully covered in [99]. Powder extrusion has commonly been used to produce precursors for formation of aluminium foams by this method [94], [95]. Three major sections are involved in this process; powder extrusion, foaming and lastly moulding. Aluminium or aluminium alloy powder is mixed with TiH_2 foaming agent then poured into a container of a powder extruder heated to 420 °C to enable extrusion. The mixture is compacted at a pressure of 100 MPa. Lastly, the mixture is extruded through a hot die and starts foaming until pores are completely developed [94].

Carbonates or nitrates are often preferred as foaming agents for Al and other metals such as zirconium, high carbon steel and ferro-alloys because of hydrogen embrittlement sensitivity.

Within the family of hydrides TiH_2 is mainly used on aluminium alloys such as $AlSiMg_2$. CaH_2 is also preferred to foam Al-Cu-Mg alloys [100], where Mg is used as a thickener [101]. ZrH_2 has been used to foam pure Al metal. As DeMeller suggested carbonates are also preferred to foam light metals [102]. $CaCO_2$ is mostly used in the Alporas processes especially with $AlSi_7M$. A comparison was made between using TiH_2 and $CaCO_3$, of which $CaCO_3$ generated larger pores compared to those produced by TiH_2[103], [104]. Dolomate $MgCa(CO_3)_2$ is also used to foam pure Al without addition of any other stabiliser [105].

4.2.3 Bonding metallic hollow spheres method

In this method, the hollow spheres are bonded together by employing a similar or different phase to form a closed-cell porous structure [106]. The structures produced are light in weight. The pore size is determined by the size of the hollow spheres which can range from a few micrometres to a few millimetres. These spheres are produced differently by several techniques such as nozzle spraying, emulsion or sacrificial core processes. The spheres are packed and joined together by gluing or brazing depending on whether the temperature allows[107], [108]. This process was successful in producing ceramic foams[45], [109], [110]. Amorphous Mg-based metal foams with ductile hollow spheres have also been successfully produced[111]. A composite of ceramic hollow sphere in an in-situ Al matrix was also successfully produced and tested [91], [112]–[115].

Wire-woven bulk Kagone (WBK) – Metal hollow sphere (MHS) hybrids were produced. The hybrids outperform the competitors with regard to deformation energy absorption due to the combination of high strength and ductility [106]. Syntactic foams may also be produced by embedding hollow spheres into a metallic matrix, ceramic or polymeric matrix. The mechanical properties of this type of foam depends on the properties of the spheres embedded

in the matrix as well as the matrix itself. The combination of the individual properties may result in better combined properties showing a great promise for crash energy absorption [1], [45].

4.2.4 Metal foam sandwich

This method involves making a foam sandwich of a closed-cell or open cell structure. The structure consists of porous structure or a foam attached between two sheets of metal. Aluminium foam sandwiches (AFS) are typical examples of sandwich foams produced by this method. They are processed based on the expansion of the precursors generated by the use of embedded blowing agents between the dense face sheets of metal. The three-layer structure of two metal sheets and compacted powders mixed with a blowing agent are involved. As already discussed in section 4.2.2, thermally modified TiH_2 is a typical blowing agent used to generate pores in aluminium powders. However, nitrates and carbonates are often required for other metals such as ferro-alloys, high carbon steels, zirconium etc.

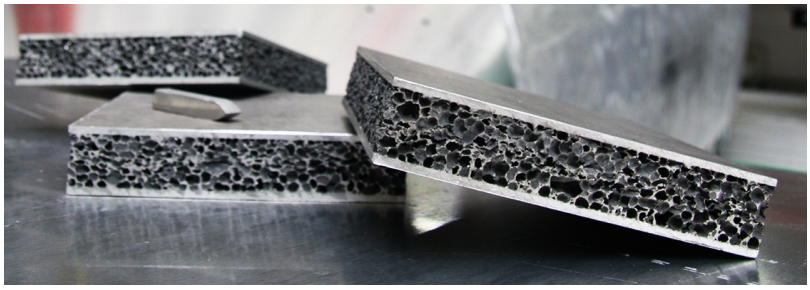

Figure 10: Aluminium foam sandwich produced by Fraunhofer IWU (Fraunhofer Institute for machine tools and forming technology IWU[116].

This is a mould-free process where the two face-sheets of metals are part of the foam sandwich and a mould at the same time. One of the major advantages of this process is that it does not include non-metallic bonding, and therefore it does not require an additional bonding step. However, there have been some attempts to produce AFS by bonding Alporus foam between two face sheets for various applications, such as mechanical engineering and the

transport industry[43]. Several alloy combinations have been tried out either as the metal used as the sandwich (core) or the two face sheets[117]. Steel face sheets have also been tried out using aluminium as a core [3], [118], and two aluminium sheets or aluminium alloy sheets and an aluminium alloy core have been produced [119] and are reviewed in Ref. [1], [3], [117]. In the case where a pure metallic bonding is required, conventional sheets of metals such as aluminium or steel are roll-clad to a sheet of foamable precursor material[3]. The core layer is then expanded by heating to the foaming temperature. There are wide applications of this type of foam; for an example Alimex (Germany) has added AFS sandwich panel to its product line where high precision and high stiffness is required, and the European 'Ariane 5' rocket uses panels in the adaptors which support the payload. It also found its first prototype application in racing bicycles [120]. Research and development of this type of metal foam or porou metals is still ongoing.

4.2.5 Other processing methods

There are many more processing strategies and developments in the field of producing closed-cell porous metals or foams, of which some of them are applied for producing open-celled structures, such as Bridgman-type directional solidification method (Gasar) (see Figure 11) [14], [20], [21], powder or fibre sintering techniques, and deposition onto a template. There has been great progress recently in this field, as-well-as characterisation of all types of porous metals or foams (closed-cell and open-celled structure).

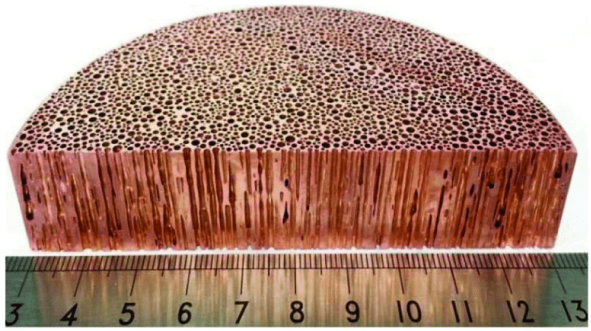

Figure 11: The image of the lotus porous copper with longitudinal pores [121]**.**

4.3 Principles of Tape Casting

Tape casting is a low cost forming technique for the manufacture of thin ceramic or multilayer structures of controlled thickness and high quality for different applications[35]. The process was heavily involved in the production of ceramics or composites [30]–[38], [41]. It involves the casting of a slurry under an exactly adjusted doctor blade onto a flat carrier surface to produce thin single or multilayer structures of various materials for various applications[31]. There are two types of tape casters, one type of tape caster is fitted with a moving doctor blade and the other type has a stationary doctor blade.

The tape caster fitted with a stationary doctor blade is commonly used. The flat carrier surface is pulled by a motor attached to the tape caster. During the subsequent drying process, the dispersing slurry is partially dried whereupon the tape thickness reduces. The tape thickness commonly ranges between 25 to 1200 μm. This process was originally developed for producing electronic ceramics and is still mainly used for this. However, tape casting has also been adopted to produce non-ceramics, metals and polymers. Tape casting is often the preferred choice in developing and producing these products because of its suitability, scaleablity, relative simplicity, and low implementation cost compared to other alternative methods such as hot or dry pressing, injection moulding, and 3D printing or slip casting.

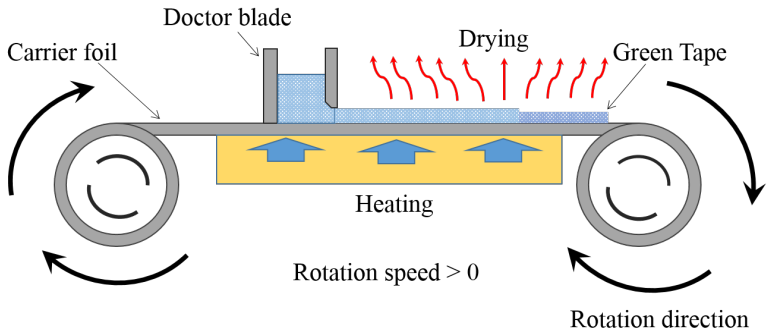

Figure 12: Schematic diagram of tape casting process.

Recently tape casting has been widely used on metals such as metal composites [40]. One must understand that tape casting is highly dependent on the quality of the slurry prior to casting. However, tape casting of different materials requires different formulations of slurry: solvents, binders, plasticizers and dispersants to fabricate high quality sheets. The most important characteristics of a tape casting slurry are (i) a well dispersed homogenous stable system, (ii) shear thinning behaviour, (iii) minimum viscosity and (iv) high solid loading. Copper based materials processed by tape casting are used in industry for heat transfer applications because of their high thermal and electrical conductivities[40].

Researchers attempted to tape cast metal powders to form copper composites such as copper/diamond[18], [37], copper/SiC [122] and copper/carbon[38] as well as alumina/copper[123] mainly for heat transfer applications. Other researchers attempted to tape cast copper alloys from powder state, mainly for tribological applications[40]. Not only copper and its composites have been produced by tape casting, Ref. [124] attempted to fabricate Al-Mg/ ZrO_2 components by tape casting, and Ref. [125] and [126] were successful in preparing metal-supported SOFC cells with Y_2O_3 stabilized ZrO_2 as the electrolyte using tape casting. Other metals and metal composites such as Ti-SiC [127], Ni[128], Mg[129], stainless steel [130], Cu-Mg system[131], Zirconia – steel [132], green sheets of ZrO_2/NiCrAlY composites and many more have also been attempted by tape casting.

4.4 Key Elements of Heat Transfer in Porous Metals

Ghosh[133], Hutter [134] and Muley [48] gave overviews based on the evaluation of different investigations of heat transfer performance of various porous metals or metallic foams. The main question of Ghosh [133] is "how good is open-cell metal foam as a heat transfer surface" or heat exchanger? From their analysis, it is clear that metallic foams or porous metals are becoming better and better alternatives for compact heat exchangers due to their properties such as superior thermodynamic characteristics, high surface area density and good mechanical properties. It is clear from the literature that the mechanism of heat transfer of porous metals or metallic foams is complex and still not fully understood and explored. The heat transfer performance of the porous metals is usually explained by four mechanisms[46]:

- Heat conduction through the metal cell walls
- Heat radiation through the metal cell walls
- Heat conduction through the pores within the porous medium
- Convection within the pores

It is not easy to accurately characterise and provide detailed information about the geometry and the specific surface of porous materials or foams. Therefore, this makes it difficult for researchers and engineers to precisely define the heat transfer coefficient. The variables of metallic foams and their effects on the heat transfer performance are summarised as follows:

Solid materia*l:* The heat transfer performance of the metal foams is highly dependent on the thermal properties of the base metal therefore, the choice of the metal is critical. The materials with higher thermal conductivity are best suited to be used as base material, such as copper

(k = 401 W/mK), aluminium (k = 205 W/mk), SiC (k = 120 W/mK) etc. Mainly, the thermal conductivity influences the heat transfer capability through the solid matrix to the cooling fluid. Boomsma and Poulikakos explained these phenomena in their work [135].

Several researchers carried out various investigations to determine the effect thermal conductivity has on the overall heat transfer of the foams or porous media. Edouard et al [136] compared experimental and numerical results of foams with varying thermal conductivities of the base material but similar morphological structure. Their work showed that materials with higher thermal conductivities such as SiC outperformed those with lower thermal conductivities such as PU[136].

Cooling fluid: the properties of the cooling fluid have effects on the heat conductivity and other heat transfer mechanisms. For example, convective heat transfer is dependent on the properties of the cooling fluid such as thermal conductivity, viscosity and the heat capacity. The radiative heat transfer mechanism depends on the properties of the air, but liquids properties are insignificant for this [134]. Due to the higher pressure drop associated with using liquids, several studies have been performed focusing on using air as a coolant.

Examples of investigations performed using liquids as a coolant include those performed by Boomsma et al [11], [137] and [135], [138], in which they investigated the thermal conductivity of fluid-saturated porous metals or metallic foams and how they can be used as heat sinks or heat exchangers. Another study was performed by Ref.[138] and Ref.[11] to determine the effect of compression of commercial metallic foams or porous metal on the flow characteristics. In this investigation, higher Nusselt number was achieved at higher compression factors. At a certain compression factor, the heat transfer start to descend. Aluminium foam with an open-celled structure achieved lower thermal resistance of at least 2-3 times compared to commercially available heat exchangers. Bhattacharya et al [139] also

investigated the effects of thermophysical properties on the performance of foams. To validate a model used to predict effective thermal conductivity, $K_{eff,}$ generated based on the two-dimensional array of hexagonal cells, experiments were carried out where flowing fluids (e.g. liquids and air) were employed on aluminium foams and reticulated vitreous carbon (RVC) foams [134].

***Porosity**:* Porosity is one of the most significant parameters in characterizing the structure of the porous metals. It is a measure of the pore or void space within a porous material. Therefore, porosity is a fraction of the volume of the pore over the total volume of the porous material, between 0 and 1 and normally expressed as a percentage ranging from 0 to 100%. Porosity is controlled by the processing method as fully described in 2.1, 2.2 and 4.2. The mechanical, physical and thermal properties are mostly dependent on the porosity.

It is well known now from the conclusions made by several researchers that porosity is one of the major factors of effective thermal conductivity. They concluded that effective thermal conductivity increases with a decreasing porosity since the thermal conductivity of solid metal is higher than that of the fluids. Authors performed this investigation in different ways but still achieved the same trend. For example, Zhao et al [140] performed this study under vacuum and achieved the same trend and conclusions, as well as Shih et al [141]. Pavel and Mohamad [142] performed their study by means of metallic screens inserted into a tube and found the same result. The study performed by Bhattacharya et al also supported this conclusion [139].

Specific surface area: it has already been mentioned above that the heat transfer of the metallic foam is dependent on the active specific surface area. Heat transfer across the solid-fluid boundary is highly dependent on the surface via a conduction heat transfer mechanism

through the solid matrix, and a radiation heat transfer mechanism and convection heat transfer through the cooling fluid.

Wall connection and ligament shape: Wall connection also has a significant impact on the heat transfer of foams. Hachesschmidt (2005) also reached the same conclusion, of which different connection methods such as soldering, and gluing were investigated, and soldering came out to be the most efficient method. Soldering achieved an overall heat transfer which is 2-3 times better than with no connections. However, the application cost of soldering is very high for metallic foams, therefore, it is hard to apply to industrial manufacturing processes.

Pore size and shape: Pore size is just one apparent parameter characterizing the structure of a porous material. In a porous material, the pore size is the diameter across a single pore as indicated in Figure 13. Even though pore size can be controlled, it is difficult to produce porous media with constant pore size [143]. Average pore size is normally used if the porous metal has uniformly distributed pores of regular shapes. Pore size is controlled differently across various methods of producing porous media. If the size and shape of the space holder can be maintained throughout the process, then porous metals with a controlled pore size can be achieved.

Pore-size has a direct influence on the porosity and the permeability of metallic foam or porous metals to fluids. A decrease in the pore size causes a decrease in the permeability of the foams and hence a higher pressure drop. For heat transfer capability of the foam, the pore size is critical for convective heat transfer. Specific surface area increases also directly cause an increase in active surface area for heat transfer. Several researchers such as Mahdi et al [144], Zhao et al [140], Hutter et al [145] and Bhattacharya and Mahajan [146] reached the same conclusion.

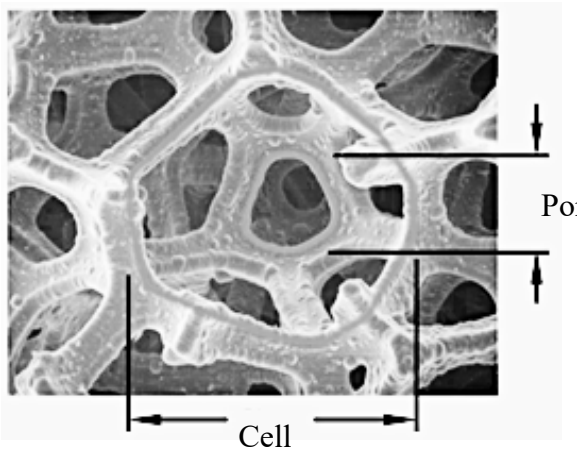

Figure 13: SEM image showing the pore and cell size of a porous material [147].

4.4.1 Heat Transfer through the porous metals

Heat transfer across a porous metal is mostly dominated by thermal conduction through the solid matrix (e.g. cell walls), with some heat transferred by thermal conduction through the fluid matrix (pores) and thermal radiation between cell walls and convection heat transfer across the pore as indicated in the schematic diagram in Figure 14 shown below. The effective thermal conduction of a porous metal will be given by the four contributions;

$$k = k_s + k_f + k_{conv} + k_{radi} \quad (2)$$

where k is the total thermal conduction, k_s is the conduction through the solid matrix, k_f is the conduction through the fluid matrix, k_{conv} is convection and k_{radi} is the radiation.

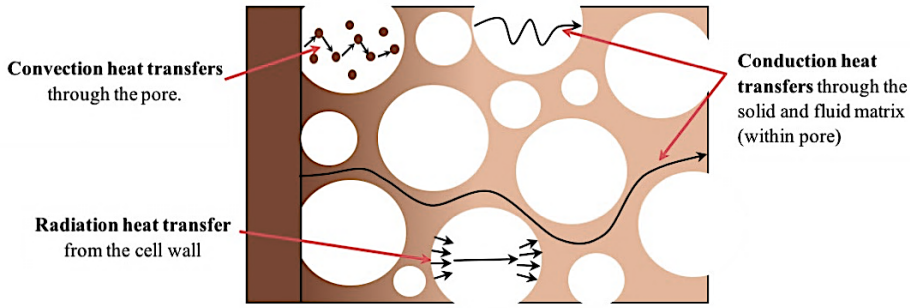

Figure 14: Heat transfer within a porous metallic structure by radiation, convection and conduction [148].

Care should be taken with such combinations of contributions however, as unlike the thermal conductivity of a dense material, which only depends on one mechanism, driven by the temperature difference across the material, the variation in conductivity with temperature for a porous material will be complex, due to the differing effects of temperature on each of the four contributions considered. The thermal conductivity of the porous metal is therefore mostly dependent on the base material and other properties such as the pore size, porosity and interconnectivity and the flow properties of the fluids through them [1].

4.4.2 Conductive heat transfer

Conduction can be understood as the mechanism which enables direct heat transfer from a higher temperature region to a lower temperature region through the solid matrix. It is mostly influenced by temperature gradient and the thermal conductivity of the conducting medium. However, the conducting medium and high temperature region have to be in direct contact with each other to enable conduction. Heat conducting through a metallic foam or porous medium has been reviewed by several authors, with some of the recent reviews performed by Russell et al [1], Kaviany [149], Nield [150], Whitaker [151], Cheng [152] and Hsu [153].

Table 5: Thermal conductivities of some of the commonly used materials [154]**.**

Materials	Thermal Conductivity	
	$Wm^{-1}K^{-1}$	$Btu^{-1}hr^{-1}ft\ °F$
Silver (pure)	400	237
Copper (pure)	385	223
Aluminium (pure)	202	117
Nickel (pure)	93	54
Iron (pure)	73	42
Carbon steel, 1%	43	25
Lead (pure)	35	20.3
Stainless steel (15%Cr, 10% NI	19	11.3
Chrome-nickel steel (18% Cr, 8% Ni)	16.3	9.4
Water (pure)	0.556	0.327
Air	0.024	0.0119

In a porous medium, the heat transfer through the solid matrix network occurs by conduction, in a similar way as in dense material, except that, within the pores, it occurs mostly by convection as already mentioned. Therefore, the rate of heat transfer across the porous medium by conduction also depends on the ability of the base material to transfer heat measured by its thermal conductivity (thermal conductivities of commonly used materials are mentioned in Table 5). However, the amount of solid matrix available for heat transfer by conduction depends on the relative density or porosity, as well as the integrity and morphology of the cell wall or the morphology of the cells [72]. With heat transfer by radiation increasing with absolute temperature it is safe to assume that from room temperature up to moderate temperature values, thermal conduction through the solid matrix dominates.

$$\frac{Q}{A} \sim \frac{\partial T}{\partial x} \tag{3}$$

If the proportionality constant is inserted in the equation above it becomes as follows;

$$Q = -kA\frac{\partial T}{\partial x} \tag{4}$$

where Q is the heat transfer rate in J per unit time, A is the surface area of the hot surface (m^2), $\partial T/\partial x$ is the temperature gradient in the direction of the heat flow (K/m), k is the thermal conductivity of the material (W/mK), and the negative sign is included in the equation to satisfy the second law of thermodynamics.

4.4.3 Radiative heat transfer

In this method, heat transport does not rely upon any contact between the heated body and cold body as is the case with heat convection and conduction. No medium is required in this method therefore, with the movement of heat usually referred to as in waves, because there are no molecules involved. Heat transfer depends on the surface properties of the hot medium such as colour, surface orientation etc. The energy is transmitted through electromagnetic waves called radiant energy generated by the thermal motion of charged particles in matter which causes heat transfer due to the temperature gradient. A hot surface may emit thermal energy at rate directly proportional to the surface area and the fourth power of the absolute temperature as follows;

$$q_{emitted} = \sigma_B A T^4 \tag{5}$$

where σ_B is the Stefan-Boltzman constant.

$$Q_r = \sigma_B \in A(T_s^4 - T_w^4) \tag{6}$$

where $\in$ is the emissivity function of the radiative surface, T_s is the temperature of the radiative surface and T_w is the temperature of the walls of a known distance from a radiative surface.

4.4.4 Convective heat transfer

Heat transport across the pores occurs mostly by convective heat transfer. It occurs when the heated fluid is caused to move away from a high temperature region, carrying heat with it, and may be ‘free convection’ or ‘forced convection’. Free convection is convective heat transfer that occurs when a hot body is exposed to cooler environments without any source of external fluid motion. The heat transport is due to the pressure gradient which in turn results from density differences induced by the temperature gradient of the fluid. In forced convection, the air is forced to flow by means of external sources such as fans, pumps or compressors. The heat transfer by fluid convection within the closed pores is usually negligible within porous metal (PM) with smaller pore size because the amount of convection that can occur in a limited volume of fluid within the pores is many times smaller than the heat transfer by conduction through the base metal. This becomes a different case with open pore structures because the possibility for heat transfer by fluid convection is significantly increased [1].

4.5 Mechanism of forced convection

Heat transfer by forced convection is complicated since it involves a fluid flow mechanism as well as heat conduction from a heat source. This topic was covered by several authors [155]–[163] in trying to understand the fluid flow and heat transfer mechanism around a hot or warm surface. Fluid flow is directly influential to the heat transfer rate. The rate of heat transfer is usually higher under forced convection because the fluid movements are quicker therefore transferring heat at a higher rate. The equation 7 below can be employed to calculate

the rate of conductive heat transfer from a hot body into the fluid expressed by Fourier's law as follows;

$$\dot{q}_{cond} = -k_f(\frac{dT}{dx})_w \quad (7)$$

where $q = q/A$ is the heat flux, k_f is the thermal conductivity of the fluid, $(dT/dx)_w$ is the temperature gradient in the wall.

The rate of convective heat transfer is expressed by Newton's law of cooling:

$$\dot{q}_{conv} = h_c(T_w - T_L) \quad (8)$$

OR

$$\dot{Q}_{conv} = h_c A(T_w - T_L) \quad (9)$$

where T_w is the wall temperature, T_L is the wall temperature some distance from the high temperature surface, h_c is the heat transfer coefficient, and A is the surface area of the material.

4.5.1 Fluid Flow Over Flat Plate

Heat transfer by convection depends on the ability of the solid material to transfer heat (heat transfer coefficient, h_c), and the surface area of the solid material as shown in Equation 9. h_c is highly dependent on the surface properties of the material (e.g. roughness, porosity etc.), fluid properties and the fluid flow type (laminar or turbulent). Therefore, it is important to understand how a simple flat and solid surface (without complex surface properties) interacts with the fluid flow. A schematic diagram in Figure 15 is a representation of the fluid flow pattern over a hot plate. As the colder air flows over a hot surface, in fluid dynamics, it is assumed that at a solid boundary, a fluid in motion comes to a complete stop and has a zero-

velocity relative to the surface. In this case, a fluid which is in direct contact with the hot solid sticks to the surface because of '*viscous effects*' allowing no slip. This is known as the '*no-slip condition'*. This condition results in a surface drag, a force exerted on the solid surface by the flow field. The presence of the hot plate along the fluid flow is felt up to a certain distance from the plate beyond which the fluid velocity remains constant. This region is referred to as the '*velocity boundary layer'*.

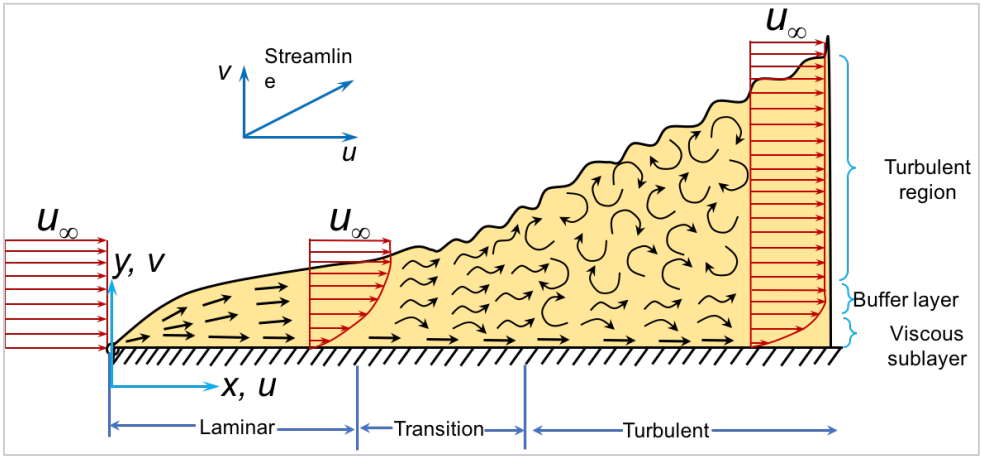

Figure 15: Velocity boundary layer over a hot flat plate [164].

The velocity boundary is thinner at the leading edge of the flat plate and increasingly widens towards the trailing edge. At the leading edge, usually called the upstream portion, the flow field pattern is generally laminar and goes through a transition region where it converts into a turbulent flow within the trailing or downstream portion. The turbulent layer is characterised by highly disordered motions and velocity fluctuations. The thickness of the boundary layer is usually referred to as the displacement thickness. The displacement thickness depends on the Reynolds number which is the ratio of the inertial forces to viscous forces, and it is as follows:

$$Re_l = \frac{ul}{v} \tag{10}$$

where u is the velocity of the fluid, l is the characteristic length of the flat plate and v is the viscosity coefficient of the cooling fluid.

4.5.2 Fluid Flow Around Circular Cylinders

A circular cylinder is a typical example of a obstacles used to explain the fluid flow because of complicated phenomena such as flow separation, and vortex shedding etc. It is also relevant to many aerodynamic engineering applications. In a certain Reynolds number range, fluid flow past a circular cylinder usually experiences boundary layer separation and flow oscillations in the wake region behind the blunt. The flow pattern and the drag on a cylinder are a function of Reynolds number $Re_D = uD/v$, which is in turn dependent on the cylindrical diameter D and the undisturbed free-stream velocity u. Flow patterns generated around a circular cylinder at varying Reynolds number from Ref. [165], are shown in Figure 17, where a combination of a uniform flow and circular surface are applied for simplicity[166]. The equations below can be used to summarise these phenomena:

$$Re_D = \frac{uD}{v} \tag{11}$$

where D is the cylindrical diameter, u is the undisturbed free-stream velocity and v is the viscosity coefficient of the cooling fluid. However, the Reynolds number is the ratio of inertial to viscous forces in the flow and the drag is commonly expressed as a coefficient

$$C_d = \frac{d}{\frac{1}{2}\sigma u D} \tag{12}$$

where d is the drag force per unit span and σ is the mass density of the fluid.

In real engineering applications, other factors such as surface roughness and non-uniform flow make it complex to study and predict the flow behaviour around circular cylinders. In an attempt to understand the effect of surface roughness on the fluid flow behaviour Ref. [167] used both computational and experimental approaches. Several researchers studied the flow field over a circular cylinder with smooth surfaces [168]. To understand and visualize

the fluid flow behaviour particle image velocimetry (PIV) is usually preferred. Said et al [159] studied the structure of the flow field around three-dimensional circular cylinders, both experimentally and using a numerical modelling using a PIV system. As expected, after studying the fluid flow around the circular cylinder exposed to air flow with different velocity, the results showed the dependence of flow structure around the circular cylinder obstacle on its Reynolds number [159]. Ref. [169], [170] also used PIV to experimentally study the flow field in the near-wake region of a surface-mounted finite circular cylinder. Ref. [163] investigated the flow field after splitter plates were inserted within the wake region. Figure 16 shows a typical flow pattern around a circular cylinder at a relatively high Reynolds number.

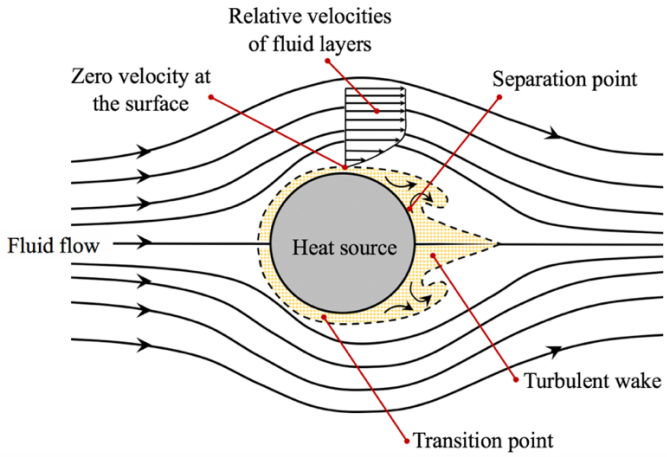

Figure 16: A typical fluid flow pattern around a cylinder at relatively high Reynolds number [156].

Figure 17 shows the flow pattern around circular cylinder within the Reynolds number range of $5 < Re_D < 3.5\times10^6$. At $Re_D < 5$, from the stagnation point, the boundary layer remains laminar though the diameter of the circular cylinder as shown in Figure 17 (a). In Figure 17 (b) (at $5\text{-}15 < Re_D < 40$), the fluid flow is laminar with a pair of vortices fixed in the wake region. At $150 < Re_D > 3 \times 10^5$, the boundary layer from the stagnation point to a separation point is laminar and the wake stream becomes turbulent leading to a three-dimensional flow of the wake region at an increasing rate. The boundary layer transforms into a turbulent layer,

resulting in a disorganised and narrower wake region[168]. A turbulent vortex stream at $Re_D > 3.5 \times 10^6$ becomes narrower than at $150 < Re_D < 3 \times 10^5$.

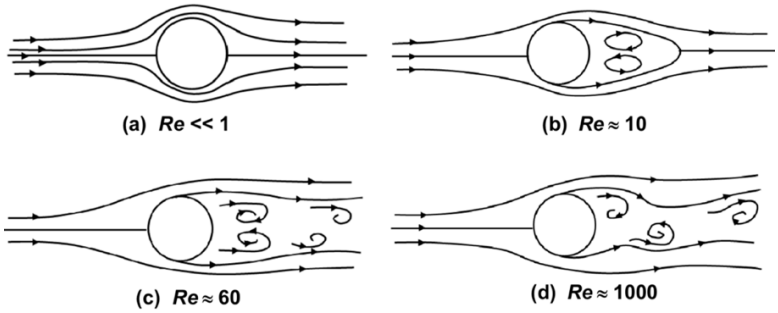

Figure 17: A sequence of different developing stages of fluid flow generated around a circular cylinder [165].

The fluid flow around a cylinder, because of complicated phenomena such as vortex shedding and flow separation behind the cylinder, has been studied by many researchers and scientists. They applied some methods and devices to control this flow. Most of these techniques work by changing the boundary layer and the wake zone to obtain the best efficiency. Methods are classified in three groups: (1) passive control, (2) active control and (3) compound control. Passive control techniques do not need any external energy during application. Additional devices in the fluid flow or changing the geometry of the bluff body such as splitter plates, base bleed and roughness are applied in this method. Active control techniques such as EHD actuators and vibrators need external energy to affect the fluid flow. When active and passive techniques are applied simultaneously, it is called a compound method.

4.6 Application – Heat exchangers

The applications of porous metals are dependent on the structure. Closed cell porous metals are mainly reserved for structural applications, while open cell porous metals are often best used where their interconnected pores and continuous nature of the porosity are exploited

[77], [171]. The main potential areas of application of porous metals are summarized in Table 6, pointing out some attributes that makes them suitable for their application [77]. This report will focus mainly on the application of open cell porous metal as heat exchangers/heat sinks.

Table 6: Potential applications and relevant attributes of porous metals.

Application	Relevant Attributes
Light weight structures	Excellent stiffness-to-weight ratio when loaded in bending
Vibration control	Porous metal panels have higher natural flexural frequencies compared to the solid panel of the same metal.
Mechanical Damping	Damping capacity is larger than solid metals, goes up to 10x
Energy absorbers e.g. packaging	Closed/open cell porous metals has the ability to absorb energy applied at an approximately constant pressure
Heat Exchangers	Open-cell porous metals are permeable with larger surface area with high thermal conductivity though the cell wall.
Acoustic absorption	Open cell porous metals have sound absorbing-capacity
Biocompatible inserts	Cell texture stimulates cell growth
Filters	Open cell porous metals for high temperature fluid and air filtration.

Convectional heat sinks are designed to maximize the surface area in contact with the fluid (e.g. air and liquid) around it [172]. The heat transfer from the component is dominated by thermal conductivity of the materials used for the porous metal and the contact and interface conditions [173]. Copper and aluminium are best suited and most commonly used for these applications because of their high thermal conductivity. Even though aluminium is cheaper, light in weight and has low cost of fabrication, copper still has a higher thermal conductivity when compared to aluminium. Copper can be a preferred alternative if the cost of fabrication

can be minimized. The other important factor in the performance of the heat sink is surface area in contact with the medium which governs heat removal mainly by convective heat transfer [11], [173]. The design of the heat sink is also one of the important factors. The performance of the heat sink can be optimized by use of design and modelling software[173], [174].

Open-pore porous metals have become a very attractive research field for heat sink applications because of their huge internal surface area and permeability for fluids [46], [48]. Geometrically flexible, highly effective and multi-functional compact heat exchangers are being fabricated out of this category of porous metals. There are several parameters and mechanisms that determine the performance of such heat exchangers such as pore size, porosity, the interaction of the solid foam materials and fluid flowing through and the quality of the metal-to-porous metal bond.

There have been several reports of investigations into the actual performance of porous metals (especially porous copper) as heat exchangers (as opposed to the underlying properties). Porous copper heat-sink were successfully produced by a space holder method (lost carbonate sintering) invented by Zhao et al [27] was investigated for heat transfer performance and reported in Refs. [72], [75]. It was further commercialised by Versarien Technologies [29] going by the name VersarienCu. VersarienCu is a ground breaking, porous metallic heat sink offering a heat transfer coefficient of approximately 150 – 200 kW/m^2K. The pore size is in the range 20 μm to 1mm with porosity levels of up to 85%. Lotus-type porous copper [21] is another type of porous copper consisting of different structural features also offering better heat transfer performance [121], [175]–[179]. Lotus-type porous copper can reach a heat transfer coefficient as high as $5W/cm^2K$ achievable when porosity is 29% and mean pore diameter is 400 μm [179]. An even larger heat transfer coefficient of 9 W/cm^2K can be

achieved by sectioning the porous copper along the vertical direction of the pore axis into four or eight equal sections aligned in the direction of the pore axis.

CHAPTER 3. EXPERIMENTAL METHODS

This chapter presents the experimental methods and step by step procedures followed during processing and assessment of the double-layered porous Cu samples. The section is split into four main sections.

Section 3.1 describes the processing routes of the sample in this research of which powder metallurgical processes were employed; lost carbonate sintering developed by Zhao et al [27] was applied to tape casting.

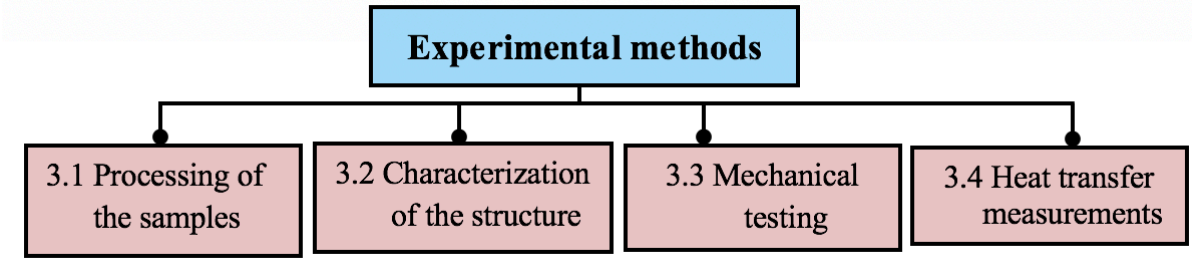

Figure 18: A flowchart of the main experimental methods

Section 3.2 covers the structural analysis of all the samples involved in this study. This includes porosity, pore structure and pore distribution, density measurements as well as the chemical composition.

Section 5.2 describe the mechanical properties of the samples involved in the study. Finally, Section 5.3 which covers the heat transfer measurements of the samples.

3.1 Processing of the Samples

The samples in this study were produced by powder metallurgical processes: the lost carbonate sintering process developed by Zhao et al [27] applied to tape casting. Combining the two processes is novel for production of porous copper or copper foams. Processing of the samples begins with material selection, which was mainly based on the literature and trial experiments in this study. The materials or chemicals entering the slurry in the production of the samples are usually classified as organic binders (or additives). The binders were mainly required to enable tape casting of the powders into thin sheets and impact green strength which is mainly required for easy handling of the sample, as well as maintaining the shape and generating porosity. Step-by-step procedures of sample processing are fully covered in this section.

3.1.1 Raw materials and chemicals

- *Primary powders:* Two primary powders were used in this approach; dendritic copper (Cu) powder (see Figure 19 (a*)* (av. particle diameter ≈ 50 μm) from Goodfellow, Cambridge, UK and potassium carbonate (K_2CO_3) from Alfa Aesar, Lancashire, UK (see Figure 19(b)) The copper powder had a purity of more than 99% and was used as the main matrix of the sample during processing. The typical dendritic copper powder and potassium carbonate powder are shown in Figure 19 below. Potassium carbonate is a leachable space holder, used to introduce and control porosity, pore size and shape of the final product. It has a solubility of 111 g per 100 g of water at 20 °C and a melting temperature of 891 °C. The density of copper and potassium carbonate was 8.96 g/cm^3 and 2.43 g/cm^3, respectively.

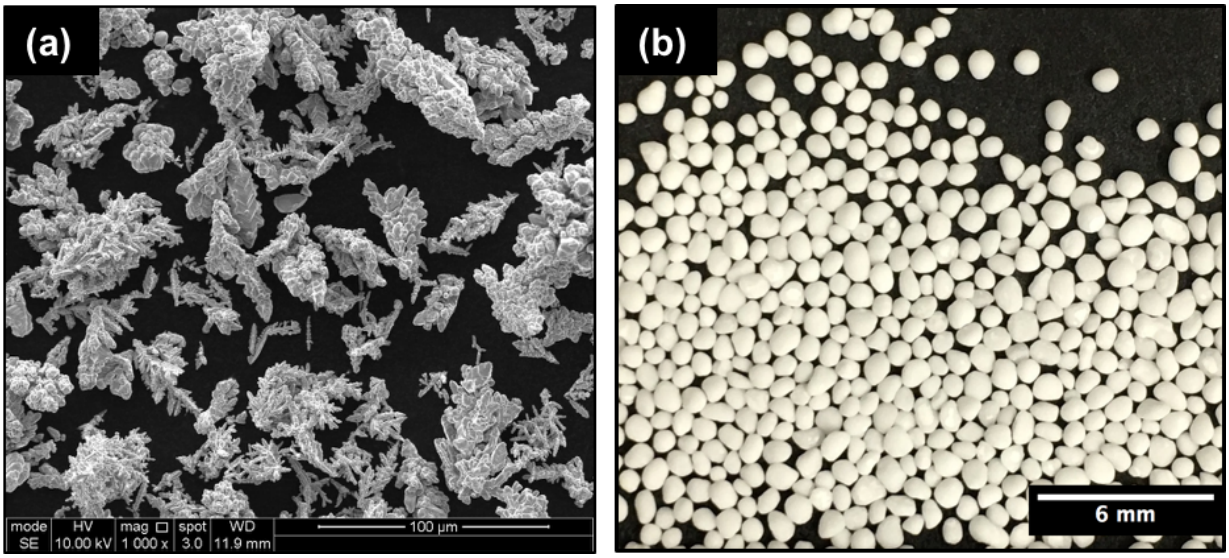

Figure 19: Two primary powders which were processed to make porous copper samples; a) dendritic copper powder with particle size of 50µm and b) potassium carbonate of average particle size 633µm used as a space-holder during processing.

- *Copper foil:* A thin copper – O.F.H.C (oxygen-free high conductive) foil supplied by Goodfellow, Cambridge, UK was used as a dense substrate in this investigation. The foil is supplied in the form of a foil of dimensions 0.125mm × 150mm (thickness × width). The foil was selected because of its compatibility with the tape caster available. The foil was 99.95% pure.
- *Solvent:* Azeotropic mixture of ethanol and 2-butanone at a ratio of 40:60 [38], [39] was selected as the solvent in this study because it has low temperature of vaporization and a low dielectric constant promoting a good wettability of both the copper powder and potassium carbonate. The mixture has a low boiling point and is also nonreactive to both copper and carbonate space holder. This allows the solvent to be easily evaporated from the green tape at low temperatures. To protect the vacuum furnace from failure and damaging the vacuum pumps, it is important to evaporate most of the solvent prior to debinding and sintering, and due to low temperature of vaporizations most of the solvent is removed using the ventilation system and heater installed on the tape caster.

- *Triphenyl Phosphate:* To ensure the best de-agglomeration and dispersion of the powders in a slurry, triphenyl phosphate was selected as a dispersant. It leads to good dispersion of primary powders in the slurry by introducing repulsive forces between the particles [9]. This occurs by electro steric mechanics, but some dispersants use an electrostatic mechanism for repulsion depending on their chemical composition.

Table 7: Chemicals entering the slurry for processing the green copper tape by tape casting.

Chemical	Role	Topologic Formula	Aspect	Degradation Point (°C)	Mass
Dendritic Copper powder	Solid Matrix	Cu (metallic)	Solid Powders (50µm) Reddish brown Colour	Melts at 1084ºC	110g
Potassium Carbonate	Space – Holder	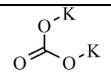	Solid powder White colour	Melts at 891ºC	-
Ethanol	Solvent	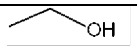	Liquid Colourless	Boils at 78.37ºC	-
2-butanone	Solvent		Liquid Colourless	Boils at 79.64ºC	-
Di-butyl Phthalate	Plasticizer	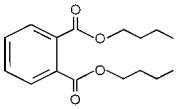	Viscous liquid Colourless	Boils at 340ºC	30g
Poly (Methyl Meth acrylate) - PMMA	Binder	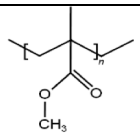	Solid powder White colour	Melts at 160ºC	20g
Tri-phenyl phosphate	Dispersant agent	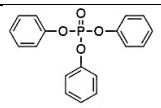	Solid flakes White colour	Melts at 50ºC	30g

- *Poly (Methyl Meth acrylate) (PMMA):* PMMA was selected as a binder, with a high molecular weight ranging from 120, 000 – 150, 000 g.mol^{-1} and a low boiling point of 160 °C. The binder transfers its mechanical strength to the green tape by forming organic bridges between the primary particles during evaporation of the solvent. Molecules of the binder bond to each other avoiding crack propagation during solvent

evaporation from the tape. Removal of the binder has to be easy, without having to reach high temperatures.

- *Dibutyl phthalate (DBP):* DBP was used as a plasticizer to ensure a good flexibility of the tape by lowering the glass transition temperature (T_g) of Poly (Methyl Meth acrylate) (PMMA). It decreases the T_g of PMMA by 45 °C, from 110 °C (PMMA only) to 65 °C (PMMA/DBP). Refs. [3] and [4] have shown that a mixture of PMMA/DBP in a ratio of 1:2 leads to excellent combination of green tape flexibility and mechanical strength. It has a low molecular weight of 300 g/mol and a boiling point of 340 °C.

3.1.2 Equipment/Machines

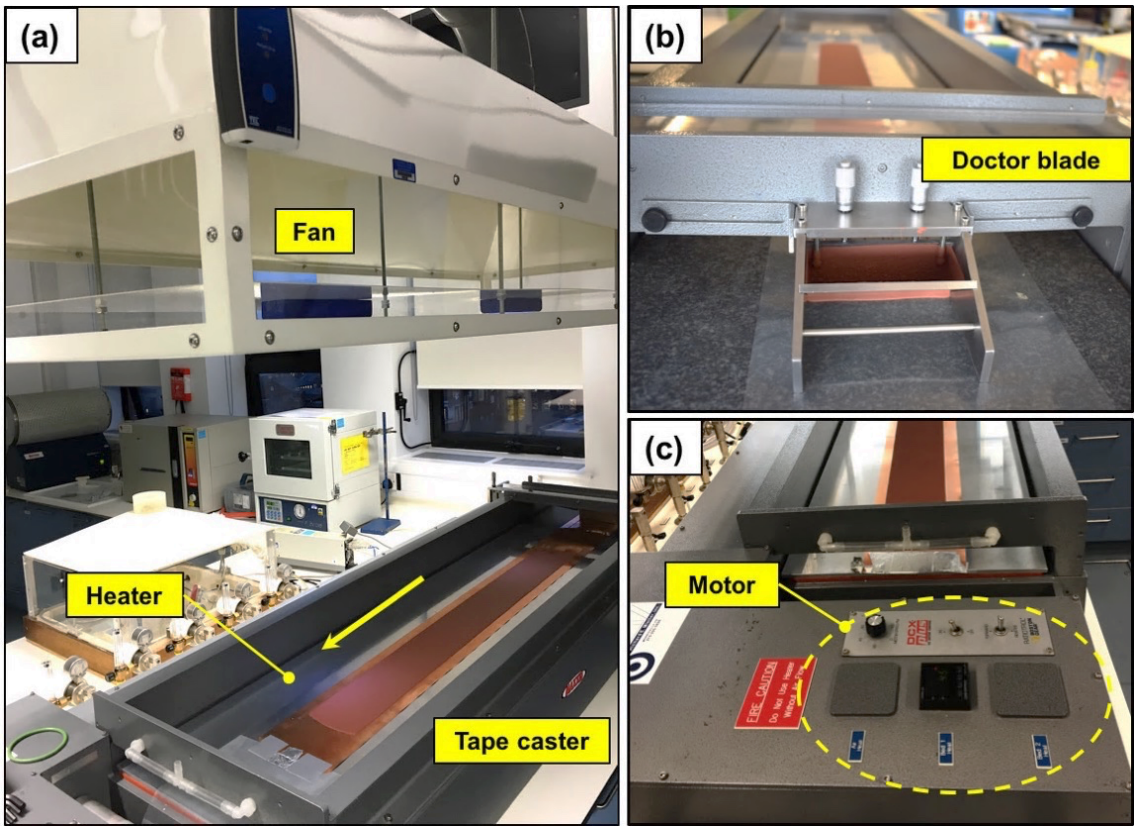

Figure 20: Tape casting machine used for processing the samples (a) tape caster, (b) adjustable doctor blade and (c) motor section.

- A **tape casting machine** was used in this work to cast a homogenously mixed copper slurry into thin tapes. It was equipped with a built-in heater and a ventilation system for drying purposes. It also consisted of an adjustable doctor blade (see Figure 20 (b)) to control thickness of the tapes, and a built-in motor for moving the tape. There are two typical tape casting machines; a moving doctor blade and a stationary doctor blade type of tape caster. In this work, a tape caster with a stationary doctor blade was used. The slurry is deposited on a carrier film (copper substrate) driven using a motor. The speed of the motor and the temperature of the heater (located on the base of the tape caster) can easily be controlled.
- **Electronic Weighing Balance** with accuracy of 0.0001g was used for weighing all the chemicals and the powders (components of the slurry) throughout sample preparations.
- To promote homogeneity, a **high-energy speed mixer (**Speedmixer^{TM} Hauschild Flak Tek DAC 400FVZ) was employed to mix the slurry at high speed. The speed mixer has a speed range of 800 rpm – 2750 rpm and has a mixing capacity of up to 300g.
- **Vacuum Furnace** offered by Wallwork Heat treatment LTD (of Bury, UK) was employed for debinding and sintering all the green sample tapes under a clean and controlled environment (e.g. argon or vacuum).
- A **water bath** (distilled water) and **hot air gun** was used to remove the space holder (by dissolution) from the sintered samples and to dry the samples respectively.

3.1.3 Processing the Green Tapes

3.1.3.1 Procedure;

Porous copper samples in this work were processed using a combination of the two processes which will be explained below. The process combines a lost carbonate sintering process

developed by Zhao et al [27] and a tape casting process. Figure 22 shows a schematic diagram for processing the porous samples.

- **Weighing and Mixing;** The primary powders (Cu and K_2CO_3) and the organic binders (see **Table 7**) entering the slurry were weighed using an electronic weighing balance with accuracy of 0.0001g. The slurry components were mixed in three stages to avoid segregation and agglomeration within the slurry. Firstly, organic binders (dispersant, binder, plasticizer and solvent) were put together in a polypropylene mixing cup and mixed using a **high-energy speed mixer (**Speedmixer^{TM} Hauschild Flak Tek DAC 400FVZ) at a speed of 1600rpm for 15 minutes. Secondly, Cu powder was added to the viscous mixture of organic binders at 5 minutes intervals and mixed at 1200 rpm between the intervals until all the powder was added and homogenously mixed (25 minutes). A solvent was also added (to control the viscosity) until a coalesced slurry was obtained.

Lastly, K_2CO_3 was added to the viscous slurry and mixed at 1800rpm for 10 minutes. It is important to degas the slurry every 5minutes to avoid the pressure building up inside the mixing cup.

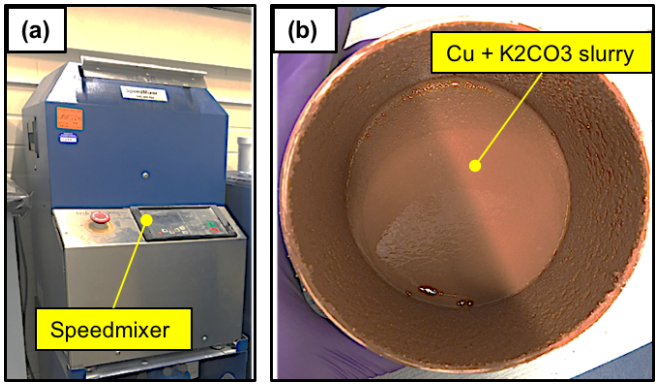

Figure 21: Preparation of the slurry for tape casting, a) high speed-mixer and b) homogenous slurry of Cu and K_2CO_3 mixed with organic binders prior to tape casting.

- **Tape Casting and Drying;** The slurry was immediately tape cast while still homogenous and viscous. The thickness and width (fixed) were controlled by an adjustable doctor blade. The speed of the moving substrate was controlled by the motor. Two processing routes were developed here to produce two batches of porous samples which are structurally different. A summarised flowchart in Figure 23 shows the two processing routes followed when tape casting the slurry. And, a step-by-step procedure of each processing route (route A and B) is explained next.

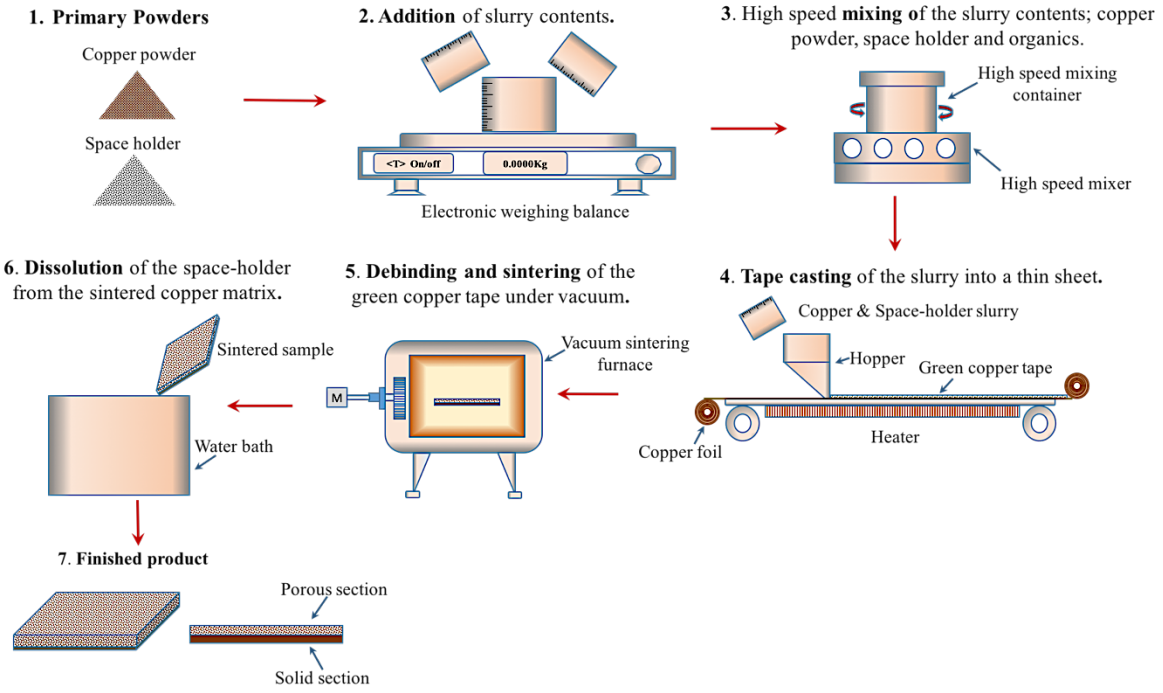

Figure 22: Schematic diagram for producing the porous samples.

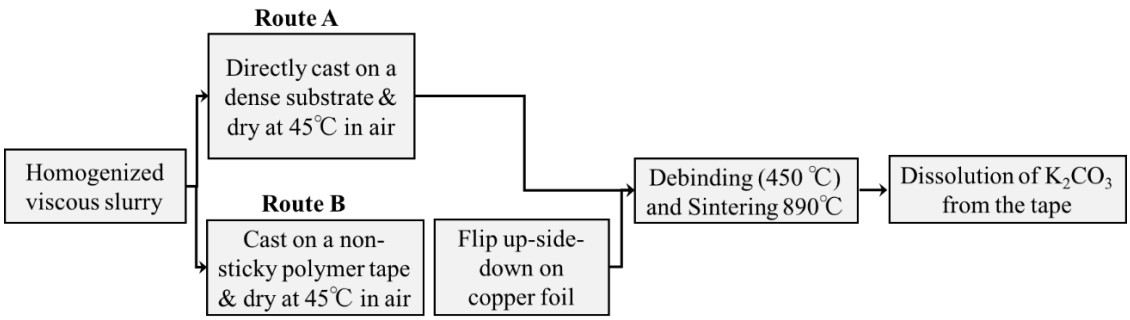

Figure 23: Two processing routes followed to produce porous copper samples by Lost Carbonate Sintering applied to Tape Casting

- ***Processing route A:*** In this route, the slurry was cast directly onto a moving copper foil through an adjustable doctor blade on the tape casting machine. The thickness and the width of the slurry were controlled by the stationary doctor blade. The slurry was then allowed to partially dry in air for 3 hours while still on the tape caster set at 40 °C. The green tape was then debinded and sintered using the Vacuum sintering furnace at 450 °C and 890 °C respectively following the heat treatment profile in Figure 30.

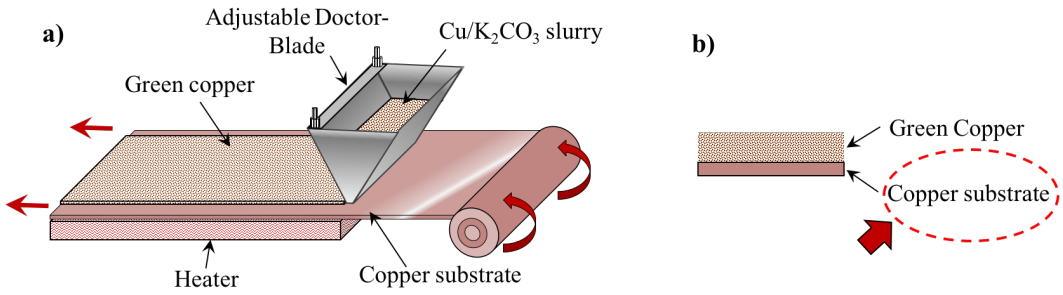

Figure 24: Schematic diagram of the tape casting process, a) a viscous slurry inside the hopper directly tape cast on to a moving dense copper substrate through an adjustable doctor blade, and b) double-layered green tape before debinding and sintering.

- ***Processing route B****:* In this route, one more step was added to the previous route (route A) during the tape casting process. The step was introduced to obtain a different pore distribution as compared to route A. Here, the slurry was deposited on to a non-sticky polymer film instead of copper substrate (silicone-mylar film) and allowed to dry under air while still on the tape casting machine set at 40 °C. Non-sticky tape allows the green copper to be easily peeled off after drying.

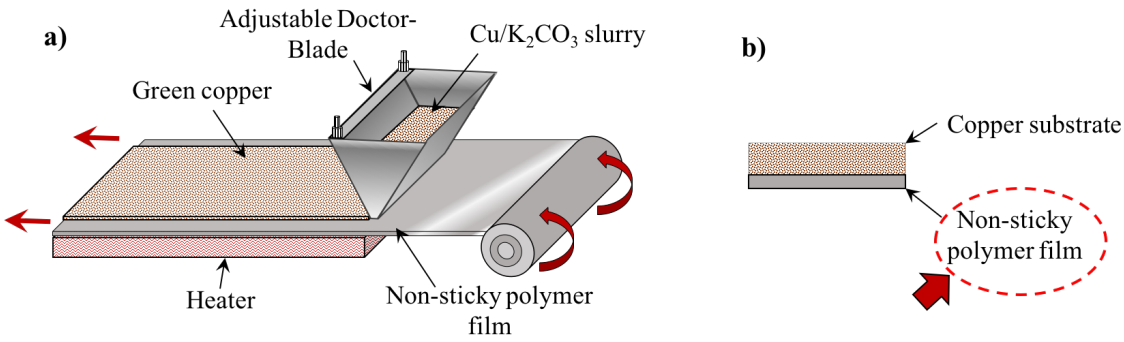

Figure 25: Schematic diagram of the tape casting process, a) a viscous slurry inside the hopper directly tape cast on to a moving dense copper substrate through an adjustable doctor blade, and b) double-layered green tape before debinding and sintering.

The solvent (azeotropic mixture of ethanol and 2-butanone) was lightly sprayed on the surface of the green tape to enhance bonding. The green tape was then immediately turned upside down (while still on the polymer film) on to the copper substrate and rolled down using a rubber roller to promote a good bond between the green section and copper foil. Similarly, the green samples were then taken through a debinding and sintering process following the heat treatment profile in Figure 30.

To generate pores in the sheets and obtain a wide range of porosities, 10-50 wt% K_2CO_3 was added during processing across both routes. Table 8 shows the quantities of K_2CO_3 in terms of weight percent, added to copper powder during production of samples with varying porosities. The pore size of K_2CO_3 particles ranged from 110 - 738µm**.**

Table 8: Amount of carbonate space holder added across the porous Cu samples produced

Processing Route	**Amount of Carbonate Space-holder Added, (Wt.%)**					
	Set 1 (0CuP)	**Set 2 (10CuP)**	**Set 3 (20CuP)**	**Set 4 (30CuP)**	**Set 5 (40CuP)**	**Set 6 (50CuP)**
A	0	10	20	30	40	50
B	0	10	20	30	40	50

3.1.4 Sample Coding

Eleven different samples were produced from processing routes A and B. Each sample was given a specific code for easy identification. A combination of letters and numbers were used in the code, which links to the fabrication process and the parameters used during processing. Figure 26 shows the breakdown of the sample code. The first two numbers in the code represent the amount of K_2CO_3 (0%, 10%, 20%, 30%, 40% and 50%) in weight percent added to copper powder during fabrication, CuP represent porous copper and the last letter represents the processing route followed when producing the sample (route A or B).

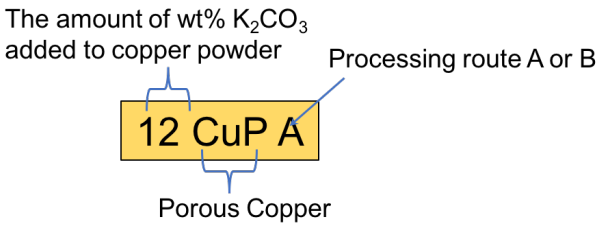

Figure 26: Breakdown of the sample code given to each porous copper sample fabricated and tested.

3.1.5 Debinding and Lost Carbonate Sintering:

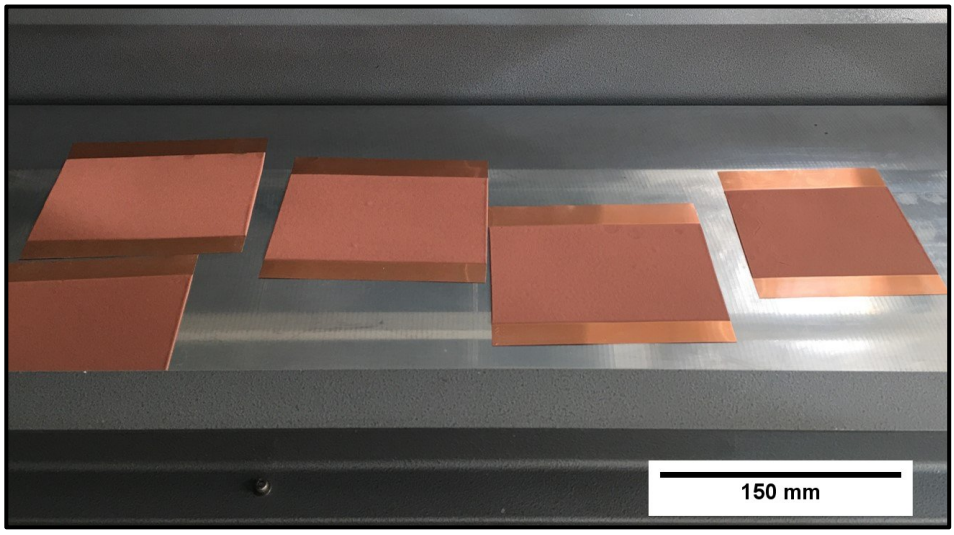

Figure 27: Green copper samples cut to smaller sizes before taken through a debinding and sintering process. The samples were tape casted on to copper substrate and dried at 40°C to evaporate most of the solvent.

“The efficiency of the debinding process was confirmed by carrying out thermogravimetric analysis (TGA) on green tape of copper” shown in Figure 27, before performing heat treatments. Some part of this work was published by the author. In this work, the decomposition behaviour of all binders used for producing the green copper tapes was investigated. The main objective was to determine the debinding temperature of the tape; the temperature at which all the binders decomposes from the tape.

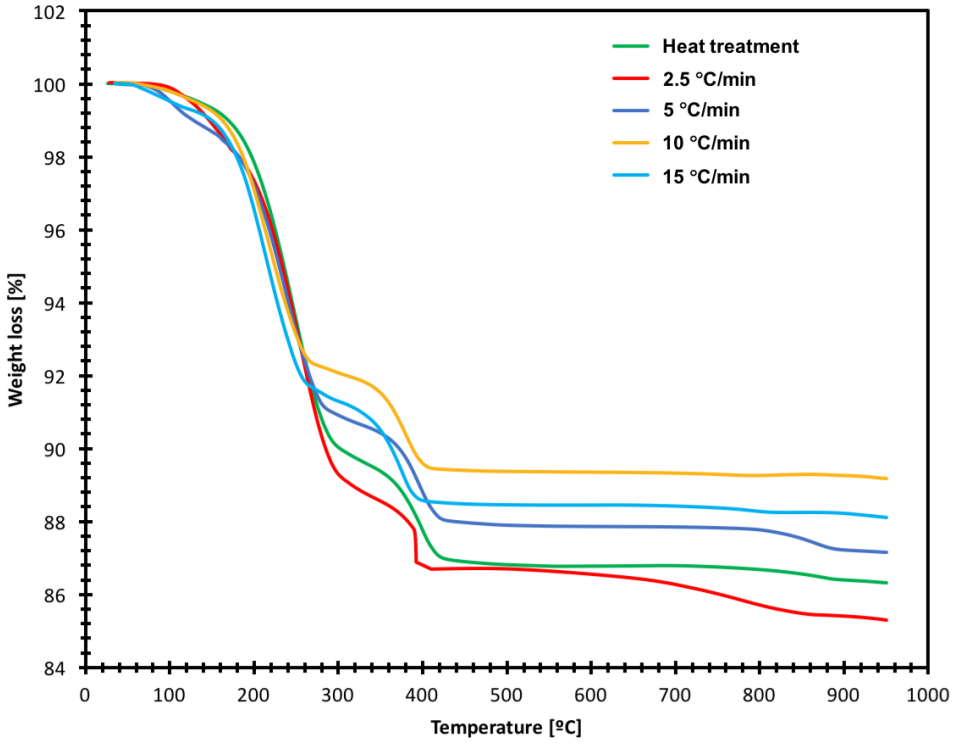

Figure 28: Thermo-gravimetric analysis results of green copper tapes, decomposed at different heat treatment rates (2.5 °C/min, 5 °C/min, 10 °C/min 15 °C/min and following heat treatment profile in Figure 30)

Figure 28 shows the graphs obtained from thermogravimetric analysis performed at different heating rates (2.5 °C/min, 5°C/min, 10°C/min, 15°C/min) and the last curve was obtained by performing TGA following the heat treatment profile shown in Figure 30. The burnout of each additive is clear from the graph (see Figure 28), the first mass loss labelled A on the graph, is the burnout of PMMA from the green tape, the second burnout labelled B corresponds to the burnout of dibutyl phthalate (DBP). It was demonstrated by the TGA

analysis that both PMMA ($T_{Melting}$ = 160 °C), DBP ($T_{Melting}$ = 340 °C) and other organics ($T_{Melting}$ <80 °C) are eliminated from the green tape after 400 °C.

It is therefore expected that, at temperatures above 400 °C, all organics are completely decomposed from the green copper tape. Therefore, 450 °C was chosen as the debining temperature throughout the debinding process. There was also a slight burnout of K_2CO_3 ($T_{Melting}$ = 890 °C) at temperatures ranging from 700 °C - 890 °C. It is evident from the graph that during TGA, the heating rate of the green tapes has slightly affected the burn out of the organics especially at slow heating rates (2.5 °C/min and 5 °C/min). 890°C was chosen as the sintering temperature of the samples.

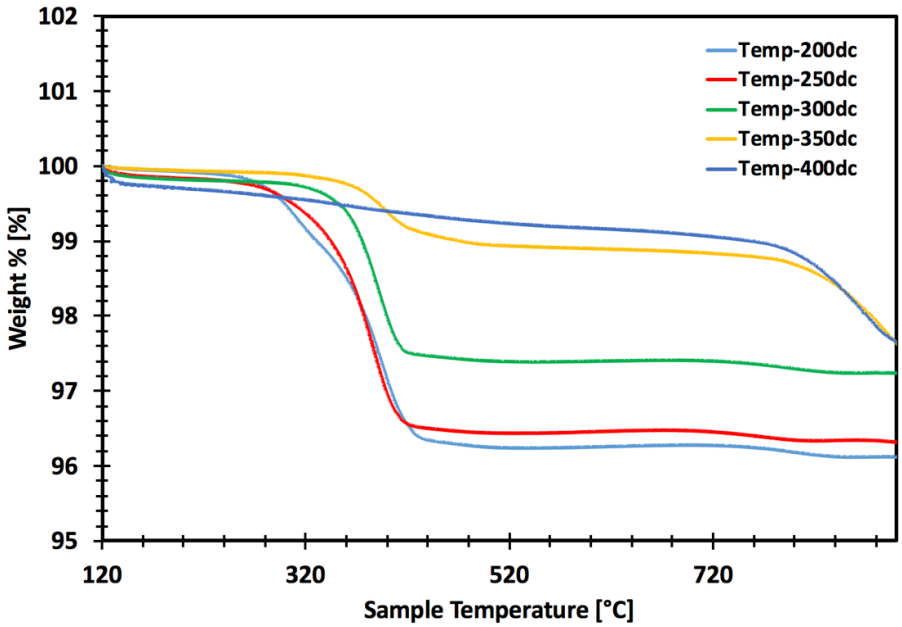

Figure 29: Thermo-gravimetric analysis on green copper tapes sintered at different temperature; 200 °C, 250 °C, 300 °C, 350 °C and 400 °C.

To confirm that all binders were decomposed at 400 °C, green copper samples were heated at five different sintering temperatures (200 °C, 250 °C, 300 °C and 400 °C), and TGA was performed on them and the results are shown in Figure 29. There was no mass loss at 400 °C on samples sintered at 400 °C, and this confirms that all binders were burned out at 400 °C. 400 °C was therefore, selected as the lowest burnout temperature throughout the processing.

After TGA, the heat treatment profile (debinding and sintering profile) is shown in Figure 30 produced and followed for all the heat treatment processes applied on the green samples. The green tapes from both processing routes were debinded and sintered for 6 hours at 450 °C and 890°C respectively following the heat treatment profile (see Figure 30). To minimise oxidation, the tapes were debinded and sintered under argon and vacuum controlled environments at Wallwork Heat treatment LTD, Bury, UK using a vacuum sintering furnace. After sintering, the samples were allowed to cool to room temperature while still under vacuum. It was ensured that the sample were kept under an air tight environment to minimise the sample reactions with air or moisture and avoid contaminations. Finally, the carbonate space holder was removed from the sintered tapes by dissolution using warm water by stirring, and the final porous sample was dried under a dry hot air.

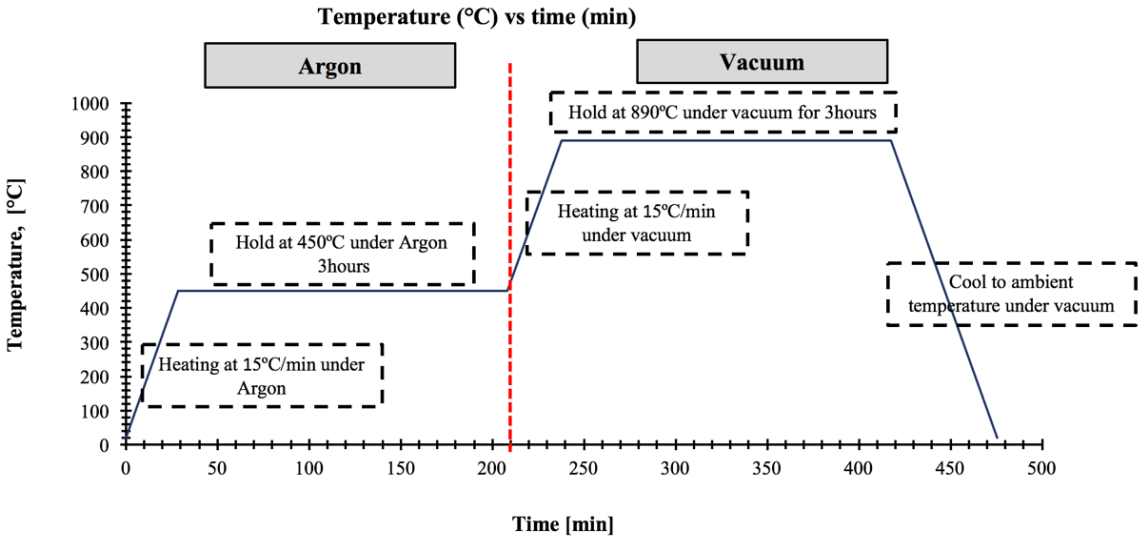

Figure 30: The heat treatment profile for debinding and sintering green copper tape.

3.1.6 Carbonate space holder removal

After sintering, the carbonate space holder was removed from the sintered structure by a dissolution route; leaching out the K_2CO_3 by stirring in a distilled water bath. To ensure that

all carbonate was removed, the dissolution was prolonged (for 10 minutes). Finally, the tapes were then dried using a hot air gun until completely dry.

To determine the appropriate technique for dissolving the K_2CO_3 from the sintered samples, three different dissolution techniques were investigated. The first technique investigated involved stirring the sample in a distilled water bath at 1 rpm. The second technique utilises an ultrasonic bath, and lastly the K_2CO_3 was dissolved by dipping the sample in a still water bath. Dissolution was carried out until all K_2CO_3 was removed from the sample. The results of the test shown in Figure 31 allows the identification of the most effective and efficient technique among the three.

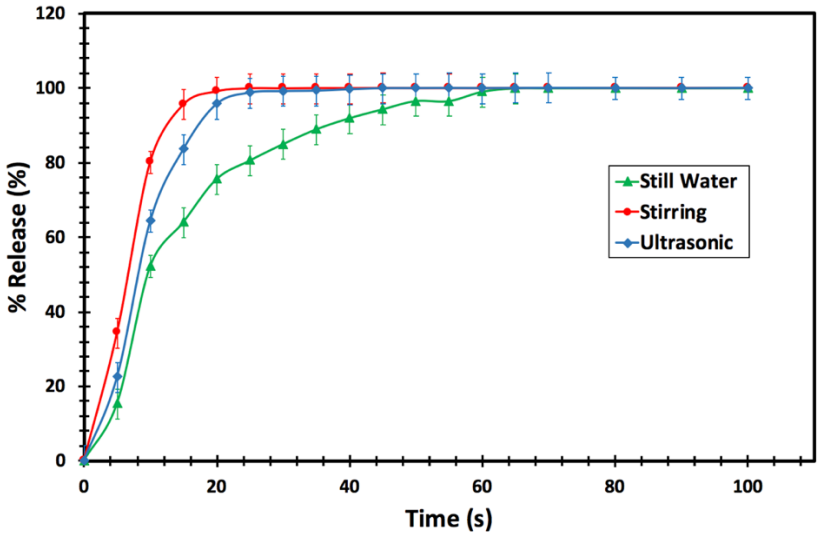

Figure 31: Dissolution tests of K_2CO_3 from sintered samples by three different approaches; dipping the sample in still water, stirring the sample in a water bath and dipping the sample in the ultrasonic bath.

3.2 Characterisation of the Structure

3.2.1 Scanning Electron Microscopy (SEM)

The porous samples produced in this work are expected to behave differently depending on their structure. The structure of the samples is, in turn, strongly influenced by the process adopted during production. SEM analysis (SEM - Inspect F in Sorby Centre, University of Sheffield) was performed to examine the structures of porous samples. SEM analysis was also used to investigate the change in structure throughout the processing steps (from tape casting, debinding and sintering of green tapes).

3.2.1.1 Sample preparation and mounting

Both green samples and sintered samples were mounted in a similar way. Approximately 15 mm by 15 mm was cut and mounted on an aluminium sample holder. Conductive carbon stickers were used to mount the sample on the sample holder. The total diameter of the holder and the sample was 32 mm and a thickness of approximately 5mm. The sintered samples were cleaned (and dried) using isopropanol in an ultrasonic bath before mounting to get rid of the grease and dirt on the sample. To mount the sample (porous tapes) along the thickness, silver paste was used to hold the sample in place.

In a case where imaging of the internal structure of the sample was required, the sample was ground to reveal the structure. However, the sample was ground before the removal of the space holder (K_2CO_3) from the sintered sample to ensure that the pore structure was not distorted during grinding. After grinding, the space holder was dissolved from the samples. Finally, the sample was cleaned and mounted on the sample holder.

3.2.1.2 SE Settings and Parameters

The SEM offers a high-resolution imaging of the sample by rastering a focused electron beam on the surface of the sample and detecting the secondary or backscattered electron signal. Samples were evaluated in an SEM- Inspect F in Secondary Electron (SE) configuration for topographical features. The tungsten filament operated at 15kV and spot size of 3. The working distance ranging from 10 – 11.5 mm was used. The smallest magnification was used to obtain images for porosity measurement to achieve a wider distribution of the macropores within the sample. For micropores and detailed imaging where great depth of field was required, a slightly higher magnification was used. To ensure quality images, astigmatism was corrected and also the aperture was aligned in between sessions.

3.2.1.3 Post Data Analysis

The data was analysed using a dedicated *ImageJ* software to give porosity, pore size distribution, fracture surfaces, and particles/organics distribution.

3.2.2 Surface Porosity

Actual size image analysis was employed to analyse the structure of the porous sample mainly to study the three different pore parameters, which are total surface porosity, pore size distribution and pore shape. The samples were photographed in low to medium light conditions. The aim was to obtain images with a clear contrast between the pores and the continuous surface regions, both micropores and macropores. High resolution SEM micrographs were also used to evaluate the micropores. Images were calibrated and processed using ImageJ [180], [181]. An individual threshold was applied to each image, taking care not to alter the apparent pore diameter. Surface defects that appeared dark but were not

identified as pores were manually removed. Particle analysis was also performed in ImageJ, obtaining the cross-sectional area, major and minor axes for each pore. Figure 32 shows the processed image where each pore was counted and measured as the closest-fitting ellipsis. The measurements obtained were analysed using Prism version 7 for Mac OS X 10.9, GraphPad Software, La Jolla California USA, which provided frequency analyses for each sample as well as K_2CO_3 particles.

$$P_{Total} = P_{Macro} + P_{Micro} \tag{13}$$

Total surface porosity (P_{Total}) was calculated as the sum of micro porosity (P_{Micro}) and macro porosity (P_{Macro}). During processing the microporosity resulted from incomplete densification of the copper particles while the macroporosity is as a result of leachable potassium carbonate. Both macroporosity and microporosity were analysed separately using *ImageJ* on images acquired by SEM.

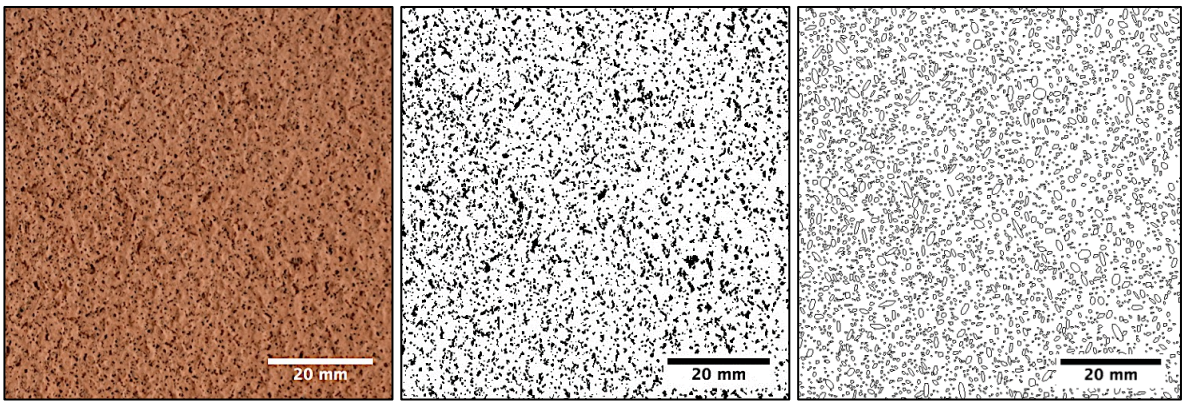

Figure 32: Actual size images obtained by Nikon D5300, and b) image processed by ImageJ and c) analysed by Prism version 7.

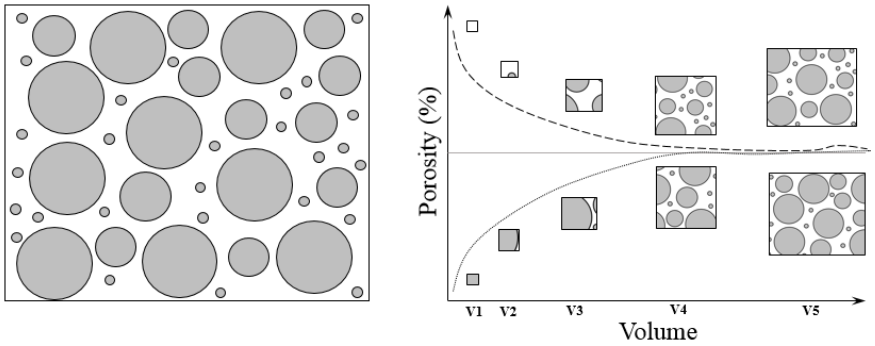

Figure 33: Representative Elementary Volume (REV) followed during imaging and porosity analysis [182].

SEM images for macroporosity analysis were acquired at a lower magnification to have a wider distribution and a reasonably good number of the pores. For microporosity analysis, higher magnification images were captured. Each image was calibrated before analysis to ensure consistency throughout the images. Representative Elementary Volume (REV) shown in the schematic diagram and the curve in Figure 33 were followed for both imaging and porosity analysis to ensure quality of the data.

Pore size: Macro pore size of the samples is highly dependent on the particle size of the space holder (potassium carbonate). From the particle size measurements, the size of the particles ranges from 360 – 890 µm.

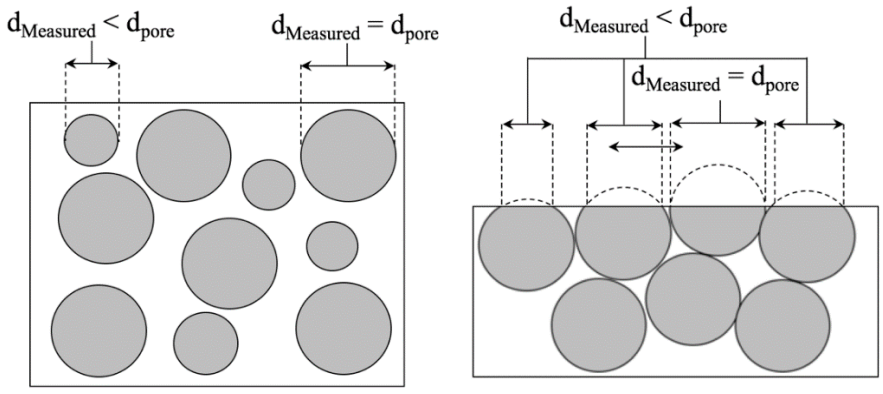

Figure 34: Schematic diagrams showing how the intersections of a random plane across the surface or thickness of a porous medium. It shows how the space-holder will produce a lower mean pore size than is actually the case on the sample [183].

Average pore size and porosity can be obtained from these simple measurements shown in Figure 34. The average measurements of these parameters will always be less than is actually the case.

3.2.3 Density Measurement

It is important to note that the density (ρ_a) of porous metal analysed here was the bulk (apparent) density not true (skeletal) density (ρ_m). To calculate the bulk density (ρ_a), the sample was first measured using Vernier callipers to obtain the total volume, V_a, (pore plus metal matrix). It was then weighed using an electronic weighing balance with a tolerance of 0.0001 g to obtain true mass (m_m) of the porous sample (solid matrix). True volume (V_m) was measured using a gas helium pycnometer *(Accupyc II 1340, Micromeritics)* to obtain true density

$$Vf_m = (1 - \frac{\varepsilon}{100}) \tag{14}$$

$$\rho_a = Vf_m \rho_m \tag{15}$$

where Vf_m is the volume fraction of the copper matrix and ε is the volumetric or bulk porosity.

3.2.4 Volumetric porosity measurements

A helium pycnometer (Accupyc 1340, Micromeritics) was employed to obtain the bulk porosity of the porous copper samples (n=3) using the following equation:

$$\varepsilon = \left(1 - \frac{V_t}{V_a}\right) \times 100$$

where ε is the volumetric or bulk porosity, V_t is the true volume of the porous samples measured using a helium pycnometer, V_a is the total volume of the porous sample

(including the pores) measured using Vernier callipers with a resolution of 0.01 mm to measure the dimensions.

3.2.5 Particle Size Measurements

The particle sizes of both primary powders (copper and potassium carbonate) were determined using a Malvern – Mastersizer 3000 particle analyser. The Dry Powder method utilising the laser diffraction technique was used in this case. Prior to the test, each powder was mixed using a Hauschild Speedmixer^{TM} DAC 400 FVZ (at 1200rpm) to obtain an even distribution of particles before sampling. The mass of the sample required to achieve reproducible results depends mostly on the polydispersity and particle size of the sample. Samples containing small particles or with less polydisperse distribution require only a small amount of the powder for measurements and otherwise. Copper particles were approximately 50 μm (estimated by SEM analysis) in diameter, therefore a smaller amount was used in this experiment, while a larger amount of K_2CO_3 was used because it had a much bigger particle size distribution.

3.2.6 3D analysis of the porous samples

Three selected porous samples produced following processing route A; 20CuPA, 40CuPA and 50CuPA were selected for this investigation, as well as three samples produced following route B; 10CuPB, 30CuPB and 50CuPB. All samples were scanned by a micro-CT scanner (*In vivo* scanner (Skyscan, 1076, *in vivo* micro-CT scanner, Skyscan NV Kontich Belgium). The porous copper was fixed on an expanded polystyrene foam having the specimen axis in common with the rotation axis of the system. Several trial scans were necessary in order to visualise all components of the porous sample by obtaining relatively good settings of the system. Scan system settings were as follows; full rotation over 180°, source voltage 100kV,

current 10 W, rotation step 0.5° aluminium filter thickness 0.5 mm, exposure time 0.59 seconds, 4 frame averaging, isotropic pixel size 17.4 µm. Skyscan *NRecon* software was employed to reconstruct the images by means of an Itered back – projection algorithm. The generated images were then processed and analysed with the use of *CTAn* software and the calculations were mainly performed in Microsoft Excel.

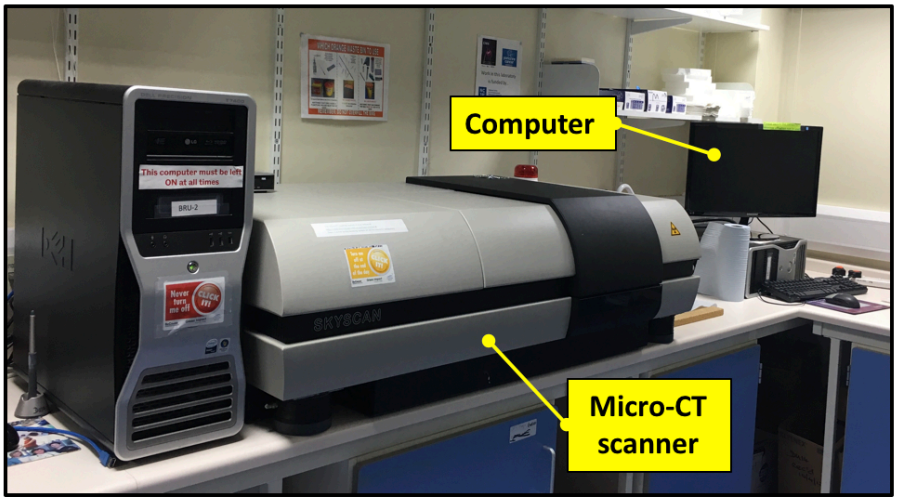

Figure 35: Skyscan in-vivo micro-CT scanner employed for 3D imaging of the porous samples to measure porosity and study the pore distribution within the samples.

3.2.7 Thermogravimetric Analysis (TGA)

It is necessary to understand how the organic binders and powders in the green tape behave when exposed to heat. The results were mainly required to generate a heat treatment profile for the debinding and sintering process. Green copper samples were taken through thermogravimetric analysis to determine the change in sample mass as a function of temperature using a Perkin Elmer's Pyris TGA 1. The samples were placed on alumina pans. Heating rate was varied between 2 °C/min and 15 °C/min. Pyris software was used to control the test.

3.2.8 Chemical Analysis of Porous Tapes

Chemical composition of the porous samples is expected to have a strong influence on their properties especially heat transfer and mechanical properties. This analysis was performed on the samples which were debinded and sintered at 450 °C and 890 °C respectively, under argon and vacuum controlled environments. The K_2CO_3 which was introduced to generate the pores on the samples was removed by dissolution (after the samples were sintered) using distilled water. Chemical analysis was performed on the samples processed by mixing copper with 10-50wt% of K_2CO_3 by polymeric binders, followed by debinding and sintering at 450°C and 890°C respectively. Chemical composition analysis of the porous metal was carried out using three techniques; (1) X-Ray diffraction analysis, (2) Raman spectroscopy and (3) energy dispersive X- ray spectroscopy (EDS).

3.2.8.1 X-Ray Diffraction Analysis (XRD)

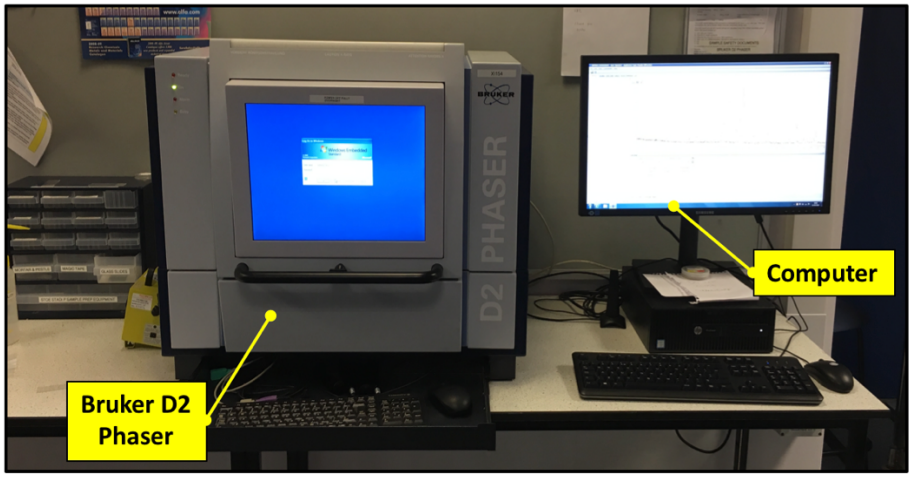

Figure 36: Bruker D2 Phaser used for X-ray diffraction analysis of the samples and raw materials employed in this study.

XRD analysis was again performed on the copper powder and porous copper samples. Fine powder samples were spread on a clear PMMA specimen holder and levelled using a microscope slide. For bulk specimens, the sample was mounted (using Apiezon putty) on a large 'deep dish' specimen holder and then flattened using a glass slide. The sample was then

loaded and scanned using a Bruker D2 (X-Ray generator running at a voltage of 30 kV and current of 10 mA) using a Cu tube with 1.54184°A and Lynxeye (1D mode) detector. Scan system settings were as follows; time step rate of 8°/min, start and stop angle of 35° to 80° and step size of 0.05°. The data was then imported in to the ICDD-PDF-4+ for phase analysis.

3.2.8.2 Raman Spectroscopy

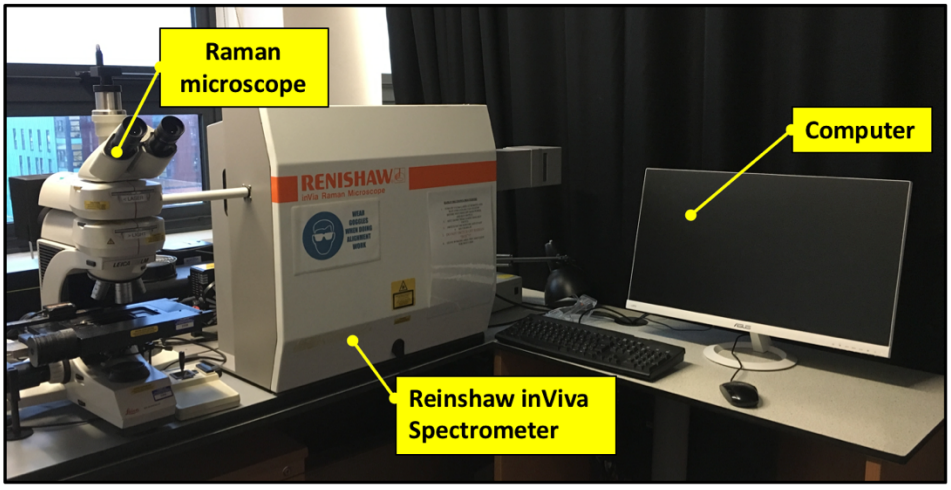

Figure 37: Renishaw inVia confocal Raman microscope used for chemical analysis of the porous copper samples and raw materials employed in this study.

Raman spectra were obtained using a Renishaw inVia confocal Raman microscope operating at a wavelength of 514.5nm green monochromatic laser light. The analysis was carried out on both copper powder and porous copper samples at room temperature, running WiRE 3.4 software. The instrument was first calibrated using a Renishaw Raman calibration source (silicon wafer reference standard). No sample preparation was necessary, the powder sample was mounted on the glass slides and flattened by squeezing between two slides. For the

porous samples, a small portion was cut and mounted directly on the glass slides under the microscope.

5.1.1.1 Energy Dispersive X-Ray Spectroscopy (EDX)

EDX is another technique used in conjunction with SEM for chemical microanalysis. It makes use of the X-ray spectrum emitted by a solid or porous sample bombarded with a focused beam of electrons to obtain a localised elemental composition. Sample preparation is essential to this analysis, the samples were thoroughly cleaned with isopropanol in an ultrasonic bath and dried prior to the analysis. The samples were mounted on aluminium sample holders using conductive carbon stickers and then scanned using an SEM Inspect F (of the Sorby Centre, University of Sheffield) in EDX mode. Each sample was calibrated before the test, and reproducibly set up. Probe current, probe diameter, working distance, stage tilt, kV, and spot size was kept consistent throughout the analysis on each sample to ensure reproducibility. EDS spectra of each sample were recorded showing elemental peaks on the sample. Subsequently, samples was examined in the microscope to allow compositional maps to be recorded across each sample.

5.1.2 Surface Roughness

5.1.2.1 Image analysis method

Surface roughness in the porous tapes was studied by image analysis prior to heat transfer analysis. The images revealing the morphology of the sample surface were captured using the Nikon digital camera (D5300 model) fitted with an 18-55 mm lens (1:3.5-5.6G). Based on the binarized images of each porous sample obtained, it was possible to generate the surface roughness profiles depicted in Figure 97. Figi software was then employed to produce surface profiles of each sample revealing the details of the sample surface. Microsoft Excel was used

to perform the statistical analysis of the profiles. Below are the equations employed to calculate all the parameters used to describe the surface roughness of the porous samples.

Arithmetic average, R_a

$$R_a = \frac{1}{n}\sum_{i=0}^{n}|y_i| \tag{16}$$

Root mean squared, R_q

$$R_q = \sqrt{\frac{1}{n}\sum_{i=1}^{n}y_i^2} \tag{17}$$

Maximum valley depth, R_v

$$R_v = \min_i y_i \tag{18}$$

Maximum peak height, R_p

$$R_p = \max_i y_i \tag{19}$$

Maximum height of the profile, R_t

$$R_t = R_p + R_v \tag{20}$$

Skewness, R_{sk}

$$R_{ku} = \frac{1}{nR_q^4}\sum_{i=1}^{n}y_i^3 \tag{21}$$

Kurtosis, R_{ku}

$$R_{ku} = \frac{1}{nR_q^4}\sum_{i=1}^{n}y_i^4 \tag{22}$$

where, y_i is the surface height relative to the mean plane, n number of data points in the x-direction,R_a is the arithmetic mean roughness value, R_q is the root mean squared, R_v is the maximum valley depth, R_p maximum peak height, R_t maximum height of the profile. The

results are summarized in Table 18 presented in section 9.1.2 of the results and discussion chapter.

5.1.2.2 Using contourGT profiler

A Bruker ContourGT-K optical profiler was employed to obtain the 3D surface topography at a sub-nanometre scale resolution. For data collection and analysis, the Bruker ContourGT-K optical profiler was fitted with Vision64® software. The system was calibrated prior to the test to obtain accurate measurements. The surface profiles of all porous Cu samples produced in this study were then obtained and presented in section 9.1.1.

5.2 Mechanical Testing

Some investigations of the room temperature mechanical properties of thin sheets of double-layered porous copper were carried out, focusing on the bending behaviour where a 3-point bend technique was employed. To carry out the 3-point bending test, two approaches were involved. In the first approach, a simple 3-point bending test was carried out, where all the samples considered in this study were tested using a standard loading nose (LN) of 30 mm diameter. In the second approach, three – point bending tests were carried out using five different loading noses designed and manufactured in-house. The dimeter of the loading noses ranged between 38 mm and 76 mm as shown in Figure 40.

5.2.1 A simple 3-point bending test

A simple three-point bending test was performed on each porous copper sample using a universal testing machine (Zwick/Roell Z050) set to three-point bending mode fitted with a 5kN load cell. The samples were bent at a rate of 0.5 mm per minute under a loading platen of 30mm diameter and a sample span of 50mm. The thickness and width (see Table 9) of the samples were measured using a digital Vernier calliper (±0.01 mm) before each stage. The samples were then placed on the supporting pins with the porous section facing down ensuring that the loading platen was perpendicular to the length of the sample as shown in Figure 39.

Table 9: Volumetric porosity, width and thickness of all the porous samples studied using 3-point bending test.

Processing routes	Sample	Volumetric porosity (%)	Width (mm)	Thickness (mm)
-	**0CuP**	50.7 ± 0.5	15.39	0.74
Route A	**10CuPA**	63.4 ± 1.4	15.21	1.12
	30CuPA	75.2 ± 1.5	15.12	1.38
	50CuPA	80.5 ± 0.5	16.14	1.24
Route B	**10CuPB**	66.3 ± 0.9	16.10	1.27
	30CuPB	79.0 ± 1.3	16.41	1.61
	50CuPB	81.5 ± 1.4	16.75	1.36

testXpert II testing software was used to perform force and deformation data analysis. Flexural stress (σ_f) and strain (ε_f) were calculated from the load/deformation data obtained from the Zwick/Roell Z050 using the following equations;

$$\sigma_f = \frac{3FL}{2bd^2} \tag{23}$$

$$\varepsilon_f = \frac{6Dd}{L^2} \tag{24}$$

Flexural modulus (E_f) was calculated using the following equation;

$$E_f = \frac{L^3 m}{4bd^3} \tag{25}$$

where F is load applied at a given point on the deflection curve (N), L is the support span (mm), D is the maximum deflection of the centre of the beam, while b and d are the width and thickness of the tested beam respectively. m is the gradient within the elastic region of the load deflection curve.

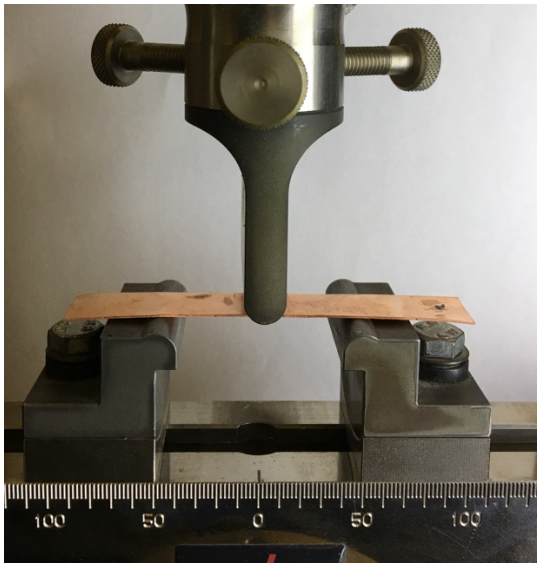

Figure 38: Three - point bending test setup on the porous sample. The sample is placed facing down on the supporting pins

For the iterations of both tapes from route A and B several flexural stress/strain curves were produced. In total four samples were tested. The results and discussion of this are presented in section 7.1.1

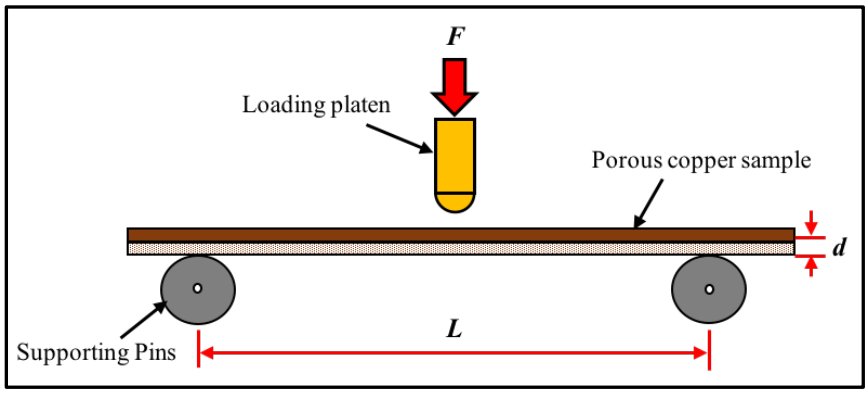

Figure 39: Schematic diagram of a simple 3-point bend test setup.

5.2.2 Modified 3-point Bend Test

To determine the bending behaviour of the double – layered copper sheets around cylinders of different circumferences, the new loading noses developed in-house were employed. These five loading noses are shown in Figure 40 (b), and have diameters ranging from 38 mm to 76

mm. Both loading noses (LN) were made from brass, flattened on one side and threaded to easily interchange on the equipment. Using a universal testing machine (Zwick/Roell Z050) in 3-point test mode using a 5kN load cell, the bending behaviour of porous samples around cylinders of different circumferences was investigated. The samples of length 150mm, sectioned to dimensions presented in Table 9, were bent at a rate of 0.5 mm per minute across a span of 100 mm using five different loading platens. A schematic diagram of the 3-point bend setup performing bending test (Figure 40 (a)) using these platens is shown in Figure 40 (b).

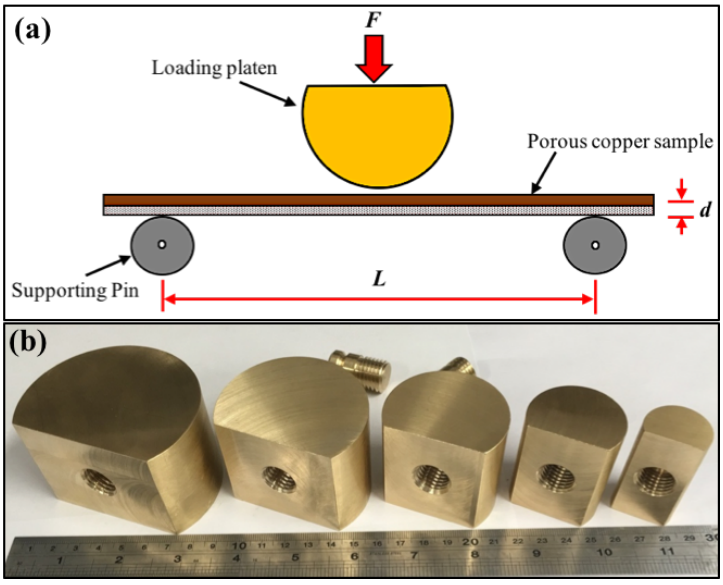

Figure 40: A setup of a 3-point bend test and an image of five different brass platens of diameters ranging from 76 mm, 64 mm, 50 mm, 38 mm.

The porous metals investigated here consist of a double layered structure: porous Cu layer adhered on to a thin Cu substrate. The sample was loaded with the porous section facing down on the supporting pins to ensure that the porous section fails under tension. Equations (23), (24) and (25) were used to calculate flexural stress, flexural strain and flexural modulus. Experimental results were also used to generate flexural stress against flexural strain plots hence studying the failure behaviour of the samples.

5.3 Heat Transfer Measurements

5.3.1 Heat transfer testing facility

The porous Cu samples produced in this study are for heat transfer applications. Therefore, it was necessary to carry out an investigation to explore their capability to transfer heat. The suitability of the porous Cu samples for heat sink applications was investigated using an open circuit external heat transfer rig using air as a coolant. **Figure 41** shows the setup of the external heat transfer rig which was designed and modified inhouse to study the samples. The heat transfer rig used in this study operates in the same manner as in previous work[184]–[188]. The rig comprises several parts, including; two centrifugal fans, an air tunnel, thermometers (microfoil T-type, J-type and K-type thermocouples), a computer system running PicoLog data acquisition software and a heating system. The purposes of each part of the rig, shown in **Figure 41** and **Figure 42** are explained next;

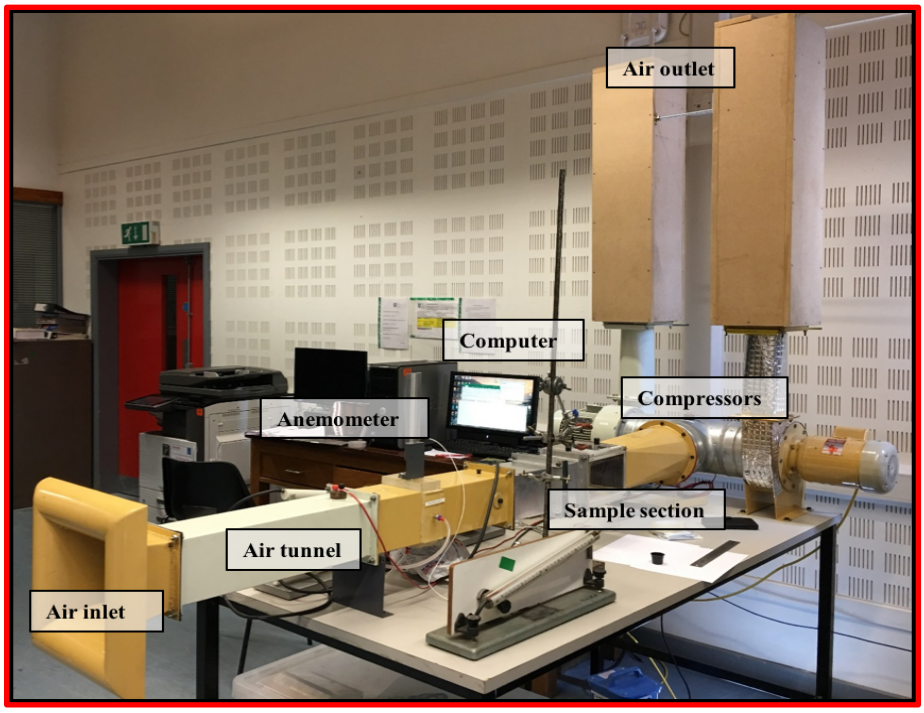

Figure 41: Open-circuit external heat transfer rig

- Two **centrifugal fans** (Albak) located at the end of the air tunnel force air into the tunnel by suction. The air flows in through an air inlet and channels through the test section, then exits the rig through the air outlet. Two graduated throttle valves located at the air outlet are used to control the air flow speed which is measured with a hot wire anemometer (HWA) system and logged using *Labview* software and a National instrument board (NI 9215).
- An **open-circuit wind tunnel** with dimensions 125 mm × 125 mm (width × height), channels the air through the test section at a controlled speed. The honeycomb flow straightener was placed behind the test section to generate laminar flow by reducing the induced bulk flows from the centrifugal fans. The test section is positioned along the air tunnel as shown in Figure 42.

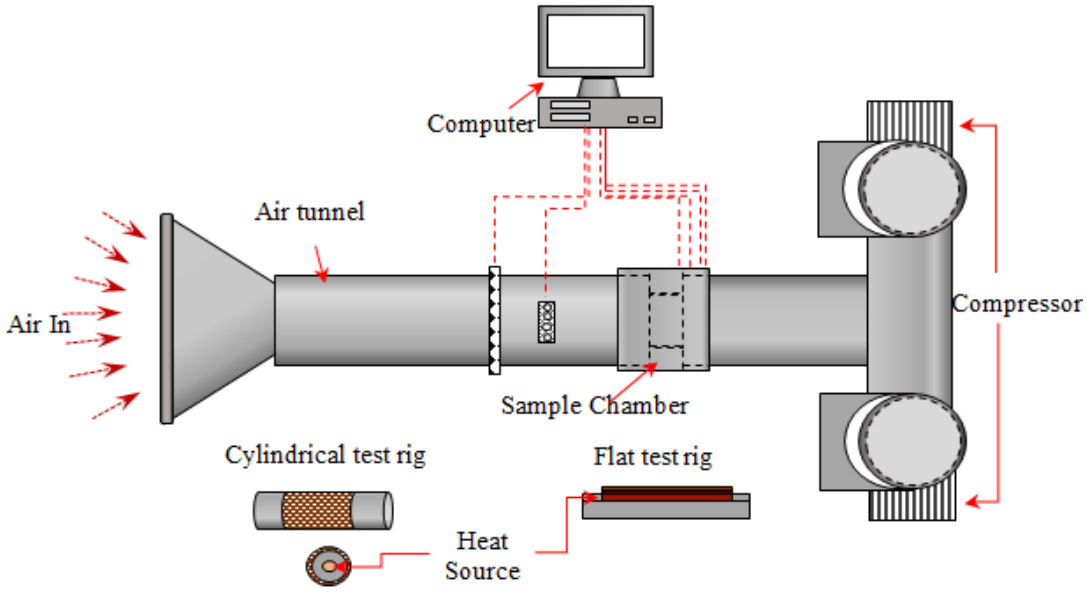

Figure 42: Schematic diagram showing the setup of the external thermal rig for heat transfer analysis.

- **K-type** and **microfoil T-type thermocouples** (≈100 μm) were used to track inlet and outlet temperature of the air and surface temperatures of the system. Temperatures were logged by *PicoLog* data acquisition software.

- There were two types of the heating systems involved for testing the samples produced in this work; **a cylindrical heating system** (CHS) and **flat heating system** (FHS). Both systems were designed and developed in-house specifically to test the samples produced in this work for heat transfer, developed specifically to fit the porous copper tapes investigated here.
- **The Cylindrical heating system** (schematic diagram is shown in Figure 43) was designed and manufactured in house, specifically to fit the porous copper tapes investigated here. The heating system is made up of an aluminium cylinder (ϕ = 50 mm), two polyether ether ketone (PEEK) insulation guards of the same diameter, on both ends of the aluminium and a 400 W cylindrical heating element (ϕ = 10 mm) firmly positioned at the centre of the aluminium cylinder to allow homogenised heat flow along the radial direction. The cartridge temperature *(T_{cart})* was measured using a J-type thermocouple.

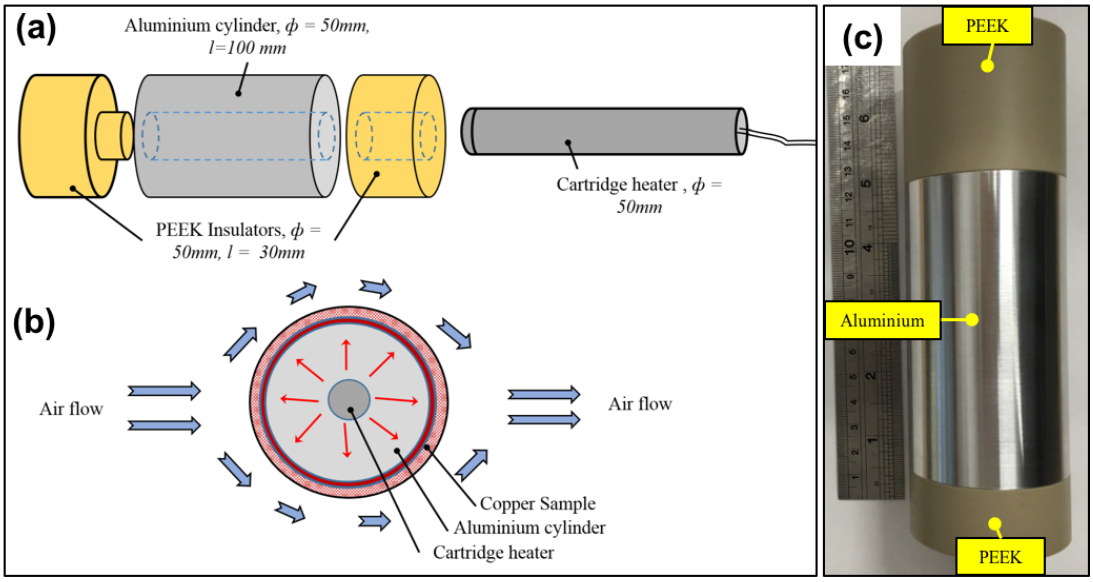

Figure 43: (a) Schematic diagram of the CHS setup, (b) a schematic diagram of the air flow around the CHS generated in the air tunnel and (c) is an image of the CHS.

- **The Flat heating system** shown in detail in Figure 44 was also designed and manufactured in house, specifically to fit the porous copper tapes investigated here. The heating system is made up of an aluminium plate of dimensions 77 × 77 mm ($l \times w$), polyether ether ketone (PEEK) insulation guard of dimensions 100 × 100 × 13 mm, on both sides of the aluminium plate except the top part, and a KH-303, 115 Vac, 10 W/in^2 flat heating element (polyimide film insulated flexible heater) of dimensions 76 × 76 mm ($l \times w$) firmly positioned below the aluminium plate to allow homogenised heat flow in one direction. A similar setup was used in Ref [185]

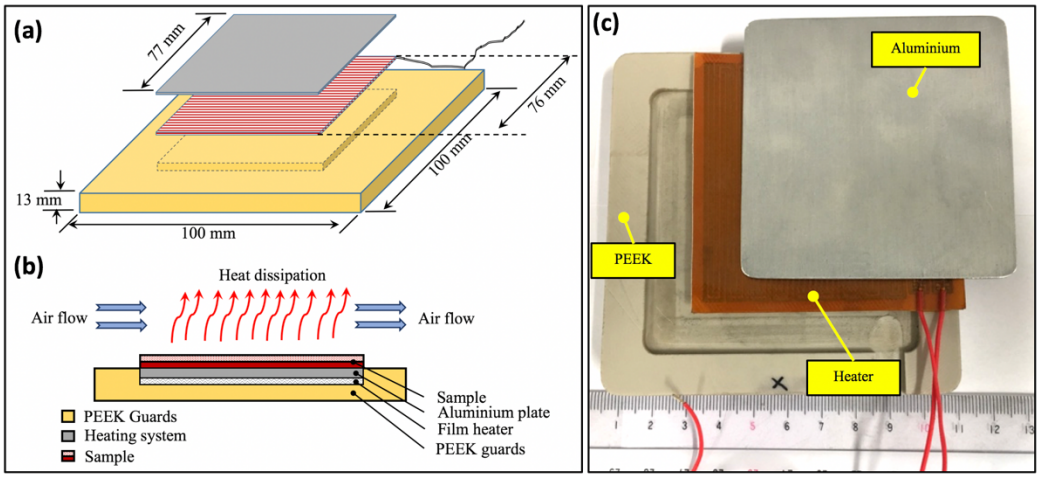

Figure 44: Schematic diagram of the FHS setup, (b) a schematic diagram of the air flow around the FHS generated in the air tunnel and (c) is an image of the FHS.

Aluminium and PEEK have thermal conductivities of 244 W/mK and 0.26 W/mK respectively. These thermal conductivities are good for thermal conduction and insulation. PEEK also has a wider service temperature of up 250°C.

5.3.2 Procedure;

The samples were cut to size using a pair of scissors (Figure 45). A thin layer of *Kryonaut High Performance thermal grease* was applied to the aluminium surface to enhance heat transfer and ensure good contact, and the sample was mounted directly on to it. The ends of

the samples were joined using thin (≈ 100 µm) double-sided adhesive tape to place the samples in good contact with the surface. In both systems, a microfoil T-type thermocouple was mounted firmly on the sample using very thin double-sided conductive tape (≈100 µm) as shown in Figure 46 (b) and Figure 47 b) below. The whole sample components, as shown in Figure 43 and Figure 46 were then placed into the sample section position along the air tunnel depending on the test being carried out, either on a CHS or a FHS (see Figure 48). Once set, the test was commenced.

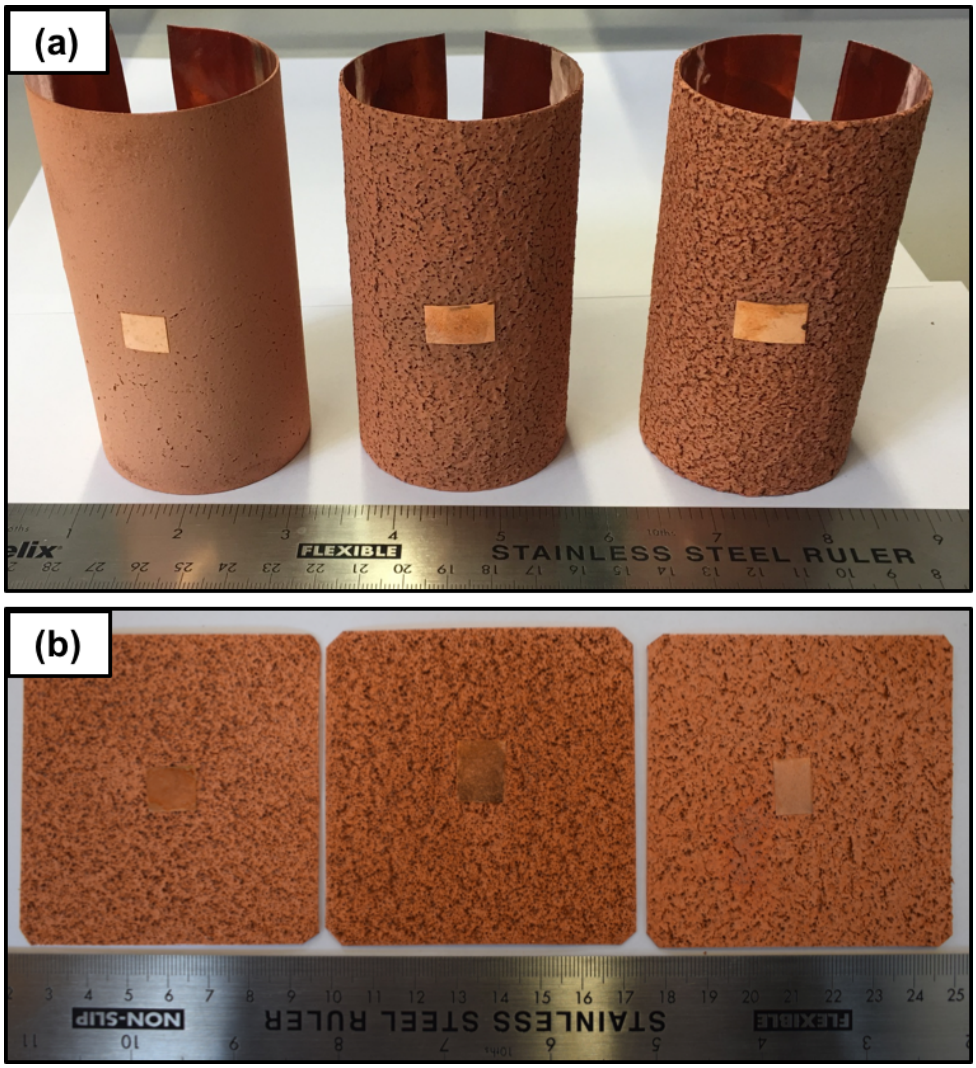

Figure 45: Cylindrical heating system used in the heat transfer measurements. a) CuP0, CuP20 and CuP40 double layer porous tapes investigated for heat transfer performance, and b) a microfoil T-type thermocouple firmly mounted on a porous sample before testing.

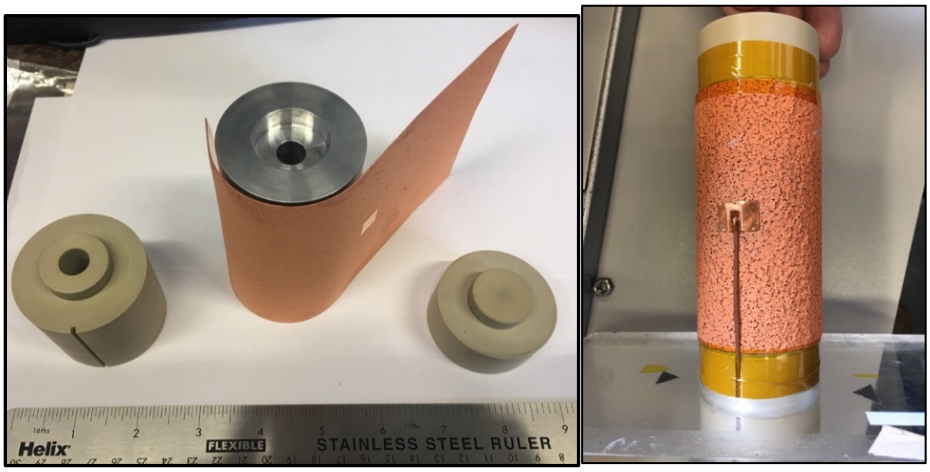

Figure 46: Mounting the sample on a cylindrical heating system and b) a microfoil T-type thermocouple firmly mounted on a porous sample before testing.

Similarly, as in CHS, the samples were cut to size and then mounted on the aluminium plate as shown in Figure 47 (b). But first, a thin layer of *Kryonaut High Performance thermal grease* was applied on the aluminium plate (see Figure 47 (a)). The sample was then mounted on the plate, pressing it down to ensure a good contact. Both the sample and the thermocouple were firmly taped down on the aluminium plate to prevent disturbance by air flowing along especially at a higher air speed.

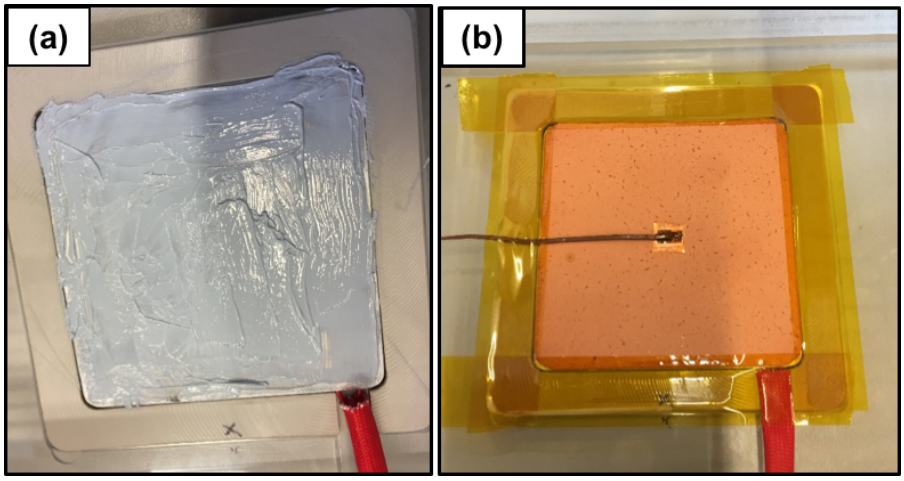

Figure 47: Preparation and mounting the sample on a flat heating system. (a) Applying thermal grease on aluminium plate, (b) sample taped down on aluminium plate.

Figure 48 shows the positioning of the CHS and FHS (with the samples mounted) in the air tunnel ready for the test. The blockage ratio of the CHS was calculated to be approximately

40% while that of FHS was found to be about 0.5%. It was ensured that there were no air leaks along the tunnel as well as within the sample section.

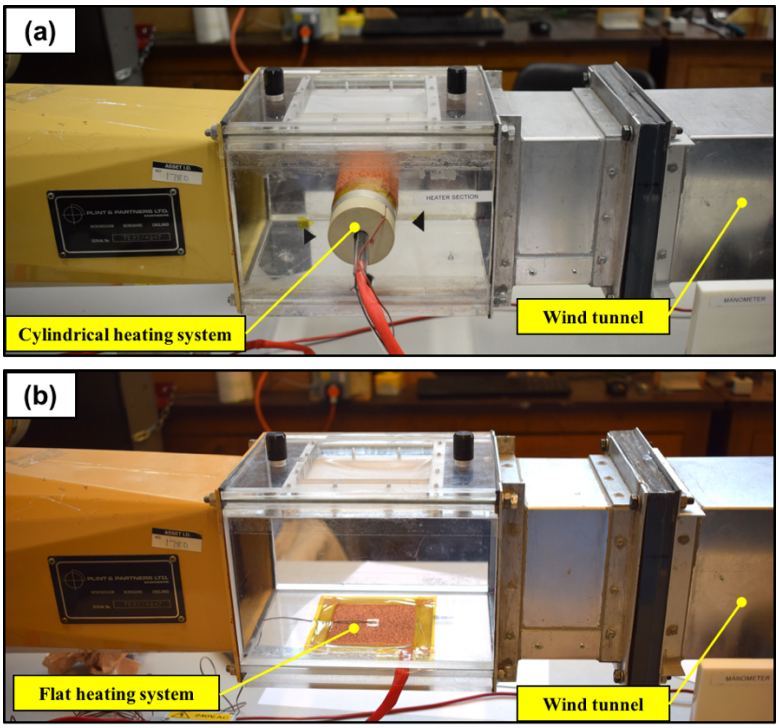

Figure 48: The sample section along the wind tunnel, (a) a cylindrical heating system installed across the air tunnel and (b) flat heating system installed at the base of the wind tunnel along the flow field.

The heating system was turned on to supply the main power *(P)*. The main portion of this thermal energy was transferred through the sample to the air by convective heat transfer (Q_{conv}), with a smaller portion transferred to the walls of the wind tunnel by radiative heat transfer (Q_{rad}). A very small amount of heat energy (≈2%) was transferred to the PEEK guards on the sides by conductive heat transfer (Q_{cond}) because of the low thermal conductivity of PEEK (0.26 W/mK), this was neglected from the calculations which follow;

$$Q_{rad} = \sigma_B \in A(T_s^4 - T_t^4) \tag{26}$$

$$Q_{cond} = kA[\frac{T_s - (T_{p1} + T_{p2})}{2}] \tag{27}$$

$$Q_{conv} = P - Q_{rad} - Q_{cond} = P - \sigma_B \in A(T_s^4 - T_t^4) - kA[\frac{T_s - (T_{p1} + T_{p2})}{2}] \tag{28}$$

where σ_B is the Stefan-Boltzmann constant (5.67×10^{-8} W/m^{2}K^2, $\in$ is the emissivity of the sample surface (=0.23). Surface temperature (T_s), and temperature of the air flowing in *(T_{in})* and out *(T_{out})* were monitored as before. T_{p1} and T_{p2} are the surface temperatures of the PEEK guards on both ends of the aluminium cylinder, and T_t is the temperature of the walls of the wind tunnel.

$$Tr = \frac{Q_{conv}}{T_s - T_a} = \frac{P - \sigma_B \in A(T_s^4 - T_t^4)}{T_s - T_a} \tag{29}$$

$$h = \frac{Q_{conv}}{A(T_s - T_a)} = \frac{P - \sigma_B \in A(T_s^4 - T_t^4)}{A(T_s - T_a)} \tag{30}$$

The cross-sectional dimensions of the air tunnel were 125 mm × 125 mm. The samples were tested at a varying air speed *(u)* ranging from 4 -21 m/s. The voltage supplied in to the heating system was measured using an RS 37259 voltmeter with ± 0.1% sensitivity.

The heat transfer performance of the two sets of double-layered porous samples were investigated by obtaining the heat transfer coefficient h (W/mK) and thermal transmittance Tr (W/K). Thermal transmittance is the rate of heat transfer through one square meter of structure, divided by the difference in temperature across the structure expressed in W/m^{2}K. As-received smooth and sand blasted copper foils (both without any porous material applied) were also tested to obtain h and Tr as references. The air velocity inside the air tunnel was expressed in terms of dimensionless Reynolds number as follows;

Cylindrical heating system;

$$Re_D = uD/v \tag{31}$$

Flat heating system;

$$Re_L = uL/v \tag{32}$$

where D (50 mm) is tested cylindrical diameter (m), L is a characteristic linear dimension

(m), and v (1.493×10^{-5} m^2/s) is the kinematic viscosity of air. Furthermore, the average heat transfer coefficient constant h was expressed as dimensionless Nusselt number as follows;

Cylindrical heating system;

$$Nu = hD/k \tag{33}$$

Flat heating system;

$$Nu = hL/k \tag{34}$$

where k is thermal conductivity of air (2.83×10^{-2} W/mK). All air properties were specified at the mean film temperature of $(Tf = (Ts\text{-}Ta)/2)$, and standard atmospheric pressure, where Ts is the surface temperature and Ta is the ambient temperature.

Mass flow rate m was also calculated as follows;

$$m = \rho uA \tag{35}$$

where ρ is the density of the cooling fluid, u is velocity of the cooling fluid and A is the area of the cross section.

Table 10: The velocity and the mass flow rate of the air flowing through the air tunnel during heat transfer measurements on the Cylindrical Heating System

Air velocity (m/s)	Mass flow rate (kg/s)
4	0.08
8	0.16
12	0.24
16	0.32
18	0.36

Table 11: The velocity and the mass flow rate of the air flowing through the air tunnel during heat transfer measurements on the Flat Heating System

Air velocity (m/s)	Mass flow rate (kg/s)
4	0.08
8	0.16
12	0.24
16	0.32
20	0.40
21	0.42

CHAPTER 4: Results and Analysis - Processing

This chapter is split into five sections to report and discuss results from processing the samples studied in this research.

1. Section 4.1 reports the processing of samples by lost carbonate sintering applied to tape casting. It starts by highlighting the selection of the raw materials/chemicals, followed by processing which includes: preparation of the copper slurry, then casting and sintering the component, and finally the removal of the space holder from the component leaving a porous copper sheet.
2. Sections 4.2 and 4.3 cover the results and discussions from surface porosity and volumetric porosity analysis of porous copper samples
3. Section 4.4 focuses on the results and discussions of the density measurements on the sample.
4. In section 4.5 the results and discussions of chemical analysis measurements are reported.
5. This chapter ends with a summary of the important points, highlighting the key features from processing.

6.1 Processing of the Porous Tapes

The main aim in this work is to create a thin porous sheet of copper for heat transfer, integrated with a dense copper layer, which can provide a superior contact to a surface where additional heat transfer is required. To achieve this, porous copper tapes were produced by a powder metallurgical process which combines tape casting and LCS. By combining these two processes, copper sheets with a wider range of porosity than previously reported and controlled thickness were produced. The fabrication of the samples was divided into four main steps: selection of the chemicals (organic binders) included in the slurry for tape casting, tape casting of the slurry into thin tapes, debinding and sintering of the green samples and finally removal of the carbonate space-holder from the sintered samples. The tapes are for heat transfer applications, and therefore the structure plays a major role in their performance. The structure of the porous sheets produced was analysed to study the influence of the process on the structure and properties. The measurements performed under this section include: surface porosity and volumetric porosity measurements, relative density analysis, chemical composition analysis, and surface roughness measurements.

6.1.1 Choice of organic components for tape casting

Raw chemicals used in the production of the samples (porous copper sheets) in this work were selected based mainly on the literature as already explained at length in Section 3.1. Two primary powders: dendritic copper powder (Av. particle size ≈ 50 μm) and K_2CO_3 were successfully mixed with organic binders after several attempts to obtain a homogenous slurry to enable tape casting. Some of the organic components of the slurry, such as the solvent (azeotropic mixture of ethanol/butanone (40/60)), and Poly MethylMethAcrylate (PMMA) were adopted from work performed by Cans et al[40] and Geffroy et al [38], [39]. It was also

found that an efficient plasticizer for PMMA is Dibutyl phthalate, therefore it was also selected. The phosphates proved to be chemically stable and compatible with the rest of the binders, as reported in the study performed by Geffroy et al [38], [39], therefore triphenyl phosphate (TPP) was selected as a dispersant. A perfect slurry found by a series of experimental trials to be suitable for tape casting was successfully produced after several trials.

6.1.2 Tape casting and structure of green samples

6.1.2.1 Initial stages – Unsuccessful sample preparations

Figure 49 shows one of the unsuccessful samples resulting from poor mixing of the slurry components. It was found out after performing several trials that poor and inhomogeneous slurry formation was due to three main reasons: (1) poor wetting of Cu powder and K_2CO_3 space holder which led to segregation between the two powders during mixing. (2) wrong selection of the mixing speed on the speed-mixer causing agglomeration and/or segregation of the powders depending on the speed, and (3) adding all the slurry components at once.

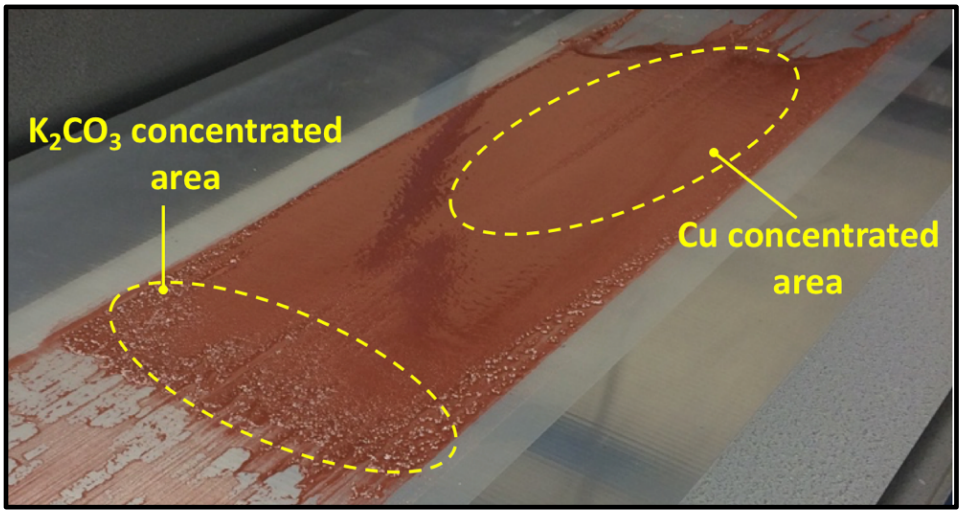

Figure 49: Unsuccessful sample resulting from poorly mixed organic components and powder of the slurry before tape casting.

The PMMA and TPP were supplied in a powder form and flakes respectively, and therefore they needed to be dissolved separately in a solvent. To prevent segregation of Cu and K_2CO_3, PMMA and TPP were homogenously dissolved in a solvent by speed-mixing, followed by addition of the Cu and K_2CO_3. Figure 50 shows an unsuccessful sample depicting agglomerated K_2CO_3 from mixing. The agglomerates formed blocked some parts of the doctor blade as the slurry flowed down the gap, resulting in defects as shown in the figure. To prevent this agglomeration of the powders from occurring, organic components were mixed separately to obtain a homogenous, viscous slurry with good homogeneity. Both Cu powder and K_2CO_3 were added in small portions to homogenously mixed organic components to ensure good wetting of the powders, hence avoiding agglomeration.

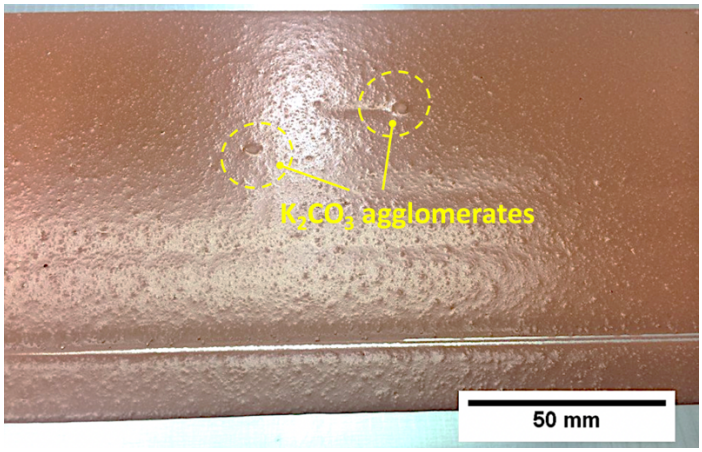

Figure 50: Unsuccessful sample resulting from agglomeration of the powders.

6.1.2.2 Final Stages – Successful sample preparations

Figure 51 (top view) and Figure 52 (side view) shows a successfully cast green tape by the tape casting process followed by drying in air at 50 °C for 3 hours. To obtain a homogenous and stable slurry, first the K_2CO_3 was sieved to remove particles larger than 800 µm, and secondly the slurry components were mixed in the right order, starting with the organic binders followed by Cu and the K_2CO_3. Finally, the right time and mixing speed were selected. The slurry components were mixed together for 1.5 hours at 800 rpm, 1200 rpm and 1800

rpm in 30 minute intervals and then cast in to a thin tape. After casting and drying under air, the sample remained flexible and easy to cut to shape for further processing. At this stage, it is necessary for K_2CO_3 to be evenly distributed across the sample to generate pores within the sample in the later stages. The K_2CO_3 appears to be evenly distributed across the samples, as shown in Figure 51 and Figure 52. It also appears to be fully immersed in the organic components and copper, except in Figure 51 (d) where some parts of the K_2CO_3 are exposed on the surface of the green tape. However, the K_2CO_3 exposed on the surface of the green sample is significant for generating an open-pore structure in the final component. In the case where K_2CO_3 was not exposed on the surface, a closed-pore structure was expected in the final component. It should also be recognised that if the structure was fully closed pores then removal of the K_2CO_3 would be difficult if not impossible.

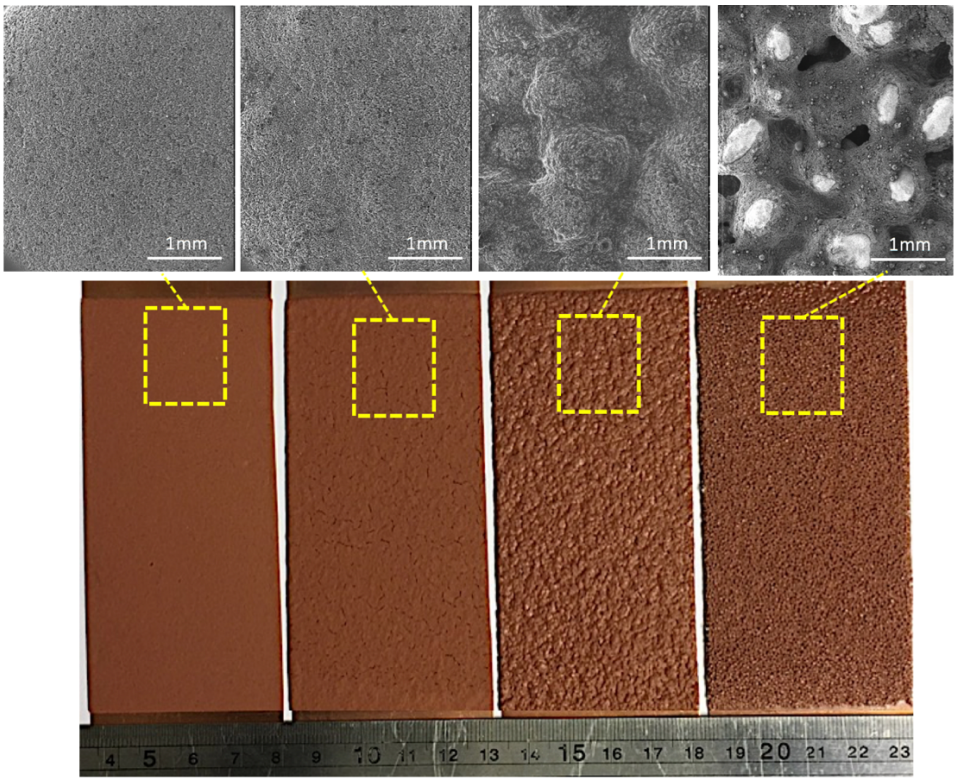

Figure 51: Successful green copper samples after tape casting directly on copper substrate and dried at 40°C under air. 0%K_2CO_3 (left), 20%K_2CO_3 (second left), 40%K2CO3 (second right) and 50%K2CO3 (right).

A side view of the green tapes is shown in Figure 52, depicting (a) images (on the left) captured by a Nikon D5300 camera set at a low magnification and (b) SEM micrographs captured at higher magnification (on the right) using an Inspect F SEM switched to secondary electron (SE) mode. The SEM micrographs (Figure 52 (b)) clearly reveal an increasing amount of K_2CO_3 space-holder in the range of 0-50 wt.% (top to bottom) across the green sample. The number of pores generated within the final component depends on the quantity of the space holder added. Therefore, the porosity generated was expected to increase as the quantity of the space holder added increases.

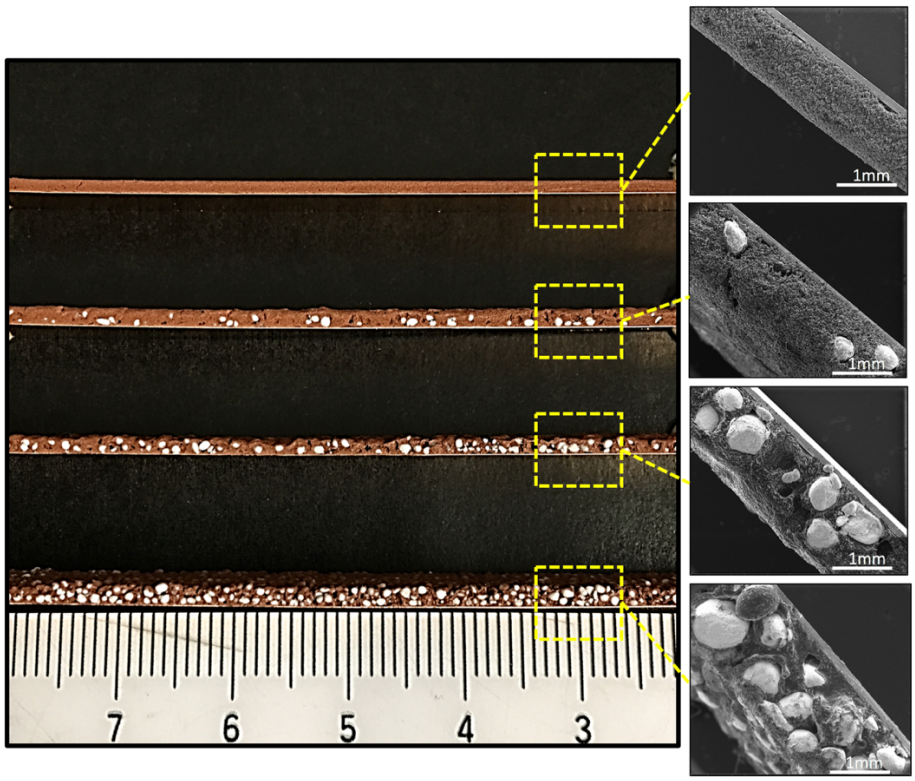

Figure 52: Side view of the green copper tapes produced by tape casting. From top to bottom: 0%K_2CO_3, 10%K_2CO_3, 30%K_2CO_3 and 50%K_2CO_3. The tapes were dried at 50°C on the tape caster to evaporate the solvent.

For defect-free casting of the thin tape, it is essential that the slurry has a non-Newtonian flow behaviour and also has sufficient strength to maintain structural integrity thereafter. This is important to minimise or potentially totally eliminate defects in the green tape before the heat

treatment process, and achieving it begins with the quality of the slurry prior to casting. SEM was employed to assess the quality of the green tape. Figure 53 shows SEM micrographs captured at higher magnification revealing the structure of the green body. The green body obtained here appears to be free from obvious defects under SEM at magnification of at least 2,000×. The organic additives bridge between the Cu and K_2CO_3 particles forming a well bonded structure with sufficiently good mechanical properties to avoid cracking during drying and for handling. To ensure good mechanical bonding and flexibility between Cu and K_2CO_3 particles, PolyMethyl MethAcrylate (PMMA) and Dibutyl phthalate were used as a binder and plasticizer respectively. A good compromise between mechanical properties and flexibility was obtained by adding a binder/plasticizer ratio of 1.3 during slurry preparation [39].

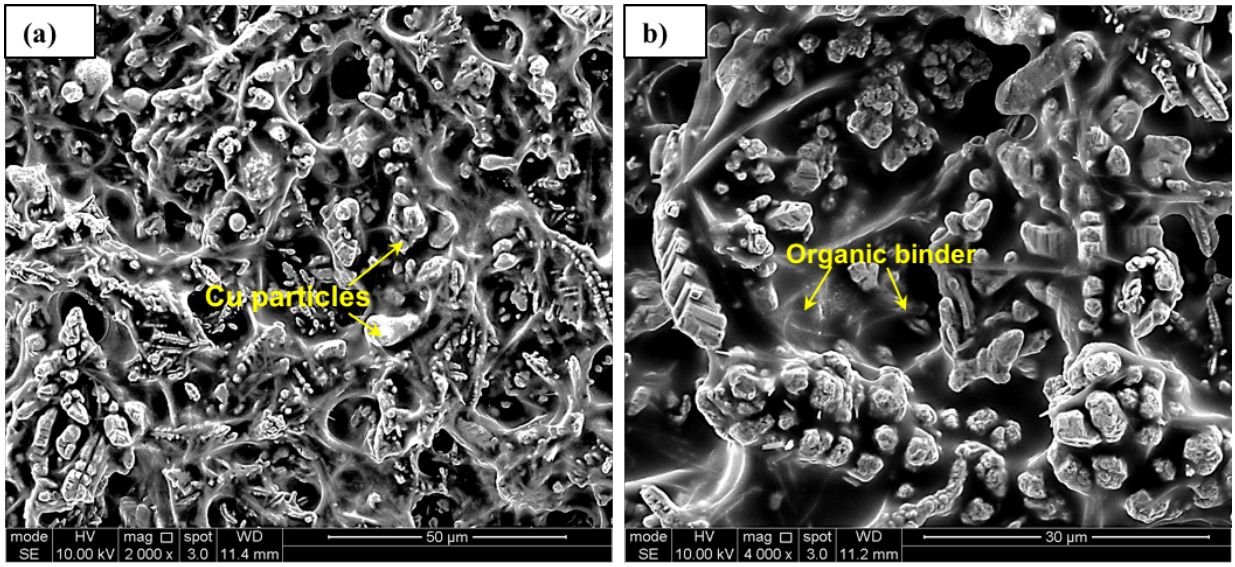

Figure 53: SEM micrographs of green copper tape. Copper particles are suspended within organic binders.

Two manufacturing routes were followed to produce two types of porous tapes which have different structural properties, especially in relation to the pore distribution, as fully described in the methodology section. Figure 53 shows SEM micrographs depicting the typical structures of the green tapes produced by the two routes. As seen in the micrographs, the green tapes produced by route A show an intact bond between the green body and the Cu foil

because here the slurry was allowed into contact with the tape while still able to undergo viscous flow. Therefore, it formed a good bond with the Cu foil due to gravitational forces (no other forces were applied). On the contrary, the green tapes fabricated by route B reveal fine gaps between the green body and the Cu foil. Figure 54 depicts a typical side view of the green tape produced by route A. The images were taken under SEM after tape casting and pre-drying in air at 40 °C, but prior to the debinding and sintering process. Casting the slurry while it is still viscous promoted a good contact between the green Cu section and the Cu substrate (foil) before the sample was taken through the debinding and sintering processes. Thus, promoting a good bond between the porous section and Cu substrate after sintering at 890 °C. Refer to Figure 55 for sintered samples.

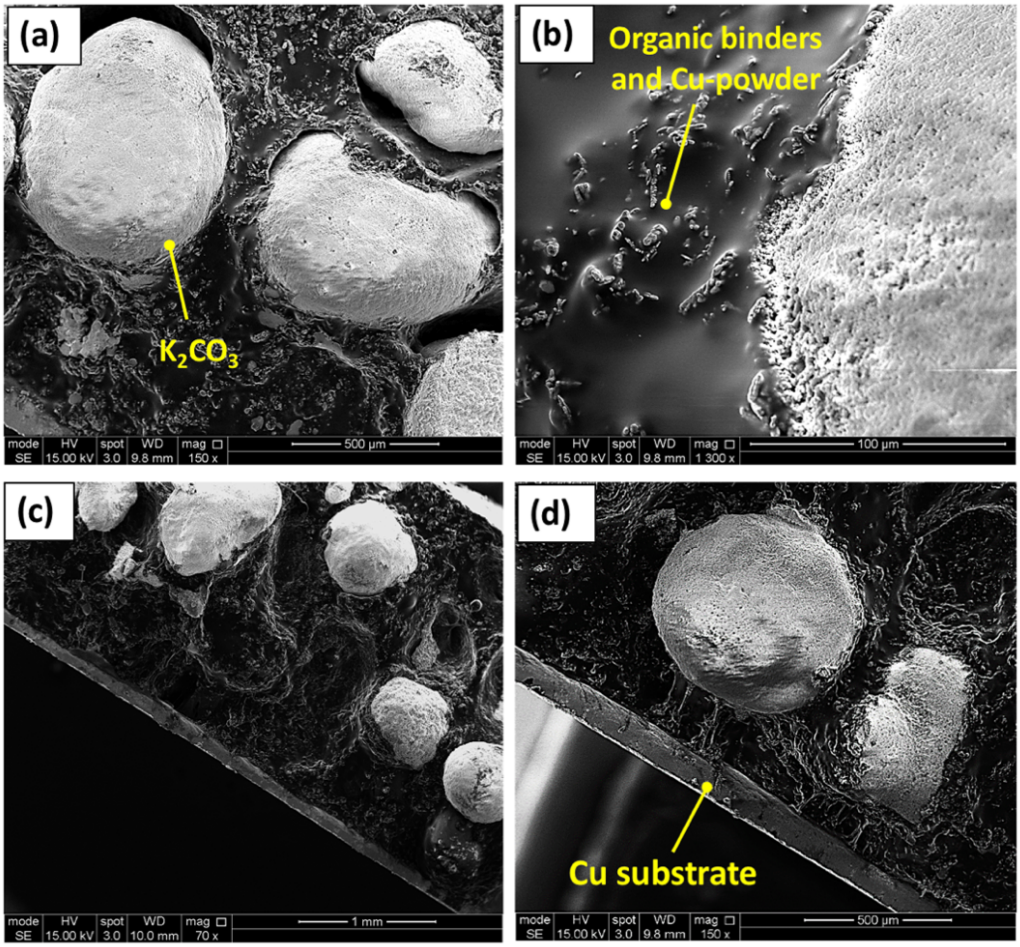

Figure 54: A typical side-view of a green tape fabricated by route A; green layer of Cu and K_2CO_3 (mixed with organic binders) cast on a thin copper substrate of thickness 0.125 mm.

6.1.3 Structure of the heat-treated samples

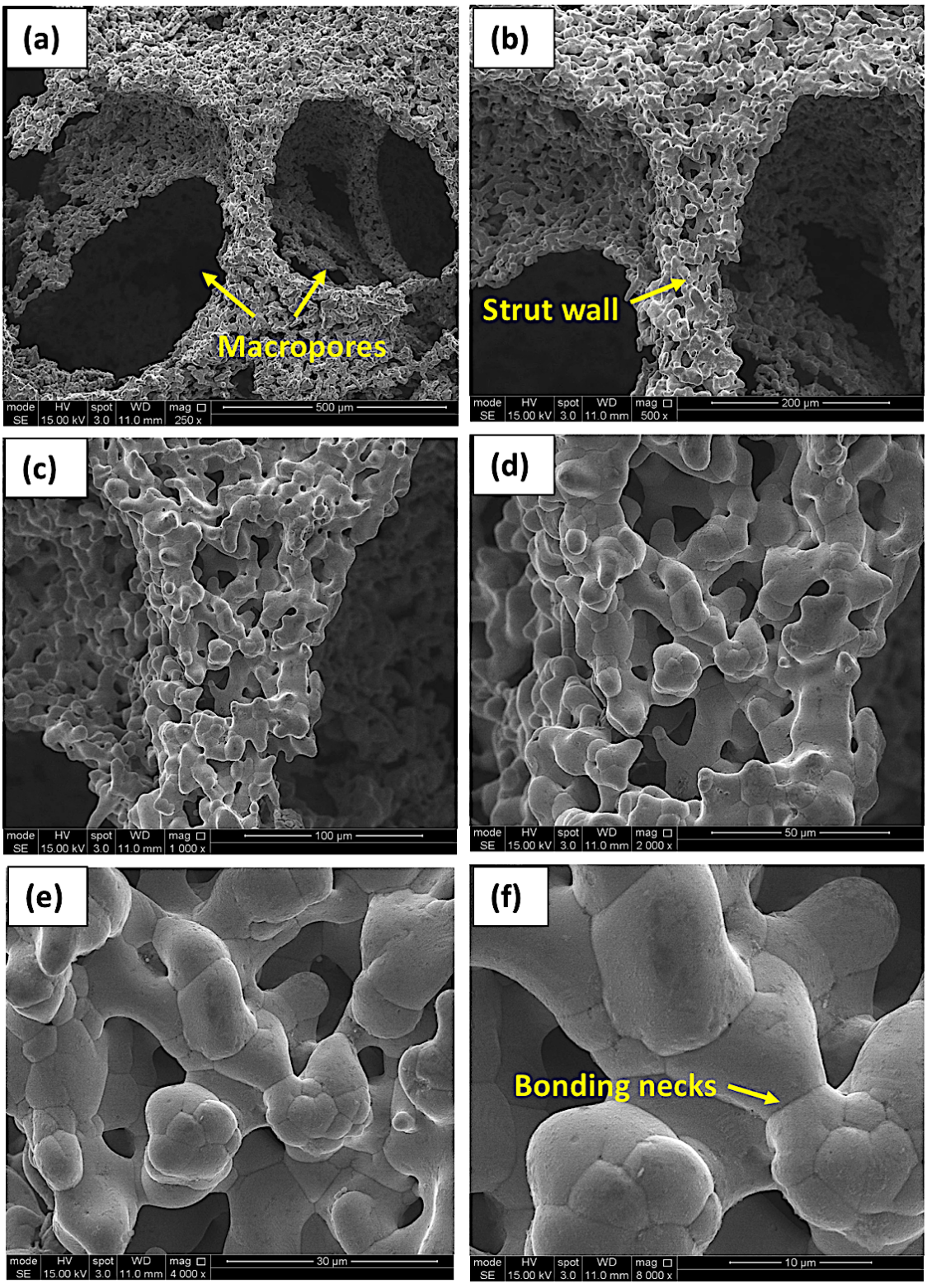

Figure 55: The structure of sintered copper particles taken at different magnifications (a) macropores connected through a network of micropores, (b) higher magnification revealing the strut walls, (c) and (d) the higher magnifications of the strut wall, (e) and (f) sintered copper particles.

The binders were only required to enable tape casting of the powders into thin sheets and to increase the green strength, which is needed for easy handling as the samples are taken through further processing. Hence, after forming and positioning, binders were extracted by thermal degradation as a fast and reliable method. The thermal stability of the binders is proportional to their molecular weight, therefore a higher debinding temperature (potentially as high as 400 °C, see Figure 28 and Figure 29) was required. To determine the appropriate debinding temperature before sintering, thermal analysis was carried out on green samples to study the degradation behaviour of the binder.

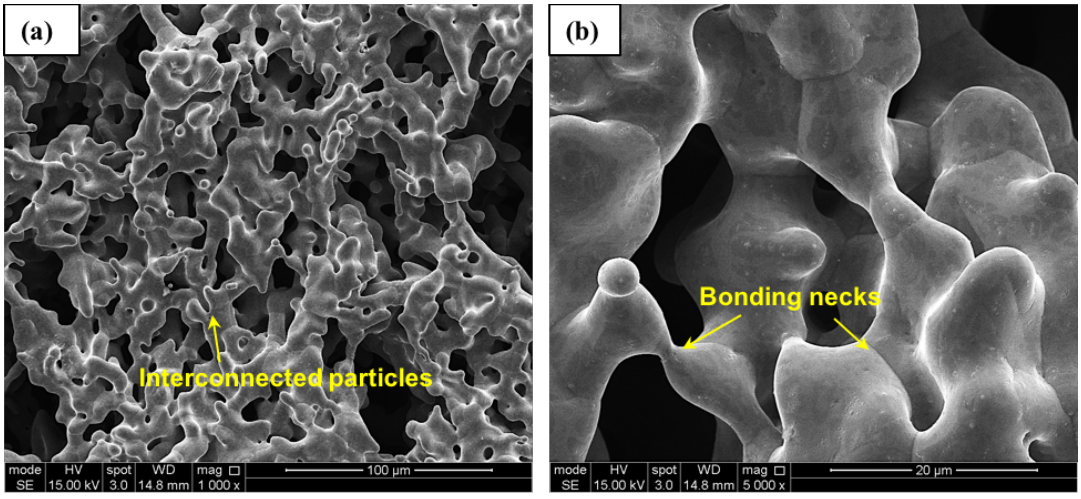

Figure 56: SEM micrographs depicting sintered copper particles interconnected after sintering.

Thermo-gravimetric analysis (TGA) was performed on the green samples under argon to elucidate the thermal degradation behaviour of the binders. The results are shown in Figure 28 in section 3.1.5, where thermal degradation was performed at different rates e.g. 2.5 °C/min, 5°C/min, 10°C/min, and 15°C/min to determine the appropriate heating rate. At the end 15°C/min was selected as the suitable heating rate to compromise between the processing time and capability of the furnace (exhaust valves output capacity). Furthermore, all heating rates were capable of extracting all binders from the sample (complete debinding) at 400 °C, hence any heating rate tested here can be applied for debinding, and also sintering.

Consequently, the heat treatment (debinding and sintering) profile (see Figure 30) applied to the green tapes was drawn based on the TGA results. That being the case, all samples produced in this work were debound and sintered following the profile in Figure 30 for consistency, and the results are presented and discussed next.

Scanning electron microscopy (SEM) analysis was employed to study the microstructural properties of the sintered tapes. Figure 56 shows the SEM micrographs of the porous tapes sintered following the heat-treatment profile presented in Figure 30. Since all the samples produced in this study were sintered following a similar heat treatment profile, Cu particles bonded in a similar pattern as shown in Figure 56. Only the porosity of the finished component was expected to be affected by addition of 10-50 wt.% K_2CO_3. As shown in the profile, the green tapes were debound and sintered at 450 °C and 890 °C respectively. The conditions inside the heating chamber were controlled, with debinding carried out under argon while the sintering process was carried out under a controlled vacuum.

After sintering, the copper particles appear to have adhered very well to each other, forming a continuous structure of copper matrix as revealed in Figure 56 (a) and (b)). The surface of the particles appears smoother after sintering compared to those imaged before sintering. This is due to the fact that, during sintering, the driving force is the reduction in energy by the reduction in the total amount of surface area, with mobility of atoms by processes like diffusion permitting rearrangement of surfaces and promoting bonding by diffusion. Fine

dendritic arms get eliminated first during heating hence smoother particle surfaces. However, the particles were bonded to each other entirely by pressureless sintering.

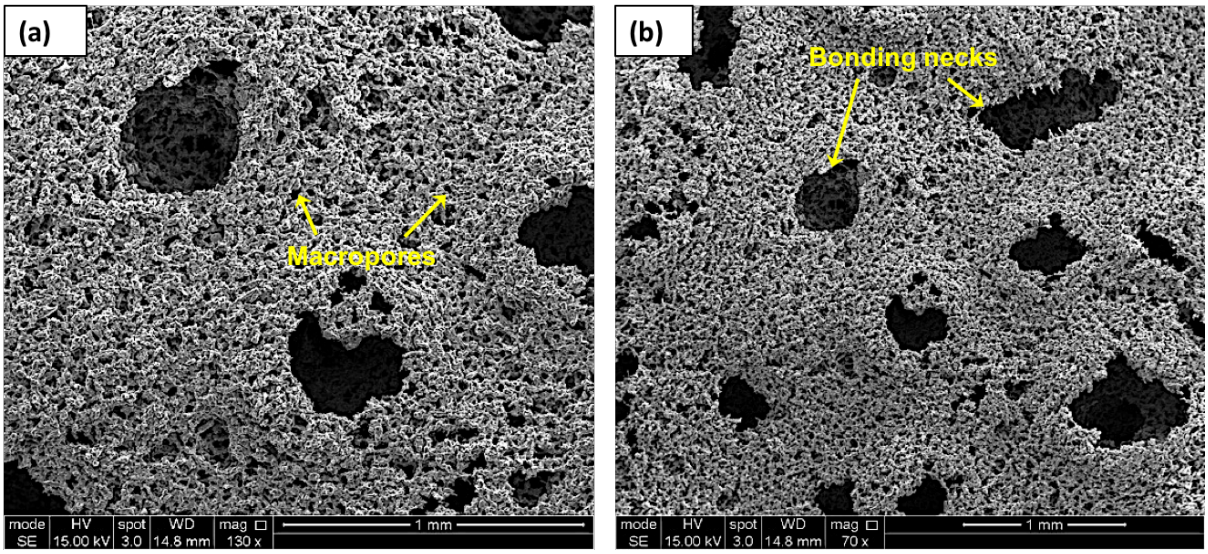

Figure 57: Top surface of porous copper samples showing the distribution of the macrpores from leachable carbonate space-holder, c) micropores resulting from incomplete densification and finally d) bonding necks of copper particles after sintering at 890 °C

As already mentioned in the previous chapters of this work, the porosity (macropores) was mainly generated by introduction of the carbonate space-holder through a process called lost carbonate sintering (LCS). Hence, K_2CO_3 was utilised as a space holder throughout this investigation. Figure 57 shows the SEM micrographs of the sintered tape revealing the surface morphology of the porous side of the sample as it was after the sintering process. Both the macropores and micropores (see also Figure 56 where micropores are more visible) are clearly seen from the micrographs. It is clear from the images that addition of K_2CO_3 during processing generated the macropores resembling the shape of the K_2CO_3 particles and thus, a large part of the porosity of the porous component can be directly controlled. Despite the fact that the pores resemble the shape of the K_2CO_3 particles, the pore size of the macropores on the top surface of the samples appears smaller than is actually the case in the sample as seen in Figure 57. To reveal the true internal morphology and actual pore size of the

macropores the top surface of the porous section was ground as shown in Figure 58 (a) and (b).

To clarify this phenomenon, the schematic diagram in Figure 59 represents how K_2CO_3 will produce a lower mean pore size than is actually the case on the sample surface, and also, the pore shape generated. Between the macropores are micropores, as shown in Figure 57 (See also Figure 56 (a) for a higher magnification micrograph). These micropores are connected to each other and hence promote connectivity within macropores and the entire porous sheet. The micropores are produced as a result of incomplete densification of copper particles during sintering.

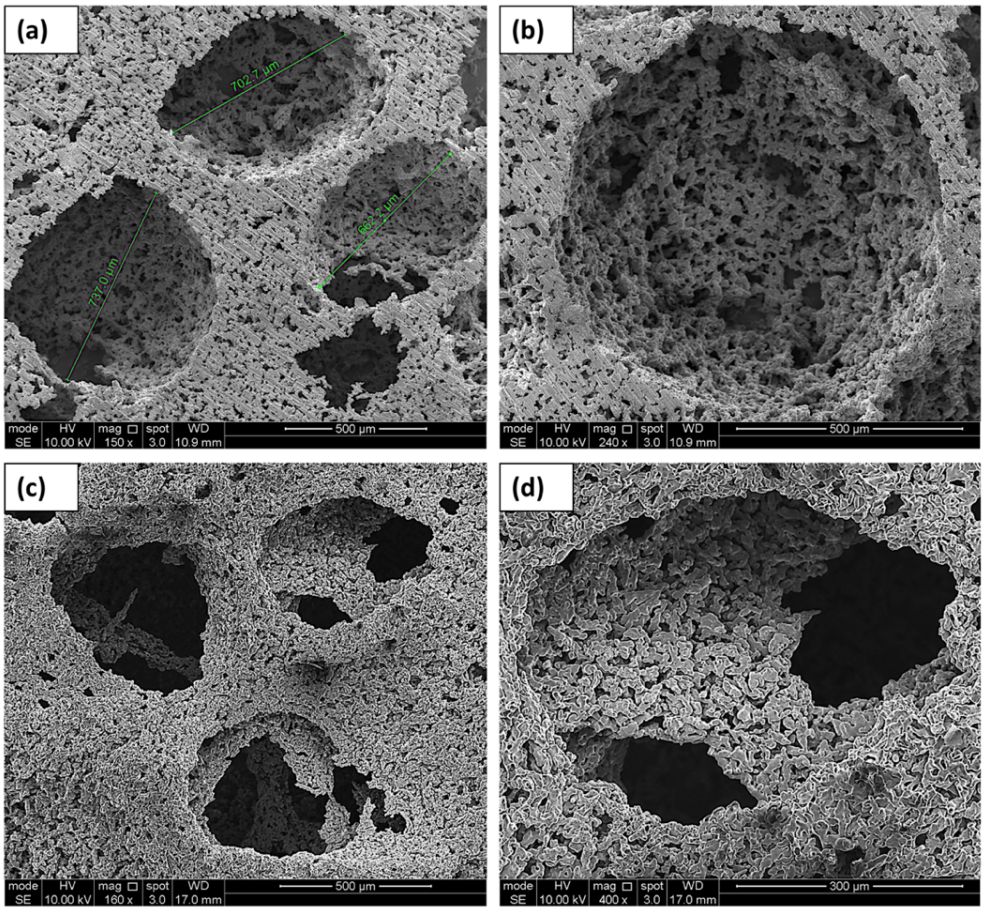

Figure 58: SEM micrographs of sintered tapes revealing the structure of the macropores; (a) and (b) ground sample to reveal the internal structure of the macropores generated by K_2CO_3 and (c) and (d) not ground to reveal a typical pore structure.

The schematic diagram in Figure 59 shows the intersection of random planes across the surface or thickness of the porous sample. This importantly shows how the space-holder sintered or hot pressed within the metal matrix will produce a lower mean pore size than is actually the case.

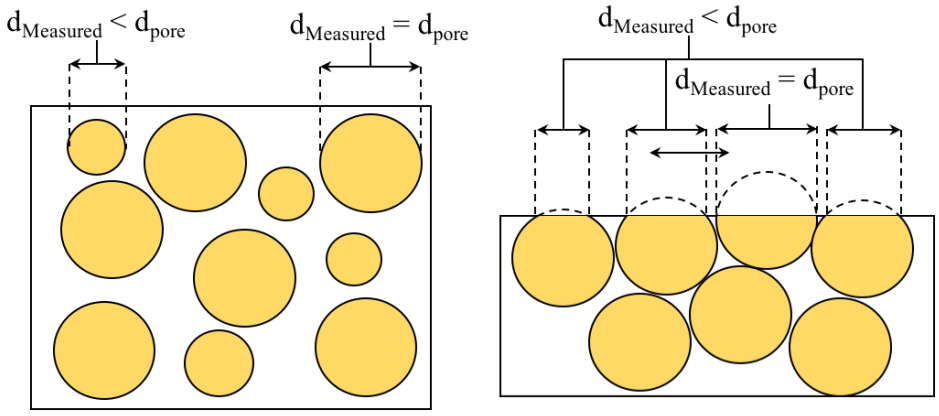

Figure 59: Schematic diagrams showing the intersections of random plane across the surface or thickness of a porous tape. It shows how the space-holder will produce a lower mean pore size than is actually the case on the sample[183].

In this work, porosity was primarily generated by introduction of macropores through a K_2CO_3 space holder, meanwhile, micropores were generated as a secondary effect of sintering. To differentiate the macropores and micropores in this study, for analysis purposes, pores with average diameter ≥ 50 µm are classified as macropores while pores with average diameter ≤ 50 µm are the micropores. Macropores play an obvious role in the finished porous component as they largely control the permeability. Meanwhile, micropores are also significant during processing of the samples, even in the functionality of the final porous component. During processing, especially during debinding of the green tape, the gaseous products from the decomposition of organic binders escape the tape mainly through micropores as demonstrated in the schematic diagram in Figure 60. Furthermore, they are beneficial for removal of K_2CO_3 particles from the metal matrix by dissolution. During sintering, Cu particles form a continuous network of Cu matrix around the K_2CO_3 particles,

K_2CO_3 becomes only accessible to water through the micropores during dissolution. Consequently, micropores contribute to the permeability of the final component (porous copper sheets) by connecting the macropores, which then bridges the air between macropores.

The shape of the macropores is dependent on the K_2CO_3 space holder while that of micropores depends mainly on the morphology of the Cu particles and sintering conditions. The irregular shape of the dendritic copper used resulted in the formation of irregular pore shapes especially of micropores, and rougher pore surfaces (see Figure 56) during sintering. During the sintering process (at 890 °C), it was found that some of the K_2CO_3 (melting point = 891°C) melted from the component after 2 hours. Therefore, the particle size of the K_2CO_3 reduces due to melting and thus results in a slight distortion of the pore shape and reduction in pore size in the final component, see section 6.4 for a detailed description.

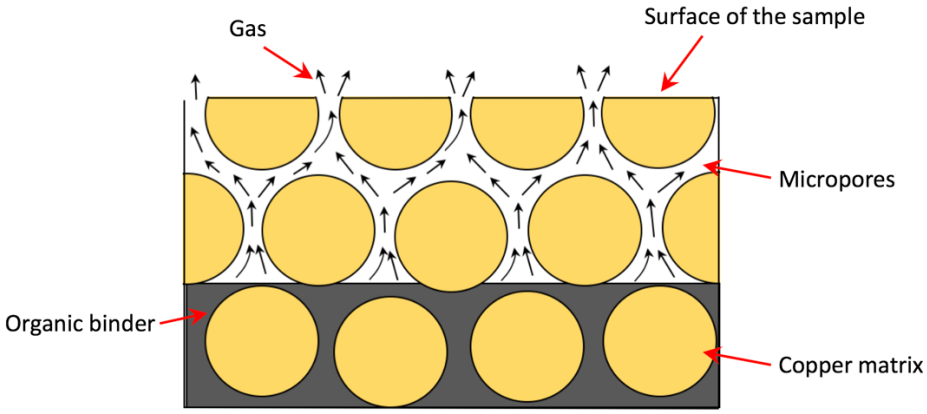

Figure 60: Schematic diagram showing the debinding model of green copper samples.

6.2 Porosity of the porous copper sheets

Porous sheets produced here can be tailored to specific applications, such as heat transfer capability by adjusting their intrinsic parameters such as porosity percentage and pore distribution. This can be defined by the weight percentage of K_2CO_3 and the processing method applied when producing the samples. In this investigation, porous copper sheets and

their porosity were varied by addition of 10-50 wt.% K_2CO_3. Pore distribution was defined by varying the fabrication route; processing route A and route B as fully described in section 3.1.3. By adjusting these two main parameters (porosity percentage and pore distribution) eleven different porous samples were produced as shown in Figure 65 and Figure 66. These two batches of the porous samples are different in terms of structure mainly the pore distribution and porosity.

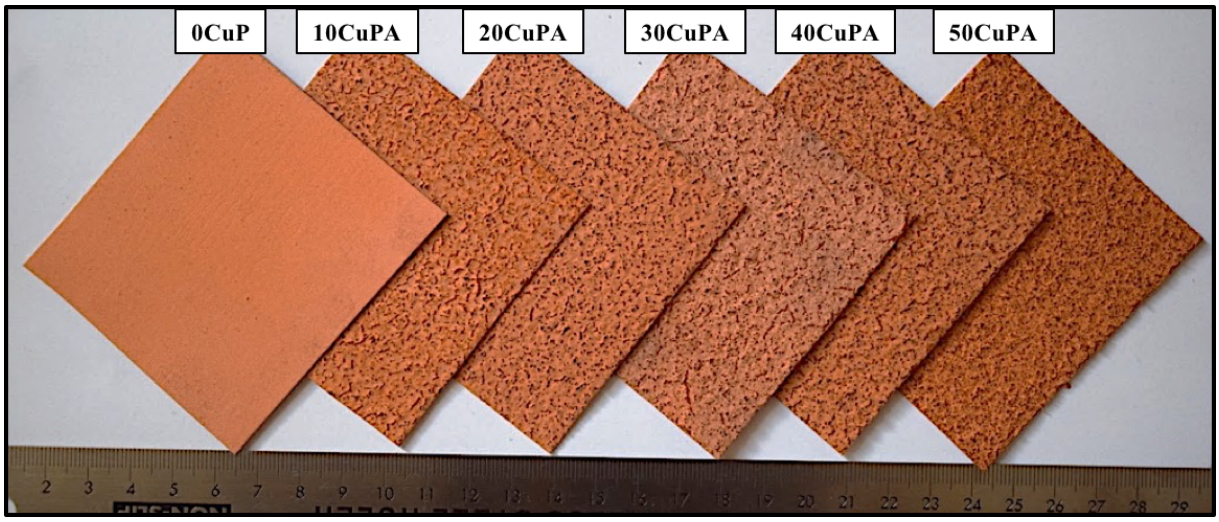

Figure 61: Porous copper tapes produced by Lost Carbonate Sintering applied to tape casting following processing route A. The tapes have volumetric porosity ranging from 50% to 81%.

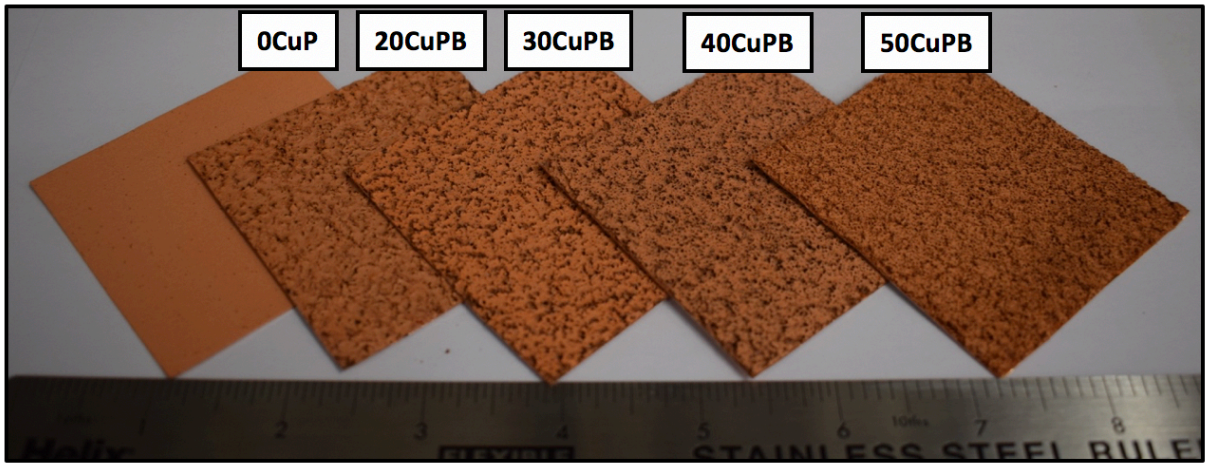

Figure 62*:* Porous copper tapes produced by Lost Carbonate Sintering applied to tape casting following processing route B. The tapes have volumetric porosity ranging from 50% to 82%.

Porosity is one of the most significant parameters across all properties in all porous metals and is usually used in the prediction of properties of the porous metals such as heat transfer capability for heat sinks[11], [48], [133], [134], [144], [175]. Because the porosity was deliberately generated in copper samples by lost carbonate sintering (LCS) where a leachable K_2CO_3 was employed, determining and understanding how processing parameters influence porosity is highly of interest. All samples produced in this work were characterised to determine both the volumetric (3D) and surface (2D) porosity generated during processing. 3D porosity was measured by employing a helium pycnometer (Accupyc 1340, Micromeritics), while 2D porosity was determined by image analysis techniques. Meanwhile, porosity consists of two parts, porosity caused by the K_2CO_3 space holder (macropores) and additional porosity caused by incomplete densification of copper powder (micropores) produced as a secondary effect. Therefore, the total porosity of the component is the sum of porosity resulting from both macropores and micropores.

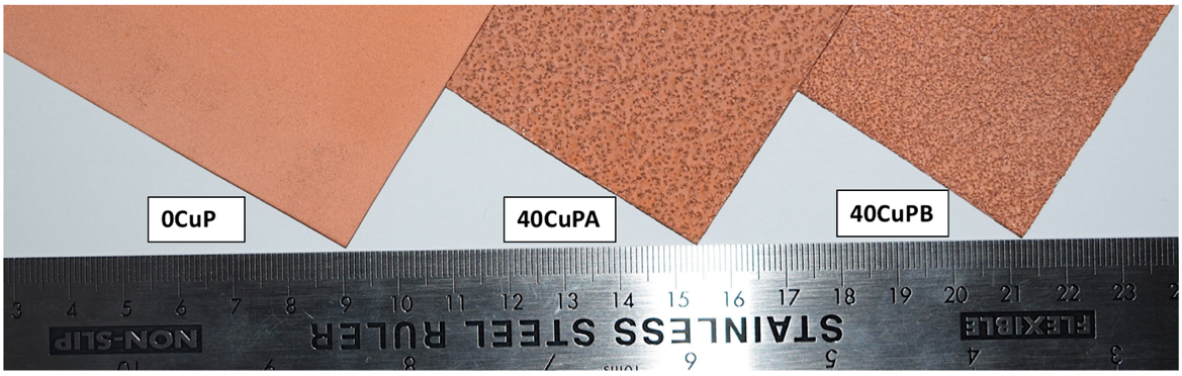

Figure 63: Images revealing the typical differences of the porous samples produced by processing route A and B. Here the samples with lower porosity and relatively high porosity are presented; 0CuP (left), 40CuPA (middle) and 40CuP (right)

6.3 Surface Porosity of the porous Cu sheets

A total of eleven samples; six of them produced by processing route A (Figure 61) and the other five samples produced by processing route B (Figure 62) were characterised to measure the surface porosity of each sample. The results were generated based on the image analysis

of SEM micrographs and photographs taken in low light to medium light conditions. Addition of 10-50wt.% K_2CO_3 during processing was expected to increase porosity across all the samples, and two different processes (processing route A and B) were also expected to change the pore distribution across the two sets of samples. **Error! Reference source not found.** s hows six samples produced by processing route A.

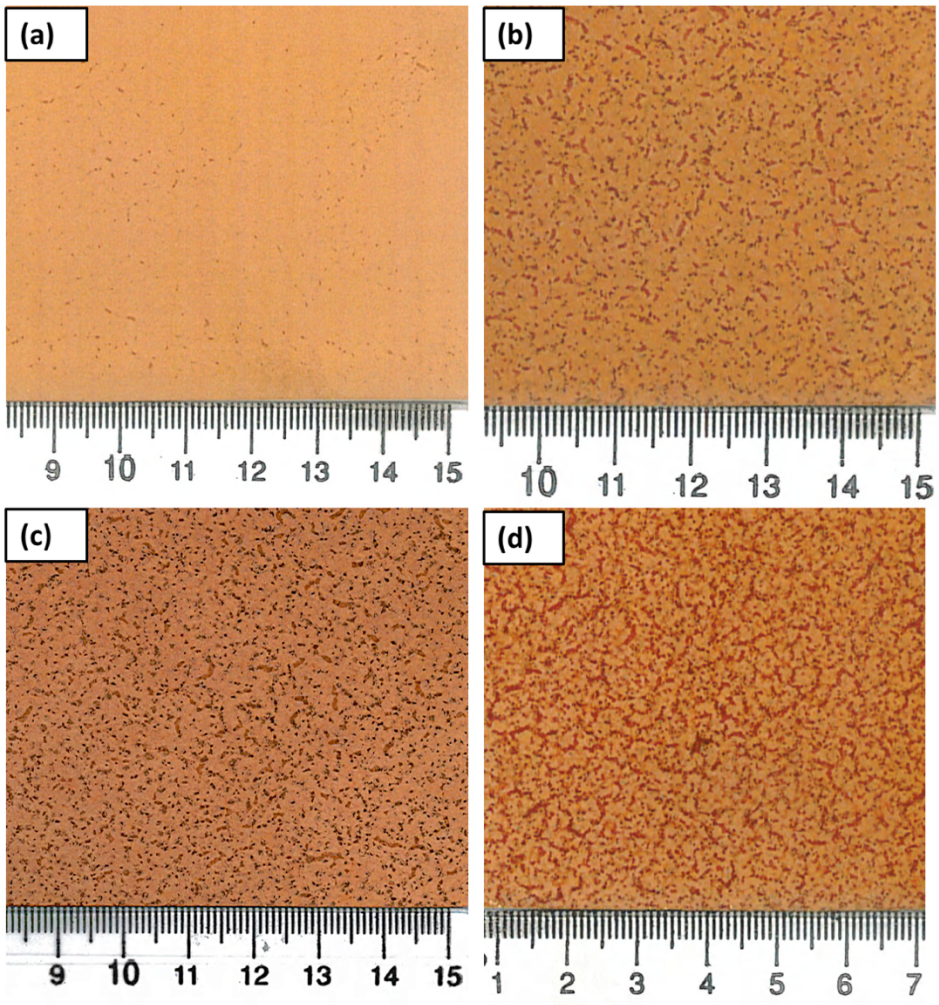

Figure 64: Images revealing the top surface of typical samples produced by processing route A: (a) 0CuP, (b) 10CuPA, (c) 30CuPA and (d) 50CuPA

All the porous samples produced and investigated in this work are presented in Table 12 where the amount of K_2CO_3 space holder added to each sample during fabrication is indicated. As already highlighted above, the total surface porosity is given by the sum of microporosity and macroporosity. For clarity, the two components of surface porosity (microporosity and macroporosity) were plotted separately, where Figure 65 presents only

the total microporosity of each sample, produced by route A and B, while Figure 66 shows the total macroporosity of each sample. The results are fully discussed below.

Table 12: A table showing the amount of K_2CO_3 space holder added during the fabrication of each sample

Processing route	Samples	Amount of K_2CO_3 added (wt.%)
A	0CuP	none
	10CuPA	10
	20CuPA	20
	30CuPA	30
	40CuPA	40
	50CuPA	50
B	10CuPB	10
	20CuPB	20
	30CuPB	30
	40CuPB	40
	50CuPB	50

6.3.1 Microporosity of the porous Cu sheets

In Figure 65, the micro porosity appears to be inversely proportional to the amount of K_2CO_3 space holder added during processing of the samples. As the addition of K_2CO_3 to copper increases in wt.% during processing, the percentage of the resulting micropores on the sample surface reduces, therefore a lower percentage of microporosity is obtained. It is well understood that, microporosity in components produced by powder metallurgical processes without using inclusions is highly dependent on the sintering parameters such as the pressure and sintering temperature. In this study, the sintering conditions were kept constant when processing all the samples. Therefore, the percentage of the microporosity generated is here governed by the processing parameters of green samples prior to sintering rather than the sintering parameters. In addition, since the sintering process was pressureless, the bonding of particles was only dependent on the sintering temperature (and the gravitational forces acting

on the sample, which are assumed to be negligible). In this regard, the formation of the micropores was due to incomplete densification of the Cu powders resulting from the selected sintering temperature and time.

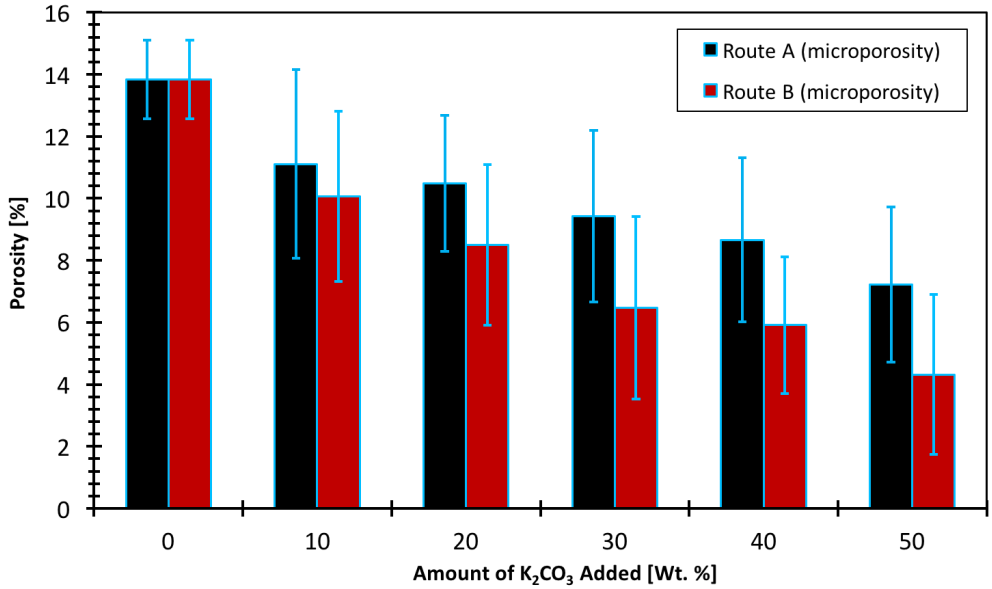

Figure 65: Surface porosity of porous copper tapes produced by both processing route A and B. Micropores and Macropores contribute to the total surface porosity.

It is clear from Figure 65 that the amount of K_2CO_3 added in weight percent is inversely proportional to the microporosity generated after sintering, hence the higher the amount of K_2CO_3 in weight percent the lower the microporosity. Because the micropores are generated within the Cu matrix forming around the K_2CO_3 during sintering, the microporosity will always be a factor of the weight percent of Cu added with the K_2CO_3 space holder. The direct relationship between the amount of microporosity and the ratio of copper powder (in weight percent) mixed with K_2CO_3 during fabrication of the samples is due to the displacement of Cu by K_2CO_3.

SEM micrographs in Figure 57 depict the distribution of micropores which were generated around K_2CO_3 (which has been dissolved to create macropores labelled in the micrograph) during sintering. Samples produced by both routes A and B follow a similar trend where the amount of microporosity in percent decreases with the addition of K_2CO_3 added during

processing in weight percent. There is a slight difference in the microporosity generated per similar amount of K_2CO_3 added between the two-processing routes. By addition of 10wt.% K_2CO_3, microporosity of 11.1% was obtained on the tapes processed by route A compared to 10.1% generated on samples processed by route B. Addition of 20wt.%, 30wt%, and 40wt.% resulted in microporosity of 10.5%, 9.4% and 8.7% respectively in route A samples, while 8.5%, 6.5% and 5.9% microporosity was obtained in the equivalent route B samples. 50wt.% K_2CO_3 resulted in microporosity of 7.2% and 4.3% for route A and route B respectively.

Generally, the samples produced by route A showed higher total microporosity compared to the samples produced by route B for a similar amount of K_2CO_3 added in weight percent. This was due to the fact that there was a less amount of macropores on the sample surface. Even though the level of microporosity decreased with the addition of K_2CO_3, the gap between the level of microporosity obtained from the two routes (route A and B) increased with the addition of K_2CO_3 as seen in Figure 65, where route A sheets achieved the higher level of microporosity between the two. The reason for this might be due to the lower level of macropores (generated by addition of K_2CO_3) in route A sheets as compared to route B sheets. In this case, the larger the number of macropores simply means there is less room for micropores to be generated as they are displaced by the macropores which are mainly generated by the addition of K_2CO_3 space holder. Generally, route B sheets have a higher amount of surface macroporosity compared to route A sheets. The schematic diagram shown in Figure 68 clearly demonstrates how there is more room for micropores compared to route B sheets which have more macropores saturated at the surface instead.

6.3.2 Macroporosity of the porous Cu sheets

Figure 66 depicts the total macroporosity from both sets of porous copper samples, where black and red bars represent the total macroporosity of porous samples processed following route A and route B respectively. Macroporosity across both sets of tapes was deliberately generated by addition of 10-50wt.% K_2CO_3. As expected, the macroporosity was directly proportional to the amount of K_2CO_3 added during processing. Samples produced without addition of K_2CO_3 space holder (0CuP) obtained a macroporosity of 9%, and this sample was processed following route A. Therefore, the macropores generated were possibly resulting from processing defects such as shrinkage cracks, air-pockets and incomplete densification during sintering. Some fine cracks were observed to form on the surface of the green samples during the drying process and also after the debinding and sintering process.

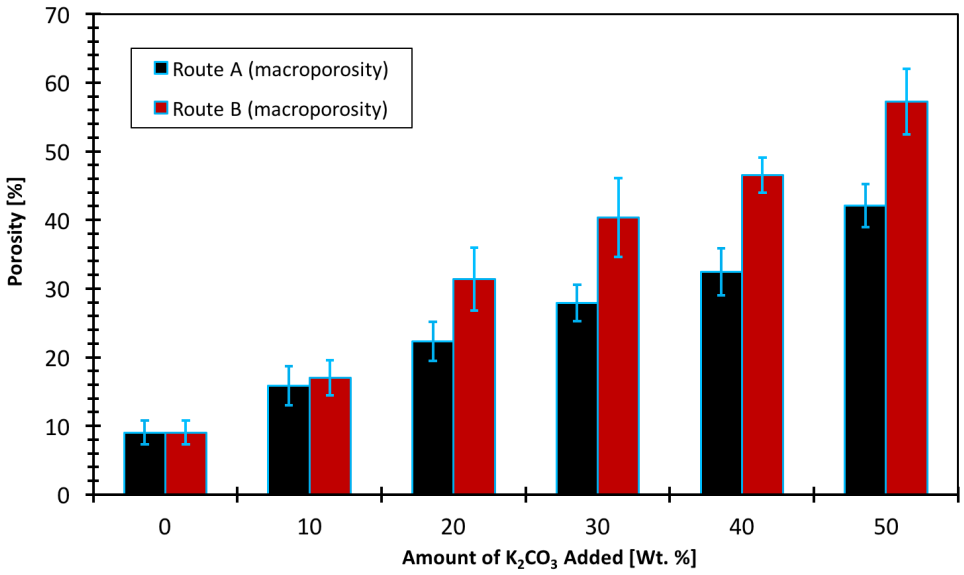

Figure 66: Surface porosity of porous copper tapes produced by both processing route A and B. Micropores and Macropores contribute to the total surface porosity.

Image analysis confirmed that the total macroporosity was not only generated from addition of K_2CO_3 but also from processing defects on the sample surface, as well as due to the dendritic shape of the raw Cu powder. Addition of 10wt.% K_2CO_3 generated a porosity of 15.9% and 17% in the porous samples produced by route A (10CuPA) and route B (10CuPB)

respectively. While, addition of 50wt.% K_2CO_3 generated the highest amount of macroporosity of 42.1% in the porous sheets produced by route A (50CuPA) compared to 57.3% obtained in the samples produced by B (50CuPB). Clearly, addition of K_2CO_3 increased the surface porosity generated in the porous sample.

As already mentioned, some macropores within the copper sheets were also generated as a result of the shape of the raw copper powder. Figure 19 clearly reveals the shape of the copper (dendritic) powder employed to produce the porous samples. The powder was not completely densified after sintering at 890°C. There were some macropores as well as micropores within the copper matrix (see Figure 56) which were clearly as a result of incomplete densification of the Cu powder, of which the dendritic shape of the powder may be the one of the major contributing factors.

6.3.3 Total surface porosity of the porous Cu sheets

The total surface porosity was calculated by the sum of microporosity and macroporosity for each sample and the results are presented in Figure 67, where the black and red bars represent the total surface porosity of the samples from route A and B respectively. Even though individually the microporosity decreased and macroporosity increased with addition of K_2CO_3, the total surface porosity increased with addition of K_2CO_3 during processing. Generally, samples produced by processing route B achieved a higher percentage of surface porosity compared to the samples produced by route A for addition of higher amounts of K_2CO_3.

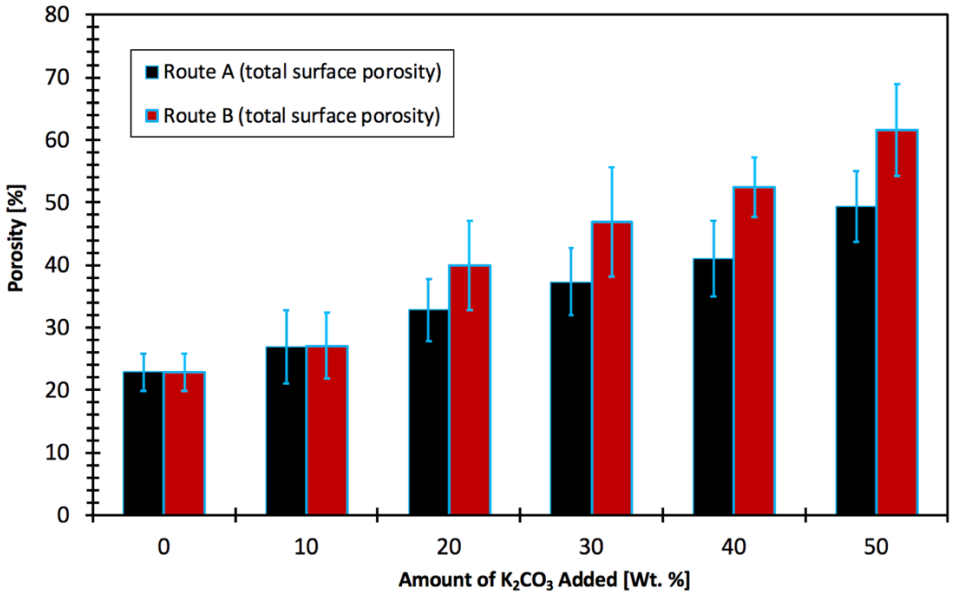

Figure 67: Total surface porosity of samples produced by both processing routes A and B.

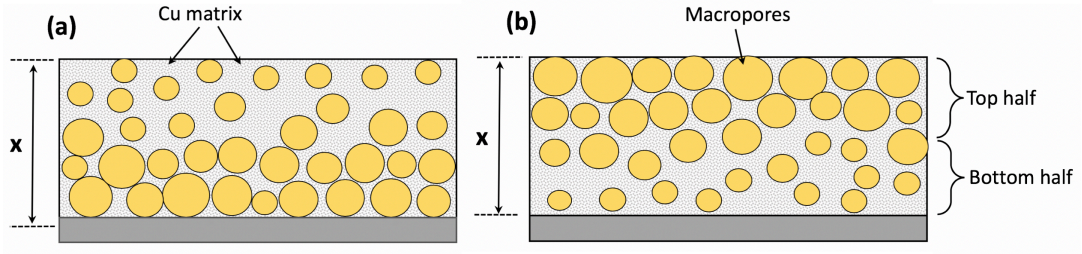

Figure 68: A Schematic diagram showing the pore size distribution across the thickness of tapes produced by processing routes (a) A and (b) B.

Addition of 10 wt.% K_2CO_3 generated the same amount of total surface porosity on 10CuPA and 10CuPB. The total surface porosity increased with the addition of 20-50wt.% K_2CO_3 across the samples produced by both routes A and B. However, samples produced by route B achieved higher percentage of total surface porosity compared to the samples produced by route A for a similar amount of K_2CO_3 added. The difference in the total surface porosity among the samples from both routes was clear with the addition of 20-50wt.% K_2CO_3, of which 20 wt.% K_2CO_3 and 30 wt.% K_2CO_3 generated a total surface porosity of 32.8% and 37.3% on samples produced by route A compared to 38.9% and 46.8% of route B samples respectively. By adding 40 wt.% and 50 wt.%, a porosity of 41.1% and 49.3% was generated

on route A samples compared to 52.4 and 61.6% on route B samples respectively. After addition of 50 wt.% K_2CO_3 route B samples were 12.3% more porous compared to route A samples. At this stage, the samples produced by route B were generally more porous on the top surface compared to the samples produced by route A.

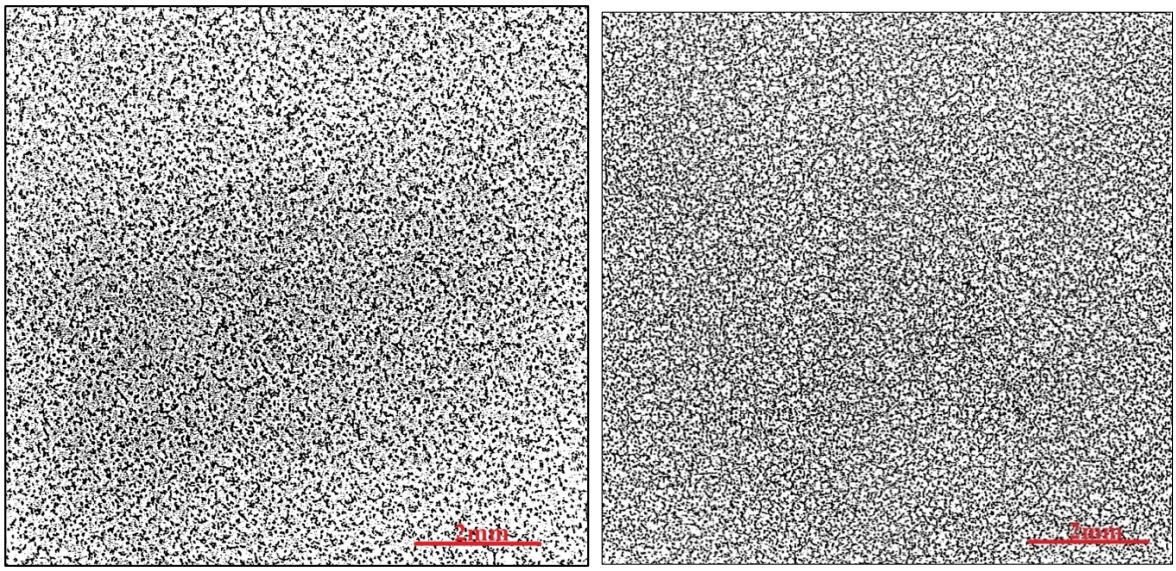

Figure 69: Images revealing the typical differences in the surface porosity of porous samples; 40CuPA(left) and 40CuPB (right)

6.3.4 Pore distribution within the samples

6.3.4.1 Pore distribution by image analysis – 2D

At the beginning of this study, the samples were only produced by processing route A, where the slurry was directly fabricated on the copper substrate through the doctor blade as shown in Figure 24, then sintered. SEM micrograph analysis was employed to carry out initial assessment of the pore distribution across the thickness of each sample. The samples were sectioned and imaged by SEM hence allowing porosity measurement using image analysis. By dividing the thickness of each sample in the image into two halves; bottom and top half porosity was measured in sections, and the results are presented in Table 13. It was found that macropores generated by K_2CO_3 are concentrated in the bottom-half of the sample rather than

the top-half for all the samples produced by route A. 20CuPA achieved 38.6 ± 2.3 % of the macropores concentrated in the top-half compared to 61.4 ± 2.6 % of the macropores mainly in the bottom-half, while 40CuPA achieved 35.6 ± 2.1% of the macropores mainly in the top part compared to 64.4 ± 2.6 % in the bottom-half. 50CuPA also obtained a similar pore distribution where 39.2 ± 2.5 % of the macropores were concentrated in the top-half compared to 60.8 ± 2.9 % in the bottom-half.

Ideally, considering the design of a heat sink, samples with higher porosity in the top-half of the component than in the bottom-half would be expected to have better heat transfer performance. By introducing processing Route B shown in Figure 25, the pore distribution was inverted, resulting in a more porous top-half than the bottom-half as clearly revealed in the Table 13. 20CuPB obtained a higher percentage of macropores in the top-half of 58.3 ± 2.8 % compared to 41.7 ± 3.1 % in the bottom-half. 40CuPA also achieved a similar pore distribution where 61.7 ± 2.5 % of the macropores were concentrated in the top-half and 38.3 ± 3.2 % in the bottom-half. Also, 50CuPB obtained 60.2 ± 2.6 % of the macropores concentrated at the top-half and 39.8 ± 3.3% in the bottom-half. Both route A and B samples were taken through further investigation, most importantly heat transfer analysis. The total surface porosity of samples processed by route B is clearly higher than that of samples produced by processing route A as observed from Figure 67.

Table 13: Average pore distribution across the thickness of the porous samples produced following processing route A and B.

Manufacturing routes		Top half porosity (%)	Bottom half porosity (%)
Processing Route A	20CuPA	38.6 ± 2.3	61.4 ± 2.6
	40CuPA	35.6 ± 2.1	64.4 ± 2.7
	50CuPA	39.2 ± 2.5	60.8 ± 2.9
Processing Route B	20CuPB	58.3 ± 2.8	41.7 ± 3.1
	40CuPB	61.7 ± 2.5	38.3 ± 3.2
	50CuPB	60.2 ± 2.6	39.8 ± 3.3

6.3.4.2 Pore distribution by microCT analysis – 3D

It was also necessary to study the pore distribution across the samples in a 3D form, hence microCT analysis was employed. From the analysis, the plots of pore volume versus thickness were generated representing how the pores (especially the macropores) are distributed in a 3D form as shown in Figure 70. Six samples were systematically selected for this investigation; 20CuPA, 20CuPB, 40CuPA, 40CuPB, 50CuPA and 50CuPB.

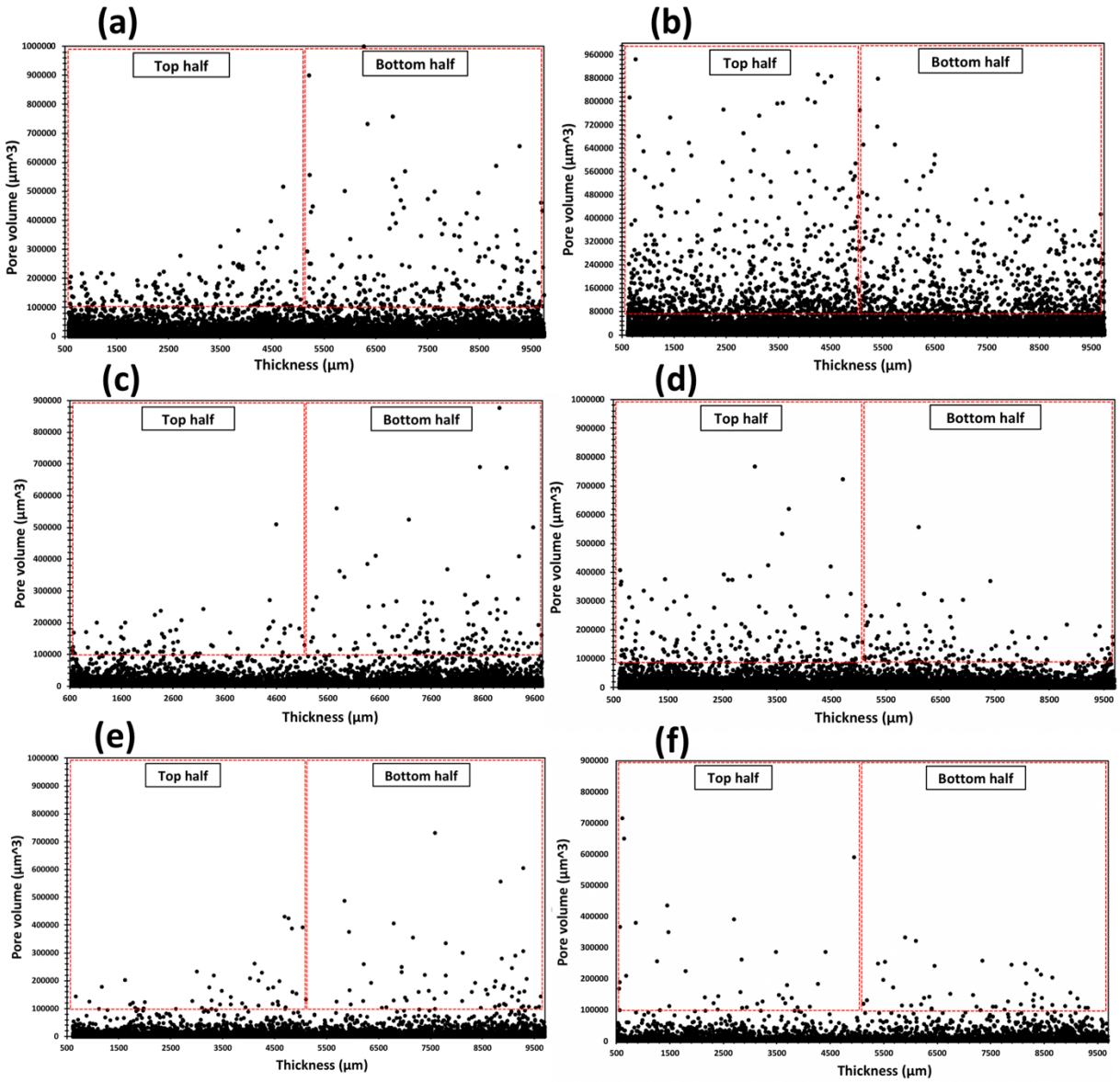

Figure 70: Pore volume distributions of the micropores and macropores across the thickness of the porous tapes (a) 20CuPA, (b) 20CuPB, (c) 40CuPA, (d) 40CuPB, (e) 50CuPA and (f) 50CuPB.

As depicted in Figure 70, the results agree with the image analysis (2D) results discussed earlier in section 6.3.4.1, where the samples produced by processing route A have a higher percentage of macropores in the bottom-half of the sintered samples than in the top-half while the samples from processing route B recorded a lower percentage of the macropores in the bottom-half of the sample compared to the top-half. The micro-CT images in Figure 71 reveal the pore distribution and pore shape across one of the six selected samples. Figure 70 (a), (c) and (e) represent 20CuPA, 40CuPA and 50CuPA and Figure 70 (b), (d) and (f) represent samples 20CuPB, 40CuPB and 50CuPB respectively. Given that pores with a volume greater than 205670 μm^3 are classified as macropores in this work, the rectangles with a dotted red outline are used in these plots to highlight the regions of macropores within the plots, either within the bottom-half or the top-half of the tested samples as labelled.

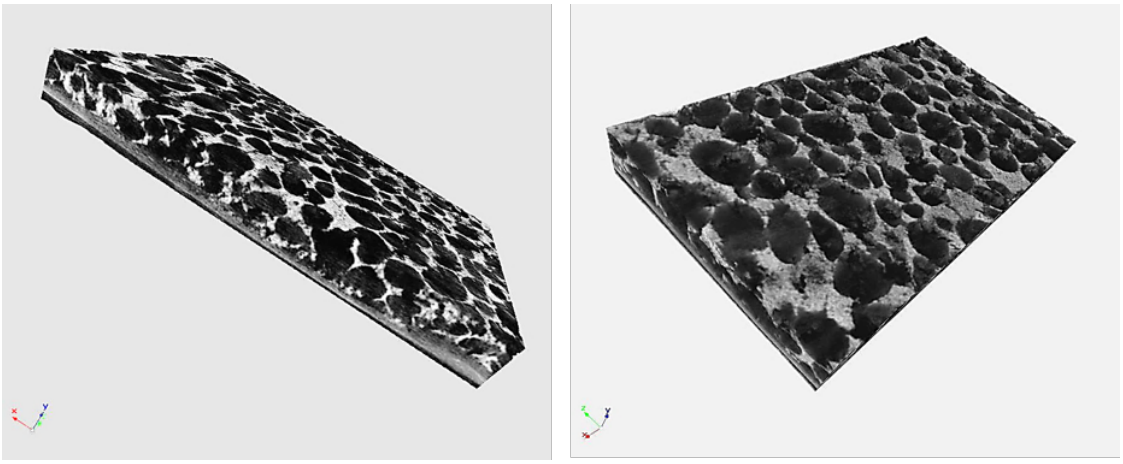

Figure 71: 3D images of porous copper sheets revealing the pore distribution across the thickness of 40CuPA.

The pore distribution was mainly influenced by two processing factors. Even though the 99.9% pure Cu (density = 8.96 g/cm^3) used in this study is denser than the K_2CO_3 (density = 2.43 g/cm^3), the mixture of the organic binders ((ρ_{PMMA} = 1.18 g/cm^3, ρ_{Ethnol} = 0.79 g/cm^3, $\rho_{2\text{-}Butanol}$ = 0.81 g/cm^3, ρ_{DBP} = 1.05 g/cm^3 and ρ_{TPP} = 1.21 g/cm^3 at 20 °C) is half as dense as the K_2CO_3 space holder. After casting the slurry, the K_2CO_3 tends to sink towards the Cu

substrate while the slurry is still viscous, resulting in higher concentration of K_2CO_3 in the bottom-half compared to the top-half, thus leading to an inhomogeneous distribution of the macropores in the final porous component.

6.4 Volumetric (3D) porosity of the porous Cu sheets

The LCS process was employed mainly to control the volumetric porosity within the porous copper sheet. Because different amounts of K_2CO_3 space holder were introduced to produce samples with a wide range of porosities, it was desirable to carry out 3D porosity (or bulk porosity) measurements to study the effectiveness of the whole process. These measurements were carried out using a helium pycnometer (Accupyc 1340, Micromeritics). The density was measured using Archimedes' method (see section 3.2.4). It is understood from previous discussions in sections 6.3.4.1 and 6.3.4.2 that the macropores were successfully generated, and homogenously distributed across the sample.

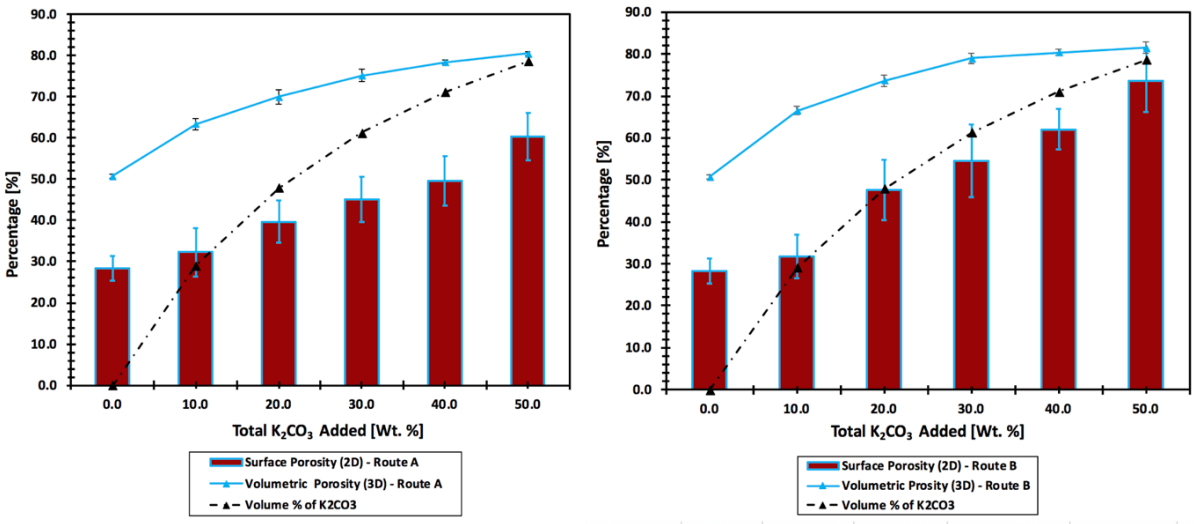

Figure 72: The two graphs showing the effect of K_2CO_3 addition on the surface porosity and volumetric porosity (3D) porosity of porous samples produced by both processing route A and B.

Figure 72 shows both the total surface porosity and volumetric porosity plotted against the amount of K_2CO_3 added to the sample during processing in weight percent (wt.%). Like surface porosity, volumetric porosity increased with the addition of the K_2CO_3. 0CuP achieved the lowest volumetric porosity of 50.7 %, while 10CuPA and 10CuPB achieved slightly higher porosity of 63.4 % and 66.5% respectively. 30CuPA and 30CuPB attained 75.2% and 79.0%. The highest percentages of volumetric porosity were achieved by 50CuPA and 50CuPB which recorded 80.5% and 81.5% respectively.

It was observed from the graph that, by adding small amounts of K_2CO_3, volumetric porosity increased gradually by larger variations in both sets of samples, either produced following route A or route B. However, adding large amounts of K_2CO_3 caused small variation of volumetric porosity. The reason for this could be due to the distortion of the macropores noticeable in the porous sample after sintering, especially in the samples with a higher percentage of porosity. In this case, addition of larger amounts of K_2CO_3, causes higher amounts of shrinkage as larger amounts of K_2CO_3 melts. Figure 73 depicts the SEM micrograph of distorted macropores resulting when larger amounts of K_2CO_3 (Xwt.% K_2CO_3 ≥ 50 wt.% K_2CO_3) was added during processing

The thermogravimetric analysis (TGA) results shown in Figure 28 reveal that during sintering ($T_{Sintering}$ = 890°C), the K_2CO_3 space holder ($T_{melting}$ = 891°C) would be expected to be partially melted, therefore proving that, even though a small percentage was melted, it was enough to distort the shape of the macropores in the final component by creating room for shrinkage of the copper matrix. Figure 73 (b) shows partially melted K_2CO_3 after sintering at 891°C under vacuum. The reason for the shape of the curves in Figure 72 (a) and (b) could be that, after addition of smaller amounts of K_2CO_3 most of the sample densified (mostly Cu particles) during sintering, hence providing mechanical strength which resists distortion in

shape and retains the resulting macropores in the starting shape of the K_2CO_3. However, addition of large amounts of K_2CO_3 space holder means lower Cu and less remaining material to provide strength.

The constraint of the already dense Cu sheet, which provides support against reduction in lateral dimensions may be another reason why densification of the sample occurs mainly in the through thickness direction (from the top surface of the sheet to the Cu substrate or the base of the sample) resulting in a decrease in the rate at which volumetric porosity increases when larger amounts of space holder is added, hence the shape of the curve.

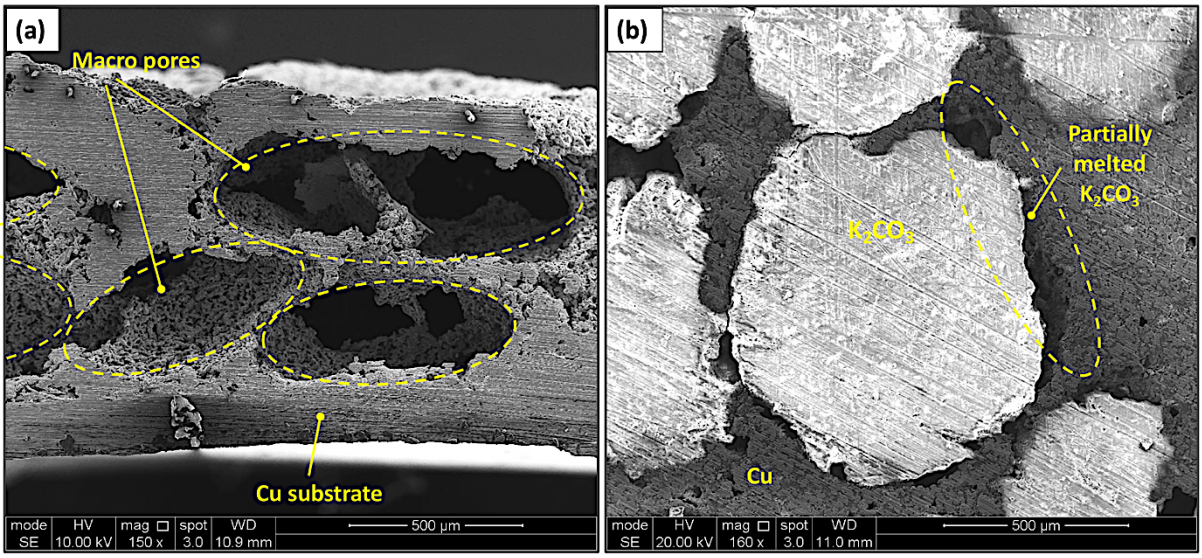

Figure 73: SEM micrograph revealing the structure of the pores across the thickness of the sample. The pores are oval-shaped, which resulted from shrinkage in the through thickness direction.

Addition of space holder greater than 50 wt.% K_2CO_3 resulted in a fragile porous structure which made it very difficult to cut or machine for further characterisation. This was due to weaker struts making the whole sample fragile especially after dissolution of the space holder. It was then decided that addition of K_2CO_3 space holder was constrained to $\leq$ 50 wt.% K_2CO_3 to compromise between the volumetric porosity and the handling strength.

It is evident from the SEM micrograph in Figure 74 that, only a small percentage ($\approx$ 5 %) of K_2CO_3 melted during sintering at a temperature ($T_{melting}$ = 890 °C) very close to the melting

temperature of K_2CO_3 ($T_{melting}$ = 891°C). This shows that the space holder is not only removed by dissolution but also by melting. The TGA results also indicate that K_2CO_3 started to melt during sintering, allowing the metal matrix to densify mainly along the through thickness direction forming oval shaped pores. This results in a reduction of the pore volume during sintering therefore affecting volumetric porosity more than surface porosity. As shown in Figure 72, volumetric porosity increases more with weight% of K_2CO_3 at the start, but then increases at a slow rate with an increase in weight% of K_2CO_3 added.

Table 14: Potassium carbonate volume added during processing and the porosity generated on the porous copper sheets

Samples	Thickness (mm)	Volumetric (3D) porosity (%)	Actual vol.% of K_2CO_3 added (vol.%)	Porosity generated by K_2CO_3 (%)
0CuP	0.74	50.7 ± 0.53	0	-
10CuPA	1.12	63.4 ± 1.42	29.1	22.6
20CuPA	1.11	70.0 ± 1.73	48.0	31.4
30CuPA	1.38	75.1 ± 1.53	61.2	39.2
40CuPA	1.07	78.4 ± 0.52	71.1	46.4
50CuPA	1.24	80.5 ± 0.51	78.7	54.0
10CuPB	1.18	66.3 ± 0.91	29.1	27.4
20CuPB	1.16	73.6 ± 1.46	48.0	42.3
30CuPB	1.61	79.0 ± 1.25	61.2	49.1
40CuPB	1.44	80.4 ± 0.68	71.1	58.7
50CuPB	1.36	81.5 ± 1.41	78.7	65.7

Both the volumetric (bulk) porosity and the surface (2D) porosity increase with the amount of the K_2CO_3 space holder added during processing. Figure 72 (a) and (b) are two plots of volumetric porosity against the surface porosity which reveals that, addition of smaller

amounts of K_2CO_3 space holder causes larger increase in both the type of porosities. However, adding larger amounts of K_2CO_3 space holder causes larger increases of surface porosity as compared to the volumetric porosity. However, the macropores as well as micropores within the porous sheets may also be due to the angular or dendritic shape of the original copper powder. As seen in Figure 56 the powder forms a network structure due to the powder shape which is maintained even after a sintering process at 890°C.

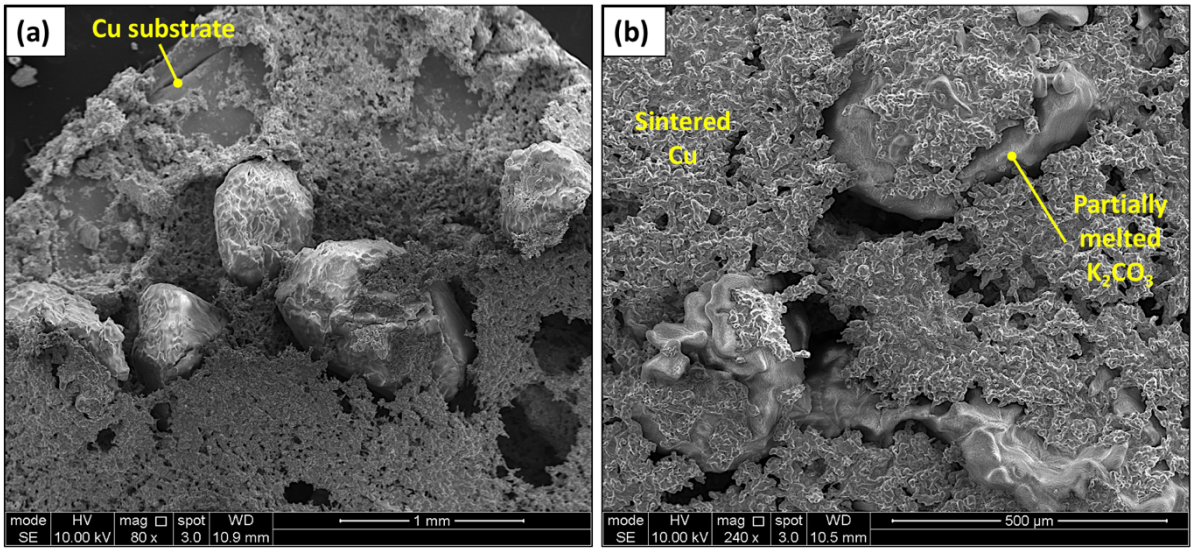

Figure 74: SEM micrograph revealing the structure of a sintered tape before the removal of the K_2CO_3 space holder.

6.5 Density of the porous samples

Relative density is one of the most significant parameters for determining the mechanical and physical properties of porous metal. In porous metals, porosity is directly related to density, whereas in homogenous or single-phase material the density is that of the bulk material. As part of this work, it was important to find the relative density of the porous samples produced here. The relative density was measured by employing volume fraction (V_m) and true densities of the bulk metal, where the helium pycnometer was used, taking the density of the solid material to be $\rho = 8.96\ g/cm^3$. The appropriate equations are given in the experimental section

and the results of the relative density (and volumetric porosity) plotted against amount K_2CO_3 (in weight percent) and are presented in Figure 75.

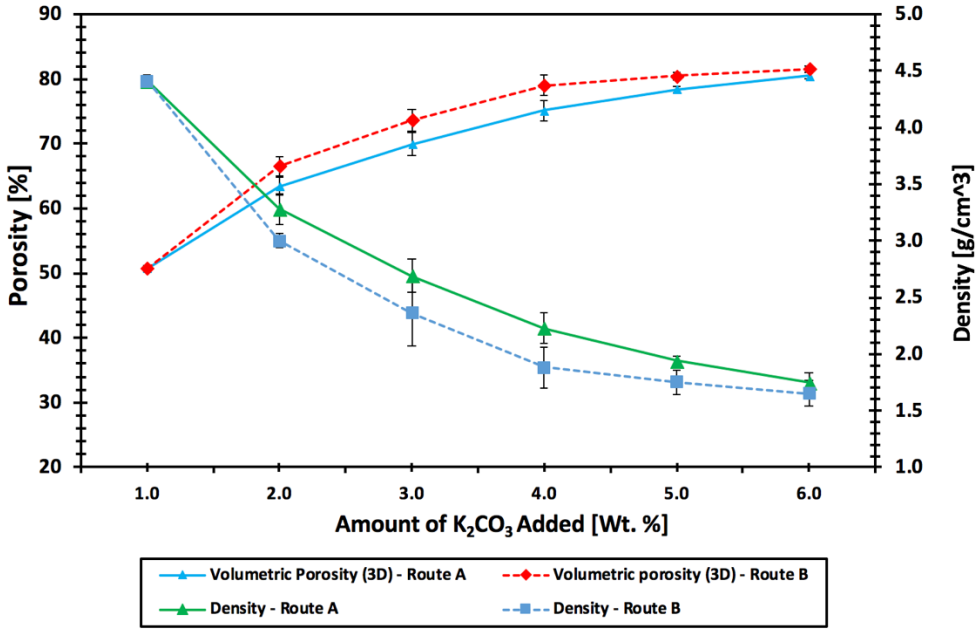

Figure 75: Density and porosity of eleven porous copper tapes under the investigation, produced by both processing route A and B

Eleven samples produced by following processing route A (0CuP, 10CuPA, 20CuPA, 30CuPA, 40CuPA and 50CuPA) and B (0CuP, 10CuPB, 20CuPB, 30CuPB, 40CuPB and 50CuPB) were investigated. It is clear from the graph that the density of the porous tapes decreases with the addition of the K_2CO_3 space holder (wt.%). At the start, the porous tape produced without addition of K_2CO_3 (0CuP) achieved a density of 4.46 g/cm^3, which is the highest density obtained from the samples considered in this investigation.

The density is clearly less than the bulk density of copper (ρ_{Cu} = 8.96 g/cm^3). In summary, 10CuPA (10 wt.% added) achieved a density of 3.31 g/cm^3 while 20CuPA, 30CuPA and 40CuPA achieved densities of 2.69 g/cm^3, 2.23 g/cm^3 and 1.94 g/cm^3 respectively. 10CuPB achieved a relative density of 3.00 g/cm^3, while 20CuPB, 30CuPB and 40CuPB achieved a relative density of 2.36 g/cm^3, 1.88 g/cm^3 and 1.75 g/cm^3. In addition, 50CuPB with a higher

percentage of porosity achieved the lowest density of 1.65 g/cm^3, while 50CuPA achieved 1.75 g/cm^3. Generally, the samples produced by route B achieved lower densities compared to samples produced by route A. Their densities decreased from 3.00 g/cm^3 to 1.65 g/cm^3 by addition of 10-50 wt.% K_2CO_3, while the density of samples processed by route A decreased from 3.28 g/cm^3 to 1.75 g/cm^3.

There is a direct relationship between porosity and density of the materials tested as clearly seen in Figure 75. The density difference in the samples investigated here (between the bulk copper powder and samples) are more likely due to (i) incomplete densification of the copper powder, (ii) macroporosity generated by K_2CO_3 and (iii) some defects resulting from processing.

Randomly distributed defects appearing on the surface might be due to processing. It is possible that some binders especially the PMMA (binder) and triphenyl phosphate (dispersant) were left undissolved, forming fine lumps trapped within the matrix during processing (i.e. debinding and sintering). Later decomposition of these lumps might have left behind some fine solidification defects or it might simply be due to rearrangement of the Cu matrix resulting in surface tearing as the binders are burnt out of the sample leaving gaps which are partially occupied by the copper.

Some air pockets were observed within the green section and also between the green layer and a dense substrate. During debinding and sintering the air pockets close to the sample surface burst on the surface leaving some defects.

6.6 Chemical composition of porous samples

The chemical properties of the porous copper is a significant factor in both the mechanical properties and thermal transfer capability. The samples produced in this study were processed using organic binders (see Table 7) and K_2CO_3 space-holder to generate pores, hence chemical analysis was required to elucidate the effects of the debinding, sintering and also the removal of space holder on the Cu particles and final porous structure. X-ray diffraction analysis (XRD), energy-dispersive x-ray spectrometry (EDS) and Raman spectrometry were employed to quantitatively determine the chemical composition of the porous samples. Only samples produced by following route A; 0CuP, 30CuPA and 50CuPA were taken through this investigation along with raw Cu powder as reference. It was considered unnecessary to investigate the samples processed following route B because they were processed under identical conditions to route A samples.

6.6.1 X-ray diffraction analysis of the porous samples

XRD patterns were achieved using a Bruker D2 Phaser. The equipment settings and testing conditions are fully described in the 'experimental methods' chapter in section 3.2.8.1. Figure 76 shows the XRD patterns of 0CuP, 10CuPA, 30CuPA and 50CuPA. All the samples were produced under the same processing conditions (e.g. tape casting, debinding and sintering conditions) except that the amount of K_2CO_3 space holder (in wt.%) varied to generate a wide range of porosity. The diffraction peaks located at 2θ values of 43.6, 50.8 and 74.4 deg corresponding to (111), (200) and (220) planes of Cu were detected across all the porous samples, and then compared with the diffraction pattern of as-received Cu powder [189]. As seen in Figure 76, no peaks related to the impurities from processing are found in the XRD pattern. However, CuO and Cu_2O[190]–[192] peaks were also absent even though they were

expected. This could be that the XRD analysis did not detect the oxides or due to them being present in too low quantity (less than about 1vol%).

The Cu peaks in the XRD patterns of as-received Cu powder (green line) appeared sharper with higher intensity compared to all porous samples tested. All porous samples had almost the same level of peak intensity. The introduction of K_2CO_3 and using a polymeric binder during processing appeared to have caused smearing and weakening of the diffraction peaks of Cu in the final porous sample. It was unclear at this stage as to where the weakening of the peak intensity of Cu could be resulting from, because there were no impurities detected in the porous sample or it might be simply that there was less material analysed (due to the pores). Therefore, the chemical composition results provided by the XRD analysis were not considered satisfactory on their own. Hence, further analysis was performed by employing other techniques of chemical analysis, Raman spectrometry and EDX, to verify the chemical composition [193]–[197].

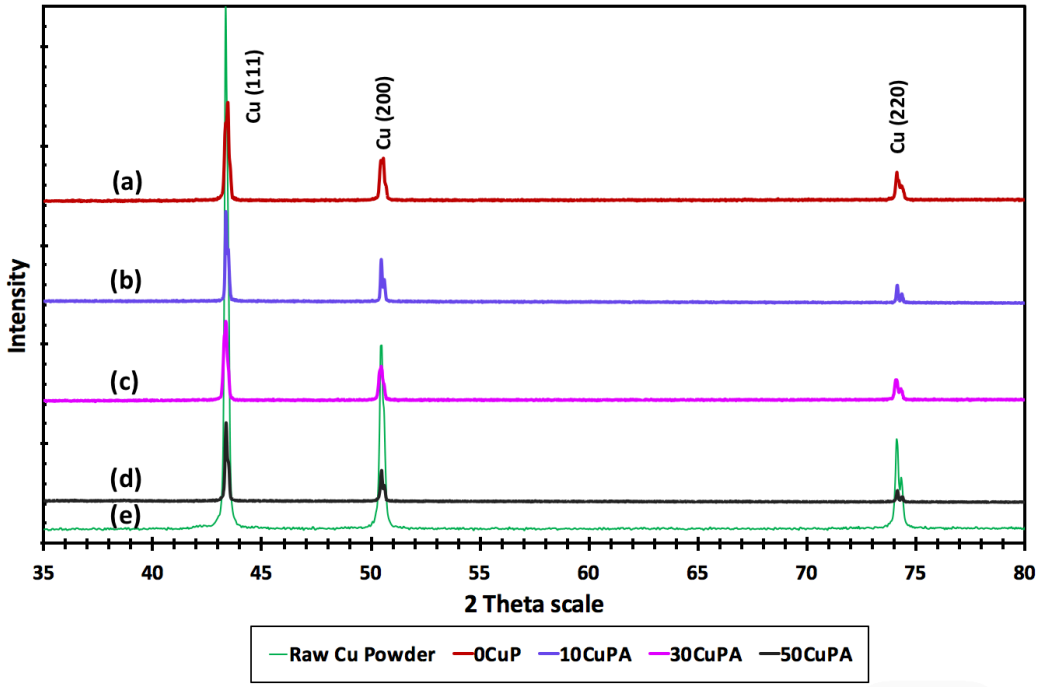

Figure 76: XRD patterns of porous samples (a) 0CuP, (b) 10CuPA, (c) 30CuPA, (d) 50CuPA and (e) as-received (raw) copper powder.

6.6.2 Raman spectrometry

Raman spectrometry analysis was carried out in addition to XRD analysis to further study the possible changes in the chemical composition occurring during processing of the porous Cu samples. Figure 77 shows the Raman spectra of porous Cu sheets with varying porosity: 0CuP, 20CuPA, 30CuPA, 40CuPA and 50CuPA along with the raw Cu powder (as-received) included as the reference.

The raw Cu powder (green line) exhibits six peaks, corresponding to CuO/Cu (112, 144, 294, 416, and 626 cm^{-1})[198] and Cu_2O/Cu (224 and 626 cm^{-1})[199]–[202]. Among the porous samples (where the first two letters indicates the weight percent of K_2CO_3 added to the Cu powder during processing as initially described in detail under Section 3.1.3), 0CuP (orange line) and 10CuP (black line) exhibit small peaks of CuO (112, 144 and 626 cm^{-1}) and Cu_2O (224 and 626 cm^{-1}) which is indicative of relatively little oxidation resulting from tape casting, debinding and sintering. 30CuP (blue line) and 50CuP (red line) display much sharper peaks of CuO (112, 144 and 626 cm^{-1}) and Cu_2O (224 and 626 cm^{-1}), clearly indicating an increasing amount of oxidation with addition of 0-50 wt.% K_2CO_3 along with addition of organic binders.

The porous sample 0CuP, produced without addition of K_2CO_3 and sample 20CuP produced by addition of 20 wt.% K_2CO_3 showed unclear Raman peaks of CuO/Cu and Cu_2O/Cu at 110/148/630 cm^{-1} and 215/630 cm^{-1}. Porous samples 30CuP and 40CuP (produced by addition of 30 wt.% K_2CO_3 and 40 wt.% K_2CO_3) showed Raman spectra at similar positions to the first samples (0CuP and 20CuP) but more visible. Sample 50CuP showed very clear Raman peaks of CuO/Cu and Cu_2O/Cu compared to all other samples, with two other peaks at 1300 cm^{-1} and 1580 cm^{-1} assigned to Cu_2O.

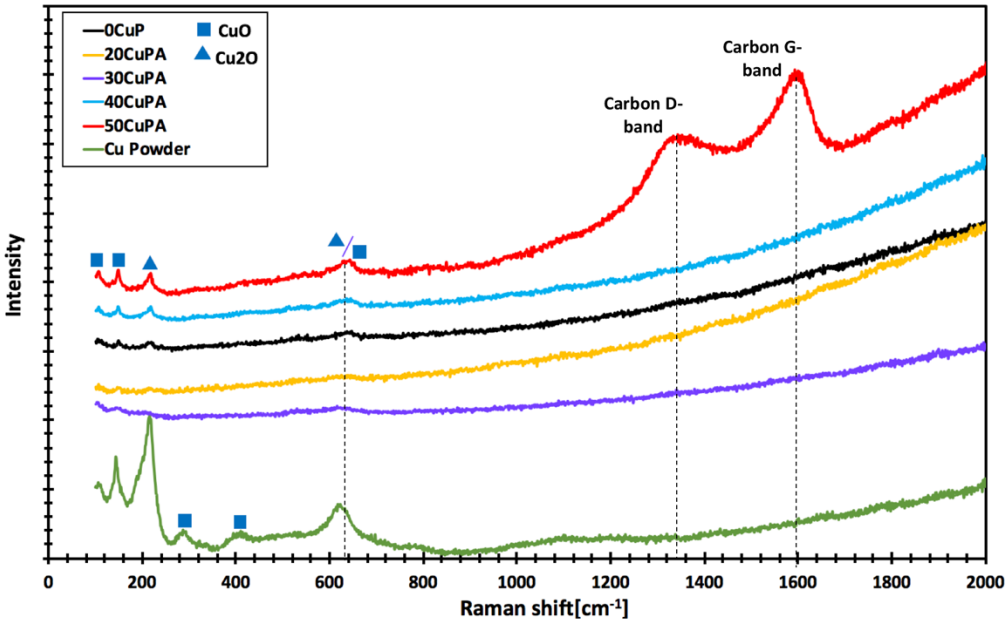

Figure 77: Raman spectra of porous copper sheets, as well as the as-received copper powder: 0CuP, 10CuP, 20CuP, 30CuP, 40CuP and 50CuP.

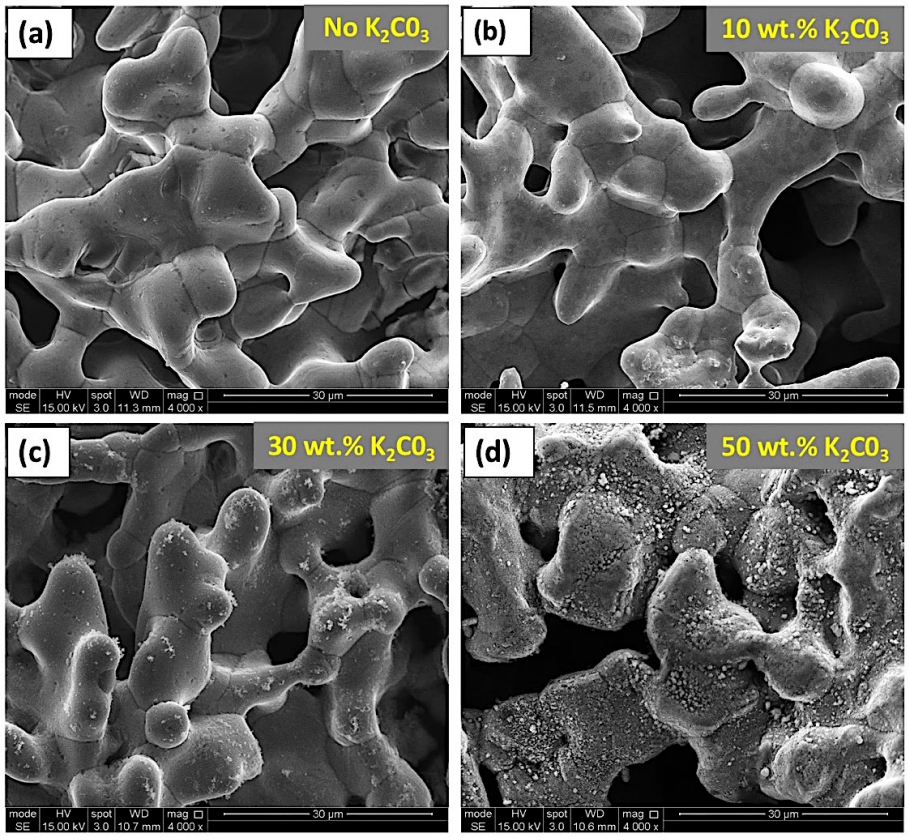

Figure 78: SEM micrographs of the fully processed porous sheets: (a) 0CuP, (b) 10CuP, (c) 30CuP and (d) 50CuP.

Raman spectra were collected at different regions across each sample. As seen in Figure 77, the Raman spectrometry detected free carbon which occurred at the wavelength band known

as ‘first order bands’ [203]. These two discernible peaks were displayed in some regions of the sample which is clearly indicative of some free carbon randomly spread across the sample [203]–[207]. The carbon was not detected in most regions of the sample. These carbon peaks occurred at two wavelength bands; the graphitic (G) band, which occurs at 1600 cm^{-1} and the disordered (D) band, which occurs at 1350 cm^{-1}. This carbon could be impurities from handling or processing.

In summary, the Raman spectrometry detected some CuO/Cu and Cu_2O/Cu compounds which were not detected by XRD analysis. This result was different from the chemical composition analysis obtained by the XRD analysis where only Cu was detected. To further verify the chemical composition of the porous Cu sheets, a third technique was employed; EDX analysis.

6.6.3 Energy Dispersive X-Ray analysis of porous copper sheets

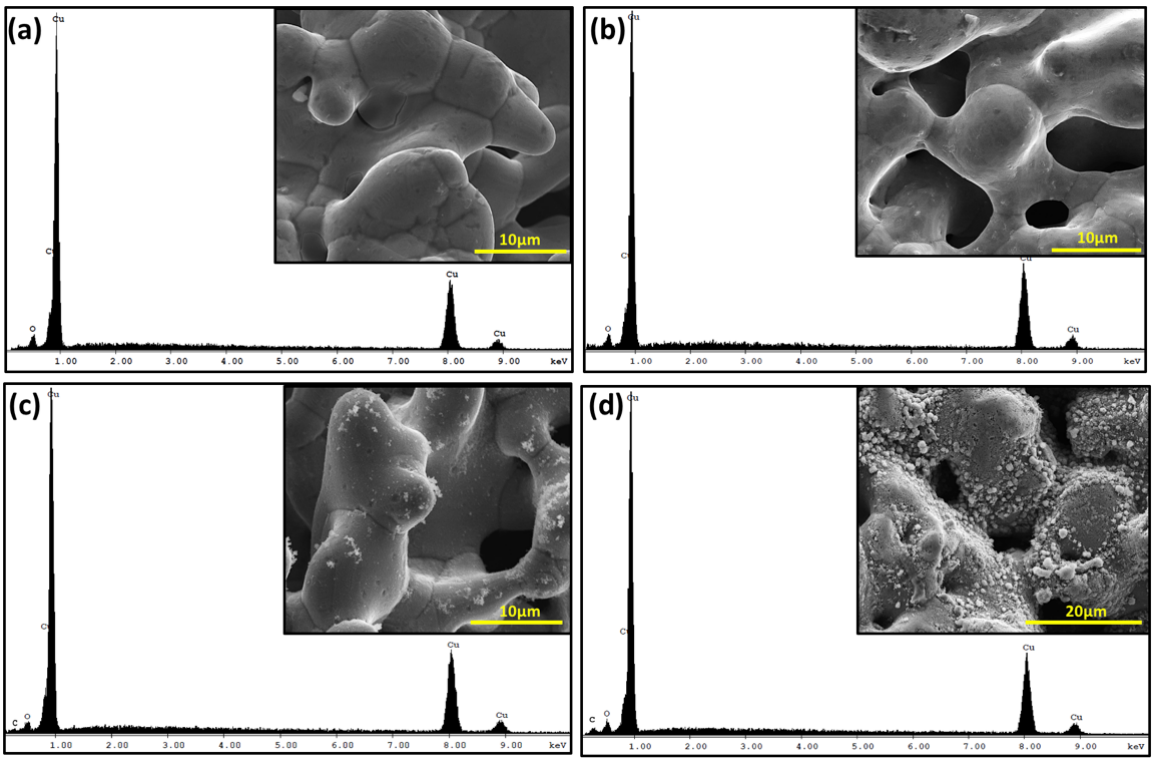

Figure 79: EDX analysis of the fully processed porous copper sheets: (a) 0CuP, (b) 10CuP, (c) 30CuP and (d) 50CuP.

The elemental composition of porous copper samples was further carried out in addition to Raman spectrometry and `XRD analysis by employing Energy Dispersive X-Ray Analysis (EDXA) using an FEI Inspect F-SEM instrument. Figure 79 shows the images of EDX spectra of all porous copper samples carried out at 10 KeV: (a) 0CuP, (b) 10CuPA, (c) 30CuPA and (d) 50CuPA. The EDX results reveal the presence of copper (Cu) and oxygen (O) in each sample. The results also displayed a uniform distribution of copper to oxygen with atomic ratio of 1:1 in CuO. The stoichiometric ratio of each porous copper sample was found to be CuO, which is lower than that for Cu_2O (1:2) which could indicate that the oxide layer is thinner than the probe depth of EDX, which therefore collects signals from the underlying Cu. The Cu, K_2CO_3, and organic binders were heated inside the furnace up to 890°C and then cooled down to room temperature under vacuum. The CuO traces could have resulted from a reaction with the additives (e.g. K_2CO_3 and organic binders) added during processing.

CuO was confirmed by the EDX analysis, which is in agreement with the results of Raman spectrometry. However, Raman spectrometry detected the presence of carbon (C) which was not present in the EDX spectra across all the samples (though the sensitivity of EDX to light elements such as C is limited). Similar results were reported elsewhere[192]. Furthermore, the SEM micrographs revealing the morphology of all the samples are also included with the spectra in Figure 79. These morphologies depict the presence of oxides in the samples. The impurities appear to be increasing quantitatively across the samples. This could mean that there was oxidation occurring in an increasing order with the amount of K_2CO_3 added during processing [192].

6.7 Summary of Processing and Structural characterisation

Thin tapes of porous copper with double-layered structure were successfully produced by LCS applied to tape casting. Surface and volumetric porosities of the porous tapes were controlled by adding 0 - 50 wt% of the leachable K_2CO_3 space holder during processing. For processing route A, addition of 0 – 50 wt% K_2CO_3 increased surface porosity from 28.3% to 60.3% and volumetric porosity from 50.7% to 80.5%. In processing route B, surface porosity and volumetric porosity also increased with addition of 0 – 50 wt% K_2CO_3 from 28.3% to 73.6% and 50.7% to 81.54% respectively. The thickness of the sintered tapes ranged between 0.74 mm and 1.61 mm. Due to an increased surface porosity of components produced by route B over route A, the component has the potential to perform better in transferring heat which is good for heat transfer applications.

In summary, after carrying out some elemental composition analysis on porous Cu samples by XRD analysis, Raman spectrometry and EDS analysis, XRD analysis only found Cu. Raman spectrometry found some CuO and Cu_2O which appeared across all samples, and EDX analysis further confirmed the presence of CuO. It could be concluded that the porous samples produced in this study were not entirely pure. Oxidation occurred on the samples, and a slight carbon contamination was present, which might have resulted from organic binders and K_2CO_3.

CHAPTER 5: Mechanical properties and further structural analysis

This chapter is split into five sections to report the results and discussions of the mechanical properties of the porous copper sheets produced in this work. All the results and discussions of the surface roughness are also covered in this chapter.

1. Section 7.1 reports the results and discussion of the simple bending tests and a modified bending test around cylinders of various diameters.
2. Sections 7.2 covers the results and discussion of the surface roughness of the porous samples investigated by both image analysis and by ContourGT profiler.
3. Section 9.2 summarises this chapter.

7.1 Mechanical Properties

7.1.1 A simple 3-point bending test

Simple three-point bending tests were carried out on all the samples shown in Table 15 by employing a universal testing machine (Zwick/Roell Z050). The machine was switched to 3-point bending test mode and fitted with a 5 KN load cell (the details of the experimental methods are fully described in section 5.2). The major structural properties (e.g. volumetric and surface porosity, relative density, roughness value (Ra) etc.) of all the samples investigated are summarised in Table 15. Flexural stress (σ_f) and stain (ε_f) were calculated from the load and deformation data from the experiment using equation (23) and equation (24). The results were presented in the form of a stress-strain curve as shown in Figure 80 and Figure 81.

Table 15: Structural characteristics and mechanical properties of porous copper sheets investigated in this work

Processing routes	Sample	Measured density (g/cm^3)	Surface porosity (%)	Volumetric porosity (%)	Width (mm)	Thickness (mm)
-	**0CuP**	4.41 ± 0.05	22.9 ± 3.0	50.7 ± 0.5	15.39	0.74
Route A	**10CuPA**	3.28 ± 0.13	26.96 ± 5.9	63.4 ± 1.4	15.21	1.12
	30CuPA	2.23 ± 0.14	37.3 ± 5.4	75.2 ± 1.5	15.12	1.38
	50CuPA	1.75 ± 0.09	49.3 ± 5.7	80.5 ± 0.5	16.14	1.24
Route B	**10CuPB**	3.00 ± 0.06	27.1 ± 5.3	66.3 ± 0.9	16.10	1.27
	30CuPB	1.88 ± 0.18	46.8 ± 8.7	79.0 ± 1.3	16.41	1.61
	50CuPB	1.65 ± 0.11	61.6 ± 7.4	81.5 ± 1.4	16.75	1.36

As described earlier, samples consist of a double – layered structure; a dense layer integrated with a porous layer. In the test, each specimen was bent with the porous layer facing down to ensure that the porous layer within the samples experiences the more demanding condition where densification is not possible and fails under tension, as shown in Figure 39. The

samples without a porous section were of course tested without the need for a particular orientation.

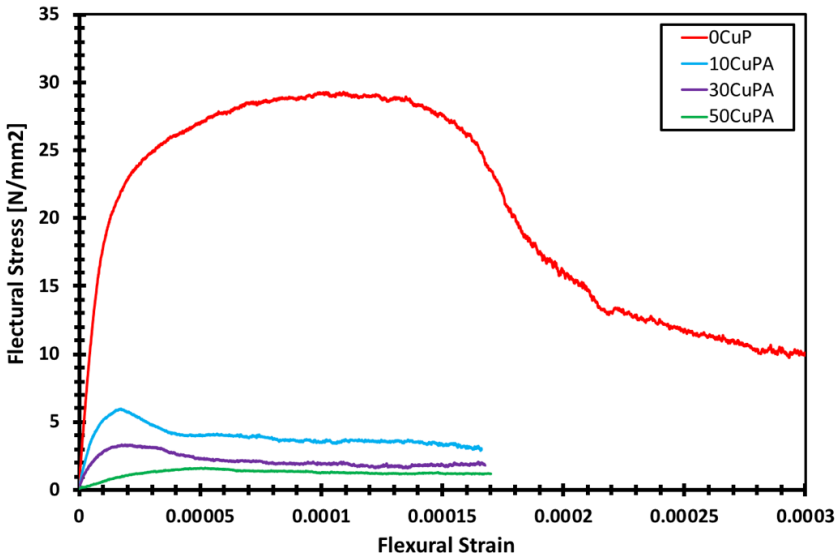

Figure 80: Example stress - strain curves of 0CuP, 10CuPA, 30CuPA and 50CuPA obtained by 3 – point bending test.

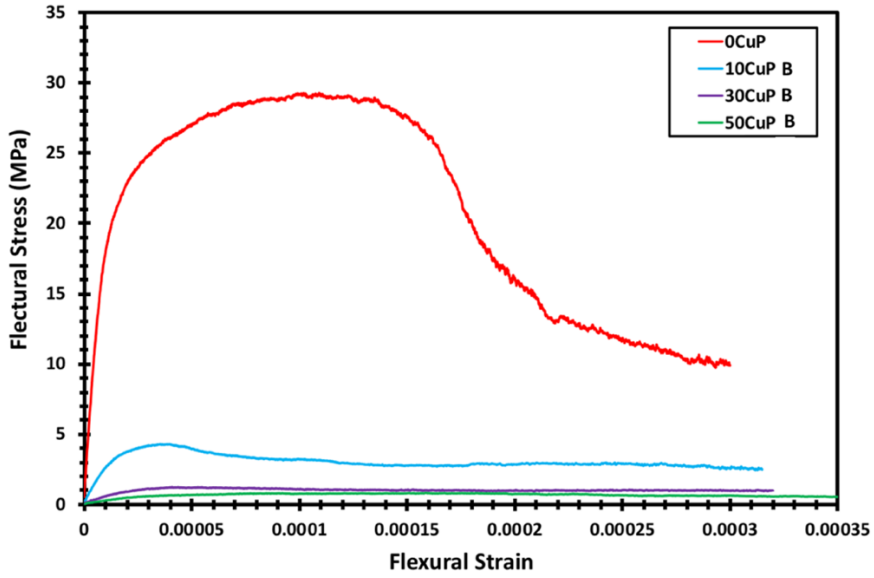

Figure 81: Example stress - strain curves of 0CuP, 10CuPB, 30CuPB and 50CuPB obtained by 3 – point bending test.

The stress – strain curves in both Figure 80 and Figure 81 resemble the classic regimes of cellular solids under bending across all the curves. Firstly, the curves exhibit the linear elastic regime, then the plastic deformation regime and finally, the failure regime. Both groups of curves appear smooth within the linear regime and show some slight stress fluctuations within the deformation regime, which worsens in the failure regime. In the linear regime, the curve

of the specimen with the lowest porosity (both volumetric and surface porosity) appear steeper especially of the sample 0CuP, indicating higher flexural modulus.

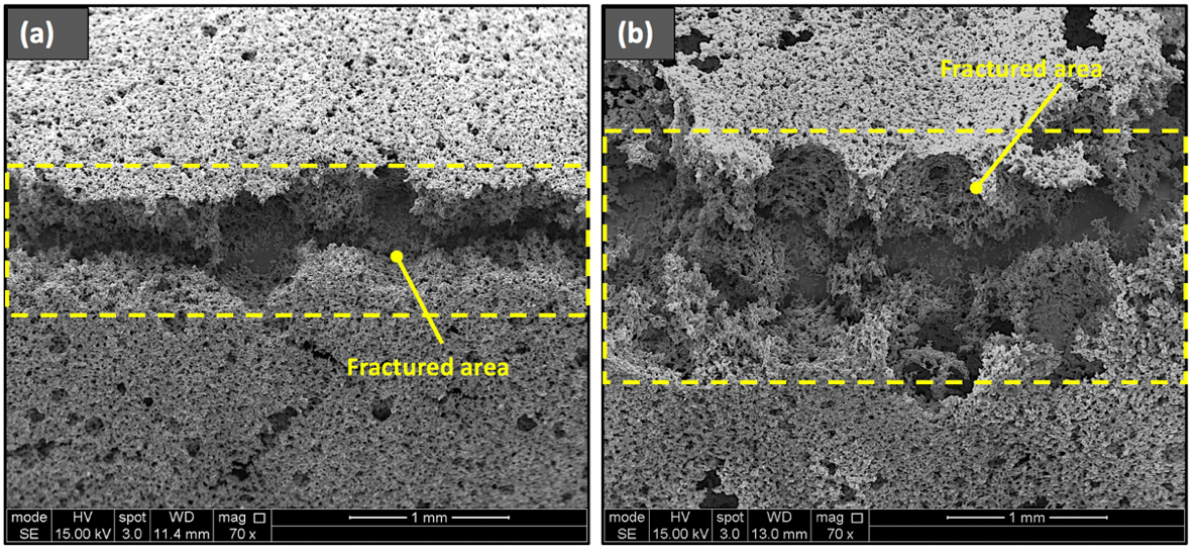

Figure 82: Fractured porous sample from the three-point bending test (a) 0CuP and (b) 40CuP

The specimens with higher porosity such as 50CuPA in Figure 80 and 50CuPB in Figure 81 displayed gentle slopes within the linear regime hence lower flexural modulus. Generally, the flexural modulus is inversely proportional to the volumetric (or bulk) porosity of the porous specimens investigated here, as would be expected for a porous material. 0CuP achieved a flexural modulus of 852.0 GPa, while 10CuPA, 30CuPA and 50CuPA achieved a flexural modulus of 651.1 GPa, 284.9 GPa and 51.6 GPa respectively. 10CuP, 30CuPB and 50CuPB achieved moduli of 258.8 GPa, 46.0 GPa and 22.2 GPa consecutively. A summary of these results is shown in Table 15.

In the plastic deformation regime, the samples with lower porosity achieved much higher ultimate flexural strength (UFS) compared to the samples with the highest porosity. Therefore, this proves that the UFS is inversely proportional to the porosity, once again as expected for porous material where higher porosity means less solid to support load. A large gap was observed between the UFS of the specimen with the lower porosity (σ_{UFS} = 29.3 ± 4.0 MPa) and that with the highest porosity (σy = 1.63 ± 0.3 MPa) among the samples

investigated. The specimen with a higher porosity failed at a lower applied strain compared to that with a lower porosity. This could be due to the pores within the porous samples, especially at the surface of the porous layer, which increase the stress concentration sites during bending while the surface is under tension. The areas with higher stress concentration are usually the bonding necks. Therefore, the higher the porosity the higher the amount of stress concentration points hence a weaker sample.

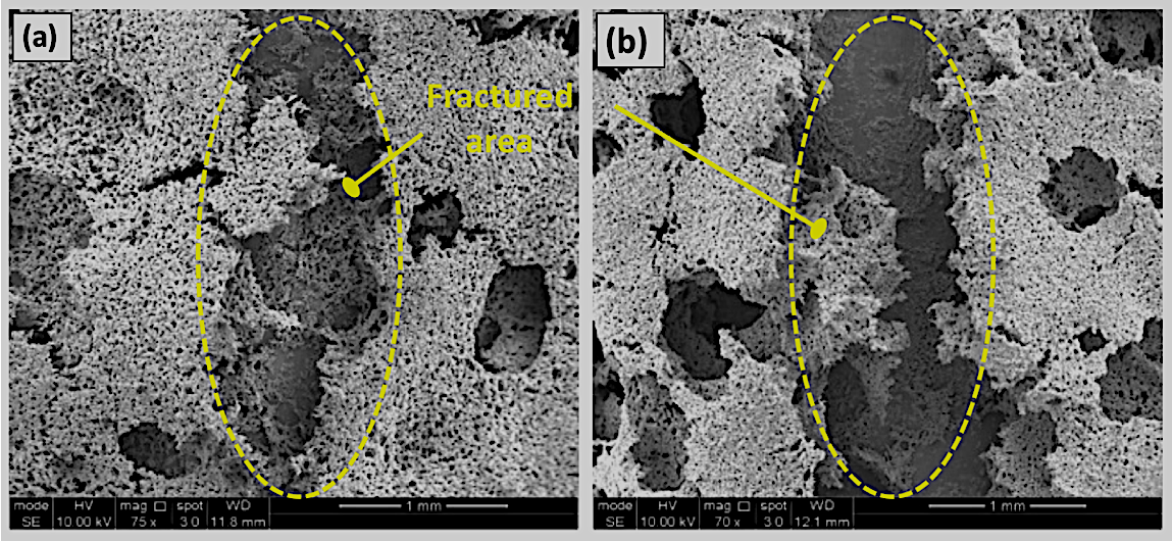

Figure 83: The typical fracture modes of the porous copper samples bent using 3-point bending test; (a) 40CuPA and (b) 40CuPB

The fracture modes of specimens 40CuPA and 40CuPB are shown in Figure 83 a) and b) respectively. A typical fracture mode is seen across all the porous samples investigated. In both SEM micrographs, the vertical fractured surface (see Figure 83) originated from the 3-point bend test. The crack initiation on the sample surface was due to tension exerted by the loading nose which led to the specimen failing or deforming under tension during bending as shown in both figures. The cracking of the sample occurred along the edge of the loading nose in both figures. Figure 83 a) depicts some parts of the porous section (sintered Cu particles) still bound to the Cu substrate. A similar behaviour was observed across the samples fabricated following processing route A. This indicates a good bond between the Cu porous

layer and a dense Cu substrate shown by the samples produced by processing route A, hence a higher yield strength and flexural modulus compared to those produced by processing route B. On the contrary, Figure 83 b), which depicts the failure mode of porous Cu sheets processed by route B indicates much fewer of the porous section parts still bound to the Cu substrate. This was an indication that the porous layer was not well bound to the substrate hence a weaker bond leading to lower ultimate flexural strength and flexural modulus for route B sheets as compared to route A sheets.

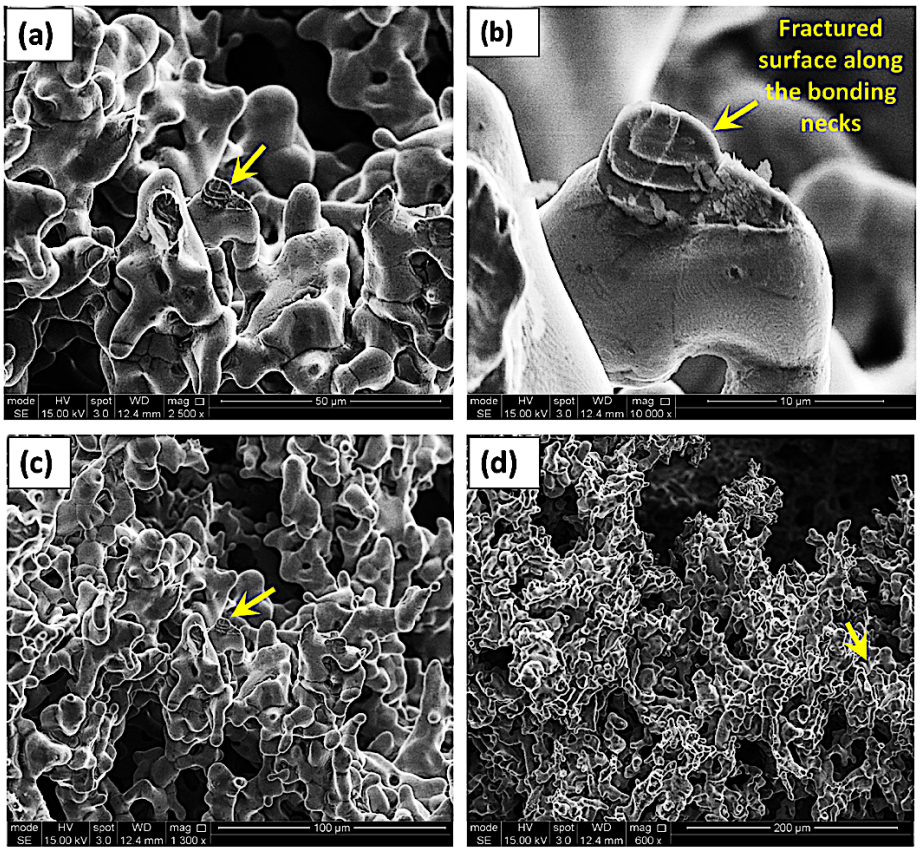

Figure 84: Fractured surface of the porous sample after 3 – point bending test. The sample fractured along the bonding necks of the particles.

Figure 84 is the SEM micrograph exhibiting the fracture surface of the sintered Cu particles. The SEM micrograph clearly depicts that the failure of porous specimens occurred at the bonding necks of the sintered Cu particles which is usually the weakest area of the specimen. In addition, the fractured surface is rough (showing micro-dimples) indicating the ductile

behaviour of the failure. The ductile nature of the porous samples might be due to the slow cooling of the samples from 890 °C to ambient temperature under vacuum. This allows the annealed copper to cool slowly, hence preserving ductility.

7.1.2 Bending around various radii

The main aim of this test is to find out how the porous samples respond to bending around curved surfaces, using the simplified situations of cylinders with different diameters. To meet this aim, 3-point bending was employed to determine the failure behaviour of the porous copper sheets. Instead of using a standard loading nose (LN) in the equipment, loading noses with varying diameters; LN 1 (∅ = 38.1 mm), LN 2 (∅ = 50.8), LN 3 (∅= 63.5 mm) and LN 4 (∅= 76.2 mm) were designed and produced inhouse to undertake this investigation. Four samples produced by processing route A were selected to carry out this investigation. These samples included 0CuP, 10CuPA, 30CuPA and 50CuPA. The samples produced by processing route B were excluded here.

The graph in Figure 86 (a) shows the force (N) – deformation (%) outcome of the 3-point bending test performed on 0CuP, where four types of loading noses with different diameters were employed, and Figure 86 (b) shows the stress – strain curve generated from the experimental results. It must be noted that the test was stopped after the sample was fully bent and wrapped around the brass loading noses as shown in Figure 85, and this was considered as the 'end point' of the test. No sign of failure was observed in sample 0CuP after bending across all the loading noses with diameters ranging from 38 – 76 mm as shown in Figure 85 (a), (b), (c) and (d).

The results were further reflected in the force – deformation curves where no sign of applied-force fluctuations were observed in Figure 86 (a), as well as in the stress – strain curves in

Figure 86 (b) where no stress fluctuations were observed. This could mean that there was no significant failure within the network of the bonded copper matrix especially at the bonding necks which are usually the weakest point in the products processed by powder metallurgy. The force fluctuations and stress fluctuations observed in Figure 86 a) and b) respectively were the usual degree of scatter resulting from vibrations during the test.

Therefore, bending 0CuP by three – point bending appears to be causing no fracture or delamination in the sample, and this material has hence proven to be capable of plastic bending around cylinders of diameter ranging from 38 – 76 mm without failure. Larger diameters cause less localised strain and should not be a problem, so 38mm marks the lower limit. While it is possible that 0CuP could be bent around curvatures of diameter smaller than 38 mm, this is the lowest tested and the material might fracture within the porous layer.

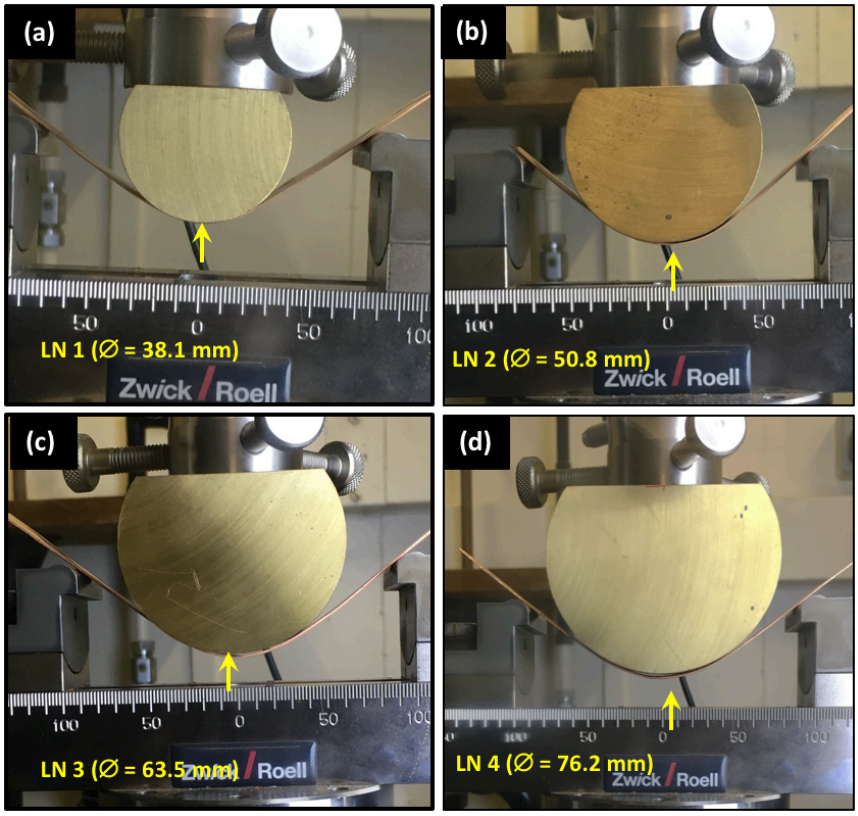

Figure 85: 3 – point bending test on porous sample. Sample 0CuP bent around loading noses (LN) of different diameters; (a) LN 1 (∅ = 38.1 mm), (b) LN 2 (∅ = 50.8 mm), (c) LN 3 (∅ = 63.5 mm) and (d) LN 4 (∅ = 76.2 mm).

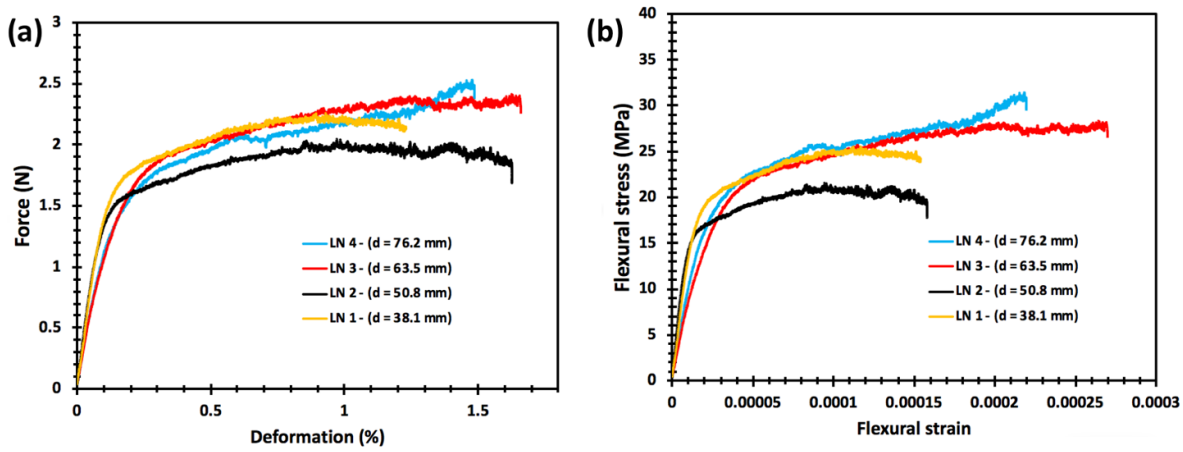

Figure 86: (a) Force (N) – deformation (%) curve and (b) stress – strain curve obtained from three-point bending tests on sample 0CuP using four different loading noses LN 1 (∅ = 38.1 mm), LN 2 (∅ = 50.8), LN 3 (∅= 63.5 mm) and LN 4 (∅= 76.2 mm)

Samples 10CuPA, 30CuPA and 50CuPA were also taken through a similar three – point bending investigation to determine how each sample responds to bending around cylinders of varying diameters. Similarly, Figure 87 shows the images of sample 10CuPA bent around the four loading noses as mentioned earlier; LN 1, LN 2, LN 3 and LN 4 in a three-point bending test. LN3 and LN4 did not cause any visible fracture in sample 10CuPA during bending, as seen in images shown in Figure 87 (c) and (d). The force (N) – deformation (%) curves in Figure 88 (a) also indicates a gradual work hardening behaviour within the plastic deformation zone in the curve. No sudden drop in the load in the curve representing deformation by LN3 (red line) and LN4 (black line) was observed, indicating that there was no clear fracture of the porous layer. There were some slight force-fluctuations and stress fluctuations observed within both force-deformation curve and stress strain curve respectively during bending of sample 10CuPA which might be indication of small failure events within the porous layer.

However, 10CuPA clearly fractured during the 3-point bending test around LN1 (green line) and LN2 (blue line). This was indicated by a sudden drop of the load in the stress-strain curve (green line) within the deformation region of the curve which represents failure against LN1.

Similar behaviour was observed when sample 10CuPA was bent using LN 2 (blue line in Figure 88 (b)) which indicated a slight drop in load in the stress-strain curve, followed by stress fluctuations in the stress – strain curve shown in Figure 88 (b) before the end of the test. These results were supported by images in Figure 87 (a) and (b) showing that the test with LN1 and LN2 samples exhibited v-shaped fracture surfaces at the point of contact with the loading nose, as is clearly seen from the images indicating failure of the component especially within the porous layer.

Within the point of contact, the crack appeared to have propagated at the bonding necks. This, and the fact that 10CuPA recorded a volumetric porosity of 63.4 % as well as a surface porosity of 27.0 % means that occurrence of crack initiation and propagation within the samples is high compared to 0CuP with lower porosity, especially when the sample is bent by loading noses with smaller diameter, such as LN 1 and LN 2.

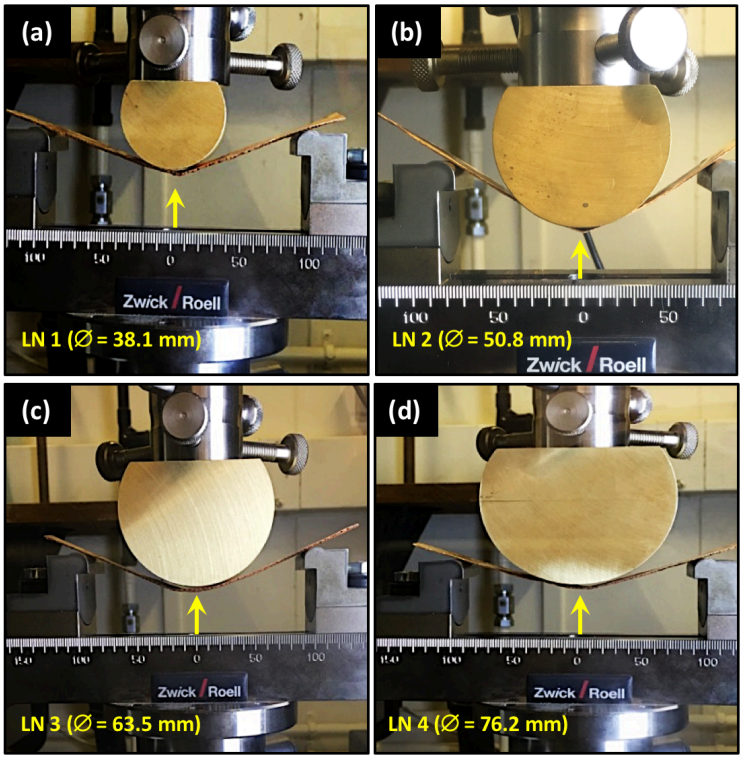

Figure 87: 3 – point bending test on porous sample. Sample 10CuPA bent around loading noses (LN) of different diameters; (a) LN 1 (∅ = 38.1 mm), (b) LN 2 (∅ = 50.8 mm), (c) LN 3 (∅ = 63.5 mm) and (d) LN 4 (∅ = 76.2 mm).

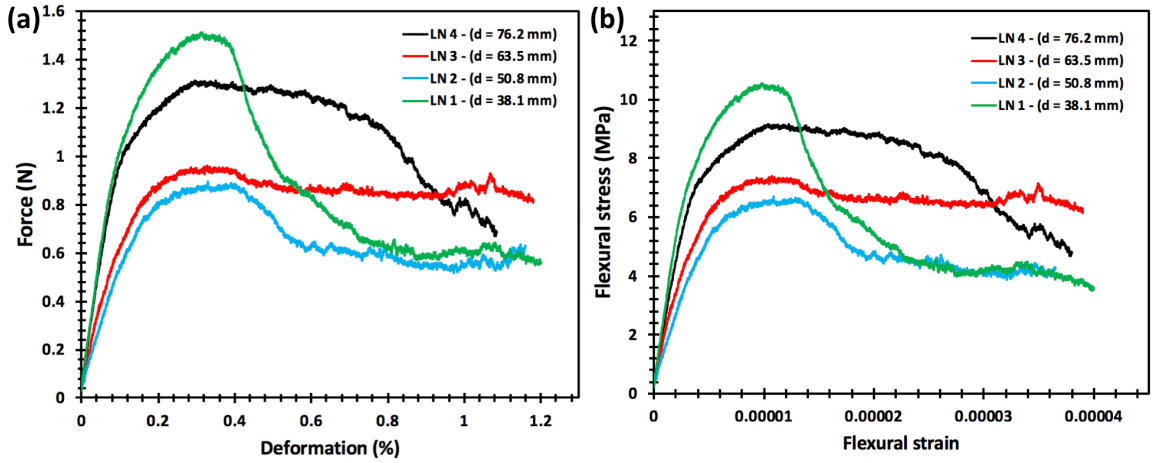

Figure 88: (a) Force (N) – deformation (%) curve and (b) stress – strain curve obtained from three-point bending tests on sample 10CuPA using four different loading noses LN 1 (∅ = 38.1 mm), LN 2 (∅ = 50.8), LN 3 (∅= 63.5 mm) and LN 4 (∅= 76.2 mm

Samples 30CuPA and 50CuPA were also bent using LN 1 (∅ = 38.1 mm), LN 2 (∅ = 50.8), LN 3 (∅ = 63.5 mm) and LN 4 (∅= 76.2 mm). Figure 89 displays the images of a bent sample of 30CuPA across all diameters. Like 10CuPA, 30CuPA did not show any sign of failure in the images when bent around LN 3 and LN 4 as indicated in Figure 89 (c) and (d) but appeared to have failed by fracture when bent around LN1 (Figure 89 (a)) and LN2 (Figure 89 (b)). Similarly, the force – deformation and stress – strain curves were employed to study how the two porous sheets responded to bending tests. The curves also show that 30CuPA failed when bent against LN1 (blue line) because of applied-force fluctuations in Figure 90 (a), as well as fluctuations in the stress – strain curves shown in Figure 90 (b). Bending against LN 2 (red line) shows a sudden drop in both curves as shown in Figure 90 which demonstrates failure of the porous layer.

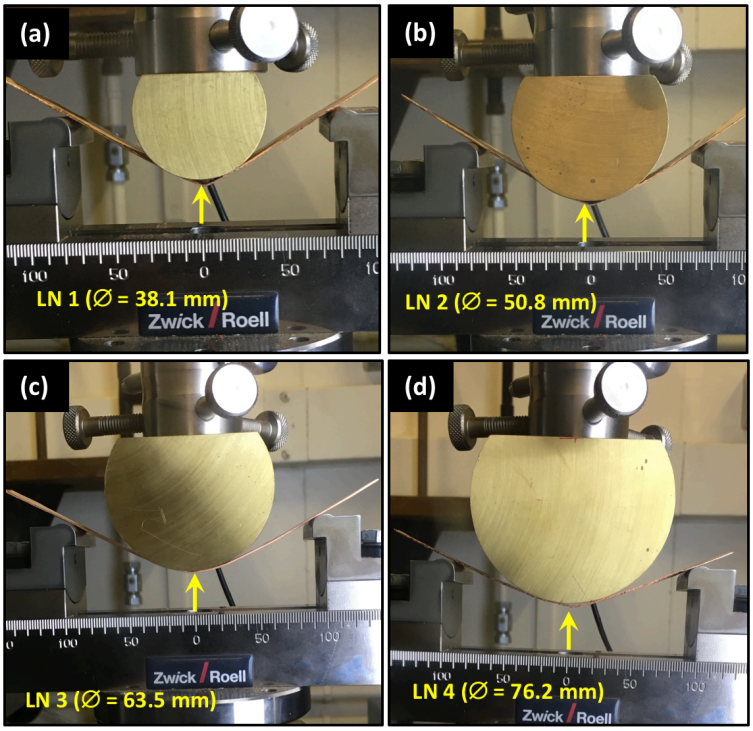

Figure 89: 3 – point bending test on porous sample. Sample 30CuPA bent around loading noses (LN) of different diameters; (a) LN 1 (∅ = 38.1 mm), (b) LN 2 (∅ = 50.8 mm), (c) LN 3 (∅ = 63.5 mm) and (d) LN 4 (∅ = 76.2 mm).

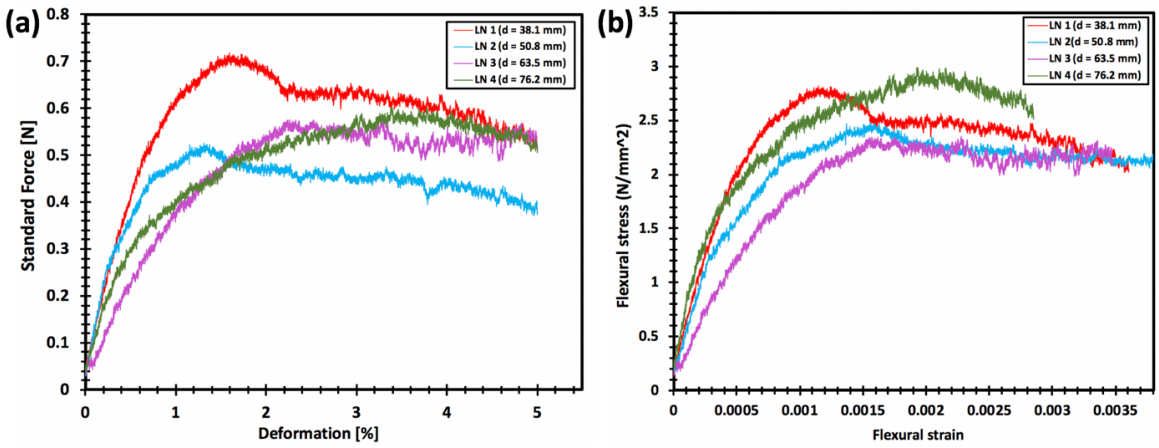

Figure 90: (a) Force (N) – deformation (%) curve and (b) stress – strain curve obtained from three-point bending tests on sample 30CuPA using four different loading noses LN 1 (∅ = 38.1 mm), LN 2 (∅ = 50.8), LN 3 (∅= 63.5 mm) and LN 4 (∅= 76.2 mm

Bending the sample 50CuPA against LN 1, LN 2 and LN 3 appeared to lead to fracture. This was clearly exhibited by force fluctuations and stress fluctuations in Figure 91 (a) and (b) respectively. 50CuPA recorded the highest volumetric porosity among all the porous samples investigated in this section, therefore the fluctuations within the curves could be due to failure

of the porous layer as the cracks propagated through the pores, or the structure collapsed. 50CuPA had a rough surface within the porous layer, and therefore, the fluctuations in the curves might also be due to the sample roughness as it slides on the supporting pins in the test machine. Bending sample 50CuPA around LN4 (orange line) shows a slightly different behaviour as revealed in Figure 91. The orange line is smoother at the start followed by force/stress fluctuation indicating slight failure.

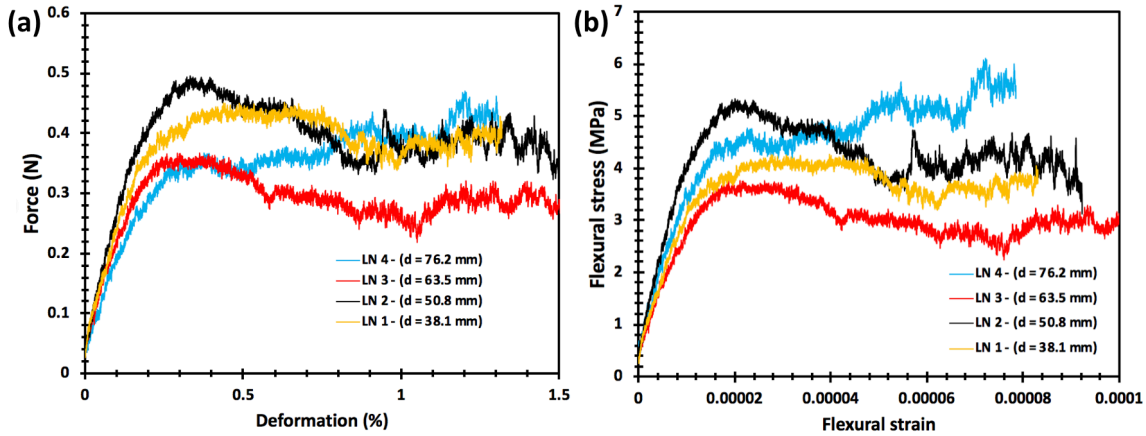

Figure 91: (a) Force (N) – deformation (%) curve and (b) stress – strain curve obtained from three-point bending tests on sample 50CuPA using four different loading noses LN 1 (∅ = 38.1 mm), LN 2 (∅ = 50.8), LN 3 (∅= 63.5 mm) and LN 4 (∅= 76.2 mm

Based on the results above, it was concluded that the 0CuP was able to bend around loading noses (or cylinders) with diameters greater than at most 38.1 mm (∅ ≥ 38.1 mm) and did not show any signs of failure. Both 10CuPA and 30CuPA were capable of bending around cylinders with a diameter greater than 63.5 mm without exhibiting any signs of failure as observed in the images, and proven by both the force – deformation and stress – strain curves. However, both sheets failed when bent around LN1 and LN2 with diameters of 50.8 mm or less (∅ ≤ 50.8 mm). Meanwhile, 50CuPA could be bent around LN4 which had a diameter of 76.2 mm (∅ ≥ 76.2 mm) without showing any signs of fracture. However, sample 50CuPA failed when bent around LN1, LN2 and LN3 with a diameter less or equal to 63.2 mm (∅ ≤ 63.2 mm). This result is summarised in Table 16.

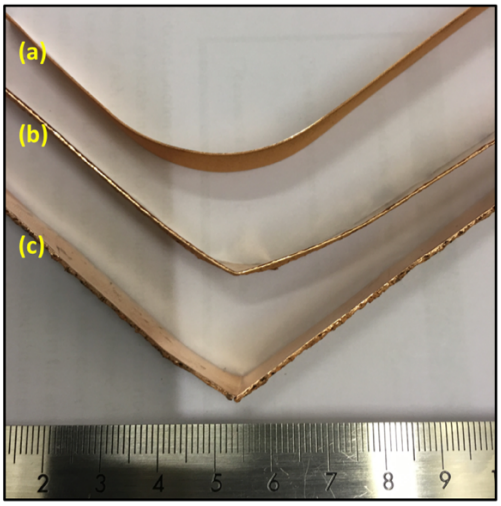

Figure 92: Typical deformed samples bent around LN2 (∅ = 50.8) using a three – point bending test (a) 0CuP. (b) 10CuPA and (c) 50CuPA

The absence of fluctuations in the force – deformation data or the stress fluctuations in the stress – strain curves means there was no brittle failure of the copper matrix. The yield strength and the flexural modulus increase with a decrease in the volumetric/bulk porosity of the samples as proven in section 7.1.2. In this case, the lower the porosity the better the capability of the porous copper samples to be bent around curved surfaces of smaller diameters. All of the porous sheets produced in this study have proven to have the capability to be bent around cylinders with diameters greater or equal to 76.2 mm (∅ ≥ 76.2 mm), without failing. Therefore, the porous samples (e.g. 0CuP, 10CuPA, 30CuPA and 50CuPA) are proven to have the potential to be used on curved surfaces with diameters of at least 76.2 mm where heat dissipation is required.

Table 16: A summary of the three-point bending tests on porous samples using four loading noses with varying diameters; LN 1 (∅ = 38.1 mm), LN 2 (∅ = 50.8), LN 3 (∅= 63.5 mm) and LN 4 (∅= 76.2 mm)

Processing routes	Sample	LN 1 (∅ = 38.1)	LN 2 (∅ = 50.8)	LN 3 (∅ = 63.5)	LN 4 (∅ = 76.2)
-	0CuP	✓	✓	✓	✓
Route A	10CuPA	X	X	✓	✓
	30CuPA	X	X	✓	✓
	50CuPA	X	X	X	✓

Legend

✓ **Not failed** X **Failed**

7.2 Surface roughness of the samples

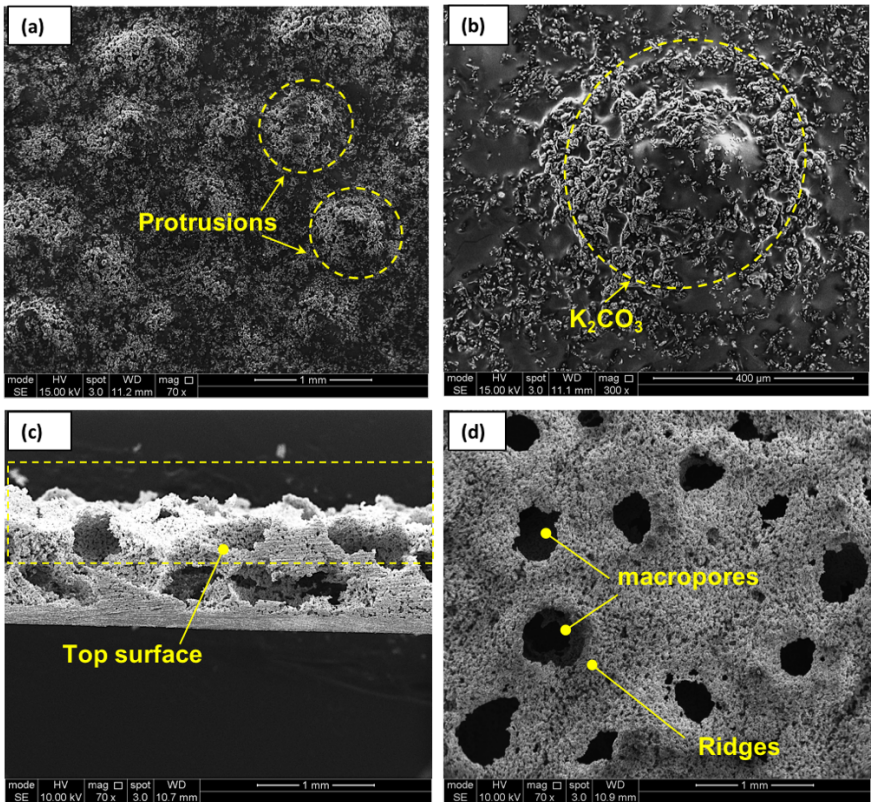

Figure 93: SEM micrograph showing protrusions on the surface of green samples. The protrusions are due to a slurry of copper and organic binders forming around the K_2CO_3 space holder prior to debinding and sintering.

During processing, a K_2CO_3 space holder was introduced to generate porosity within the sample. However, as Figure 93 shows, not only was porosity generated in the samples by addition of the space holder but also surface roughness was introduced as a secondary effect. Figure 93 (a) and (b) are the SEM micrographs of green samples after tape casting, which reveal K_2CO_3 particles protruding from the surface, forming uneven surface structures due to copper powders forming around the space holder. The samples maintain uneven surfaces even after sintering and removal of the space holder from the sample. This in turn remains as rough surfaces after sintering.

Artificially roughened surfaces are known to enhance heat transfer in heat sinks [185]. Due to the rough surfaces in the porous copper samples produced in this study, it was necessary to characterise the roughness on the sample surface in order to understand how roughness is affected by the processing parameters such as addition of K_2CO_3 space holder. It is worth remembering that, the samples produced in this study are aimed at heat transfer applications, where both the surface roughness and porosity play a major role.

Two non-destructive methods were employed to measure the surface roughness; first by an image analysis approach and secondly by using the Contour GT optical profiler. The step-by-step procedure of both methods were covered in section5.1.2.1 and 5.1.2.2.

9.1.1 Non-contact surface measurements using contourGT profiler

3D optical profiling using contourGT offers many benefits over other measurement techniques for non-contact surface measurements. It provides custom analysis, automated measurements and is also non-destructive inspection. In this work, the samples investigated were porous, therefore it was impossible to obtain a continuous profile of the sample surface across all samples investigated. Figure 94, Figure 95 and Figure 96 show unsuccessful profiles obtained using the contourGT profiler. The average particle size of K_2CO_3 used as a space holder for generating porosity is 633 μm, and from image analysis, the average pore size generated is 620 μm on each sample tested except sample 0CuPA (which has no space holder)

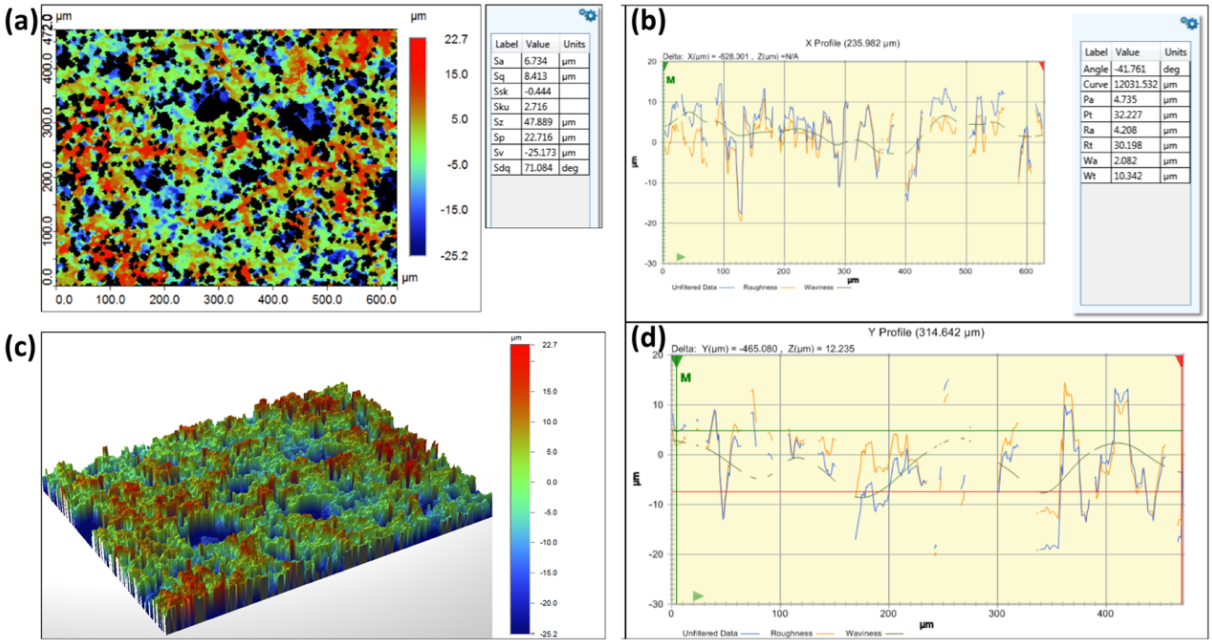

Figure 94: Surface morphological characterisation of a flat surface of 0CuPA using contourGT profiler; (a) 2D map of surface morphology, (b) X-profile, (c) 3D map of the surface morphology and (d) Y-profile**.**

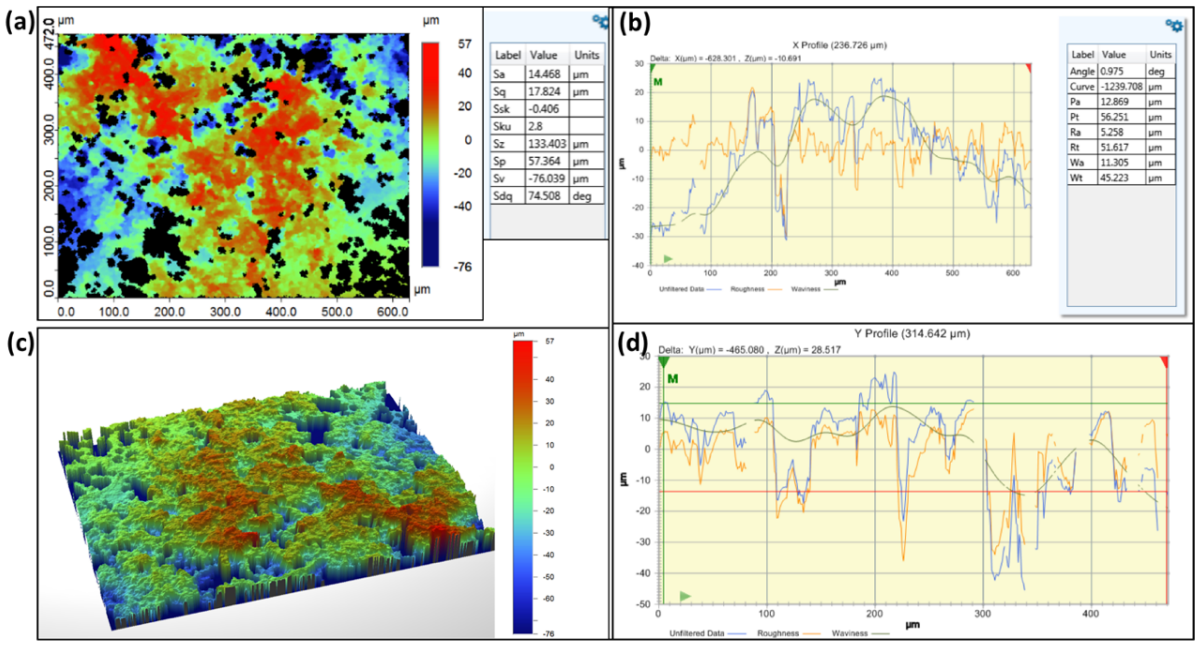

Figure 95: Surface morphological characterisation of a flat surface of 20CuPA using contourGT profiler; (a) 2D map of surface morphology, (b) X-profile, (c) 3D map of the surface morphology and (d) Y-profile**.**

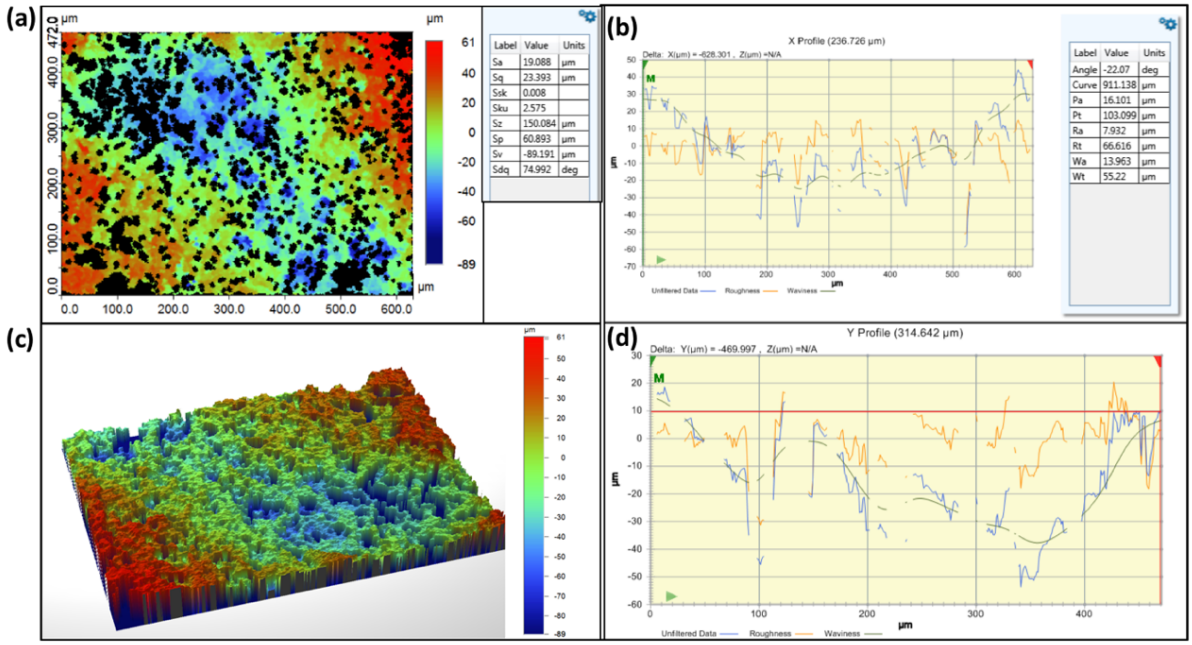

Figure 96: Surface morphological characterisation of a flat surface of 30CuPA contourGT profiler; (a) 2D map of surface morphology, (b) X-profile, (c) 3D map of the surface morphology and (d) Y-profile.

9.1.2 Image analysis software

The porous samples (except 0CuP) produced in this study had higher level of porosities, therefore obtaining a continuous profile using contourGT became a challenge, hence unsuccessful profiling. Image analysis was then employed as an alternative to obtain the surface profile of each porous sample. Images of surfaces in polished cross sections were captured using a Nikon D5300 digital SLR camera fitted with an 18-55 mm VR lens kit, processed using Fiji ImageJ to generate the surface profile shown in Figure 97. The surface profiles of the eleven samples produced in this study were constructed, which included the porous sheets processed by the following routes A: 0CuP, 10CuPA, 20CuPA, 30CuPA, 40CuPA and 50CuPA, and those processed following route B: 10CuPB, 20CuPB, 30CuPB, 40CuPB and 50CuPB.

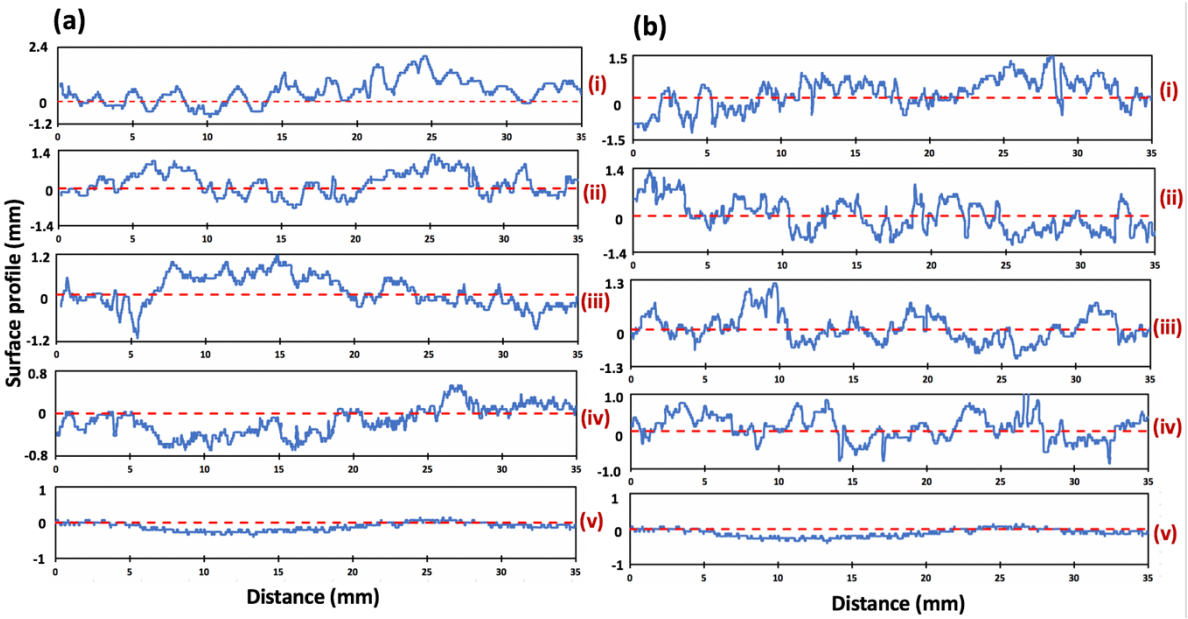

Figure 97: Surface profiles of porous copper samples. (a(i)) 50CuPA, (a(ii) 40CuPA, (a(iii)) 30CuPA, (a(iv)) 20CuPA and (a(v)) 0CuP. (b(i)) 50CuPB, (b(ii)) 40CuPB, (b(iii)) 30CuPB, (b(iv)) 20CuPB and (b(v)) 0CuP.

Based on the binarized images of each porous sample obtained, it was possible to generate the surface roughness diagrams depicted in Figure 97. In each plot, the dotted red line across each profile labelled 0.0 is the average value of surface height and depth. However, the blue line represents the vertical distance of the surface of the sample from the mean line in each point of the surface. From the plots, the commonly used parameters describing surface roughness in 2D were computed, such as, arithmetic average (calculated using equation(16)), root mean squared (calculated using equation (17)) , maximum valley depth (calculated using equation (18)), maximum peak height of the profile (calculated using equation (19)), skewness (calculated using equation (20)) and kurtosis (calculated using equation (22)) The equations used are summarised in Table 17, and the results are presented in Table 18.

As seen from SEM micrographs of the green sample in Figure 93 (a) and (b), the protrusions and dimples on each sample surface resulted from the K_2CO_3 space holder. Also, Figure 93 (c) and (d) shows the resulting rough structure of the porous samples after sintering. Therefore, it was expected that the number of protrusions on the surface of the sample

increases with the addition of 20-50 wt.% K_2CO_3. The peaks and valleys in the surface profiles shown in Figure 97 result from such protrusions and pores on the sample surfaces. Considering some samples produced by route A, 20CuPA has an arithmetic mean roughness value (R_a) and average peak per centimetre (PPC) of 0.11 mm and 3.43 peak/cm respectively. 30CuPA has R_a and PPC of 0.88 mm and 4.29 peak/cm consecutively. While 40CuPA and 50CuPA achieved Ra of 0.96 mm and 1.21 mm respectively, and PPC of 4.57 peak/cm and 4.86 peak/cm consecutively.

Table 17: The equations used for surface analysis of the porous copper samples

Parameter	Description	Formula
R_a	Arithmetic mean roughness value	$R_a = \frac{1}{n}\sum_{i=0}^{n} \lvert y_i \rvert$
R_q	Root mean squared	$R_q = \sqrt{\frac{1}{n}\sum_{i=1}^{n} y_i^2}$
R_v	Maximum valley depth	$R_v = \min_i y_i$
R_p	Maximum peak height	$R_p = \max_i y_i$
R_t	Maximum height of the profile	$R_t = R_p + R_v$

On the other hand, the samples produced by route B, 20CuPB and 30CuPB achieved R_a and PPC of 0.56 mm and 0.84 mm and PPC of 3.72 peak/cm and 4.29 peak/cm, while 40CuPB and 50CuPB achieved Ra of 0.96 and 1.03 mm respectively and PPC of 4.57 peak/cm and 5.43 peak/cm respectively. Generally, the results show that R_a values and PPC of the samples increased with the amount of K_2CO_3 space holder added during processing. 50CuPA and 50CuPB achieved the highest R_a and PPC and hence had higher roughness compared to 0CuP which achieved the lowest Ra and PPC and has the lowest porosity. Therefore, the higher the amount of K_2CO_3 space holder added during processing the higher the roughness, as well as the porosity.

Table 18: A summary of surface profiles of porous copper samples produced by both route A and route B.

Processing Route	Samples	Roughness value, *Ra (mm)*	Peak Per Centimetre (PPC)	Root mean squared (mm)	Max. valley depth/height, *Rv, Rp (mm)*	Max. peak height, *Rt (mm)*
	0CuPA	0.032	-	0.026	0.109	0.218
Route A	**20CuPA**	0.411	3.43	0.119	0.69	1.380
	30CuPA	0.884	4.29	1.351	1.18	2.360
	40CuPA	0.960	4.57	1.767	1.229	2.458
	50CuPA	1.209	4.86	2.777	1.512	3.024
Route B	**20CuPB**	0.559	3.72	1.499	0.925	1.850
	30CuPB	0.841	4.29	1.836	1.201	2.402
	40CuPB	0.957	4.57	1.853	1.321	2.642
	50CuPB	1.030	5.43	0.124	1.429	2.858

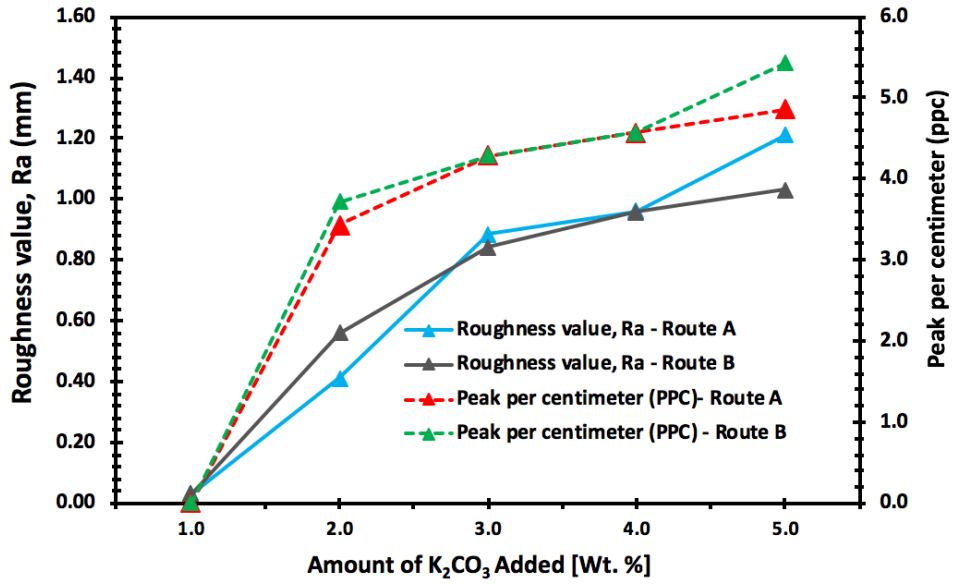

Figure 98: The surface roughness of the porous copper sheets plotted in terms of roughness value, Ra and peak per centimetre against the amount of the potassium carbonate space holder added during processing.

9.2 Summary of the mechanical properties and further characterisation

In summary, the porous samples were taken through a simple three-point bending test, as well as the modified three-point bending test where the loading noses with a varying diameter were employed to bend the sample. From the investigation, it is proven that, the flexural modulus and flexural strength increase with decreasing surface porosity and volumetric (or bulk) porosity of the sample as shown in ***Table 19***. The sample with the lowest porosity, 0CuP, achieved the highest flexural modulus and ultimate flexural strength of 2000 GPa and 29.3 MPa respectively, while 50CuPA and 50CuPB with the highest surface and volumetric porosity among the samples investigated here achieved a flexural modulus of 51.7 GPa and 22.2 GPa and UFS of 1.63 MPa and 0.83 MPa respectively.

In the three-point bending test using loading noses with diameters in the range of 38 – 76.2 mm, 0CuP was able to bend around loading noses with diameters in the range of 38 – 76.2 mm, while 10CuPA and 30CuPA was able to bend around loading noses of diameters greater or equal to 63.5 mm ($\varnothing \geq 63.5$ mm). But 50CuPA samples showed some signs of failure when bent using loading noses of diameters greater or equal to 63.5 mm ($\varnothing \geq 76.2$ mm).

After unsuccessful surface roughness measurements by using a contourGT profiler, an image analysis approach was employed to obtain the surface profiles. The results showed that the roughness of the sample increased with the amount of the K_2CO_3 space holder added during processing, of which 50CuPA and 50CuPB recorded the highest roughness.

Table 19: Flexural modulus and ultimate flexural strength of the porous copper samples.

Processing routes	Sample	Surface porosity (%)	Volumetric porosity (%)	Flexural modulus (GPa)	Ultimate Flexural Strength (MPa)
-	**0CuP**	22.9 ± 3.0	50.7 ± 0.5	852.0	29.3 ± 4.0
Route A	**10CuPA**	26.96 ± 5.9	63.4 ± 1.4	651.1	5.96 ± 0.6
	30CuPA	37.3 ± 5.4	75.2 ± 1.5	284.9	3.32 ± 0.4
	50CuPA	49.3 ± 5.7	80.5 ± 0.5	51.7	1.63 ± 0.3
Route B	**10CuPB**	27.1 ± 5.3	66.3 ± 0.9	258.8	4.29 ± 0.5
	30CuPB	46.8 ± 8.7	79.0 ± 1.3	46.0	1.24 ± 0.2
	50CuPB	61.6 ± 7.4	81.5 ± 1.4	22.2	0.82 ± 0.1

CHAPTER 6: Results and Analysis – Heat Transfer Performance of Porous Copper Sheets

In this chapter, the porous sheets with volumetric porosity ranging from 50% to 82% and thickness down to 1.4 mm were investigated for heat transfer performance. The porous copper samples were successfully produced by a novel process combining lost carbonate sintering (LCS) and tape casting, and characterised to obtain their structural properties, as well as their mechanical properties. The processing techniques were varied (see section 3.1) to produce porous Cu samples with different structural properties as described in the 'experimental methods section' in chapter 5. The structure of the tapes consisted of two layers; a porous layer with porosity in the range of 50 to 82%, deposited on a dense substrate of 0.125 mm thickness. Table 20 shows a summary of the major characteristics of all the porous copper sheets which were evaluated for heat transfer capability.

Table 20: Characteristics of porous copper samples evaluated for heat transfer performance

Processing routes	Sample	Measured density (g/cm^3)	Surface porosity (%)	Volumetric porosity (%)	Peak per centimetre (PPC)	Roughness Value, *Ra* (mm)	Thickness (mm)
-	**0CuP**	4.41 ± 0.05	22.9 ± 3.0	50.7 ± 0.53		0.032	0.74
Route A	**20CuPA**	2.69 ± 0.15	32.8 ± 5.0	70.0 ± 1.73	3.43	0.411	1.11
	30CuPA	2.23 ± 0.14	37.3 ± 5.4	75.1 ± 1.53	4.29	0.884	1.38
	40CuPA	1.94 ± 0.05	41.1 ± 6.1	78.4 ± 0.52	4.57	0.960	1.07
	50CuPA	1.75 ± 0.09	49.3 ± 5.7	80.5 ± 0.51	4.86	1.209	1.24
Route B	**20CuPB**	2.36 ± 0.29	39.9 ± 7.2.	73.6 ± 1.46	3.72	0.559	1.16
	30CuPB	1.88 ± 0.18	46.8 ± 8.7	79.0 ± 1.25	4.29	0.841	1.61
	40CuPB	1.75 ± 0.11	52.4 ± 4.8	80.4 ± 0.68	4.57	0.957	1.44
	50CuPB	1.65 ± 0.11	61.6 ± 7.4	81.5 ± 1.41	5.43	1.030	1.36

As described in section 5.3.1, among all the potential coolants, air-cooling is highly preferred to dissipate thermal energy generated within electronic devices. Air was selected as a coolant throughout the investigation. It is important to note that, a material with excellent heat transfer performance has the highest heat transfer coefficient, as well as the thermal transmittance, and could be considered as an optimal heat exchanger. To verify the porous copper samples produced in this study, their suitability for heat sink applications was investigated with simple assessments of the thermal properties under forced convection using air as a coolant. An open circuit heat transfer rig was used. The flow rate of air passing through the samples was varied between the range of 0.1 – 0.5 kg/s. Microfoil T- type sensors, and J-type and K-type thermocouples were installed in the system to track inlet and outlet temperatures of air and surface temperatures of the system and samples. This allowed the behaviour of heat dissipation by porous copper tapes to be effectively studied. Smooth (non-porous) copper tapes were also tested under the same conditions to provide a reference.

However, in tests of this type, different sample forms can be used. This reflects the fact that the flow of the cooling air will not always be directly incident on, or parallel to the surface of the sheet. The porous sheets investigated in this work were produced in flat form, and therefore, they can be easily mounted on hot flat surfaces to dissipate heat. But the porous sheets have also been proven to have the capability to be bent around curved surfaces down to a radius of 50 mm without failing, from the bending tests in section 7.1.2. The porous sheets proved that they have the potential to be used on curved surfaces where heat dissipation is required. It was therefore necessary to investigate their ability to dissipate heat from cylindrical hot surfaces in addition to the flat hot surface.

Two types of heating system designed in-house were employed; a flat heating system (FHS) and a cylindrical heating system (CHS) (see Section 5.3.1). The heat transfer performance

results of the porous copper sheets tested on CHS and FHS are covered in Section 10.1 and Section 10.3.

10.1 Heat transfer performance of porous sheets on cylindrical heating system

The main objective of this section is to explore the heat transfer capabilities of the porous samples produced in-house, bent around a curved heated surface referred to as a cylindrical heating system (CHS). The CHS was designed and developed in-house (see section 5.3.1). All the samples in Table 20 were evaluated on a CHS to determine the heat transfer coefficient and thermal transmittance at a range of controlled air velocities generated by an open-circuit heat transfer rig. The heat transfer rig was also designed and developed in-house.

It is well known that mass-flow rate is one of the most likely variables of heat exchangers while in use. Therefore, all samples were tested at flow rates ranging from 0.1 – 0.5 kg/s, which was later expressed in terms of dimensionless Reynolds number calculated using Equation (31). The heat transfer coefficient constant h was calculated using Equation (30), and further expressed as the dimensionless Nusselt number calculated using Equation (33). Lastly, the thermal transmittance Tr was calculated using Equation (29). The heat transfer performance results of all the porous sheets tested here were presented in two different ways; as Tr versus Re and Nu versus Re plots. Heat transfer performance was further evaluated against a range of porosity (both surface porosity and volumetric porosity) and surface roughness. To simplify the presentation of results and their discussions, the plots of porous sheets processed by route B are covered separately from those produced by route B, before comparison between them.

10.1.1 Thermal transmittance and Nusselt number of porous sheets on CHS

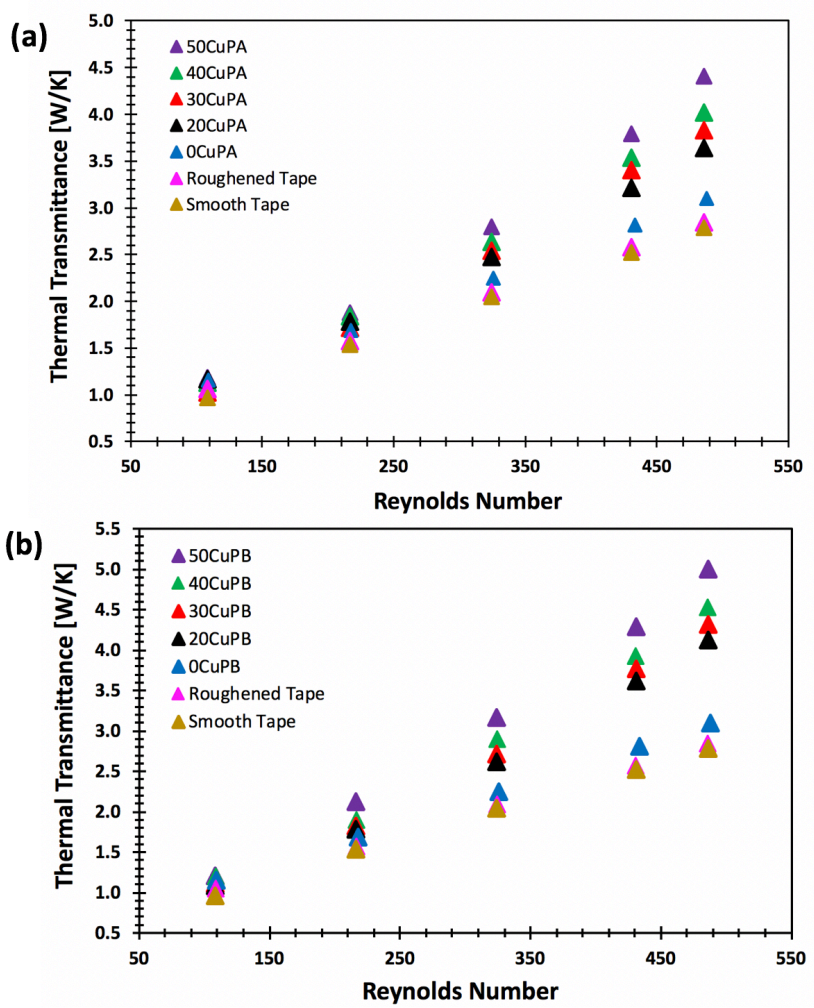

Figure 99: A plot of experimental results showing the heat transfer results of porous sheets (0CuP, 20CuPB, 30CuPB, 40CuP and 50CuPB) along with as-received smooth copper and sand blasted copper tape. Thermal transmittance plotted against dimensionless Reynolds number (a) porous sheets produced following route A and (b) porous sheets produced following route B.

Figure 99 (a) and (b) shows the *Tr* versus *Re* plots for samples produced by processing route A and route B respectively, along with the plots of as-received smooth copper and sand blasted copper sheets as references. It is clear that the introduction of the porous layer on to the tapes improves the thermal transmittance of the tapes by at least twice the amount obtained on the as-received smooth tape. It was also noticed in both Figure 99 (a) and (b) that, the thermal transmittance achieved on the porous copper samples increased with porosity (to be

discussed further). Roughened as-received copper sheet (by sand blasting) has a slightly higher thermal transmittance compared to smooth tape.

Table 21 and Table 22 show the deviations of *Tr* of porous sheets produced by route A and B respectively with reference to the as-received smooth tapes. Sample 50CuPA achieved 38% higher thermal transmittance than as-received Cu sheet, and 28% higher compared with sample 0CuP (porous sheet with the lowest porosity of 50.7%). While 40CuPA and 30CuPA achieved 29.7% and 22.6% higher *Tr* compared with as-received Cu sheet. And lastly, 20CuPA and 0CuP obtained a *Tr* value which is 22.9% and 10.7% higher, respectively, compared to as-received Cu sheet. As shown in Table 22, 50CuPB achieved a *Tr* which is 52.7% higher than smooth as-received Cu sheet, while 40CuPB and 30CuPB obtained values of *Tr* which are 41.2% and 34.3% greater. The samples with the lowest level of porosity, 20CuPB and 0CuP achieved values of *Tr* which are 29.5% and 10.7% higher than the as-received copper sheet (smooth) respectively. It is important to note that 0CuP has the lowest porosity (50.7%) among the porous samples studied from both processing routes, and it has obtained the lowest thermal transmittance which is only 10.7% increased over that of the smooth tape.

Generally, the samples with higher porosities obtained higher thermal transmittance within the entire range tested here. This is due to the fact that thermal transmittance is dependent on the fluid dynamics interaction between the active surface and flow field [184], and, as shown earlier, the tapes with higher porosity have a larger active surface area and are more permeable to the cooling fluid. Therefore, the structure of the sample plays a major role. The structure of this type of porous tape consists of macropores, micropores and some defects from processing which all contribute to the total surface porosity and volumetric porosity of the porous sheets. To determine the effects of these structural parameters on the heat transfer

performance, separate plots were generated from the experimental results and are discussed in the following sections. These parameters include; volumetric porosity, surface porosity and surface roughness generated as a secondary effect from processing.

10.1.2 Comparison of thermal transmittance of porous sheets against smooth copper sheets

Table 21: The deviations of thermal transmittance of porous copper produced by processing route A from that of smooth copper tapes tested on a CHS.

Reynold Number	Smooth	0CuPA	Deviation (%)	20CuPA	Deviation (%)	30CuPA	Deviation (%)	40CuPA	Deviation (%)	50CuPA	Deviation (%)
486	2.79	3.09	10.75	3.63	30.11	3.82	36.92	4.01	43.73	4.39	57.35
431	2.52	2.81	11.51	3.21	27.38	3.40	34.92	3.53	40.01	3.78	50.00
324	2.04	2.24	9.80	2.47	21.08	2.54	24.51	2.63	28.92	2.79	36.76
217	1.53	1.68	9.80	1.78	16.34	1.71	11.76	1.84	20.26	1.88	22.88
109	0.97	1.15	18.55	1.16	19.59	1.02	5.15	1.12	15.46	1.18	21.65
Mean Deviation			**10.7**		**22.9**		**22.6**		**29.7**		**37.7**

Table 22: The deviations of thermal transmittance of porous copper produced by processing route B from that of smooth copper tapes on a CHS.

Reynold Number	Smooth	0CuPB	Deviation (%)	20CuPB	Deviation (%)	30CuPB	Deviation (%)	40CuPB	Deviation (%)	50CuPB	Deviation (%)
486	2.79	3.09	10.75	4.12	47.67	4.32	54.84	4.52	60.01	5.00	79.21
431	2.52	2.81	11.51	3.61	43.25	3.77	49.60	3.93	55.95	4.29	70.24
324	2.04	2.24	9.80	2.61	27.94	2.71	32.84	2.90	42.16	3.16	50.90
217	1.53	1.68	9.80	1.78	16.34	1.82	18.95	1.90	24.18	2.12	38.56
109	0.97	1.15	18.55	1.09	12.37	1.12	15.46	1.20	23.71	1.21	24.74
Mean Deviation			**10.7**		**29.5**		**34.3**		**41.2**		**52.7**

10.1.3 Nusselt number vs Reynolds number

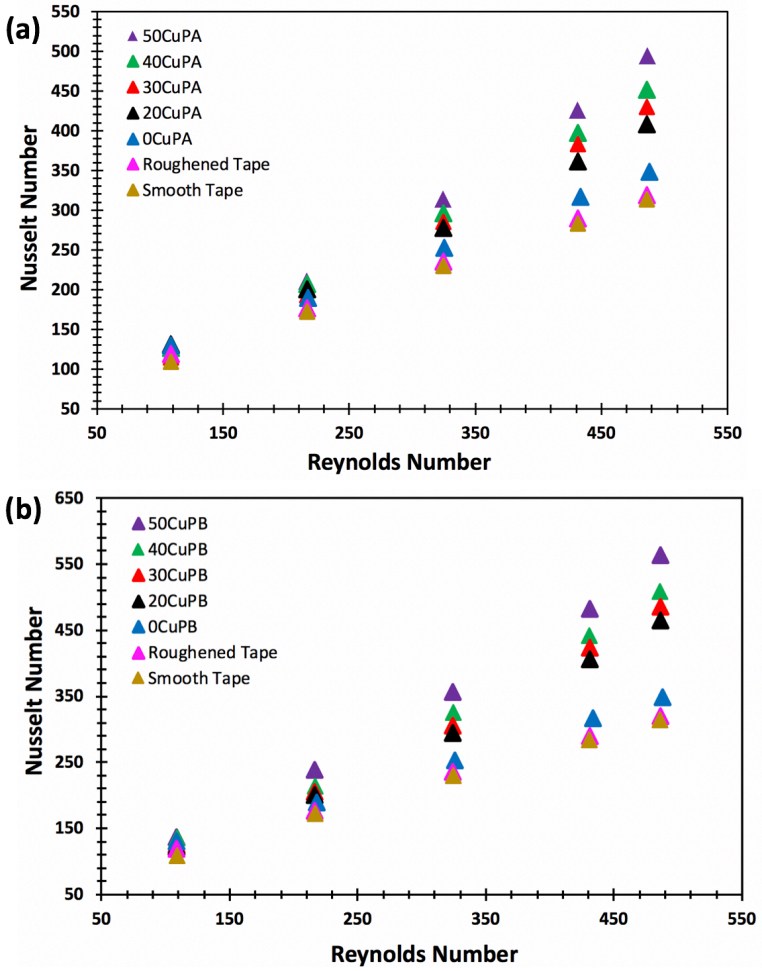

Figure 100: A plot of experimental results showing the heat transfer results of porous sheets (0CuP, 20CuPB, 30CuPB, 40CuP and 50CuPB) along with as-received smooth copper and sand blasted copper tape. Dimensionless Nusselt number plotted against dimensionless Reynolds number (a) porous sheets produced following route A and (b) porous sheets produced following route B.

The heat transfer coefficient was expressed in terms of the Nusselt number to give a comparison between heat transfer by conduction and convection. Figure 100 (a) and (b) shows the *Nu* versus *Re* plots obtained from experimental results of porous sheets produced by route A and B respectively. The plots show similar trends to the *Tr* versus *Re* plots in Figure 99 (a) and (b), where 50CuPA achieved higher values of *Nu* especially at higher *Re*, followed by 40CuPA and 30CuPA respectively. These were then followed by 20CuPA and 0CuPA. And lastly, roughened sheet achieved the lowest *Nu.* A similar trend was observed

with porous sheets processed following route B where 50CuPB with the highest level of porosity achieved the highest *Nu,* at higher *Re* regimes (Re = 486) of all the porous samples tested. 0CuP achieved the lowest *Nu* in the higher *Re* regime. Generally, the *Nu* of porous sheets tested at higher *Re* decreased with increasing level of porosity.

To understand the effect of volumetric porosity of the porous copper sheets on the *Tr* (or *Nu*), Tr and Nu were plotted against volumetric porosity as shown in Figure 101 and Figure 102. All the discussions are covered in section 10.2.1.

10.2 Discussions

10.2.1 Effect of volumetric porosity on the heat transfer performance of porous sheets

Volumetric porosity is the dominant parameter contributing to the differences in the heat transfer capability of the porous sheets studied in this work. This is due to the fact that, the open-pore structured sheets with higher volumetric porosity allow a higher amount of cooling air to flow through them, therefore accelerating heat dissipation. It was directly controlled by the amount of the carbonate space-holder added during processing of the sample, and thus the heat transfer capability could be optimised. The porous sheets also consist of a wide range of pore sizes (30 – 790 μm), classified as micropores ($d \leq 50$ μm) and macropores ($d \geq 50$ μm) in this study. Figure 101 (a) and Figure 102 (a) show the plots of thermal transmittance versus volumetric porosity of sheets produced by processing route A and B respectively. The dimensionless Nusselt number versus volumetric porosity plots were also included for each set of samples as shown in Figure 101 (b) and Figure 102(b).

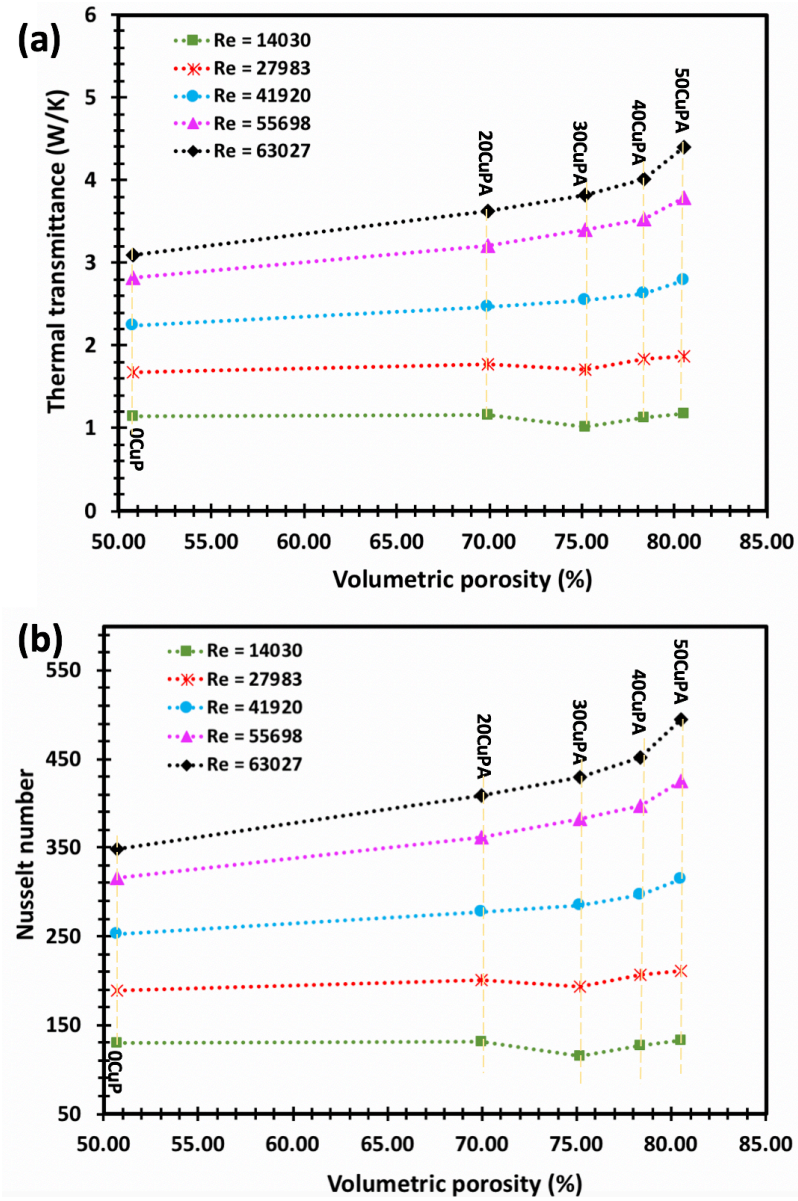

Figure 101: Two plots showing the experimental result of *Tr* and *Nu* of porous sheets (produced by route A) against volumetric porosity, tested on a cylindrical heating system: (a) thermal transmittance versus surface roughness of porous sheets and (b) dimensionless Nusselt number versus dimensionless surface roughness of copper samples.

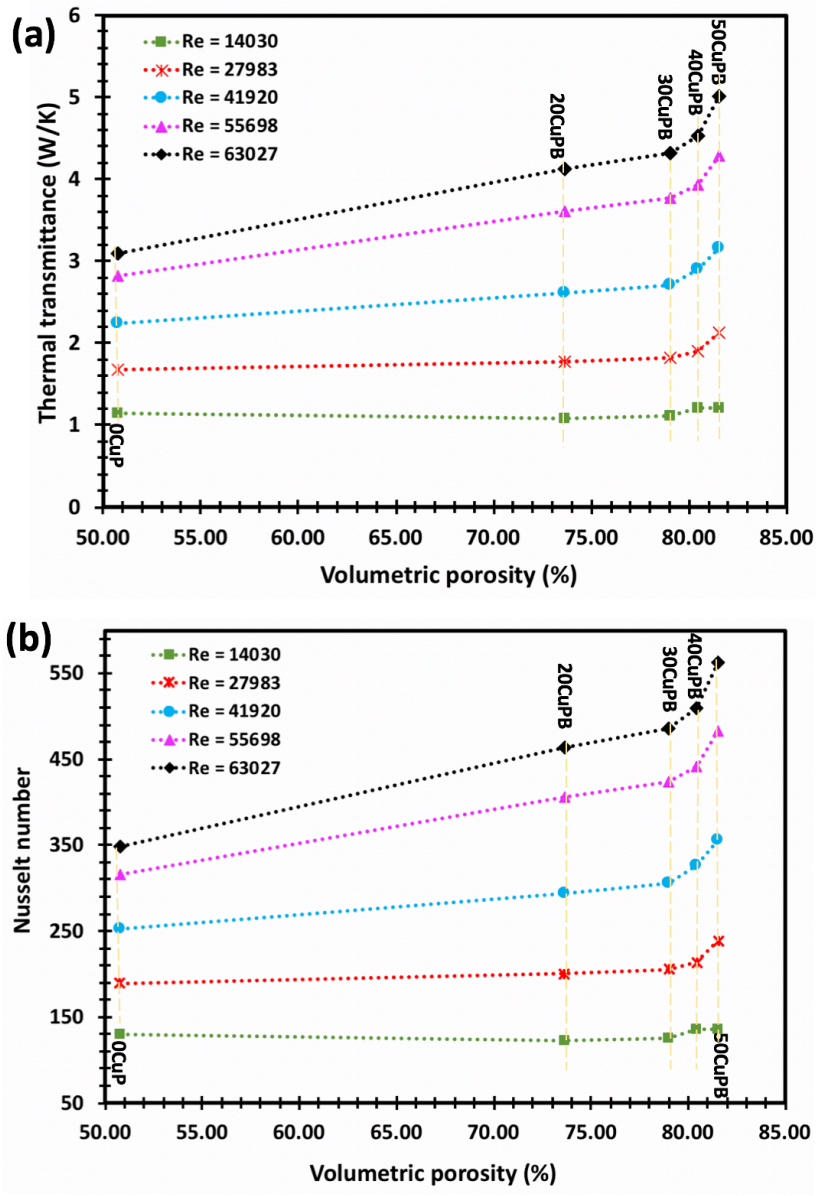

Figure 102: Two plots showing the experimental result of *Tr* and *Nu* of porous sheets (produced by route B) against volumetric porosity, tested on a cylindrical heating system: (a) thermal transmittance versus surface roughness of porous sheets and (b) dimensionless Nusselt number versus dimensionless surface roughness of copper samples.

From Figure 101, the porous sheets produced by route A having a volumetric porosity ranging from 50 % to 80.5% achieved a Nusselt number within the range of 347.8 (sample 0CuP) to 494.7 (sample 50CuPA) under a high Reynolds number regime (*Re* = 486), while porous sheets produced by route B achieved a Nusselt number of 347.8 (sample 0CuP) to 562.8 (sample 50CuPB) for samples having a volumetric porosity ranging from 50 to 81.5%. At the

higher Re regime, sample 50CuPA (*Vp* = 80.5%) obtained almost 1.4 times higher *Tr* compared with 0CuP with a lower volumetric porosity of 50.7 %. Among the set of porous sheets produced by route B, sample 50CuPB with higher porosity achieved a *Tr* which is 1.6 times higher than 0CuP. 50CuPA and 50CuPB obtained 1.6 and 1.8 times higher *Tr* compared to the smooth as-received sheet respectively. Table 23 provides a summary of *Tr* and *Nu* at a high Reynolds number regime investigated (*Re* = 486). Their influence on the overall heat transfer performance of each porous sample are highlighted and discussed next.

Table 23: Thermal transmittance and dimensionless Nusselt number of porous copper sheets produced following route A and B taken at Reynolds number of 486.

Processing routes	Sample	Volumetric porosity (%)	*Tr* at *Re* = 486	*Nu* at *Re* = 486
-	**0CuP**	50.7 ± 0.53	3.09	347.8
Route A	**20CuPA**	70.0 ± 1.73	3.63	408.4
	30CuPA	75.1 ± 1.53	3.82	429.7
	40CuPA	78.4 ± 0.52	4.01	451.5
	50CuPA	80.5 ± 0.51	4.39	494.7
Route B	**20CuPB**	73.6 ± 1.46	4.13	464.1
	30CuPB	79.0 ± 1.25	4.32	486.1
	40CuPB	80.4 ± 0.68	4.52	508.8
	50CuPB	81.5 ± 1.41	5.00	562.8

Figure 103 is a schematic diagram showing a porous sample bent around a cylindrical heating system, and then immersed in the airflow field inside the test rig. It also shows how airflow could possibly interact with the porous section of the sample during testing and thus how the structural properties of the whole component could affect *Tr* or *Nu.* The direction of the airflow is indicated by the black arrows, while the heat flow is shown by the red arrows. The region highlighted in red is the porous layer of the double layered sample. The discussions in this section focus on how the volumetric porosity, and also pore distribution could affect *Tr* and *Nu* of the porous samples. The heat transfer through the copper matrix of the porous sheet

occurs by conduction. While the heat transfer in the cooling air within the pores of the porous section and on the sample-surface occurs mainly by convection.

Besides the volumetric porosity and pore size and pore distribution, other structural parameters were kept constant to only investigate the influence of those factors on the heat transfer performance of porous sheets. There were some slight differences in the thickness of the porous sheets produced in this work, and this could be due to different amount of shrinkage of the samples during processing. An increase in the volumetric porosity had an important influence on the heat transfer performance. Volumetric porosity was varied across the samples by the quantity of the K_2CO_3 space holder added during processing, which also determined the amount of macroporosity generated.

It is possible that the active surface area would be increased with the amount of the macroporosity (or volumetric porosity) which was generated. It is known that the active surface area plays a major role in the heat transfer to the cooling air. The cooling air flows over the sample surface and also through the porous layer of the sample. Therefore, porous samples with a larger active surface area were expected to have a higher *Tr* or *Nu* especially at a higher *Re.* 50CuPA and 50CuPB obtained higher values of Tr and Nu which might be as a result of a higher active surface. It must be noted that higher porosity does not necessarily mean the porous samples have a higher active surface. And also, the layer placed in contact with the heat source was dense therefore providing a good contact with the heat source to optimise the heat transfer from the walls of the heat source to the porous heat sink.

Pore distribution is one of the major structural properties that is believed to have affected the heat transfer performance of the porous sheets. It was defined by the processing route followed to make the porous sample. Porous sheets produced by following route B had higher macroporosity of approximately 60% (see section 6.3.4.1 and 6.3.4.2) in the top half of the

porous layer compared to the bottom half which was approximately 40%, while for route A, where the sample is not flipped, these values were inverted. First of all, and most importantly, the route B porous sheets outperformed route A porous sheets. This is because route B porous sheets obtained slightly better heat transfer performance compared to the porous sheets produced by following route A. A slightly higher *Tr* and also *Nu* of route B sheets against route A sheets could be due to the fact that the sheets consist of a highly porous top half of the porous layer of the samples. This allows the structure of the sheets produced by route B to be accessible to the flowing fluid. At higher *Re,* the inward and outward flow of air into the pores causes disturbances in the flow within the boundary layer and also inside the pores. This could have resulted in a faster heat transfer into the air within the boundary layer and also into the air inside the pores.

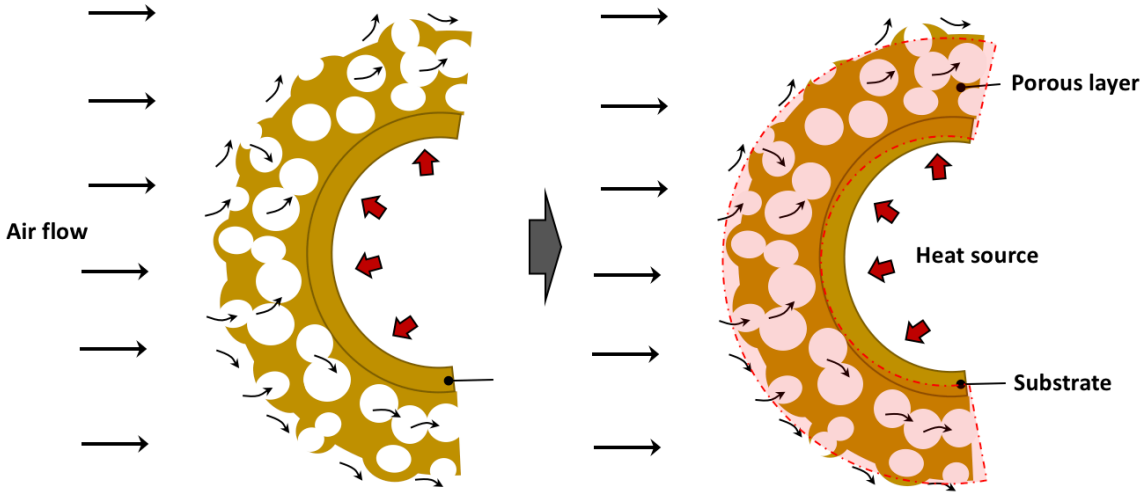

Figure 103: Schematic diagram showing the interaction of the air flow and rough and porous sheets of copper, where the schematic diagram on the right indicates the porous layer of the sample wrapped around a heat source.

A slightly lower *Tr* and *Nu* achieved by porous tapes produced by processing route A was also due to the way the pores are distributed across the sheets, as the route A sheets consist of a highly porous bottom half of the porous layer compared to the top layer. The top layer therefore reduces the airflow into the porous layer, hence reducing the heat transfer capability

of the porous section in to the air flow. This was proven by lower values of Tr and Nu recorded by the porous sheets which were lower than that of porous sheets produced by route B.

In summary, *Tr* or *Nu* increased with the volumetric porosity especially at higher Re regime. The higher the volumetric porosity the higher the active surface area of the porous sheet for heat transfer in to the airflow. Route B porous sheet outperformed route A tapes due to the way pores are distributed across the component. The sheets produced by route B have higher porosity on the top half of the sample and less in the bottom half of the sample, and achieved higher values of *Tr* and *Nu.* The thickness was kept constant across all the samples, the resulting differences being due to shrinkage during processing (debinding and sintering).

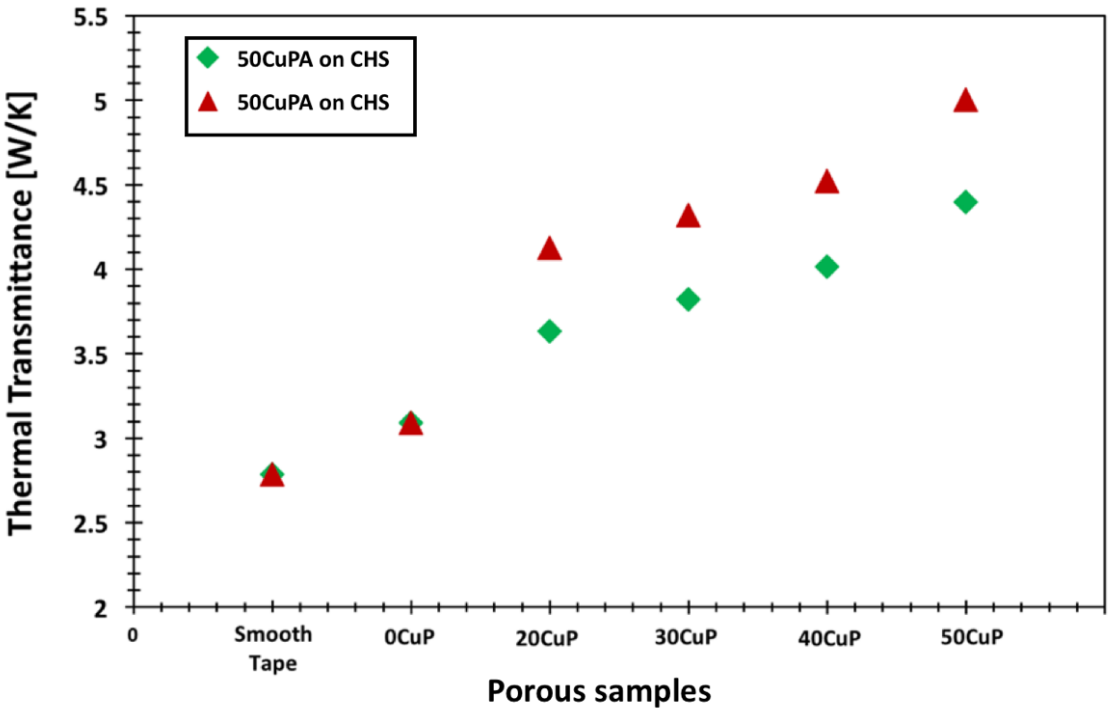

Fig. 104: Thermal transmittance of the porous sheets that has the highest porosity (50CuPA and 50CuPB) among all sheets produced from each processing route at a high Reynolds number (Re = 486)

10.2.2 Effect of surface porosity on the heat transfer performance of porous sheets

Microstructural image analysis has previously been performed on these porous sheets, proving that macropores were generated by the carbonate space holder added during processing and micropores resulted from incomplete densification. It also proved that surface porosity is directly controlled by varying the amount of space holder, hence increasing the amount of macropores throughout the whole sample, the sample surface included. Therefore, it is necessary to investigate and discuss the effect of the surface porosity on the overall heat transfer performance of the whole component.

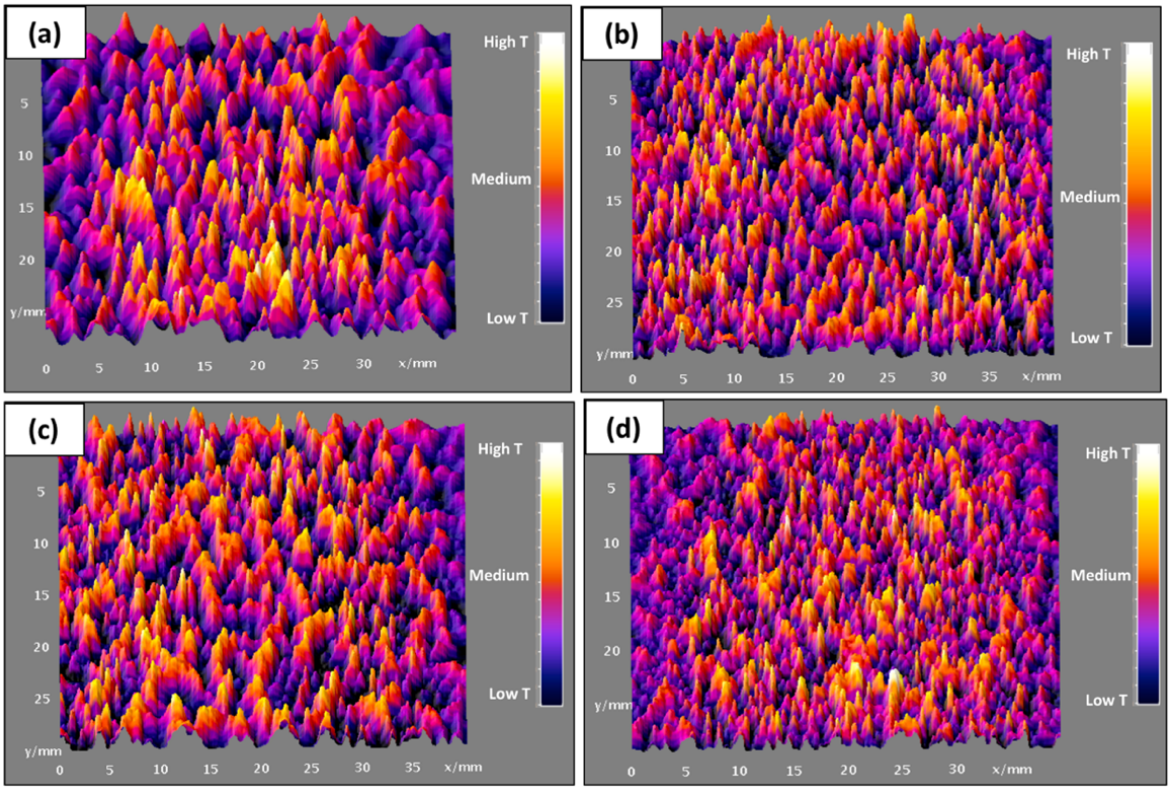

Figure 105: Thermal images of porous copper samples mounted on a cylindrical heating source; (a) 20CuPA, (b) 50CuPA, (c) 20CuPB and (d) 50CuPB.

Based on the structural characteristics of the porous sheets produced in this work, it is almost impossible to quantify the contribution of the surface porosity in isolation to the overall heat transfer performance. However, it is a clear fact that pores on the sample surface allow in and

out the flow of fluids (e.g. air in this study) in to the whole porous sheet. Therefore, it is strongly believed that increasing the surface porosity increases the inflow and outflow of cooling air through the porous sample hence improving the interaction of the airflow with the active surface area of the porous sheet. Optimising the interaction of the airflow with the active surface area of the sample would surely improve the rate of heat removal. During the heat transfer experiments, the interaction of airflow and porous sheet is highly significant.

Figure 107 and Figure 108 show the thermal transmittance of the porous sheets produced by Route A and B plotted against surface porosity respectively. The samples were tested on a cylindrical heating system (CHS) immersed in the airflow generated by an open-circuit heat transfer rig. The airflow rate was varied between 0.1 to 0.5 kg/s. As expected, the thermal transmittance of both sets of porous sheets increased with increasing surface porosity at high Reynolds number as seen from the two graphs in Figure 107 and Figure 108. The surface porosity was given by the sum of total macroporosity (from macropores) and microporosity (from micropores) of each sample previously described in Section 6.3. Generally, the porous sheets produced by route B have higher surface porosity compared to those produced by route A as discussed in Section 6.3 (also summarised in Table 20) and achieved higher *Tr* and *Nu* values compared to route A porous sheets.

Figure 105 and Figure 106 are the thermal images revealing the surface temperature distribution of regions of sample 20CuPA (Figure 105 (a) and Figure 106 (a), 20CuPB (Figure 105 (b) and Figure 106 (b), 50CuPA (Figure 105 (c) and Figure 106 (c)) and 50CuPB (Figure 105 (d) and Figure 106(d)). The porous samples with higher surface porosity are easily accessible to air, therefore have larger active surface areas and they were expected to obtain higher thermal transmittances especially under a higher Reynolds number regime.

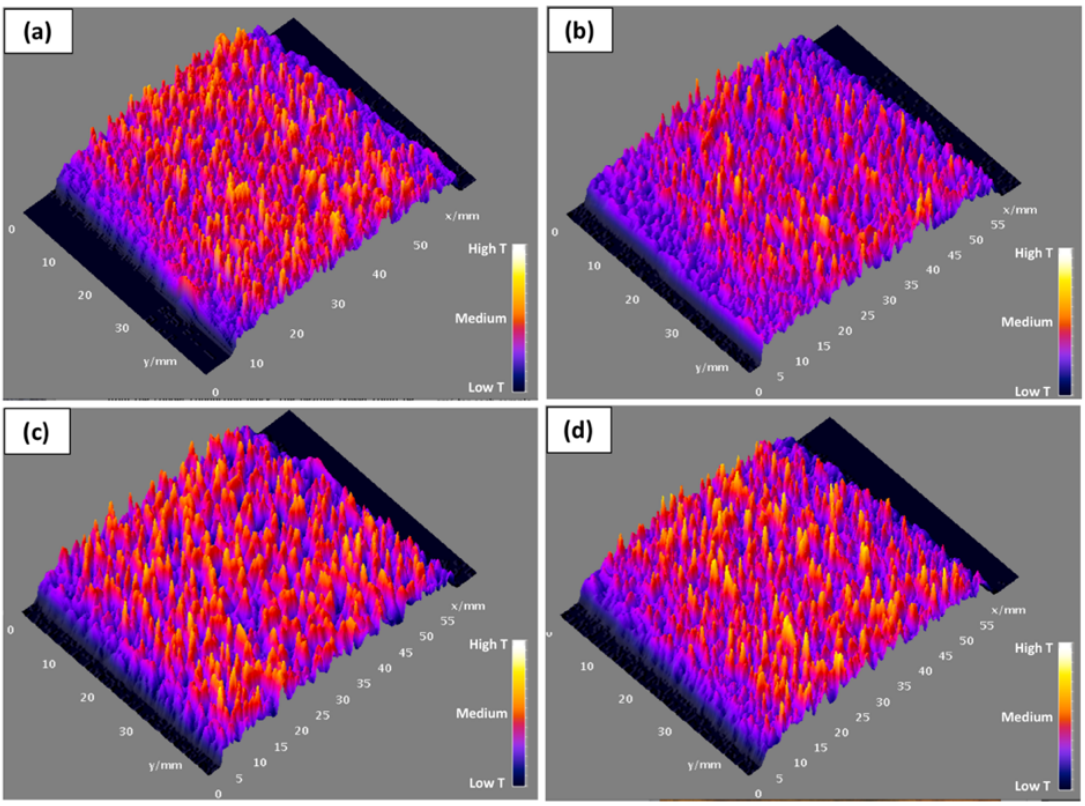

Figure 106: Thermal images of porous copper samples mounted on a cylindrical heating source; (a) 20CuPA, (b) 50CuPA, (c) 20CuPB and (d) 50CuPB.

In the graphs, the samples with lower porosity; 20CuPA and 20CuPB with surface porosity of 39.7% and 47.6% respectively achieved a thermal transmittance of 3.63 W/K (*Nu* = 408.4) and 4.13 W/K (*Nu* = 464.1) while the samples with higher surface porosity; 50CuPA and 50CuPB achieved *Tr* of 4.39 W/K (*Nu* = 494.7) and 5.00 W/K (*Nu* = 562.8) respectively. There is a linear relationship for both *Tr* and *Nu* plotted against surface porosity. As already mentioned above, pores on the surface allow inward and outward flow of the cooling air into the porous section of the sample. It is this 'inward and outward flow' of the cooling air that increases the heat transfer performance of the porous sheets. The inward and outward flow causes disturbances to the boundary layer especially at higher *Re*. Therefore, at higher surface porosity a high amount of cooling air was allowed into the porous layer, hence increasing this 'inward and outward flow' which accelerates the heat dissipation

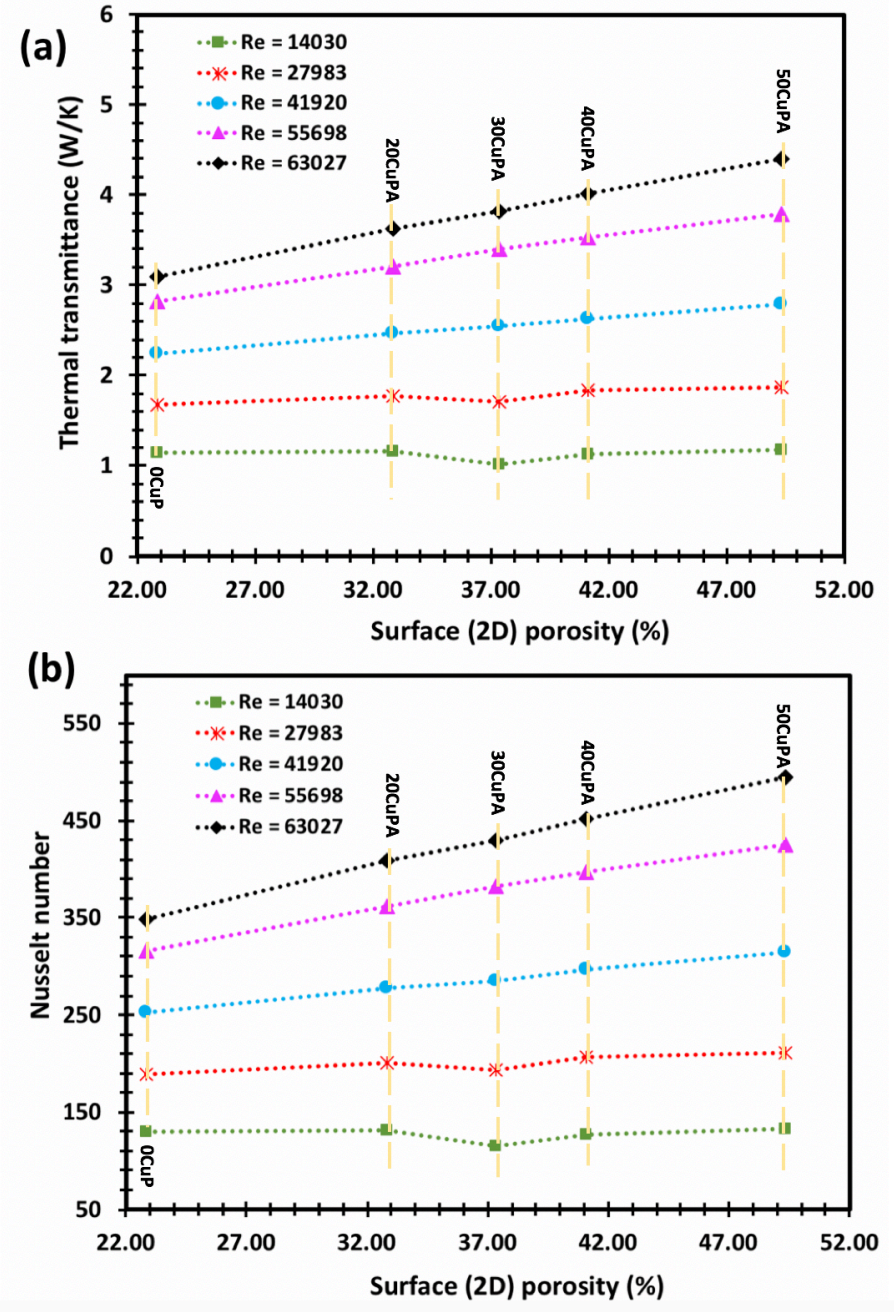

Figure 107: Two plots showing the experimental result of *Tr* and *Nu* of porous sheets (produced by route A) against surface (2D) porosity, tested on a cylindrical heating system: (a) thermal transmittance versus surface porosity of porous sheets and (b) dimensionless Nusselt number versus dimensionless surface porosity of copper samples.

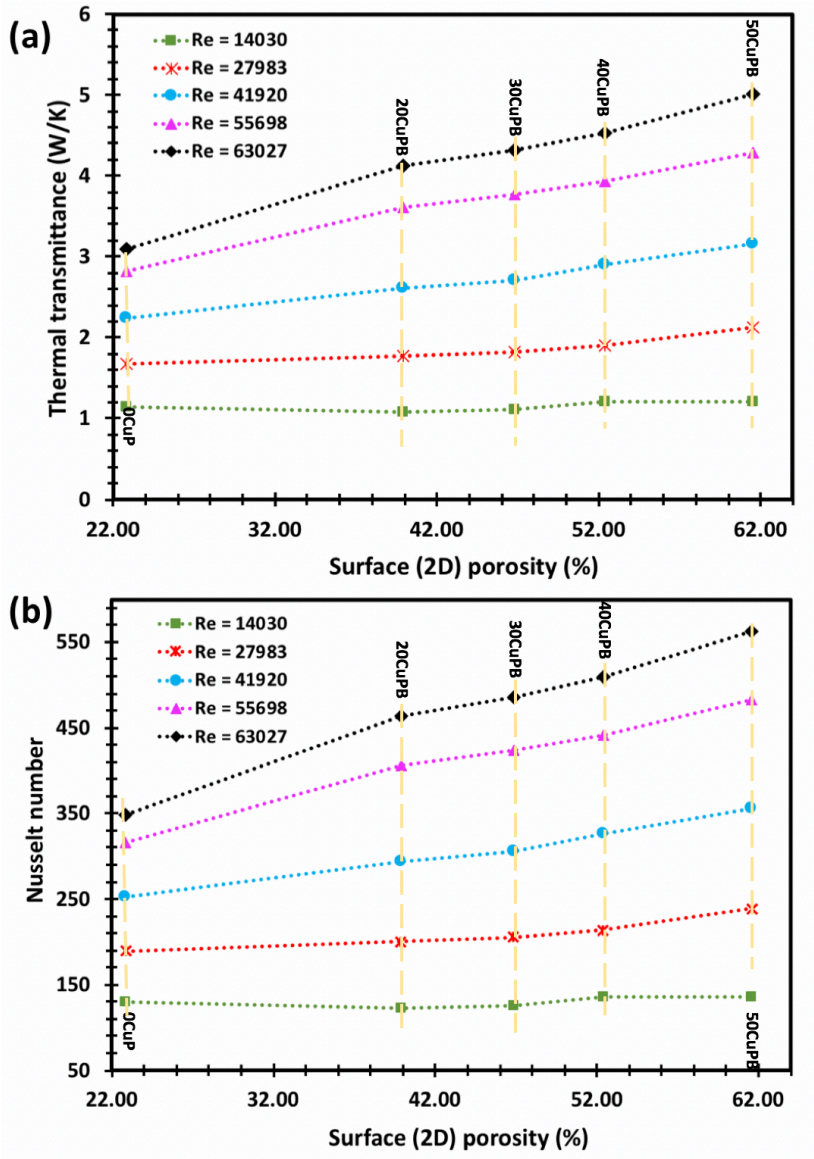

Figure 108: Two plots showing the experimental result of *Tr* and *Nu* of porous sheets (produced by route B) against surface (2D) porosity, tested on a cylindrical heating system: (a) thermal transmittance versus surface porosity of porous sheets and (b) dimensionless Nusselt number versus dimensionless surface porosity of copper samples.

10.2.3 Effect of surface roughness on the heat transfer performance of porous sheets

It was also observed that, not only is the porosity of the tapes increased during processing by the introduction of carbonate space holder but there was also an increase in the roughness of the sample surface. Table 20 shows a summary of the surface analysis results of the porous

copper tapes considered in this investigation initially discussed in full in section 7.2. 0CuP obtained the lowest average peak height (A.P.H) of 117 μm and roughness value of 0.032 mm and achieved the lowest *Tr* and *Nu* of 3.09 W/K and 347.8 respectively. While 20CuPA had an average peak height of 256 μm and 3.4 peaks/cm and achieved a roughness value of 0.411 mm, while 30CuPA (*Ra =0.88)* and 40CuPA (*Ra = 0.96 mm)* had 274 μm and 323 μm of A.P.H and 4.3 peak/cm and 4.6 peak/cm respectively. Lastly, 50CuPA (*Ra = 1.209 mm)* had an APH of 328 μm and 4.86 peak/cm. Porous tapes produced by processing route B follow a similar trend with 50CuPB recording an APH of 326 μm and 5.4 peak/cm.

During processing, the carbonate space holder particles protrude from the surface, forming uneven surface structures due to copper powders forming around the space holder. The samples maintain this surface roughness even after sintering and removal of the space holder in the final component. This resulting surface roughness affects thermal transmittance in two ways; first, the protrusions on the surface affect the fluid dynamic interaction between the active surface and the flow field, therefore enhancing convective heat transfer. Secondly, the samples with higher surface roughness could have higher surface area (due to uneven surface or protrusions) for convective heat transfer and therefore they were expected to have higher thermal transmittance.

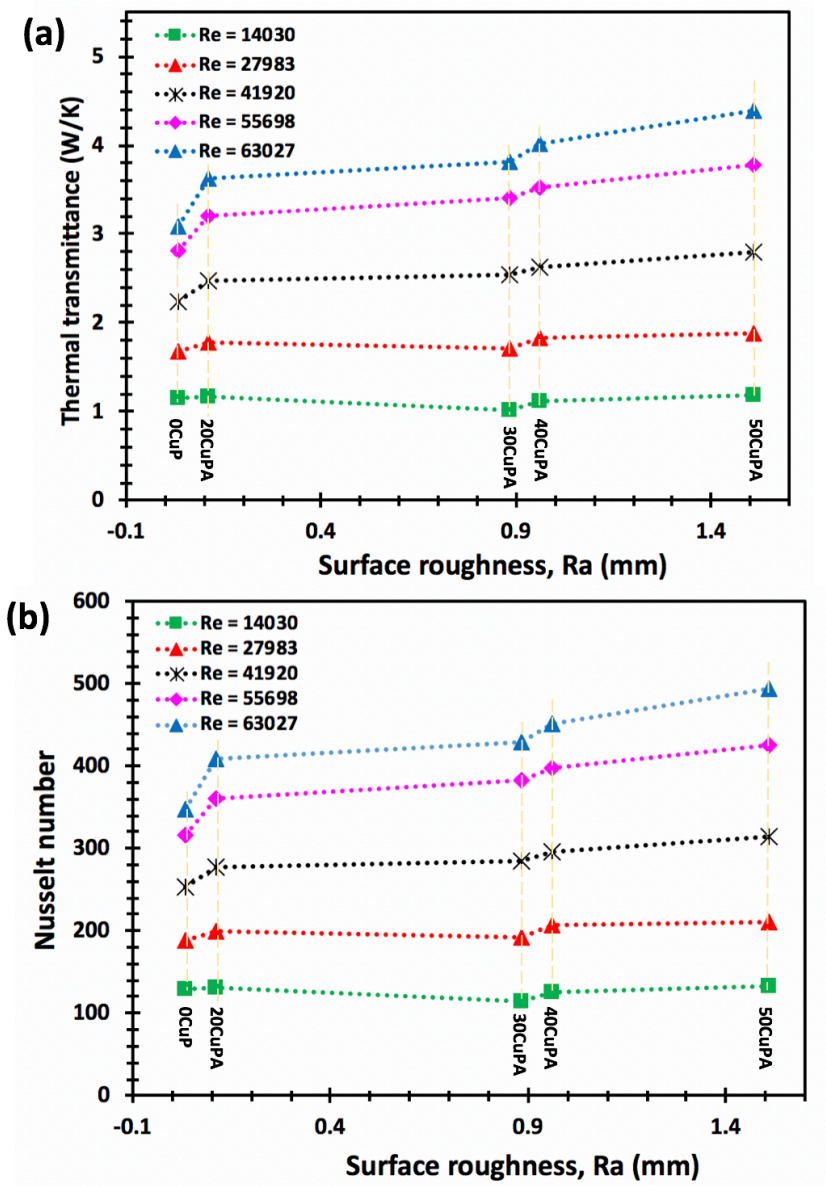

Figure 109: Two plots showing the experimental result of *Tr* and *Nu* of porous sheets (produced by route A) against surface roughness, tested on a cylindrical heating system: (a) thermal transmittance versus surface roughness of porous sheets and (b) dimensionless Nusselt number versus surface roughness of copper samples.

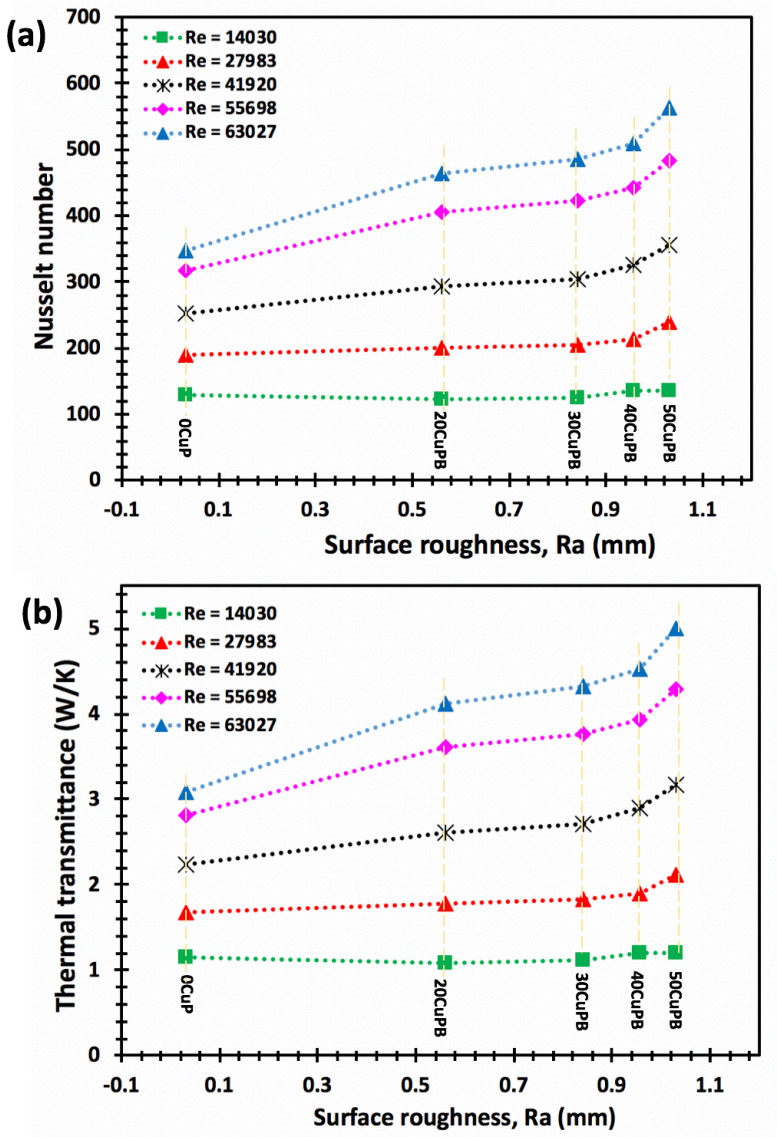

Figure 110: Two plots showing the experimental result of *Tr* and *Nu* of porous sheets (produced by route B) against surface roughness, tested on a cylindrical heating system: (a) thermal transmittance versus surface roughness of porous sheets and (b) dimensionless Nusselt number versus dimensionless surface roughness of copper samples.

The convective heat transfer is dependent mainly on the boundary layer conditions which are at the same time affected by the surface roughness, pore morphology and pore wall morphology. But here, the fluid flow behaviour around the heat source plays a major role which leads to the differences in the heat transfer performance evidenced by the results (Table 21 and Table 22). The surface morphology of the porous tape mounted on both heating systems is both porous and rough, and therefore some of the air is forced to flow through the

pores of the porous heat exchanger and part of it is forced to flow round rough surfaces. There is a high rate of heat transfer due to increased active surface area by the availability of the macropores and protrusions (dimples) on the surface of this type of porous heat exchanger.

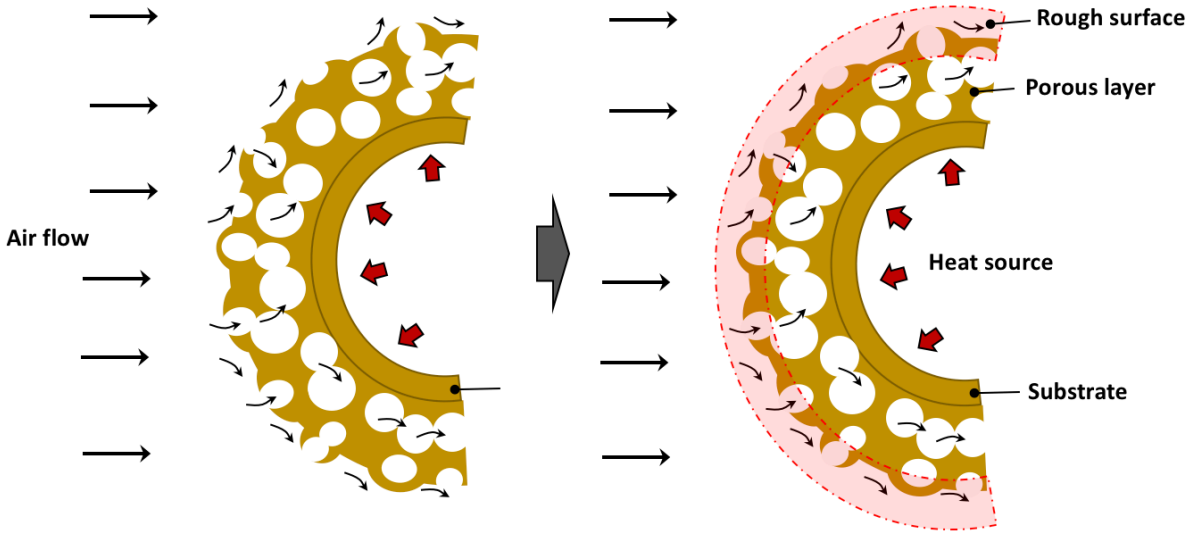

Figure 111: Schematic diagram showing the interaction of the air flow and rough and porous sheets of copper, where the schematic diagram on the right highlights the rough surfaces of the porous sample wrapped around a heat source.

It was also observed from the same graphs (Figure 109 and Figure 110) that roughening smooth copper tape slightly improved the thermal transmittance by 1.2% within the high Reynolds number regime. This was due to a slight increase in active surface area by roughening the sample which slightly improved convective heat transfer by affecting the fluid dynamics interaction between the active surface and the flow field. However, the degree of roughness introduced in such a thin sheet by sand blasting is much less than that engendered by porous material production.

In summary, the double layer porous copper tapes produced here, showed higher thermal transmittance, arising not only from higher porosities but also from increased surface roughness which was introduced onto the sample surface during processing as a secondary effect of generating pores. Introduction of porosity and artificial roughness result in a high convective heat transfer enhancement compared to just roughened or dimpled surfaces or

porous samples alone, and significant improvements can be obtained even in situations where reduced volume does not permit a large porous network to be used.

10.3 Heat transfer performance of porous sheets on flat heating system

As already mentioned at the beginning of Section 10, the samples listed and described in Table 20 were again investigated for heat transfer performance on a flat heating system (FHS) (a schematic diagram of the setup of FHS is shown in Figure 44). The samples were tested under the same conditions as for the cylindrical heating system (CHS) where the flow rate of air passing through the samples was varied between the ranges of 0.1 – 0.5 kg/s using an open-circuit heat transfer rig. The heat transfer performance of the porous sheets was investigated by monitoring the inlet and outlet temperatures of air and surface temperatures using thermocouples in a similar way as in the CHS.

10.3.1 Effect of porosity on the heat transfer performance of copper

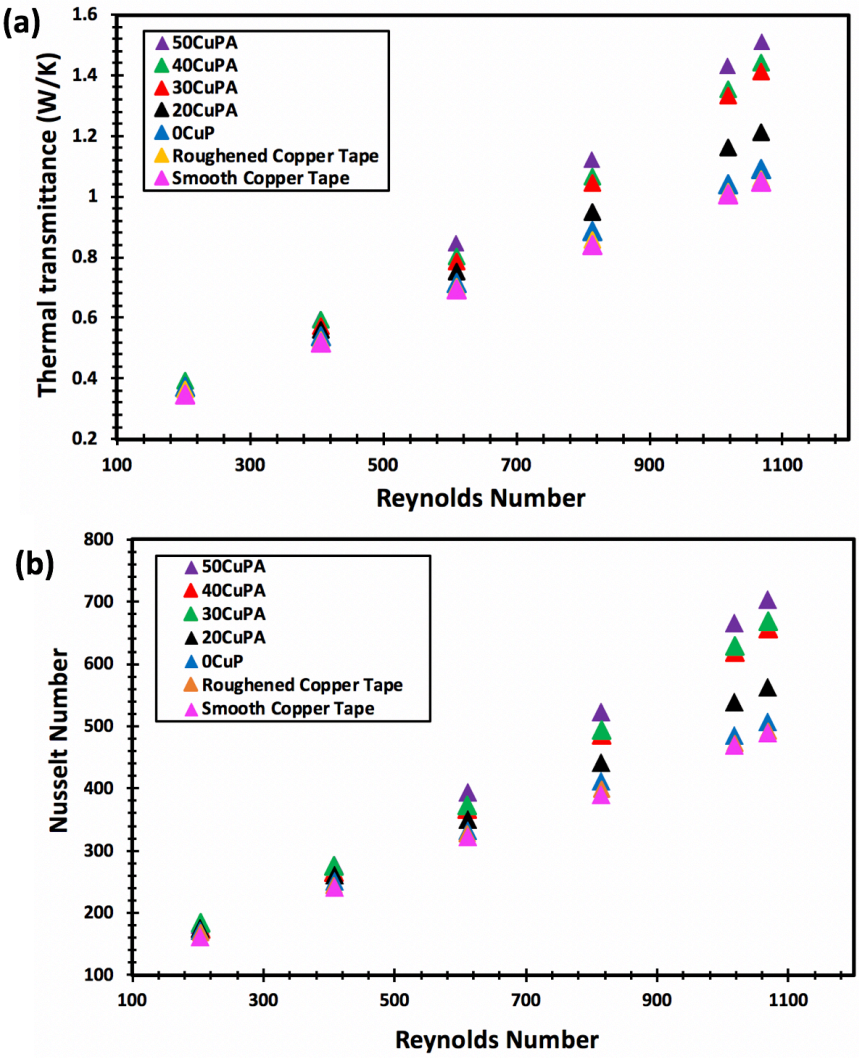

Figure 112: A plot showing the heat transfer results of porous sheets (0CuP, 20CuPB, 30CuPB, 40CuP and 50CuPB) along with as-received smooth copper and sand blasted copper tape; (a) thermal transmittance against Reynolds number and (b) dimensionless Nusselt number against dimensionless Reynolds number.

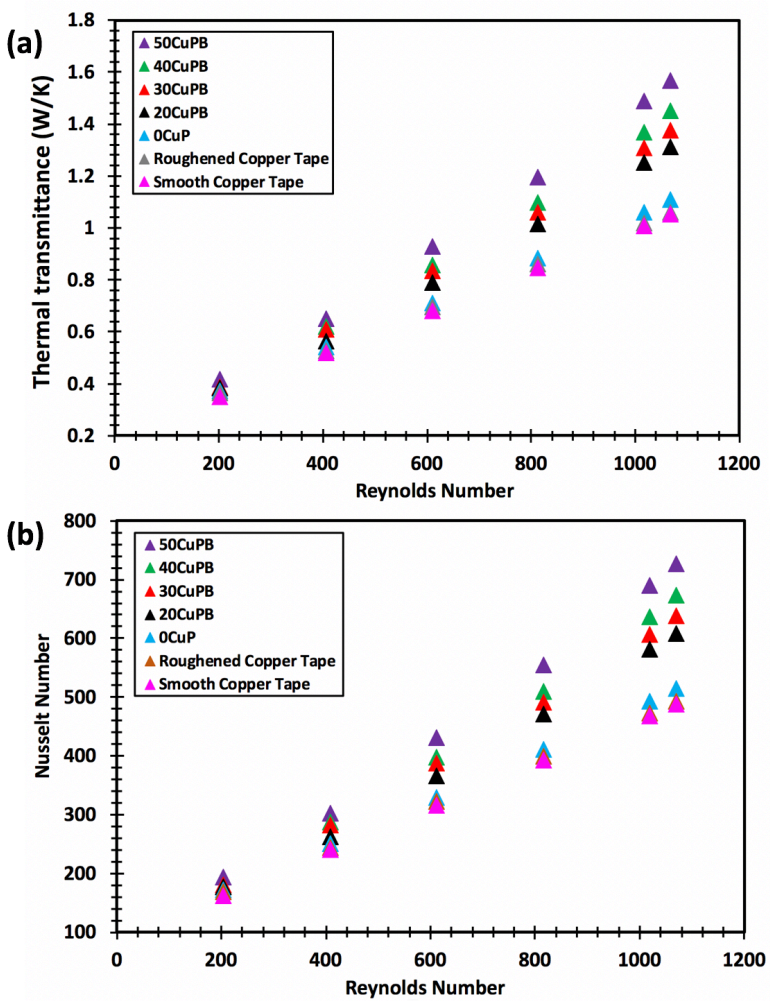

Figure 113: A plot showing the heat transfer results of porous sheets (0CuP, 20CuPB, 30CuPB, 40CuP and 50CuPB) along with as-received smooth copper and sand blasted copper tape; (a) thermal transmittance against Reynolds number and (b) dimensionless Nusselt number against dimensionless Reynolds number.

Figure 112 (a) and Figure 113 (a) show the experimental results of the thermal transmittance (calculated using equation (29)) of the porous tapes produced by route A and route B respectively, plotted against dimensionless Reynolds number (calculated using equation (32)), along with as-received smooth copper and sand-blasted copper sheet as references. And Figure 112 (b) and Figure 113 (b) show plots of dimensionless *Nu* (calculated using equation (34) versus dimensionless *Re*. A similar trend was observed between Figure 112 (*Tr* versus *Re* plot of porous sheets produced by route A) and Figure 113 (*Tr* versus *Re* plot of porous sheets produced by route B) where, firstly the introduction of the porous layer into the tapes

improved thermal transmittance of the copper tapes, and secondly, the *Tr* and *Nu* increases with porosity of the samples (refer also to Table 20). From Figure 112 (a), 50CuPA achieved a thermal transmittance *(Tr)* of 1.51 W/K within the high Reynolds number regime (Re = 1069) while 40CuPA and 30CuPA achieved *Tr* of 1.44 W/K and 1.41 W/K respectively, still within the high Reynolds number regime, while samples with the lowest porosity, 20CuPA and 0CuP, obtained *Tr* of 1.21 W/K and 1.09 W/K consecutively. The *Tr* of both the smooth copper sheet (reference) and the sand-blasted copper sheet achieved the lowest *Tr* where each sample recorded 1.04 W/K and 1.05 W/K respectively

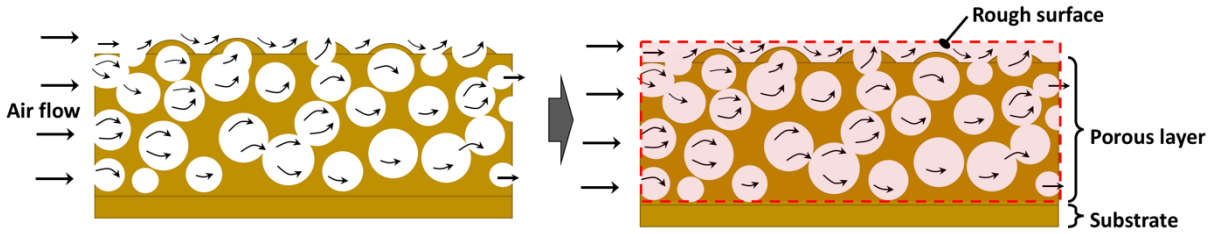

Figure 114: Schematic diagram showing the interaction of the air flow and rough and porous sheets of copper

At higher Reynolds number, the *Tr* of the porous sheets processed by route B was directly proportional to their porosity (volumetric porosity and surface porosity). The highly porous sheets (50CuPB) recorded a higher *Tr* of 1.56 W/K at a higher Reynolds numbers, followed by 40CuPB, 30CuPB and 20CuPB which recorded a *Tr* of 1.45 W/K, 1.37 W/K and 1.31 W/K respectively. 0CuP recorded the lowest *Tr* of 1.09 W/K among the porous sheets tested. The as-received smooth sheet and sand blasted sheet recorded *Tr* of 1.04 W/K and 1.05 W/K respectively. Figure 113 (b) shows a plot of dimensionless Nu versus dimensionless *Re* of tapes processed by route B.

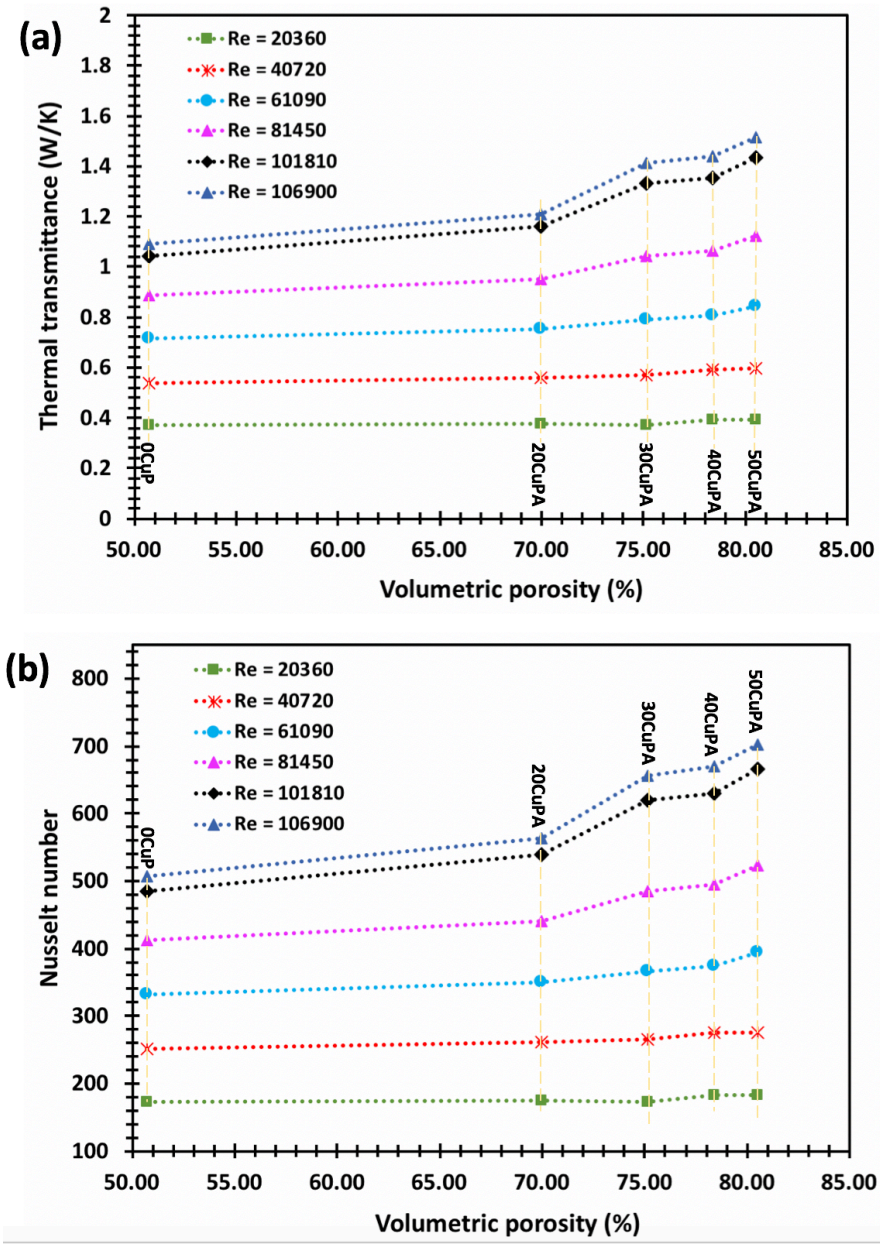

Figure 115: Two plots showing the experimental result of *Tr* and *Nu* of porous sheets (produced by route A) against volumetric porosity, tested on a flat heating system: (a) thermal transmittance versus volumetric porosity of porous sheets and (b) dimensionless Nusselt number versus dimensionless volumetric porosity of copper samples.

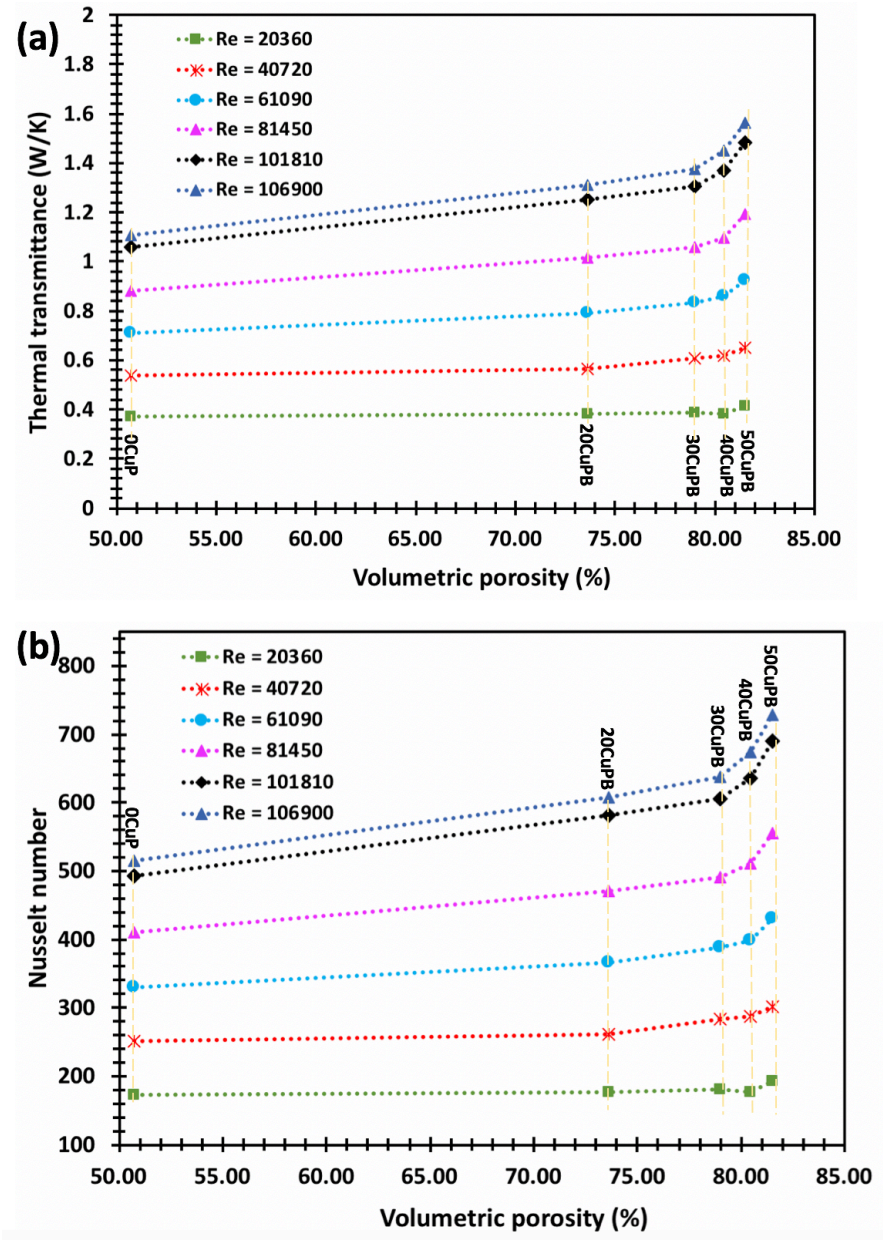

Figure 116: Two plots showing the experimental result of *Tr* and *Nu* of porous sheets (produced by route B) against volumetric porosity, tested on a flat heating system: (a) thermal transmittance versus volumetric porosity of porous sheets and (b) dimensionless Nusselt number versus dimensionless volumetric porosity of copper samples.

It is important to understand the significance of creating a thin porous sheet of copper integrated with a dense copper layer (thickness = 0.125 mm) for the total heat transmittance capabilities of the whole component with reference to a dense smooth sheet. The *Tr* achieved on porous copper sheets with a range of porosities was compared against the *Tr* of the reference sample (as-received smooth copper sheet).

Table 24 provides a summary of heat transfer performance (*Tr*) all porous copper sheets produced by route A compared to as-received copper sheet as a reference sample. In 50CuPA produced by introducing a highly porous layer on to a dense substrate, the thermal transmittance was improved by 25.1 % compared to the smooth copper sheet at high *Re* regime (*Re* = 1069). The rest of the samples with lower porosities achieved much lower thermal transmittance, where 40CuPA recorded 20% higher than the smooth tapes, and, 30CuPA and 20CuP achieved 18% and 8% respectively, all tested in the high *Re* regimes (*Re* = 1069). 0CuPA has the lowest volumetric porosity and surface porosity of 51% and 28% consecutively among all the tapes investigated. It has recorded the lowest heat transmittance of 1.09 W/K, which is 5% in reference to the smooth tape at high Reynolds number regimes.

Table 25 shows a summary of the experimental results of the thermal transmittance of the porous copper sheets produced by processing route B in reference to the as-received copper sheet (smooth). A similar trend in Figure 116 (a) (and Table 25)is observed in Figure 116 (b), where high porosity samples show high transmittance. 50CuPB obtained high thermal transmittance of 1.56 W/K at high Reynolds numbers, which is 33% in reference to the smooth tape, followed by 40CuPB, 30CuPB, 20CuPB and 0CuPB. Generally, fabricating a porous layer (ε_{vol} = 82%) on to a thin substrate by processing route B resulted in an improved thermal transmittance as high as 1.56 W/K, which is 49% better than the reference smooth copper tape when tested in the high Reynolds number regime. Sample 40CuPB obtained a thermal transmittance of 1.45 W/K, which deviated by 38% in reference to the smooth copper tape. 30CuPB obtained a thermal transmittance of 1.37 W/K, which deviated by 30% in reference to the smooth tape. 20CuPB and 0CuP achieved the lowest thermal transmittances of 1.31 W/K and 1.09W/K respectively at *Re* = 106899 (the highest Reynolds number regime), which deviated by 13.8% and 1.7% consecutively.

Table 24: The deviations of thermal transmittance of porous copper produced by processing route A from that of smooth copper tapes tested on a FHS.

Present Work	Smooth	0CuP	Deviation (%)	20CuP	Deviation (%)	30CuP	Deviation (%)	40CuP	Deviation (%)	50CuP	Deviation (%)
Re = 1069	1.05	1.09	3.81	1.21	15.24	1.41	34.29	1.44	37.14	1.51	43.81
Re = 1018	1.01	1.04	2.97	1.16	14.85	1.33	31.68	1.35	33.66	1.43	41.58
Re = 814	0.84	0.89	5.95	0.95	13.10	1.04	23.81	1.06	26.19	1.12	33.33
Re = 611	0.69	0.71	2.90	0.75	8.70	0.79	14.49	0.80	15.94	0.85	23.19
Re = 407	0.57	0.54	-5.26	0.56	-1.75	0.57	0.00	0.59	3.51	0.59	3.51
Re = 204	0.37	0.37	0.00	0.37	0.00	0.38	2.70	0.39	5.41	0.39	5.41
Mean Deviation		**1.7%**		**8.4%**		**17.8%**		**20.3%**		**25.1%**	

Table 25: The deviations of thermal transmittance of porous copper produced by processing route B from that of smooth copper tapes tested on a FHS.

Present Work	Smooth	0CuP	Deviation (%)	20CuP	Deviation (%)	30CuP	Deviation (%)	40CuP	Deviation (%)	50CuP	Deviation (%)
Re = 1069	1.05	1.09	3.81	1.31	1.31	1.37	30.48	1.45	38.10	1.56	48.57
Re = 1018	1.01	1.04	2.97	1.25	1.25	1.30	28.71	1.37	35.64	1.48	46.53
Re = 814	0.84	0.89	5.95	1.01	1.01	1.06	26.19	1.10	30.95	1.19	41.67
Re = 611	0.69	0.71	2.90	0.78	0.78	0.83	20.29	0.86	24.64	0.93	34.78
Re = 407	0.57	0.54	-5.26	0.56	0.56	0.61	7.02	0.62	8.77	0.65	14.04
Re = 204	0.37	0.37	0.00	0.38	0.38	0.39	5.41	0.38	2.70	0.42	13.51
Mean Deviation		**1.7%**		**13.8%**		**19.7%**		**23.5%**		**33.2%**	

10.3.2 Effect of surface roughness on the heat transfer performance of porous copper sheets

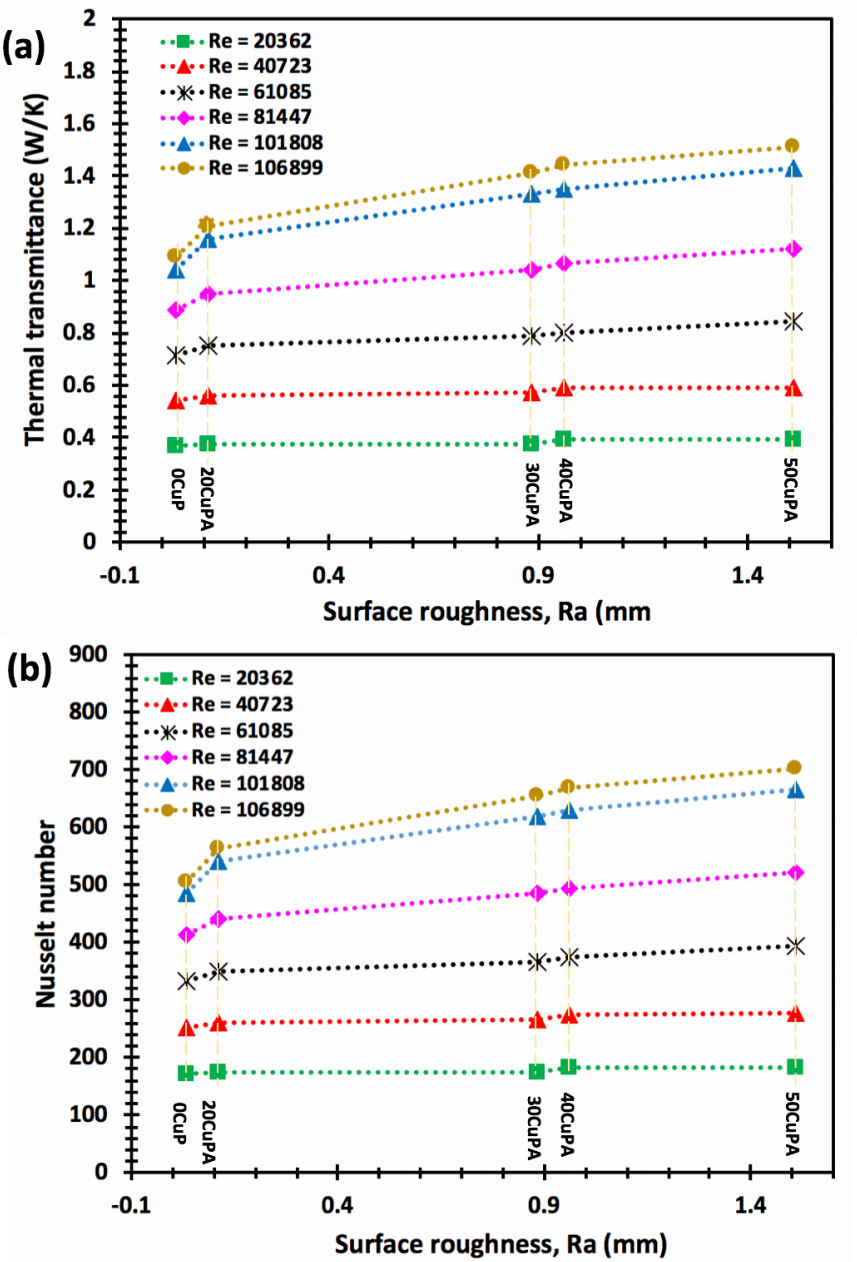

Figure 117: Two plots showing the experimental result of *Tr* and *Nu* of porous sheets (produced by route A) against surface roughness, tested on a flat heating system: (a) thermal transmittance versus surface roughness of porous sheets and (b) dimensionless Nusselt number versus dimensionless surface roughness of copper samples.

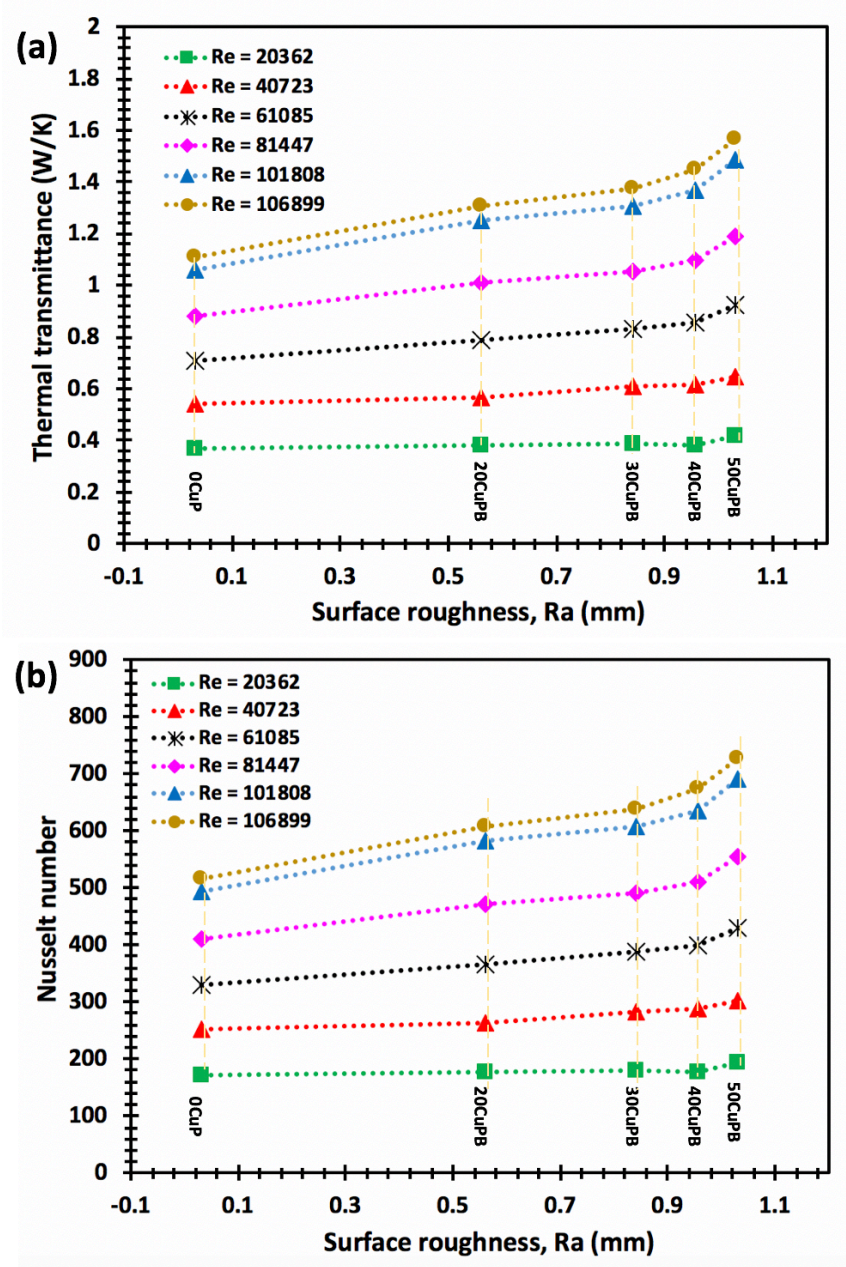

Figure 118: Two plots showing the experimental result of *Tr* and *Nu* of porous sheets (produced by route B) against surface roughness, tested on a flat heating system: (a) thermal transmittance versus surface roughness of porous sheets and (b) dimensionless Nusselt number versus dimensionless surface roughness of copper samples.

The surface roughness shows a similar effect on the heat transfer performance when tested on a FHS compared to when it was tested on a CHS. As already discussed in section 10.2.3, the dimples and protrusions of the porous samples cause an increase in the active surface area for heat transfer from the porous section. The only difference here was the geometrical dimensions of the heating system which influenced the fluid flow mechanism around the

rough surfaces. The boundary layer conditions in FHS are different from the conditions in the CHS when placed along the path of the cooling fluid as discussed in section 4.5.

Even though a similar trend was observed in the *Tr/Nu* versus *Re* plots, *Tr* and *Nu* values obtained in the CHS were higher than those achieved in the FHS. The blockage ratio (blockage ratio frontal area of the tunnel / cross-section area of the test section) in the air tunnel when CHS is installed was calculated to be about 40% compared to FHS where it is less than 0.5%. The ratios were calculated based on the dimensions of each test section placed along the air tunnel. The lower blockage ratio could be one of the reasons for the lower values of *Tr/Nu* recorded. At a lower blockage ratio a slightly lower amount of cooling air is forced around the rougher surfaces, and through the pores within the porous layer hence a slower heat dissipation from the sample surface into the cooling fluid.

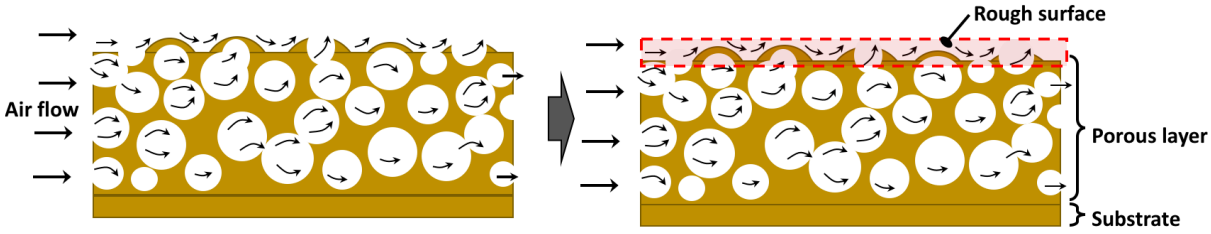

Figure 119: Schematic diagram showing the interaction of the air flow with rougher surface and the porous section of the double-layered sheets of copper

10.3.3 Overall thermal performance comparisons

Generally, the porous sheets produced by processing route B obtained higher thermal transmittance compared to those produced by processing route A. The difference in the heat transfer performance is due to the microstructural parameters of the porous sheets, such as porosity, pore distribution and pore morphology. Surface roughness also has a major effect on the heat transfer performance. The porous sheets with higher porosities had larger active surface and they were expected to obtain higher thermal transmittance at higher Reynolds

number. This resulting surface roughness affects thermal transmittance in two ways; first, the protrusions on the surface affect the fluid dynamic interaction between the active surface and the flow field, therefore enhancing convective heat transfer. Secondly, the samples with higher roughness have higher surface area for convective heat transfer and therefore are expected to have higher thermal transmittance.

This is due to the fact that 50CuPB had both higher volumetric porosity and surface porosity compared to 50CuPA. It is now obvious that the thermal transmittance increases with porosity, therefore, to compare the two sets of sheets, 50CuPA and 50CuPB both with higher porosity can be used. It can be clearly seen from Table 20 that 50CuPA and 50CuPB porous samples had similar volumetric porosity of 81% and 82% but somewhat different surface porosities of 60% and 74% respectively As seen from Table 24 and Table 25 50CuPA and 50CuPB achieved a thermal transmittance of 1.56 W/K and 1.51 W/K. The thermal transmittance of 50CuPB deviated by 49% from the reference copper foil while 50CuPA deviated by 44%.

10.4 Comparison of the flat and cylindrical heating systems

Figure 120 shows the experimental results of the dimensionless *Nu* of nine different porous copper sheets with varying porosities tested at high *Re* regime on two different heating systems; CHS (*Re* = 431) and FHS (*Re* = 407) along with as-received smooth copper sheet as reference. It is clear from the plot in Figure 120 (b) that, *Re* = 431, the samples tested using the cylindrical heating source have higher *Nu*, and the samples produced by route B have the highest *Nu* followed by those produced by route A. However, the same samples tested on the

flat heating system recorded lower *Nu* compared to those tested on the cylindrical heating system at *Re* = 407. The samples produced by processing route B recorded the highest Nu compared to those produced by route A when tested using the flat heating system

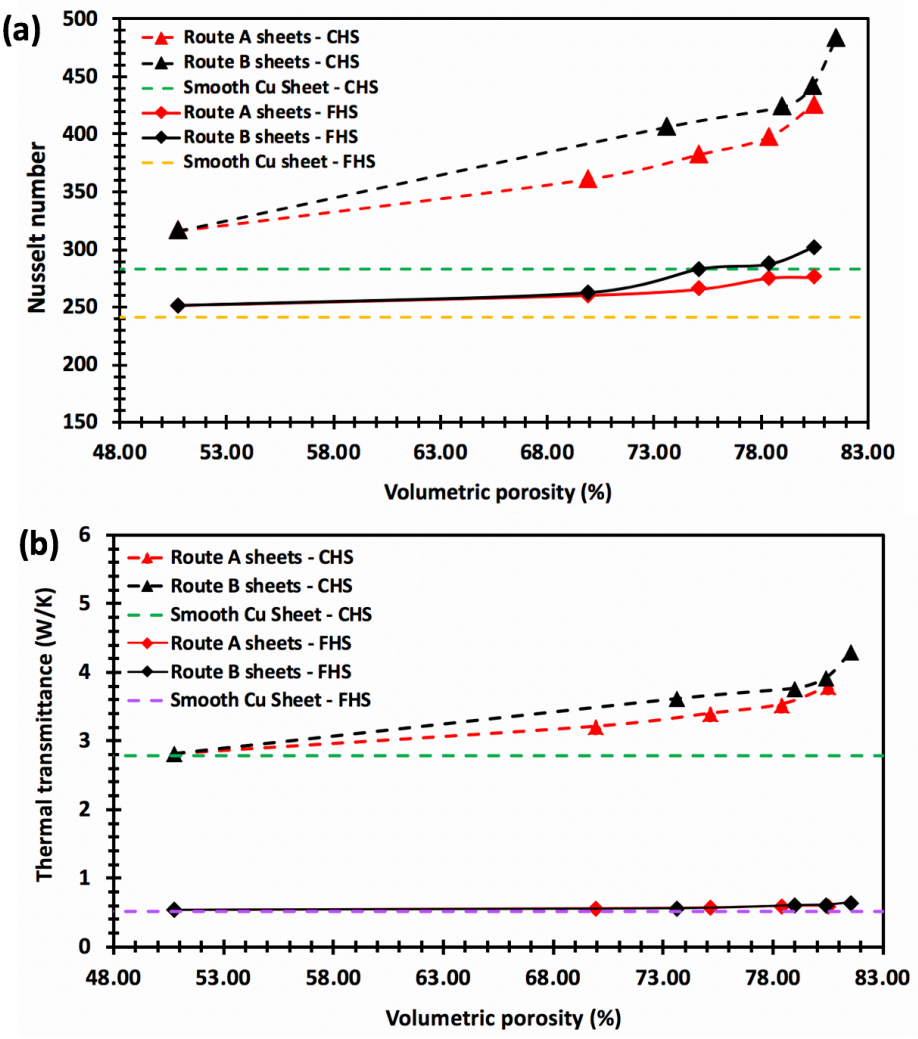

Figure 120: The *Tr* and dimensionless *Nu* versus dimensionless *Re* of different porous copper tapes and smooth tape tested at *Re* = 431 on cylindrical heating system and *Re* = 407 on flat heating system.

The differences in the Nusselt number of the porous sheets (route A and route B) achieved on the CHS and the FHS shown in Figure 120 could be due to two main factors; (i) fluid flow mechanism and (ii) the blockage ratio of the systems.

Table 26: The dimensionless Nusselt numbers of porous copper samples; 50CuPA and 50CuPB with high porosities investigated in high Reynolds number regime. The tapes were tested on F.H.S (*Re* = 407) and C.H.S (*Re* = 431) for comparison.

Samples	Nusselt Number - F.H.S (Re = 407)	Nusselt Number - C.H.S (Re = 431)
0CuP	250.9	316.4
20CuPA	261.0	361.1
20CuPB	262.1	406.5
50CuPA	276.2	425.8
50CuPB	301.7	482.9

Fluid flow mechanics: The geometrical shapes of the two systems are different, therefore the fluid mechanics around the samples were expected to be different. The difference in the Nusselt number between the two heating systems is due to the difference in the forced convection which involves fluid motion as well as heat conduction. The fluid motion around the heat source enhances heat transfer (the higher the mass flow rate the higher the heat transfer rate), but here the dimensionless *Re* (Re = 407 and Re = 431) were almost identical, therefore it was neglected in this discussion. The convective heat transfer is dependent mainly on the boundary layer conditions, which are at the same time affected by structural characteristics such as surface roughness, pore morphology and pore wall morphology. But here, the fluid flow behaviour around the heat source plays a major role in the heat transfer performance of the porous samples hence the difference in the *Nu* as shown in Figure 120 and Table 26.

The surface morphology of the porous sheets mounted on both heating systems is both porous and rough, and therefore some of the air is forced to flow through the pores of the porous heat exchanger and part of it is forced to flow round rough surfaces. These inward and outward flows of air into the pores, and also around the dimples or protrusions on the sample surface, cause disturbances within the boundary layer. It is these disturbances or turbulence that occurs

within the boundary layer that enhances the heat transfer from the sample. There is high rate of heat transfer due to the increased active surface area due to the availability of the macropores and protrusions (dimples) on the surface of this type of porous heat exchanger. The mechanics of fluid flow around the two heating systems (a cylindrical, and a flat heating system) employed in the investigation are different and so are the heat transfer capabilities.

Difference in the flow path: It is clear from Figure 120 and Table 26 that testing 50CuPA on the CHS has higher Nusselt number compared to testing it on the FHS. A similar behaviour was obtained also with 50CuPB where a *Nu* of 430 was achieved compared to 563 achieved by the CHS. Generally, 50CuPB achieved a higher Nusselt number on both heating systems compared to 50CuPA. The CHS was positioned across the air tunnel in the test section of the test rig, which is in the path of the cooling air flow as shown in Figure 48 (a), therefore this setup makes the fluid flow direction head on with the sample. By contrast, the FHS was positioned at the base of the air tunnel, also within the test section of the test rig as shown in Figure 48 b), which makes the air flow to be parallel to the samples.

In the results presented in Figure 120, it is clear that values of *Tr* and *Nu* of porous sheets tested on CHS are high compared to those tested on FHS. This might be due to differences in the way the air flow interacts with the porous sample. On the CHS, the airflow is head on with the sample causing a large amount of cooling air to flow in and out of the porous sheets tested (see the schematic diagram in Figure 103), therefore increasing the rate of heat dissipation from the porous samples. Whereas, those porous samples tested on FHS were placed parallel to the air flow (see a schematic diagram in Figure 114) and so a smaller amount of cooling air was expected to flow through the porous sample hence smaller values of *Tr* and *Nu*.

Generally, the higher the amount of air forced in to the pores the higher the amount of heat dissipation, therefore higher values of *Tr* and *Nu*, especially at high *Re* values. On FHS, the

main factor in heat transfer from the porous samples to the cooling air could be the surface roughness of the sample, because the porous section was not entirely accessible to the cooling air.

In this part, a conclusion was made that the higher values of *Tr* and *Nu* obtained when the samples are tested on CHS might be due to the higher amount of cooling air being forced in to the pores of the sample due to the way the heating systems are positioned in the test section. While this indicates the roles of the test conditions in the values of the *Tr* and *Nu* obtained, it should be remembered that thin sheets of the materials like those produced here would be suitable for use where enhancement of heat transfer is required on a curved or flat surface, so the prevailing fluid flow conditions are likely to be similar to different heating source while in use.

10.5Performance as heat sinks

The double-layered porous tape successfully produced in this work has an improved heat transfer performance compared to the dense and smooth as-received 99.8 % pure copper sheets. A thin porous layer of Cu integrated with a dense Cu substrate improved their performance, however a smooth copper surface is not necessarily the competitor material in such applications, and a variety of the materials have been used to passively enhance heat transfer. It is therefore appropriate to assess the relative merit of these materials in such applications. Direct comparison of heat transfer coefficient shows that the porous sheets made here are not as good as the existing porous copper already in the market such as VersarienCu with porosity of up to 85% and average pore diameters from 20 μm to 1,000 μm offering a heat transfer coefficient ranging from 150 – 200 kW/m^{2}K, which itself is 5-8 times better than the conventional groove fins [29], [75]. Another work performed by [208] presented single

layer and a double layer porous samples also produced by LCM combined with hot pressing. A 5mm thick single-layer sample of 62.5% porosity obtained an HTC of approximately 36 kW/m^{2}K at 0.167 m/s, while a double layer sample achieved an HTC of approximately 37 kW/m^{2}K, and lotus-type porous copper consisting of long cylindrical pores or channels in one direction with average pore diameter of 550 μm and the porosity level of 60 % offering a heat transfer coefficient of 2,000 W/m^{2}K, 7.7 times higher than the conventional groove fins [175], [209]. A meaningful quantitative comparison is difficult because of the different setups e.g. type of material, tunnel geometry of the test rig, type of coolant and flow conditions.

[210] also performed some air heat transfer and pressure drop experiments through copper foams produced in a sandwich-like arrangement where the copper foam is brazed between 10mm thick copper plates. The best performing porous sample that has a porosity of 90.5% achieved an HTC of 1190 W/m^{2}K when tested under air flowing at 5m/s. In this case, the heat transfer performance improved with a decreasing pore density.

Table 27: A comparison of copper heat sinks, and conventional heat sink with the porous copper sheet produced in this work

Heat sink	Heat transfer coefficient (W/m^{2}K)	Porosity (%)	Pore size (μm)	Reference
VersarienCu heat sink	150,000 – 200,000	$\varepsilon \leq 85$	20 – 1,000	Ref. [29], [75]
Double layer porous Cu	37000	$\varepsilon \leq 62.5$		Ref. [208]
Single layer porous Cu	37000	$\varepsilon \leq 62.5$		Ref. [208]
Sandwich like Cu foam	1190	$\varepsilon \leq 90.5$		Ref. [210]
Lotus copper heat sink	70,000 – 90,000	$\varepsilon \leq 60$	550 (Av.)	Ref. [175], [209].
Conventional grove fins	14,000 – 15,000	-	-	[20]
Porous copper (in this study)	190 - 320	$\varepsilon \leq 82$	30 - 790	-
Pure smooth copper	13	0	-	-

Table 27 shows a general comparison of the porous heat sinks produced in this work with other existing copper heat sinks known to have good performance for dissipation of heat in portable electronics. Porous copper sheets produced in this work have a wide range of porosities up to 82% and pore diameters ranging from 30 μm to 790 μm. These porous sheets offer the heat transfer coefficient in the range of 190 – 320 W/m^2K which is significantly lower compared to VersarienCu, lotus copper heat sink as well as conventional groove fins, although a fair comparison is required where samples are tested under comparable conditions such as; cooling medium, heat transfer medium (i.e. water, air etc.) flow rate, driving temperature difference etc.

However, the materials examined here do have an advantage in applications where space is limited. The porous sheets produced in this study offer heat transfer coefficient 24 times better than the dense sheets of pure copper with smooth surfaces. They have been explored in a wide range of thicknesses down to 850 μm and porosity up to 82%. More importantly, these porous sheets are capable of bending around curvatures with diameters down to 76 mm. The sheets achieved a flexibility of 22 – 852 GPa which could be beneficial in the case where heat dissipation is required in curved surfaces, in small spaces. This may be encountered in existing devices and equipment where enhanced cooling is needed, but full redesign is not possible, and so these materials could be applied as a retro-fit solution.

10.6Conclusion of heat transfer performance of porous samples

In conclusion, it was demonstrated that two sets of double-layered porous copper sheets with a wide range of porosities, as well as surface roughness, were successfully produced by LCS applied to tape casting. The porous tapes were then investigated for heat transfer performance on a CHS and a FHS using an open-circuit wind tunnel under forced convection. The investigation was carried out on porous sheets with a volumetric porosity and surface porosity ranging from 50-82% and 28-74% respectively, following two different processing routes classified as route A and route B.

Porous sheets processed by route A achieved a thermal transmittance and dimensionless Nu as high as 4.4 W/K and 494.7 W/K respectively on a CHS at Re = 486, but achieved 1.5 W/K and 393.2 on a FHS at Re = 1,069. While those produced by route B achieved *Tr* and Nu as high as 5.0 W/K and 562.8 on CHS at Re = 486 but obtained 1.6 W/K and 430.7 on FHS at Re = 1,069. This result shows that porous sheets produced by route B outperformed those produced by route A. The main reason for a better performance was due to their structural parameters especially the pore distribution, as well as volumetric and surface porosity, and surface roughness. The route B porous sheets outperformed route A sheets on either of the heating systems; CHS and FHS.

In comparison with commercial products and some of the promising porous heat sinks obtained from the literature, the double-layered porous copper produced in this work performs very well and has promising aspects

CHAPTER 7: CONCLUSIONS AND FUTURE WORK

This chapter gives an overview of the most significant findings of the work and the potential future direction of this study.

11.1 Conclusions

1. Thin sheets of porous copper heatsink with a double-layered structure were successfully produced by LCS applied to tape casting. The double-layered structure consists of a thin porous layer of copper, integrated with a dense Cu substrate. Structural parameters of the porous Cu such as pore shape and distribution, surface porosity and volumetric porosity were controlled by addition of 0 - 50 wt.% leachable K_2CO_3 space holder during processing. Two processing routes were introduced in this study: processing route A and B. Both processing routes were introduced to alter the structural properties of the porous Cu samples. For processing-route A, addition of 0 – 50 wt.% K_2CO_3 increased surface porosity from 28.3% to 60.3% and volumetric porosity from 50.7% to 80.5%. It also achieved a density decrease in the range of 4.46 to 1.75 g/cm^3. Porous sheets produced following processing route B achieved surface porosity and volumetric porosity ranging from 28.3% to 73.6% and 50.7% to 81.54% respectively. Both types of porosities increased with addition of carbonate space holder in the range of 0 – 50 wt.% K_2CO_3. The porous sheets achieved a density decrease of 4.46 g/cm^3 to 1.65 g/cm^3 and thickness that ranged between 0.74 mm and 1.61 mm.

2. After carrying out some elemental composition analysis on porous Cu samples by XRD analysis, Raman spectrometry and EDS analysis, XRD analysis could not discern any oxidation on the porous Cu samples investigated, instead only Cu was observed across all samples. However, Raman spectrometry indicated some CuO and Cu_2O which appeared across all samples. EDX analysis further confirmed the presence of CuO where Cu and O elements were reflected. It could be concluded that the porous samples produced in this study were not entirely pure, at least at the surface. Oxidation might have occurred on the samples, and a slight carbon contamination which might have resulted from organic binders and K_2CO_3.
3. An attempt to perform surface roughness measurements on porous copper using a contourGT profiler was unsuccessful. However, an image analysis approach was employed to carry out these measurements. The results showed that roughness of the sample increased with the amount of the K_2CO_3 space holder added during processing of the sample, of which 50CuPA and 50CuPB recorded the highest R_a values of 1.21mm and 1.03 mm respectively. While the 0CuP sheets with the lowest porosity achieved R_a value of 0.03mm
4. The porous samples were also taken through some simple three-point bending tests, as well as the modified three-point bending test where the loading platens with a varying diameter were employed to bend the sample. From the investigation, the flexural modulus and flexural strength increases with decreasing surface porosity and volumetric (or bulk) porosity of the sample. The sample with the lowest porosity, 0CuP, achieved the highest flexural modulus and ultimate tensile strength of 852 GPa and 29.3 MPa respectively, while 50CuPA and 50CuPB with the highest surface and volumetric porosity among the samples investigated here achieved a flexural modulus of 51.7 GPa and 22.2 GPa, and a UTS of 1.63 MPa and 0.83 MPa respectively.

After three-point bending tests using loading noses with diameters in the range of 38 – 76.2 mm, 0CuP was able to bend around loading noses with diameters in the range of 38 – 76.2 mm, while 10CuPA and 30CuPA was able to bend around loading noses of diameters greater or equal to 63.5 mm ($\varnothing \geq 63.5$ mm). But 50CuPA samples showed some signs of failure when bent using loading noses of diameters greater or equal to 63.5 mm ($\varnothing \geq 76.2$ mm).

5. The double-layered porous Cu sheets produced in this study was investigated for heat transfer performance using an open-circuit heat transfer rig developed inhouse. The study demonstrates that introduction of a porous layer that has a volumetric porosity ranging from 50% to 82% improves the thermal transmittance. Route A porous sheets with volumetric porosity in the ranges of 50% and 81% and surface roughness values (R_a) in the range of 0.03 mm to 1.16 mm achieved a thermal transmittance in the range of 3.09 W/K and 4.39 W/K and a Nu of 347.8 and 494.7 at Re of 486 when evaluated on a CHS. However, the same porous sheets were tested on a FHS system and achieved a *Tr* in the range of 1.05 W/K to 1.51 W/K for route A sheets, while route B sheets achieved *Tr* ranging from 1.05 W/K and 1.56 W/K when evaluated at *Re* = 1,069. Porous copper tapes produced here, obtained higher thermal transmittance not only from higher porosities but also from higher surface roughness which was introduced onto the sample surface during processing as a secondary effect of the incorporation of pores.

The tapes from route B achieved higher thermal transmittance compared to the tapes produced by route A due to their high surface porosity of 74% while tapes from route A have only 60%. Not only high porosities are achieved on the tapes, but also, a reasonably elevated surface roughness which contributes to the heat transfer. This type of porous tape has the potential to be used in compact devices and situations where the space is limited because such structures can be achieved at thicknesses down to 0.74 mm by this process.

The tapes have the capability to be bended around curved surfaces which therefore widens their functionality.

11.2 Future work

1. Dendritic copper powder (d ≈ 50 μm) was selected and used in the production of the porous samples in this research. However, some researchers have proven that components made from spherical copper powder tends to transfer heat better when compared to components made from dendritic or irregular copper powder due to higher permeability and capillary speed [26]. Therefore, further work is suggested in understanding the effect of copper powder in the heat transfer performance and mechanical properties of the porous copper sheets produced.
2. In this study, only K_2CO_3 was employed as a space holder to generate the pores within the component. However, the melting point of K_2CO_3 is 891 °C, which is on the lower side as far as the sintering temperature of pure copper powder is concerned. In this work, all samples were sintered at 890 °C due to the space holder employed; at this sintering temperature some parts of the carbonate have already started melting (≈ 5% of K_2CO_3) as shown in the thermo-gravimetrical analysis presented in section 3.1.5 and 6.1.3. However, 'decomposition of K_2CO_3' is another route which is usually employed to remove the space holder from the sintered metal matrix at higher temperatures than the melting point ($T_{Sintering} \geq 891°C$) of the K_2CO_3 space holder. This is another alternative of removing the space holder from the space holders which could be trialled if a higher sintering temperature is required. Further work is suggested in understanding effects of sintering copper powder at a much higher temperature than 890 °C, where such a technique of removing the space holder from the sintered matrix would be needed.

3. In addition, the pore size in the range of 30 – 790 μm was generated by introduction of the carbonate space holders of particle size in the range of 360 - 890 μm. However, pore size is known to affect the permeability of a porous medium in general, which could therefore affect the heat transfer capabilities of the component. A similar study was performed by Ref. [75] on porous copper where the samples with pore size in the range of 425 – 710μm outperformed those in the pore size range of 150 – 250μm and 1,000 – 1,500μm. Further work is suggested in understanding the effect of pore size, not only from the carbonate space holder but other space holders on the functional and mechanical properties hence affecting the heat transfer capabilities of the porous sheets.
4. Tape casting provides the flexibility to directly control thickness of the green sheets during processing as already discussed in the literature review presented in section 4.3. In this work, the capability of the equipment was not fully explored because the thickness of the sheets was kept constant throughout the research. The difference in the thickness across the porous sheets was due to shrinkage. Therefore, further work is suggested in understanding the effects of shrinkage on the thickness of the porous sheets and how the thickness of the sintered porous sheet could be accurately achieved.
5. Ductility plays a major role in the bending properties of the porous sheets produced in this study. However, heat treatment (e.g. annealing) is well known to enhance ductility in the porous or dense structure of the copper component. Based on the few trials of annealing performed on the porous samples produced in this work, ductility could be affected as expected. Further work is suggested to understand the effects of heat treatment of the final component and how the bending properties could be positively affected.

References

[1] R. Goodall and A. Mortensen, “24 – Porous Metals,” in *Physical Metallurgy*, 2014, pp. 2399–2595.

[2] J. Banhart, “Manufacture, characterisation and application of cellular metals and metal foams,” *Prog. Mater. Sci.*, vol. 46, no. 6, pp. 559–632, 2001.

[3] J. Banhart, “Manufacturing routes for metallic foams,” *JOM*, vol. 52, no. 12, pp. 22–27, 2000.

[4] B. L. Lefebvre, J. Banhart, and D. C. Dunand, “Porous Metals and Metallic Foams : Current Status and Recent Developments **,” vol. 10, no. 9, pp. 775–787, 2008.

[5] B. Zhao, A. K. Gain, W. Ding, L. Zhang, X. Li, and Y. Fu, “A review on metallic porous materials: pore formation, mechanical properties, and their applications,” *Int. J. Adv. Manuf. Technol.*, pp. 2641–2659, 2017.

[6] G. J. Davies and S. Zhen, “Metallic foams: their production, properties and applications,” *J. Mater. Sci.*, vol. 18, no. 7, pp. 1899–1911, 1983.

[7] L. J. Gibson, “Mechanical behavior of metallic foams,” *Annu. Rev. Mater. Res.*, vol. 30, no. 1, pp. 191–227, 2000.

[8] W. Yuan, Y. Tang, X. Yang, B. Liu, and Z. Wan, “Manufacture, characterization and application of porous metal-fiber sintered felt used as mass-transfer controlling medium for direct methanol fuel cells,” *Trans. Nonferrous Met. Soc. China*, vol. 23, no. 7, pp. 2085–2093, Jul. 2013.

[9] A. M. Parvanian, M. Saadatfar, M. Panjepour, A. Kingston, and A. P. Sheppard, “The effects of manufacturing parameters on geometrical and mechanical properties of copper foams produced by space holder technique,” *Mater. Des.*, vol. 53, pp. 681–690, 2014.

[10] K. K. Bodla, S. V. Garimella, and J. Y. Murthy, “3D reconstruction and design of porous media from thin sections,” *Int. J. Heat Mass Transf.*, vol. 73, pp. 250–264, 2014.

[11] K. Boomsma, D. Poulikakos, and F. Zwick, “Metal foams as compact high performance heat exchangers,” *Mech. Mater.*, vol. 35, no. 12, pp. 1161–1176, 2003.

[12] G. Kavei and K. Ahmadi, “Processing of aluminium foams using NaCl powder with controlled particle size and studying the microstructural and mechanical properties of

the foams," *Spec. Top. Rev. Porous Media - An Int. J.*, vol. 1, no. 4, pp. 337–344, 2010.

[13] P. M. Kamath, C. Balaji, and S. P. Venkateshan, "Convection heat transfer from aluminium and copper foams in a vertical channel - An experimental study," *Int. J. Therm. Sci.*, vol. 64, pp. 1–10, 2013.

[14] X. Liu, Y. Li, and Y. He, "Fabrication of High-Porosity Lotus-Type Porous Aluminum in Vacuum," *Metall. Mater. Trans. A Phys. Metall. Mater. Sci.*, vol. 48, no. 3, pp. 1264–1272, 2017.

[15] A. Hassani, A. Habibolahzadeh, and H. Bafti, "Production of graded aluminum foams via powder space holder technique," *Mater. Des.*, vol. 40, pp. 510–515, 2012.

[16] H. Bafti and A. Habibolahzadeh, "Production of aluminum foam by spherical carbamide space holder technique-processing parameters," *Mater. Des.*, vol. 31, no. 9, pp. 4122–4129, 2010.

[17] S.-S. Hsieh, R.-Y. Lee, J.-C. Shyu, and S.-W. Chen, "Thermal performance of flat vapor chamber heat spreader," *Energy Convers. Manag.*, vol. 49, no. 6, pp. 1774–1784, 2008.

[18] T. Schubert, Ł. Ciupiński, W. Zieliński, A. Michalski, T. Weißgärber, and B. Kieback, "Interfacial characterization of Cu/diamond composites prepared by powder metallurgy for heat sink applications," *Scr. Mater.*, vol. 58, no. 4, pp. 263–266, 2008.

[19] A. L. Moore and L. Shi, "Emerging challenges and materials for thermal management of electronics," *Mater. Today*, vol. 17, no. 4, pp. 163–174, 2014.

[20] H. Chiba, T. Ogushi, S. Ueno, and H. Nakajima, "Heat Transfer Capacity of Lotus-Type Porous Copper Heat Sink for Air Cooling," *J. Therm. Sci. Technol.*, vol. 5, no. 2, pp. 222–236, 2010.

[21] T. Ogushi, H. Chiba, and H. Nakajima, "Development of Lotus-Type Porous Copper Heat Sink," *Mater. Trans.*, vol. 47, no. 9, pp. 2240–2247, 2006.

[22] S. C. Wong, K. C. Hsieh, J. Da Wu, and W. L. Han, "A novel vapor chamber and its performance," *Int. J. Heat Mass Transf.*, vol. 53, no. 11–12, pp. 2377–2384, 2010.

[23] M. S. El-Genk, H. H. Saber, and J. L. Parker, "Efficient spreaders for cooling high-power computer chips," *Appl. Therm. Eng.*, vol. 27, no. 5–6, pp. 1072–1088, 2007.

[24] T. E. Tsai, H. H. Wu, C. C. Chang, and S. L. Chen, "Two-phase closed thermosyphon vapor-chamber system for electronic cooling," *Int. Commun. Heat Mass Transf.*, vol. 37, no. 5, pp. 484–489, 2010.

[25] S. Xie and J. R. G. Evans, "High porosity copper foam," *J. Mater. Sci.*, vol. 39, no. 18, pp. 5877–5880, 2004.

[26] Y.-J. Lin and K.-S. Hwang, “Effects of Powder Shape and Processing Parameters on Heat Dissipation of Heat Pipes with Sintered Porous Wicks,” *Mater. Trans.*, vol. 50, no. 10, pp. 2427–2434, 2009.

[27] Y. Y. Zhao, T. Fung, L. P. Zhang, and F. L. Zhang, “Lost carbonate sintering process for manufacturing metal foams,” *Scr. Mater.*, vol. 52, no. 4, pp. 295–298, 2005.

[28] P. M. Shahzeydi Hosein Mohammad, “Production and Characterization of Highly Porous Copper Foams Synthesized By Sodium Carbonate Space Holder,” pp. 90–95, 2013.

[29] Versarien Technologies LTD, “Passive Heat sinks,” *Versarien Technologies*, 2015. [Online]. Available: http://www.versarien-technologies.co.uk/passive-heat-sinks. [Accessed: 05-Aug-2018].

[30] R. K. Nishihora, P. L. Rachadel, M. G. N. Quadri, and D. Hotza, “Manufacturing porous ceramic materials by tape casting—A review,” *J. Eur. Ceram. Soc.*, vol. 38, no. 4, pp. 988–1001, 2018.

[31] D. Hotza and P. Greil, “Review: aqueous tape casting of ceramic powders,” *Mater. Sci. Eng. A*, vol. 202, no. 1–2, pp. 206–217, Nov. 1995.

[32] L. Ren, X. Luo, and H. Zhou, “The tape casting process for manufacturing low-temperature co-fired ceramic green sheets: A review,” *J. Am. Ceram. Soc.*, vol. 101, no. 9, pp. 3874–3889, 2018.

[33] K. P. Plucknett, C. H. Cáceres, and D. S. Willinson, “Tape Casting of Fine Alumina/Zirconia Powders for Composite Fabrication,” *J. Am. Ceram. Soc.*, vol. 77, no. 8, pp. 2137–2144, 1994.

[34] J. Koong, K. Sun, D. Zhou, J. Qiao, and J. Li, “Anode-Supported IT- SOFC anode Prepared by Tape CastingTechnique,” in *2006 International Forum on Strategic Technology*, 2006, pp. 186–189.

[35] K. G. V. Kumari, K. Sasidharan, M. Sapna, and R. Natarajan, “Dispersion and rheological studies of Y-PSZ tape casting slurry,” *Bull. Mater. Sci.*, vol. 28, no. 2, pp. 103–108, 2005.

[36] Y. Tang, S. Qiu, M. Li, and K. Zhao, “Fabrication of alumina/copper heat dissipation substrates by freeze tape casting and melt infiltration for high-power LED,” *J. Alloys Compd.*, vol. 690, pp. 469–477, 2017.

[37] T. Guillemet, J. F. Silvain, J. M. Heintz, N. Chandra, and Y. F. Lu, “Fabrication By Tape Casting and Hot Pressing of Copper Diamond Composite Films,” *Composites*, pp. 1–5, 2011.

[38] P. M. Geffroy, T. Chartier, and J. F. Silvain, “Preparation by tape casting and hot pressing of copper carbon composites films,” *J. Eur. Ceram. Soc.*, vol. 27, no. 1, pp. 291–299, 2007.

[39] P. Geffroy, J. Silvain, and J. Heintz, “Elaboration and Properties of Carbon Fibre Reinforced Copper Matrix Composites,” *Adv. Compos. Mater. - Ecodesign Anal. Dr. Brahim Attaf (Ed.), ISBN 978-953-307-15*, 2011.

[40] M. Cans, H. Hamdam, Y. Öner, and J. Bidaux, “Tape Casting of Copper Alloys for Tribological Applications,” *Euro PM2008 - Adv. Powder Metall.*, no. October, pp. 27–32, 2015.

[41] J. Bidaux, H. Girard, V. Sonney, and H. Hamdan, “Tape Casting of Copper Based Shape-Memory Alloys,” in *European Powder Metallurgy Conference, Euro PM2009*, 2009, vol. 1, pp. 371–376.

[42] J. Ru, B. Kong, H. Zhu, Z. Shi, and D. Z. Tongxiang Fan, “Microstructure, capillary performance and gas permeability of biporous copper fabricated by tape casting,” *Powder Technol.*, vol. 256, pp. 182–187, Apr. 2014.

[43] L. P. Lefebvre, J. Banhart, and D. C. Dunand, “Porous metals and metallic foams: Current status and recent developments,” *Adv. Eng. Mater.*, vol. 10, no. 9, pp. 775–787, 2008.

[44] S. Singh, “A survey of fabrication and application of metallic foams (1925–2017),” *J. Porous Mater.*, vol. 25, pp. 537–554, 2018.

[45] P. Colombo and H. P. Degischer, “Highly porous metals and ceramics,” *Mater. Sci. Technol.*, vol. 26, no. 10, pp. 1145–1158, 2010.

[46] J. M. Baloyo, “Open-cell porous metals for thermal management applications: fluid flow and heat transfer,” *Mater. Sci. Technol. (United Kingdom)*, vol. 33, no. 3, pp. 265–276, 2017.

[47] J. Banhart, “Metallic foams : challenges and opportunities,” in *Eurofoam2000*, 2000, pp. 13–20.

[48] A. Muley, C. Kiser, B. Sundén, and R. K. Shah, “Foam heat exchangers: A technology assessment,” *Heat Transf. Eng.*, vol. 33, no. 1, pp. 42–51, 2012.

[49] X.-H. Han, Q. Wang, Y.-G. Park, C. T’Joen, A. Sommers, and A. Jacobi, “A Review of Metal Foam and Metal Matrix Composites for Heat Exchangers and Heat Sinks,” *Heat Transf. Eng.*, vol. 33, no. 12, pp. 991–1009, 2012.

[50] S. H. N. G. Queheillalt Douglas T, Sypeck David J, “Ultrasonic characterization of cellular metal structures,” *Mater. Sci. Eng. A323*, pp. 138–147, 2002.

[51] B. Mansoor, H. Nassar, V. C. Shunmugasamy, and M. K. Khraisheish, “Three dimensional forming of compressed open-cell metallic foams at elevated temperatures,” *Mater. Sci. Eng. A*, vol. 628, pp. 433–441, 2015.

[52] Y. Conde *et al.*, “Replication Processing of Highly Porous Materials,” *Adv. Eng. Mater.*, vol. 8, no. 9, pp. 795–803, 2006.

[53] S. Asavavisithchai, E. Nisaratanaporn, and Y. Boonyongmaneerat, “A Novel Method to Produce Silver Foams with Multi- level Porosities,” *Chiang Mai J. Sci.*, vol. 36, no. 3, pp. 296–301, 2009.

[54] A. Jinnapat and A. Kennedy, “The Manufacture and Characterisation of Aluminium Foams Made by Investment Casting Using Dissolvable Spherical Sodium Chloride Bead Preforms,” *Metals (Basel).*, vol. 1, no. 1, pp. 49–64, 2011.

[55] Y. Y. Zhao and D. X. Sun, “A Novel Sintering Dissolution Process for Manufacturing Al Foams,” *Scr. Mater.*, vol. 44, no. 44(1), p. 105–110., 2001.

[56] A. Moloodi and R. Raiszadeh, “Fabricating Al foam from turning scraps,” *Mater. Manuf. Process.*, vol. 26, no. 7, pp. 890–896, 2011.

[57] D. X. Sun and Y. Y. Zhao, “Phase changes in sintering of Al/Mg/NaCl compacts for manufacturing Al foams by the sintering and dissolution process,” *Mater. Lett.*, vol. 59, no. 1, pp. 6–10, 2005.

[58] M. Hakamada, Y. Yamada, T. Nomura, Y. Chen, H. Kusuda, and M. Mabuchi, “Fabrication of Porous Aluminum by Spacer Method Consisting of Spark Plasma Sintering and Sodium Chloride Dissolution,” *Mater. Trans.*, vol. 46, no. 12, pp. 2624–2628, 2005.

[59] B. Jiang, N. Q. Zhao, C. S. Shi, X. W. Du, J. J. Li, and H. C. Man, “A novel method for making open cell aluminum foams by powder sintering process,” *Mater. Lett.*, vol. 59, no. 26, pp. 3333–3336, 2005.

[60] B. Jiang, N. Q. Zhao, C. S. Shi, and J. J. Li, “Processing of open cell aluminum foams with tailored porous morphology,” *Scr. Mater.*, vol. 53, no. 6, pp. 781–783, 2005.

[61] S. Asavavisithchai, N. Itthipornkul, and K. Eamsard, “ScienceDirect Production of open-cell Al composite foams by direct casting with silica-gel beads,” *Mater. Today Proc.*, vol. 5, no. 3, pp. 9506–9511, 2018.

[62] K. Sen Chou and M. A. Song, “A novel method for making open-cell aluminum foams with soft ceramic balls,” *Scr. Mater.*, vol. 46, no. 5, pp. 379–382, 2002.

[63] Y. Zhao, F. Han, and T. Fung, “Optimisation of compaction and liquid-state sintering in sintering and dissolution process for manufacturing A1 foams,” *Mater. Sci. Eng. A*,

vol. 364, no. 1–2, pp. 117–125, 2004.

[64] C. E. Wen *et al.*, "Processing of fine-grained aluminum foam by spark plasma sintering," *J. Mater. Sci. Lett.*, vol. 22, no. 20, pp. 1407–1409, 2003.

[65] Y. Chen *et al.*, "Manufacturing of graded titanium scaffolds using a novel space holder technique," *Bioact. Mater.*, vol. 2, pp. 248–252, 2017.

[66] N. Jha, D. P. Mondal, J. Dutta Majumdar, A. Badkul, A. K. Jha, and A. K. Khare, "Highly porous open cell Ti-foam using NaCl as temporary space holder through powder metallurgy route," *Mater. Des.*, vol. 47, pp. 810–819, 2013.

[67] M. M. Shbeh and R. Goodall, "Open pore titanium foams via metal injection molding of metal powder with a space holder," *Met. Powder Rep.*, vol. 71, no. 6, pp. 450–455, 2016.

[68] P. M. Shahzeydi Hosein Mohammad, "Production and charactirization of hihly porous copper foams synthesized by sodium carbonate space holder," pp. 90–95, 2013.

[69] L. P. Zhang and Y. Y. Zhao, "Fabrication of high melting-point porous metals by lost carbonate sintering process via decomposition route," *Proc. Inst. Mech. Eng. Part B J. Eng. Manuf.*, vol. 222, no. 2, pp. 267–271, 2008.

[70] Y. Zhao and L. E. Monaghan, "A novel manufacturing method for titanium foam for biomedical applications," in *Proceedings of the 2008 World congress on powder metallurgy and particulate materials*, 2008, pp. 340–348.

[71] S. Harjanto and F. Ika, "Copper Foam Manufacturing by the Process of Powder Metallurgy and Dissolution of Carbonates."

[72] D. J. Thewsey and Y. Y. Zhao, "Thermal conductivity of porous copper manufactured by the lost carbonate sintering process," *Phys. Status Solidi Appl. Mater. Sci.*, vol. 205, no. 5, pp. 1126–1131, 2008.

[73] Z. Xiao, "Heat transfer , fluid transport and mechanical properties of porous copper manufactured by Lost Carbonate Sintering," University of Liverpool, 2013.

[74] A. M. Parvanian and M. Panjepour, "Mechanical behavior improvement of open-pore copper foams synthesized through space holder technique," *Mater. Des.*, vol. 49, pp. 834–841, 2013.

[75] L. Zhang, D. Mullen, K. Lynn, and Y. Zhao, "Heat Transfer Performance of Porous Copper Fabricated by the Lost Carnonate Sintering Process," *Mater. Res. Soc. Symp. Proc.*, vol. 1188, 2009.

[76] A. M. Parvanian and M. Panjepour, "Development of Open Pore Copper Foams to Use as Bipolar Plates in Polymer Electrolyte Membrane Fuel Cell Stacks," *Iran. J. Energy*

Environ., vol. 4, no. 2, pp. 99–103, 2013.

[77] A. Kennedy, "Porous Metals and Metal Foams Made from Powders," in *Powder Metallurgy*, K. Kondoh, Ed. Rijeka: IntechOpen, 2012.

[78] C. Y. Zhao, W. Lu, and S. A. Tassou, "Thermal analysis on metal-foam filled heat exchangers. Part II: Tube heat exchangers," *Int. J. Heat Mass Transf.*, vol. 49, no. 15, pp. 2762–2770, 2006.

[79] W. Zhou *et al.*, "Characterization of three- and four-point bending properties of porous metal fiber sintered sheet," *Mater. Des.*, vol. 56, pp. 522–527, 2014.

[80] J. Kerns, "Powder-Metallurgy Process," *Informa - Machine Design*, 2016. [Online]. Available: https://www.machinedesign.com/metals/powder-metallurgy-processes. [Accessed: 04-Apr-2019].

[81] D. A. Ramirez *et al.*, "Open-cellular copper structures fabricated by additive manufacturing using electron beam melting," *Mater. Sci. Eng. A*, vol. 528, no. 16–17, pp. 5379–5386, 2011.

[82] M. A. Lodes, R. Guschlbauer, and C. Körner, "Process development for the manufacturing of 99.94% pure copper via selective electron beam melting," *Mater. Lett.*, vol. 143, pp. 298–301, 2015.

[83] M. R. Sriraman, S. S. Babu, and M. Short, "Bonding characteristics during very high power ultrasonic additive manufacturing of copper," *Scr. Mater.*, vol. 62, no. 8, pp. 560–563, 2010.

[84] Q. Xu, *Nanoporous Materials; Synthesis and Applications*. Osaka: CRC Press, 2013.

[85] M. Li, Y. Zhou, and H. Geng, "Fabrication of nanoporous copper ribbons by dealloying of Al-Cu alloys," *J. Porous Mater.*, vol. 19, no. 5, pp. 791–796, 2012.

[86] Z. Dan, F. Qin, A. Makino, Y. Sugawara, I. Muto, and N. Hara, "Fabrication of nanoporous copper by dealloying of amorphous Ti–Cu–Ag alloys," *J. Alloys Compd.*, vol. 586, pp. S134–S138, 2014.

[87] Z. Dan, F. Qin, Y. Sugawara, I. Muto, A. Makino, and N. Hara, "Nickel-stabilized nanoporous copper fabricated from ternary TiCuNi amorphous alloys," *Mater. Lett.*, vol. 94, pp. 128–131, 2013.

[88] Y. Xu *et al.*, "A strategy for fabricating nanoporous gold films through chemical dealloying of electrochemically deposited Au-Sn alloys," *Nanotechnology*, vol. 25, no. 44, p. 445602, 2014.

[89] M. Li, H. Geng, Y. Zhou, and L. Ding, "Fabrication of nanoporous copper ribbons by dealloying of Mn 70Cu30 alloy and fractal characterization of their porosity," *Rev.*

Adv. Mater. Sci., vol. 33, no. 1, pp. 56–60, 2013.

[90] A. H. Brothers and J. Banhart, "Verfahren zur Herstellung eines Metallmatrix-Nanoverbundwerkstoffes, Metallmatrix-Nano- verbundwerkstoff und seine Anwendung," 2007.

[91] K. Heim, G. S. Vinod-Kumar, F. García-Moreno, and J. Banhart, "Stability of various particle-stabilised aluminium alloys foams made by gas injection," *J. Mater. Sci.*, vol. 52, no. 11, pp. 6401–6414, 2017.

[92] K. Heim, G. S. Vinod-Kumar, F. García-Moreno, A. Rack, and J. Banhart, "Stabilisation of aluminium foams and films by the joint action of dispersed particles and oxide films," *Acta Mater.*, vol. 99, pp. 313–324, 2015.

[93] S. C. Tzeng and W. P. Ma, "A novel approach to the manufacturing and experimental investigation of closed-cell Al foams," *Int. J. Adv. Manuf. Technol.*, vol. 32, no. 5–6, pp. 473–479, 2007.

[94] M. Shiomi and T. Fukaya, "Forming of aluminum foams by using rotating mold," *Procedia Eng.*, vol. 81, no. October, pp. 664–669, 2014.

[95] M. Shiomi, S. Imagama, K. Osakada, and R. Matsumoto, "Fabrication of aluminium foams from powder by hot extrusion and foaming," *J. Mater. Process. Technol.*, vol. 210, no. 9, pp. 1203–1208, 2010.

[96] T. Shi, X. Chen, Y. Cheng, and Y. Li, "Foaming Process and Properties of 6063 Aluminum Foams by Melt Foaming Method," *Mater. Trans.*, vol. 58, no. 2, pp. 243–248, 2017.

[97] A. Uzun and M. Turker, "The effect of production parameters on the foaming behavior of spherical-shaped aluminum foam," *Mater. Res.*, vol. 17, no. 2, pp. 311–315, 2014.

[98] M. F. Ashby, A. Evans, N. A. Fleck, L. J. Gibson, J. W. Hutchinson, and N. G. Hayden, "Book reviews," pp. 119–120, 2002.

[99] M. F. Ashby, A. Evans, N. A. Fleck, L. J. Gibson, J. W. Hutchinson, and N. G. Hayden, "Chapter 2 - Making metal foams," M. F. Ashby, A. G. Evans, N. A. Fleck, L. J. Gibson, J. W. Hutchinson, and H. N. G. B. T.-M. F. Wadley, Eds. Burlington: Butterworth-Heinemann, 2000, pp. 6–23.

[100] V. Rajput, D. P. Mondal, S. Das, N. Ramakrishnan, and A. K. Jha, "Effect of SiCp addition on age-hardening of aluminium composite and closed cell aluminium composite foam," *J. Mater. Sci.*, vol. 42, no. 17, pp. 7408–7414, 2007.

[101] T. Fukui, Y. Nonaka, and S. Suzuki, "Fabrication of Al-Cu-Mg Alloy Foams Using Mg as Thickener through Melt Route and Reinforcement of Cell Walls by Heat

Treatment," *Procedia Mater. Sci.*, vol. 4, pp. 33–37, 2014.

[102] M. A. De Meller, "Produit métallique pour l'obtention d'objets laminés, moulés ou autres, et procédés pour sa fabrication," 147, 1925.

[103] A. Byakova, S. Gnyloskurenko, and T. Nakamura, "The Role of Foaming Agent and Processing Route in the Mechanical Performance of Fabricated Aluminum Foams," *Metals (Basel).*, vol. 2, no. 2, pp. 95–112, 2012.

[104] A. Byakova, I. Kartuzov, S. Gnyloskurenko, and T. Nakamura, "The role of foaming agent and processing route in mechanical performance of fabricated aluminum foams," *Adv. Mater. Sci. Eng.*, vol. 2014, pp. 109–114, 2014.

[105] D. P. Papadopoulos, H. Omar, F. Stergioudi, S. A. Tsipas, H. Lefakis, and N. Michailidis, "A novel method for producing Al-foams and evaluation of their compression behavior," *J. Porous Mater.*, vol. 17, no. 6, pp. 773–777, 2010.

[106] M. Z. Li, G. Stephani, and K. J. Kang, "New cellular metals with enhanced energy absorption: Wire-woven bulk kagome (WBK)-metal hollow sphere (MHS) hybrids," *Adv. Eng. Mater.*, vol. 13, no. 1–2, pp. 33–37, 2011.

[107] C. Augustin and W. Hungerbach, "Production of hollow spheres (HS) and hollow sphere structures (HSS)," *Mater. Lett.*, vol. 63, no. 13–14, pp. 1109–1112, 2009.

[108] O. Friedl, C. Motz, H. Peterlik, S. Puchegger, N. Reger, and R. Pippan, "Experimental investigation of mechanical properties of metallic hollow sphere structures," *Metall. Mater. Trans. B Process Metall. Mater. Process. Sci.*, vol. 39, no. 1, pp. 135–146, 2008.

[109] B. Neirinck, J. Fransaer, O. Van der Biest, and J. Vleugels, "A novel route to produce porous ceramics," *J. Eur. Ceram. Soc.*, vol. 29, no. 5, pp. 833–836, 2009.

[110] J. Luyten, S. Mullens, J. Cooymans, A. M. De Wilde, I. Thijs, and R. Kemps, "Different methods to synthesize ceramic foams," *J. Eur. Ceram. Soc.*, vol. 29, no. 5, pp. 829–832, 2009.

[111] A. H. Brothers, D. C. Dunand, Q. Zheng, and J. Xu, "Amorphous Mg-based metal foams with ductile hollow spheres," *J. Appl. Phys.*, vol. 102, no. 2, 2007.

[112] P. Yu and M. Qian, "Metal injection moulding of in-situ formed AlN hollow sphere reinforced Al matrix syntactic foam parts," *Mater. Chem. Phys.*, vol. 137, no. 2, pp. 435–438, 2012.

[113] J. A. Santa Maria, B. F. Schultz, J. B. Ferguson, and P. K. Rohatgi, "Al-Al2O3 syntactic foams - Part I: Effect of matrix strength and hollow sphere size on the quasi-static properties of Al-A206/Al2O3 syntactic foams," *Mater. Sci. Eng. A*, vol. 582, pp.

415–422, 2013.

[114] B. Katona, G. Szebényi, and I. N. Orbulov, “Fatigue properties of ceramic hollow sphere filled aluminium matrix syntactic foams,” *Mater. Sci. Eng. A*, vol. 679, pp. 350–357, 2017.

[115] Y. Liu, H. X. Wu, and B. Wang, “Gradient design of metal hollow sphere (MHS) foams with density gradients,” *Compos. Part B Eng.*, vol. 43, no. 3, pp. 1346–1352, 2012.

[116] K. Kornei, “New Aluminum ‘Foam’ Makes Trains Stronger, Lighter, and Safer,” 2014. [Online]. Available: https://www.wired.com/2014/12/aluminum-foam-trains/. [Accessed: 15-Aug-2018].

[117] J. Banhart and H. Seeliger, “Recent Trends in Aluminium Foam Sandwich Technology Industrial Implementation of AFS Technology,” *Adv. Eng. Mater. Montpellier*, pp. 1–13, 2011.

[118] H. Luo, H. Lin, Z. Zhao, Y. Liu, and G. Yao, “Preparation of Aluminum Foam Sandwich Reinforced by Steel Sheets,” *Procedia Mater. Sci.*, vol. 4, no. 2008, pp. 39–43, 2014.

[119] Y. Wang, X. Ren, H. Hou, Y. Zhang, and W. Yan, “Processing and pore structure of aluminium foam sandwich,” *Powder Technol.*, vol. 275, pp. 344–350, 2015.

[120] J. Banhart and H. W. Seeliger, “Aluminium Foam Sandwich Panels: Metallurgy, Manufacture and Applications,” *Helmholtz-Berlin.De*, vol. sdfdsf, pp. 4–7, 1996.

[121] Y. Liu, H. F. Chen, H. W. Zhang, and Y. X. Li, “Heat transfer performance of lotus-type porous copper heat sink with liquid GaInSn coolant,” *Int. J. Heat Mass Transf.*, vol. 80, pp. 605–613, 2015.

[122] P.-M. Geffroy, T. Chartier, and J.-F. Silvain, “Innovative Approach to Metal Matrix Composites Film by Tape Casting Process,” *Adv. Eng. Mater.*, vol. 9, no. 7, pp. 547–553, 2007.

[123] Y. Tang, S. Qiu, M. Li, and K. Zhao, “Fabrication of alumina/copper heat dissipation substrates by freeze tape casting and melt infiltration for high-power LED,” *J. Alloys Compd.*, vol. 690, pp. 469–477, 2017.

[124] S. F. Corbin, X. Zhao-jie, H. Henein, and P. S. Apte, “Functionally graded metal/ceramic composites by tape casting, lamination and infiltration,” *Mater. Sci. Eng. A*, vol. 262, pp. 192–203, 1999.

[125] Y. Kong, B. Hua, J. Pu, B. Chi, and L. Jian, “A cost-effective process for fabrication of metal-supported solid oxide fuel cells,” *Int. J. Hydrogen Energy*, vol. 35, no. 10, pp.

4592–4596, 2010.

[126] K. Li *et al.*, “High performance ni-Fe alloy supported SOFCs fabricated by low cost tape casting-screen printing-cofiring process,” *Int. J. Hydrogen Energy*, vol. 39, no. 34, pp. 19747–19752, 2014.

[127] C. M. Lobley and Z. X. Guo, “Processing of Ti-SiC metal matrix composites by tape casting,” *Mater. Sci. Technol.*, vol. 14, no. 9–10, pp. 1024–1028, 1998.

[128] W. Liu and N. Canfield, “Development of thin porous metal sheet as micro-filtration membrane and inorganic membrane support,” *J. Memb. Sci.*, vol. 409–410, pp. 113–126, 2012.

[129] J. Li, G. Luo, Q. Shen, L. Zhang, H. Zhu, and C. Deng, “Preparation of non-aqueous Mg green tapes by tape casting,” *Synth. React. Inorganic, Met. Nano-Metal Chem.*, vol. 42, no. 5, pp. 758–763, 2012.

[130] E. Mercadelli, A. Gondolini, P. Pinasco, and A. Sanson, “Stainless steel porous substrates produced by tape casting,” *Met. Mater. Int.*, vol. 23, no. 1, pp. 184–192, 2017.

[131] R. T. Krone, L. P. Martin, J. R. Patterson, D. Orlikowski, and J. H. Nguyen, “Fabrication and characterization of graded impedance impactors for gas gun experiments from hot-pressed magnesium and polyethylene powders,” *Mater. Sci. Eng. A*, vol. 479, no. 1–2, pp. 300–305, 2008.

[132] T. Slawik *et al.*, “Metal-ceramic layered materials and composites manufactured using powder techniques,” *Adv. Eng. Mater.*, vol. 16, no. 10, pp. 1293–1302, 2014.

[133] I. Ghosh, “How Good Is Open-Cell Metal Foam as Heat Transfer Surface?,” *J. Heat Transfer*, vol. 131, no. 10, p. 101004, 2009.

[134] C. Hutter, D. B, V. Zuber, and P. R. V. R. Ã, “Heat transfer in metal foams and designed porous media,” *Chem. Eng. Sci. J.*, vol. 66, pp. 3806–3814, 2011.

[135] K. Boomsma and D. Poulikakos, “On the effective thermal conductivity of a three-dimensionally structured fluid-saturated metal foam,” *Heat Mass Transf.*, vol. 44, pp. 827–836, 2001.

[136] D. Edouard, T. Truong Huu, C. Pham Huu, F. Luck, and D. Schweich, “The effective thermal properties of solid foam beds: Experimental and estimated temperature profiles,” *Int. J. Heat Mass Transf.*, vol. 53, no. 19–20, pp. 3807–3816, 2010.

[137] K. Boomsma, D. Poulikakos, and Y. Ventikos, “Simulations of flow through open cell metal foams using an idealized periodic cell structure,” *Int. J. Heat Fluid Flow*, vol. 24, no. 6, pp. 825–834, 2003.

[138] K. Boomsma and D. Poulikakos, “The Effects of Compression and Pore Size Variations on the Liquid Flow Characteristics in Metal Foams,” *J. Fluids Eng.*, vol. 124, no. 1, p. 263, 2002.

[139] A. Bhattacharya, V. Calmidi, and R. Mahajan, “Thermophysical properties of high porosity metal foams,” *Int. J. Heat …*, vol. 45, no. June 2001, 2002.

[140] C. Y. Zhao, T. J. Lu, H. P. Hodson, and J. D. Jackson, “The temperature dependence of effective thermal conductivity of open-celled steel alloy foams,” *Mater. Sci. Eng. A*, vol. 367, no. 1–2, pp. 123–131, 2004.

[141] W. H. Shih, W. C. Chiu, and W. H. Hsieh, “Height Effect on Heat-Transfer Characteristics of Aluminum-Foam Heat Sinks,” *J. Heat Transfer*, vol. 128, no. 6, p. 530, 2006.

[142] B. I. Pavel and A. A. Mohamad, “Experimental Investigation of the Potential of Metallic Porous Inserts in Enhancing Forced Convective Heat Transfer,” *J. Heat Transfer*, vol. 126, no. 4, p. 540, 2004.

[143] F. A. L. Dullien, *Porous Media Fluids Transport and Pore Structure*. New York: Academic Press Inc, 1991.

[144] H. Mahdi, J. Lopez, A. Fuentes, and R. Jones, “Thermal performance of aluminium-foam CPU heat exchangers,” *Int. J. Energy Res.*, vol. 30, no. 11, pp. 851–860, 2006.

[145] C. Hutter, C. Allemann, S. Kuhn, and P. Rudolf von Rohr, “Scalar transport in a milli-scale metal foam reactor,” *Chem. Eng. Sci.*, vol. 65, no. 10, pp. 3169–3178, 2010.

[146] A. Bhattacharya and R. L. Mahajan, “Metal Foam and Finned Metal Foam Heat Sinks for Electronics Cooling in Buoyancy-Induced Convection,” *J. Electron. Packag.*, vol. 128, no. 3, p. 259, 2006.

[147] ERG Materials & Aerospace, “Duocel Metal, carbon, and ceraic foams can be used in many custom applications,” 2011. [Online]. Available: http://ergaerospace.com. [Accessed: 02-Aug-2018].

[148] D. U. Heinemann and Z. Bayern, “Insulation through vacuums,” *A Compact Guid. to energy Res.*, p. 20, 2011.

[149] M. Kaviany, *Principles of heat transfer in Porous Media*. New York: Springer, 1991.

[150] D. A. Nield and A. Bejan, *Convection in porous media*, Second Edi. New York: `Springer, 1999.

[151] S. Whitaker, *The method of averaging volume*. Boston: Kluwer Academic Publishers, 1999.

[152] P. Cheng and C. T. Hsu, “Heat conduction,” in *Transport phenomena in porous media*,

D. B. Ingham and I. Pop, Eds. UK: Pergamon Press, 1998, pp. 57–76.

[153] C. T. Hsu, “Heat conduction in porous media,” in *Handbook of Porous Media*, K. Vafai, Ed. New York: Marcel Dekker, 2000, pp. 171–200.

[154] T. Rodgers, “Heat Transfer 2013,” 2013.

[155] J. J. Chattot and M. M. Hafez, *Theoretical and applied aerodynamics: And related numerical methods*. Springer Science + Business Media Dordrecht, 2015.

[156] H. Schlichting and K. Gersten, “Boundary-Layer Theory,” pp. 29–50, 2017.

[157] C. Farell and S. K. Fedeniuk, “Effect of end plates on the flow around rough cylinders,” *J. Wind Eng. Ind. Aerodyn.*, vol. 28, no. 1, pp. 219–230, 1988.

[158] J. M. Corsan, “A compact thermal conductivity apparatus for good conductors,” *J. Phys. E.*, vol. 17, pp. 800–807, 1984.

[159] N. Mahjoub Said, H. Mhiri, H. Bournot, and G. Le Palec, “Experimental and numerical modelling of the three-dimensional incompressible flow behaviour in the near wake of circular cylinders,” *J. Wind Eng. Ind. Aerodyn.*, vol. 96, no. 5, pp. 471–502, 2008.

[160] M. Bahrami, “Forced Convection Heat Transfer Mechanism of Forced Convection,” vol. 388, pp. 3–11.

[161] M. P. Juniper, “Chapter 8 Handout - External Flow and Drag,” *Introd. to Fluid Dyn.*, pp. 1–11, 2015.

[162] R. S. Subramanian, “Heat transfer in Flow Through Conduits,” *Convect. tubes*, vol. 1, pp. 1–9, 2006.

[163] S. Reza-zadeh, “Investigation of fluid flow around a cylinder with EHD actuation on inclined plates behind the cylinder,” pp. 212–217, 2013.

[164] M. H. Kaffash, D. D. Ganji, and M. H. Nobakhti, “An analytical solution of turbulent boundary layer fluid flow over a flat plate at high Reynolds number,” *J. Mol. Liq.*, vol. 230, pp. 625–633, 2017.

[165] M. Sato and T. Kobayashi, “A fundamental study of the flow past a circular cylinder using Abaqus / CFD,” *SIMULIA Community Conf.*, pp. 1–15, 2012.

[166] A. Alper Ozalp and I. Dincer, “Laminar Boundary Layer Development Around a Circular Cylinder: Fluid Flow and Heat-Mass Transfer Characteristics,” *J. Heat Transfer*, vol. 132, no. 12, p. 121703, 2010.

[167] R. Merrick and G. Bitsuamlak, “Control of flow around a circular cylinder by the use of surface roughness: a computational and experimental approach,” *4th Int. Conf. Adv. Wind Struct.*, pp. 1–15, 2008.

[168] B. Dargahi, “The turbulent flow field around a circular cylinder,” *Exp. Fluids*, vol. 8,

pp. 1–12, 1989.

[169] N. Rostamy, D. Sumner, D. J. Bergstrom, and J. D. Bugg, “Local flow field of a surface-mounted finite circular cylinder,” *J. Fluids Struct.*, vol. 34, pp. 105–122, 2012.

[170] D. Sumner, N. Rostamy, D. J. Bergstrom, and J. D. Bugg, “Influence of aspect ratio on the flow above the free end of a surface-mounted finite cylinder,” *Int. J. Heat Fluid Flow*, vol. 56, pp. 290–304, 2015.

[171] F. García-Moreno, “Commercial applications of metal foams: Their properties and production,” *Materials (Basel).*, vol. 9, no. 2, pp. 20–24, 2016.

[172] Y. A. Cengel, “15 - Cooling of electronic equipment,” *Heat Transf. A Pract. Approach*, pp. 785–854, 2002.

[173] M. F. Ashby, “Metal foams: A survey,” *Sci. China Ser. B*, vol. 46, no. 6, p. 521, 2003.

[174] N. Dukhan, P. D. Quiñones-Ramos, E. Cruz-Ruiz, M. Vélez-Reyes, and E. P. Scott, “One-dimensional heat transfer analysis in open-cell 10-ppi metal foam,” *Int. J. Heat Mass Transf.*, vol. 48, no. 25–26, pp. 5112–5120, 2005.

[175] H. Chiba, T. Ogushi, S. Ueno, and H. Nakajima, “Heat Transfer Capacity of Lotus-Type Porous Copper Heat Sink for Air Cooling,” *J. Therm. Sci. Technol.*, vol. 5, no. 2, pp. 222–236, 2010.

[176] K. Muramatsu, T. Ide, H. Nakajima, and J. K. Eaton, “Heat Transfer Performance of Lotus-Type Porous Metals,” no. 44786. pp. 31–40, 2012.

[177] H. F. Chen, Y. Liu, L. T. Chen, and Y. X. Li, “Heat Transfer Performance of Lotus-Type Porous Copper Micro-Channel Heat Sink,” *Mater. Sci. Forum*, vol. 749, pp. 414–420, 2013.

[178] H. Du *et al.*, “Heat dissipation performance of porous copper with elongated cylindrical pores,” *J. Mater. Sci. Technol.*, vol. 30, no. 9, pp. 934–938, 2014.

[179] H. Zhang, L. Chen, Y. Liu, and Y. Li, “Experimental study on heat transfer performance of lotus-type porous copper heat sink,” *Int. J. Heat Mass Transf.*, vol. 56, no. 1–2, pp. 172–180, 2013.

[180] J. Schindelin *et al.*, “Fiji: an open-source platform for biological-image analysis,” *Nat Meth*, vol. 9, no. 7. Nature Publishing Group, a division of Macmillan Publishers Limited. All Rights Reserved., pp. 676–682, Jul-2012.

[181] J. Schindelin, C. T. Rueden, M. C. Hiner, and K. W. Eliceiri, “The ImageJ ecosystem: An open platform for biomedical image analysis,” *Mol. Reprod. Dev.*, vol. 82, no. 7–8, pp. 518–529, 2015.

[182] J. Bear, “Hydraulics of groundwater.” McGraw-Hill Book Co., New York, 1979.

[183] R. Goodall, “Thermomechanical Properties of Highly Porous , Fire-Resistant Materials,” 2003.

[184] L. Ventola, L. Scaltrito, S. Ferrero, G. Maccioni, E. Chiavazzo, and P. Asinari, “Micro-structured rough surfaces by laser etching for heat transfer enhancement on flush mounted heat sinks,” *J. Phys. Conf. Ser.*, vol. 525, p. 012017, 2014.

[185] L. Ventola *et al.*, “Rough surfaces with enhanced heat transfer for electronics cooling by direct metal laser sintering,” *Int. J. Heat Mass Transf.*, vol. 75, pp. 58–74, 2014.

[186] E. Chiavazzo, L. Ventola, F. Calignano, D. Manfredi, and P. Asinari, “A sensor for direct measurement of small convective heat fluxes: Validation and application to micro-structured surfaces,” *Exp. Therm. Fluid Sci.*, vol. 55, pp. 42–53, May 2014.

[187] H. Y. Li, M. H. Chiang, C. I. Lee, and W. J. Yang, “Thermal performance of plate-fin vapor chamber heat sinks,” *Int. Commun. Heat Mass Transf.*, vol. 37, no. 7, pp. 731–738, 2010.

[188] L. Ventola, E. Chiavazzo, F. Calignano, D. Manfredi, and P. Asinari, “Heat transfer enhancement by finned heat sinks with micro-structured roughness,” *J. Phys. Conf. Ser.*, vol. 494, no. 1, 2014.

[189] T. Theivasanthi and M. Alagar, “X-Ray Diffraction Studies of Copper Nanopowder,” *Arch. Phys. Res.*, vol. 1, no. 2, pp. 112–117, 2010.

[190] G. Varughese, V. Rini, S. . Suraj, and K. . Usha, “Characterisation and optical studies of copper oxide nanostructures doped with lanthanum ions,” *Adv. Mater. Sci.*, vol. 13, no. 3, pp. 17–25, 2013.

[191] N. Topnani, S. Kushwaha, and T. Athar, “Wet Synthesis of Copper Oxide Nanopowder,” *Int. J. Green Nanotechnol. Mater. Sci. Eng.*, vol. 1, no. 2, 2010.

[192] I. Z. Luna, L. N. Hilary, A. M. S. Chowdhury, M. A. Gafur, N. Khan, and R. A. Khan, “Preparation and Characterization of Copper Oxide Nanoparticles Synthesized via Chemical Precipitation Method,” *OALib*, vol. 02, no. 03, pp. 1–8, 2015.

[193] A. Chen, H. Long, X. Li, Y. Li, G. Yang, and P. Lu, “Controlled growth and characteristics of single-phase Cu2O and CuO films by pulsed laser deposition,” *Vacuum*, vol. 83, no. 6, pp. 927–930, 2009.

[194] Z. H. Gan, G. Q. Yu, B. K. Tay, C. M. Tan, Z. W. Zhao, and Y. Q. Fu, “Preparation and characterization of copper oxide thin films deposited by filtered cathodic vacuum arc,” *J. Phys. D. Appl. Phys.*, vol. 37, no. 1, pp. 81–85, 2004.

[195] T. H. Tran and V. T. Nguyen, “Phase transition of Cu2O to CuO nanocrystals by selective laser heating,” *Mater. Sci. Semicond. Process.*, vol. 46, pp. 6–9, 2016.

[196] Y. Deng, A. D. Handoko, Y. Du, S. Xi, and B. S. Yeo, "*In Situ* Raman Spectroscopy of Copper and Copper Oxide Surfaces during Electrochemical Oxygen Evolution Reaction: Identification of Cu ^{III} Oxides as Catalytically Active Species," *ACS Catal.*, vol. 6, no. 4, pp. 2473–2481, 2016.

[197] M. Rashad, M. Rüsing, G. Berth, K. Lischka, and A. Pawlis, "CuO and Co3O4 Nanoparticles : Synthesis , Characterizations , and Raman Spectroscopy," vol. 2013, 2013.

[198] V. S. Levitskii *et al.*, "Raman spectroscopy of copper oxide films deposited by reactive magnetron sputtering," *Tech. Phys. Lett.*, vol. 41, no. 11, pp. 1094–1096, 2015.

[199] S. Chen *et al.*, "Oxidation Resistance of Graphene- Coated Cu and Cu / Ni Alloy," *ACS Nano*, vol. 5, no. 2, pp. 1321–1327, 2011.

[200] J. Chrzanowski and J. C. Irwin, "Raman scattering from cupric oxide," *Solid State Commun.*, vol. 70, no. I, pp. 11–14, 1989.

[201] H.-Y. Lin and R.-C. Wang, "Efficient surface enhanced Raman scattering of Cu2O porous nanowires transformed from CuO nanowires by plasma treatments," *Mater. Chem. Phys.*, vol. 136, pp. 661–665, 2011.

[202] C. Toparli, A. Sarfraz, A. D. Wieck, M. Rohwerder, and A. Erbe, "In situ and operando observation of surface oxides during oxygen evolution reaction on copper," *Electrochim. Acta*, vol. 236, pp. 104–115, 2017.

[203] C. Brolly, J. Parnell, and S. Bowden, "Raman spectroscopy: Caution when interpreting organic carbon from oxidising environments," *Planet. Space Sci.*, vol. 121, pp. 53–59, 2015.

[204] X. Yuan, L. Cheng, L. Kong, X. Yin, and L. Zhang, "Preparation of titanium carbide nanowires for application in electromagnetic wave absorption," *J. Alloys Compd.*, vol. 596, no. 3, pp. 132–139, 2014.

[205] A. Kaniyoor and S. Ramaprabhu, "A Raman spectroscopic investigation of graphite oxide derived graphene," *AIP Adv.*, vol. 2, no. 3, 2012.

[206] E. J. Heller *et al.*, "Theory of Graphene Raman Scattering," *ACS Nano*, vol. 10, no. 2, pp. 2803–2818, 2016.

[207] S. A. Chernyak *et al.*, "Oxidation, defunctionalization and catalyst life cycle of carbon nanotubes: a Raman spectroscopy view," *Phys. Chem. Chem. Phys.*, vol. 19, no. 3, pp. 2276–2285, 2017.

[208] Z. Xiao and Y. Zhao, "Heat transfer coefficient of porous copper with homogeneous and hybrid structures in active cooling," *J. Mater. Res.*, vol. 28, no. 17, pp. 2545–2553,

2013.

[209] N. Dukhan, *Metal Foams: Fundamentals and Applications*. Destech Publications, 2013.

[210] S. Mancin, C. Zilio, A. Diani, and L. Rossetto, “Experimental air heat transfer and pressure drop through copper foams,” *Exp. Therm. Fluid Sci.*, vol. 36, pp. 224–232, 2012.

Appendices

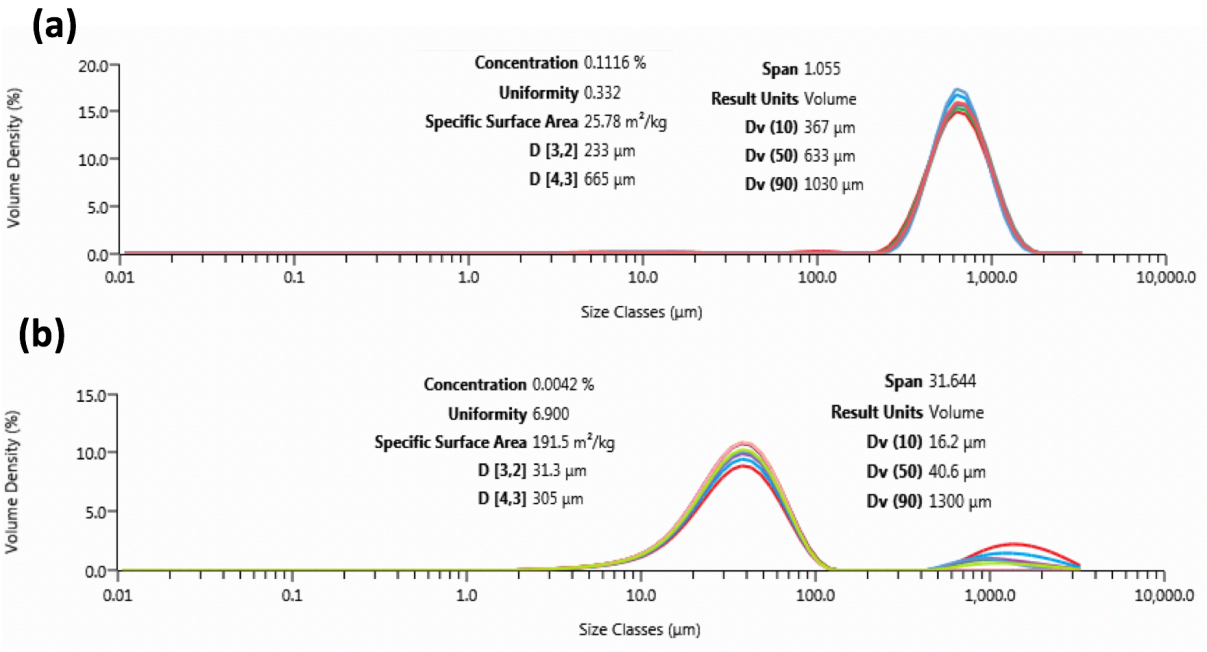

Figure 121: Size distribution of 5s measurements of K_2CO_3 coarse particles; (a) K_2CO_3 granules and (b) dendritic copper powder.

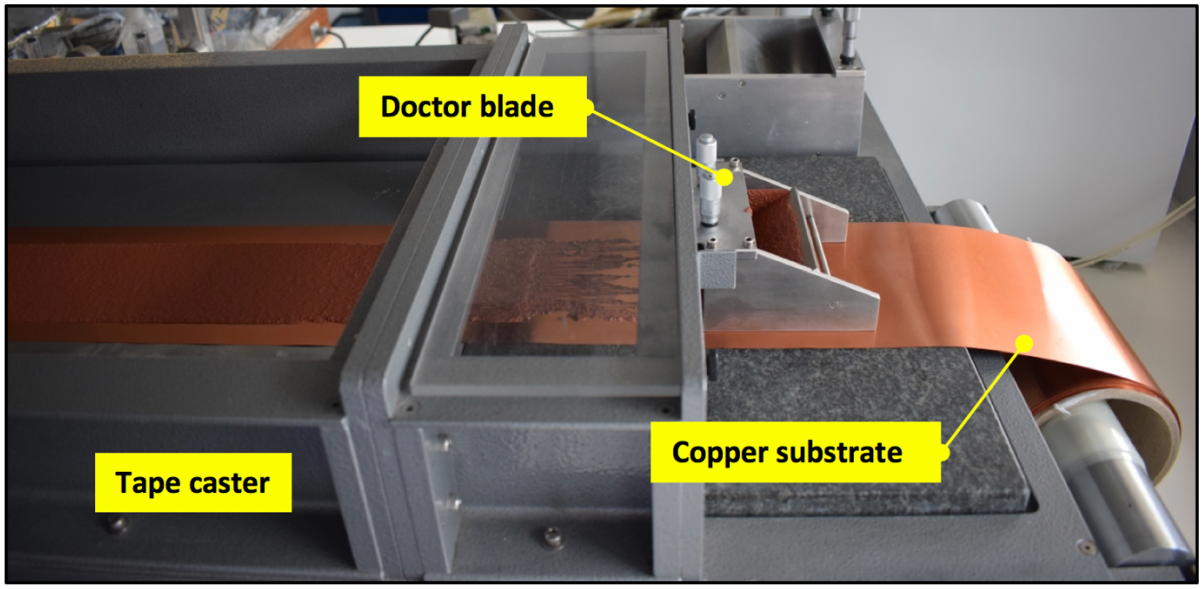

Figure 122: Tape casting set up, after casting the slurry on to the Cu substrate (Cu sheet).

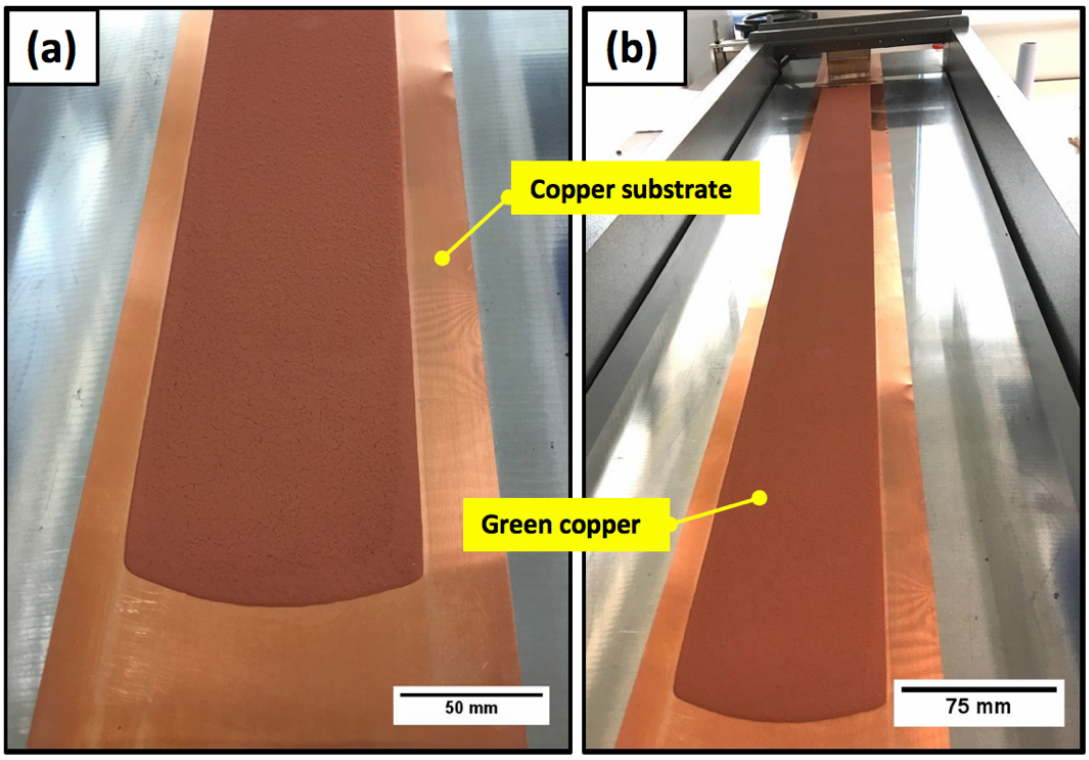

Figure 123 Successful green copper samples after tapes cast directly on copper substrate following processing route A and dried at 40°C under air.

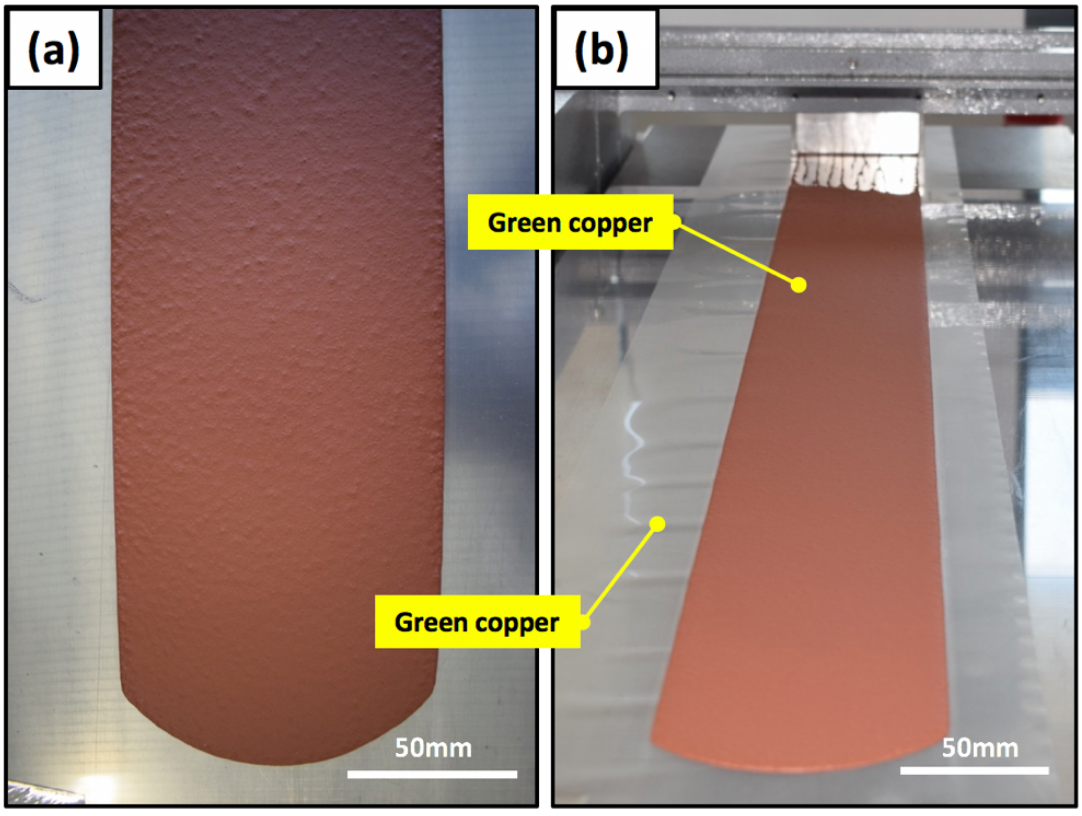

Figure 124: Successful green copper samples after tapes cast directly on non-sticky polymer sheet and dried at 40°C under air.

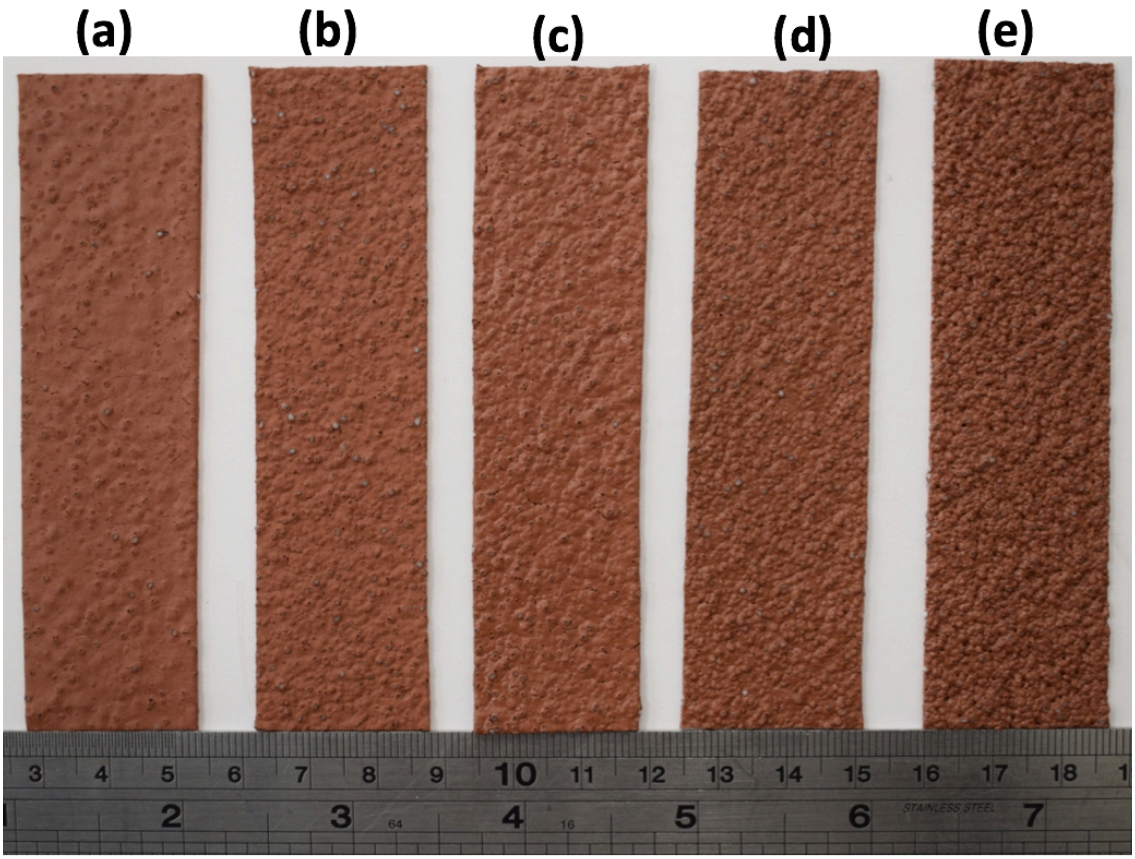

Figure 125: Green copper samples after tapes cast directly on copper substrate and dried at 40°C under air: (a) 10CuPA, (b) 20CuPA, (c) 30CuPA, (d) 40CuPA and (e) 50CuPA.

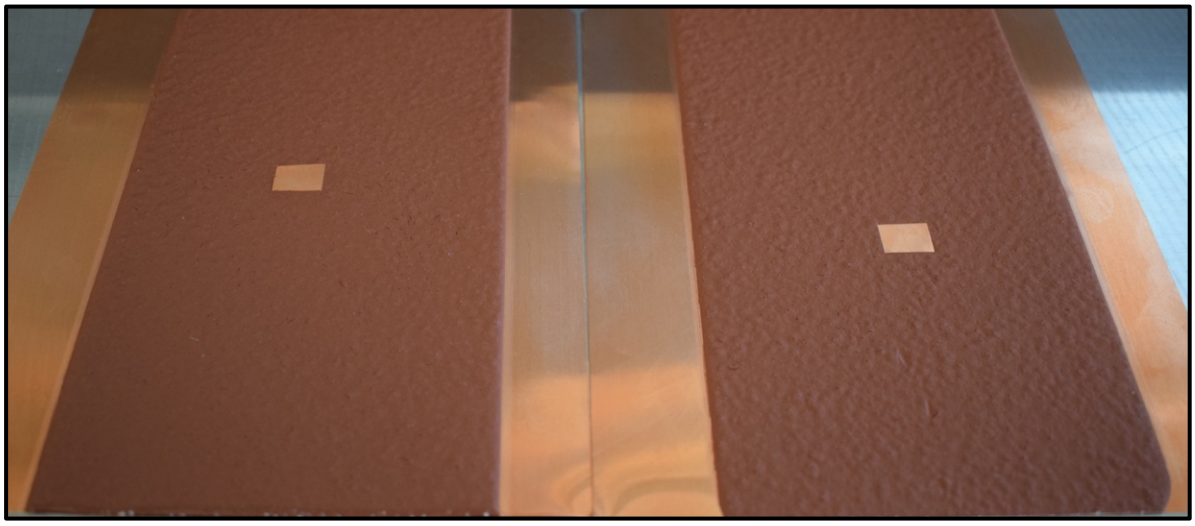

Figure 126: Green copper samples specially prepared for heat transfer measurements

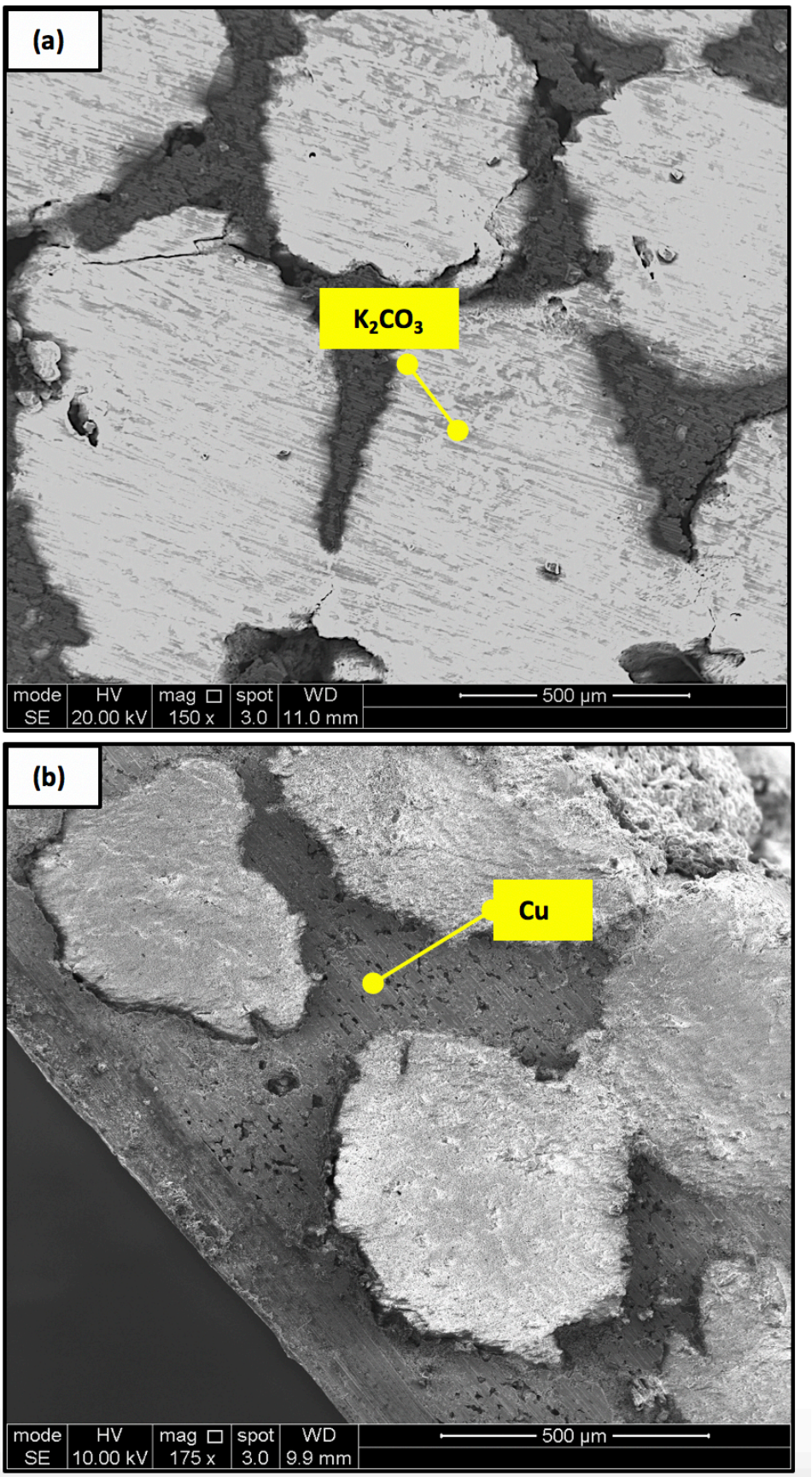

Figure 127: Sintered copper with K_2CO_3 still embedded within the matrix; (a) top view and (b) side view (through thickness)

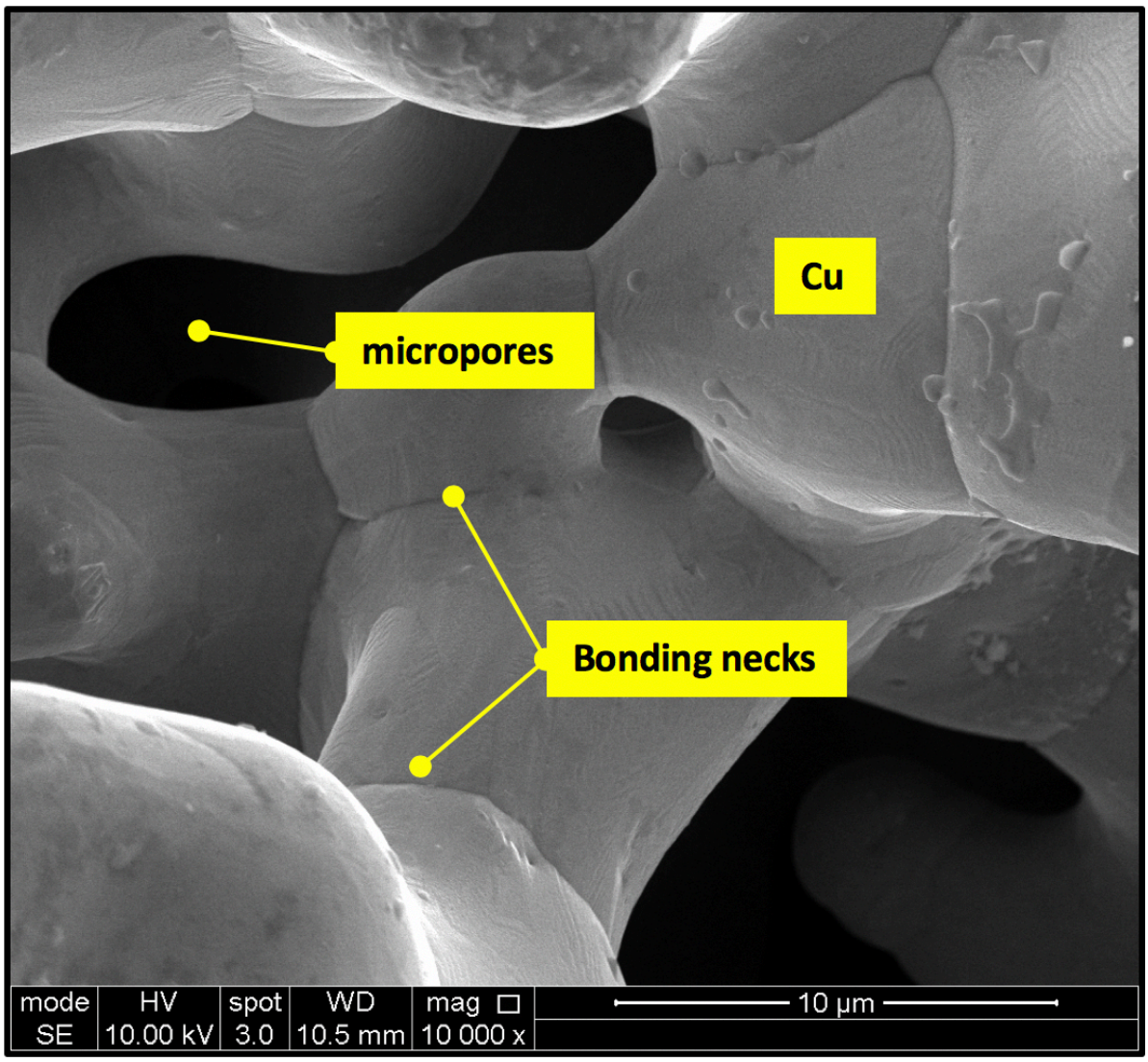

Figure 128: SEM micrograph revealing the Cu particles adhered together after sintering at 890 °C under vacuum.

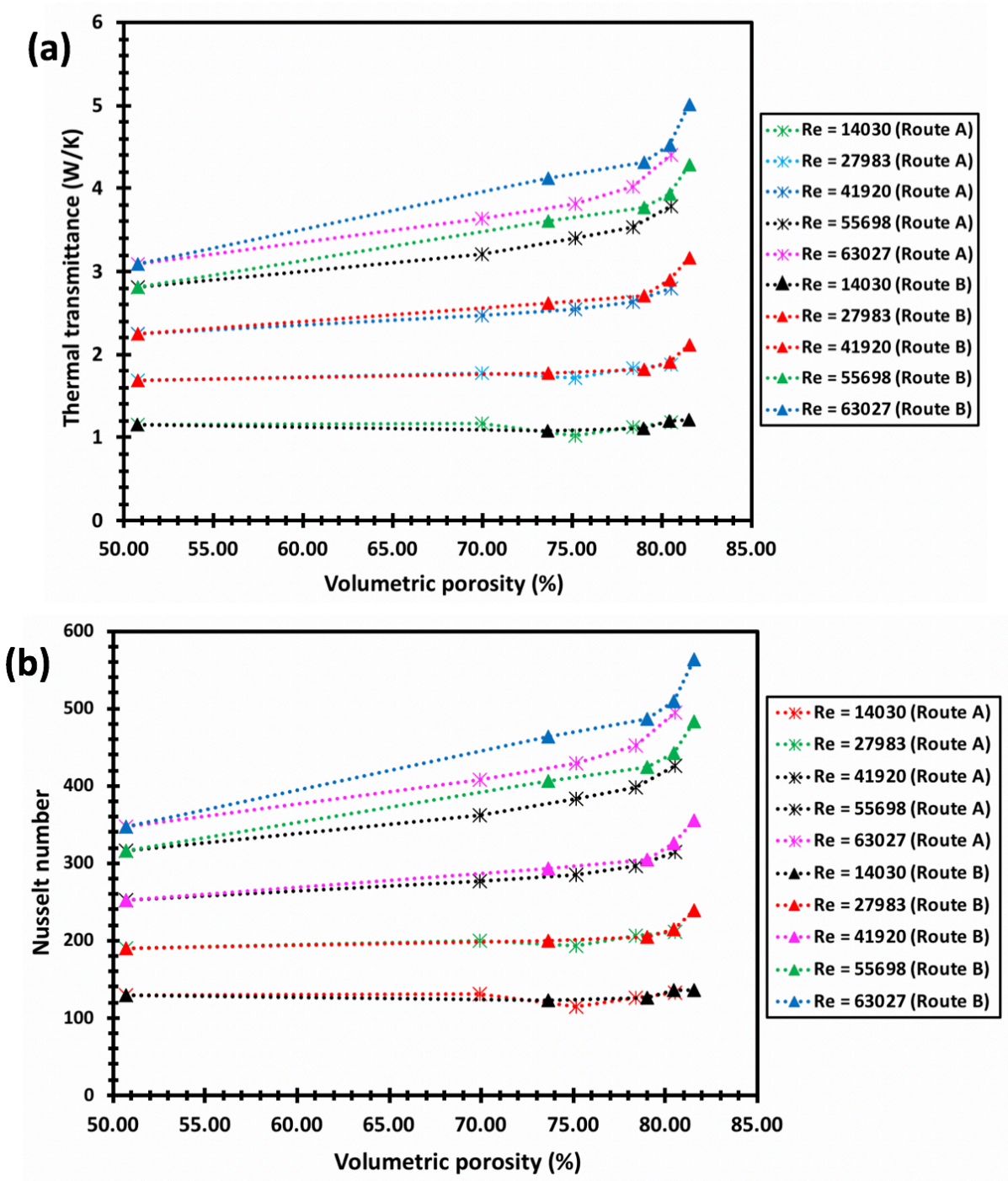

Figure 129: Two plots showing the experimental result of heat transfer performace of porous sheets (produced by route An and route B) with varrying porosity and surface roughness tested on a *cylindrical heating system,* (a) thermal transmittance versus surface roughness of porous sheets and (b) dimensionless Nusselt number versus volumetric porosity of copper samples.

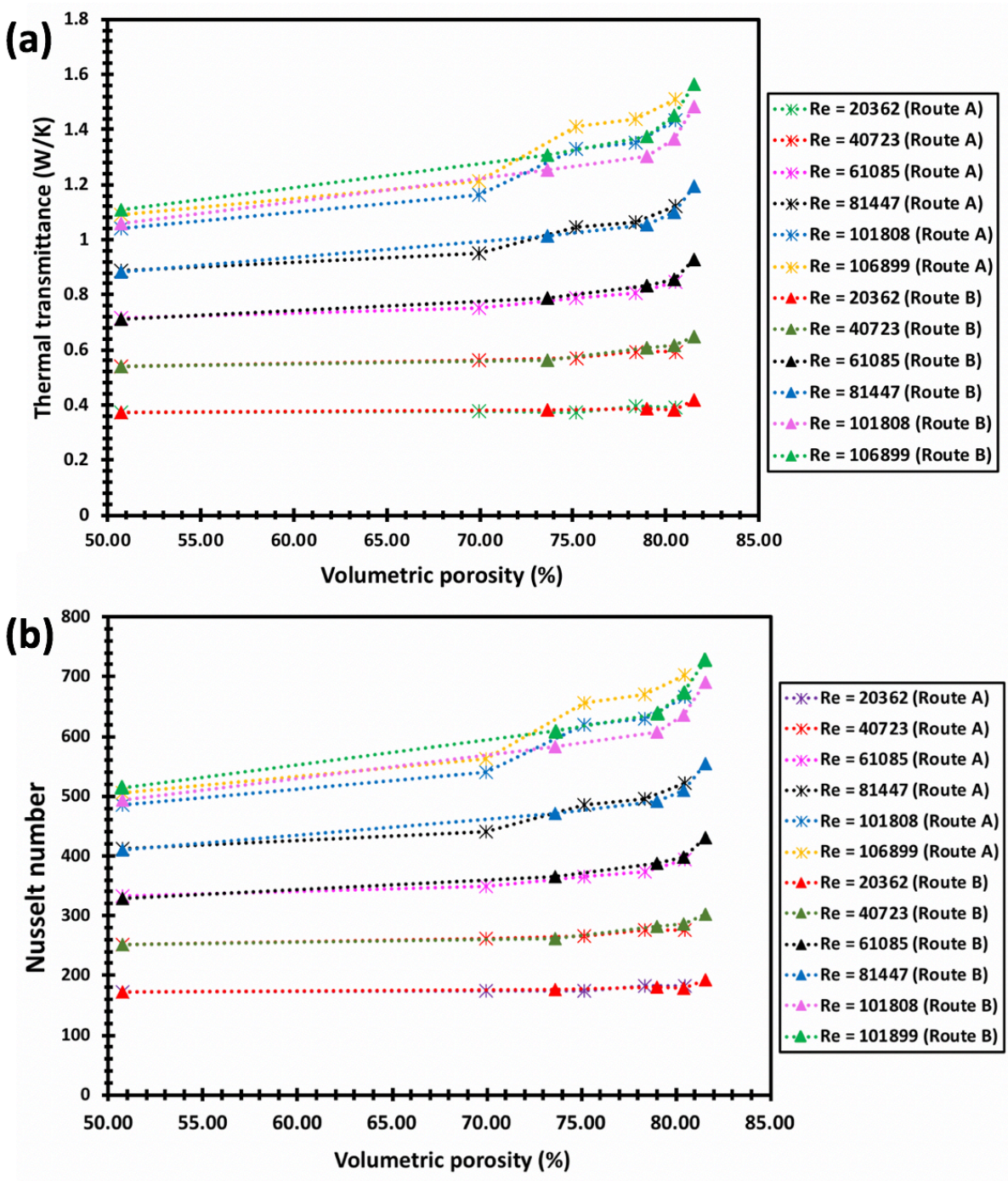

Figure 130: Two plots showing the experimental result of heat transfer performace of porous sheets (produced by route A and route B) with varrying porosity and surface roughness tested on a *flat heating system,* (a) thermal transmittance versus surface roughness of porous sheets and (b) dimensionless Nusselt number versus volumetric porosity (bulk porosity) of copper samples.

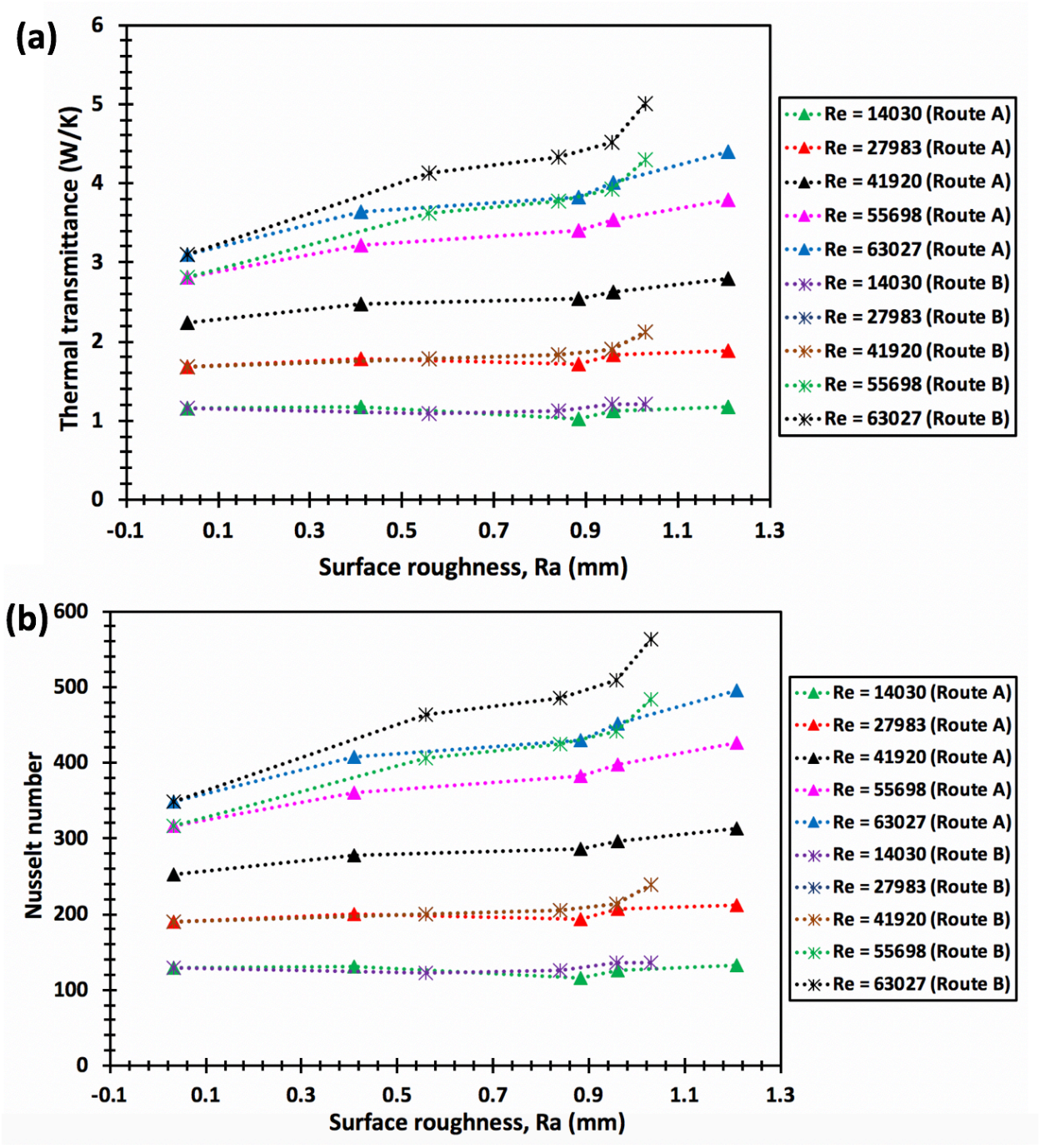

Figure 131: Two plots showing the experimental result of heat transfer performace of porous sheets (produced by route A and route B) with varrying porosity and surface roughness tested on a *cylindrical heating system*, (a) thermal transmittance versus surface roughness of porous sheets and (b) dimensionless Nusselt number versus surface roughness of copper samples.

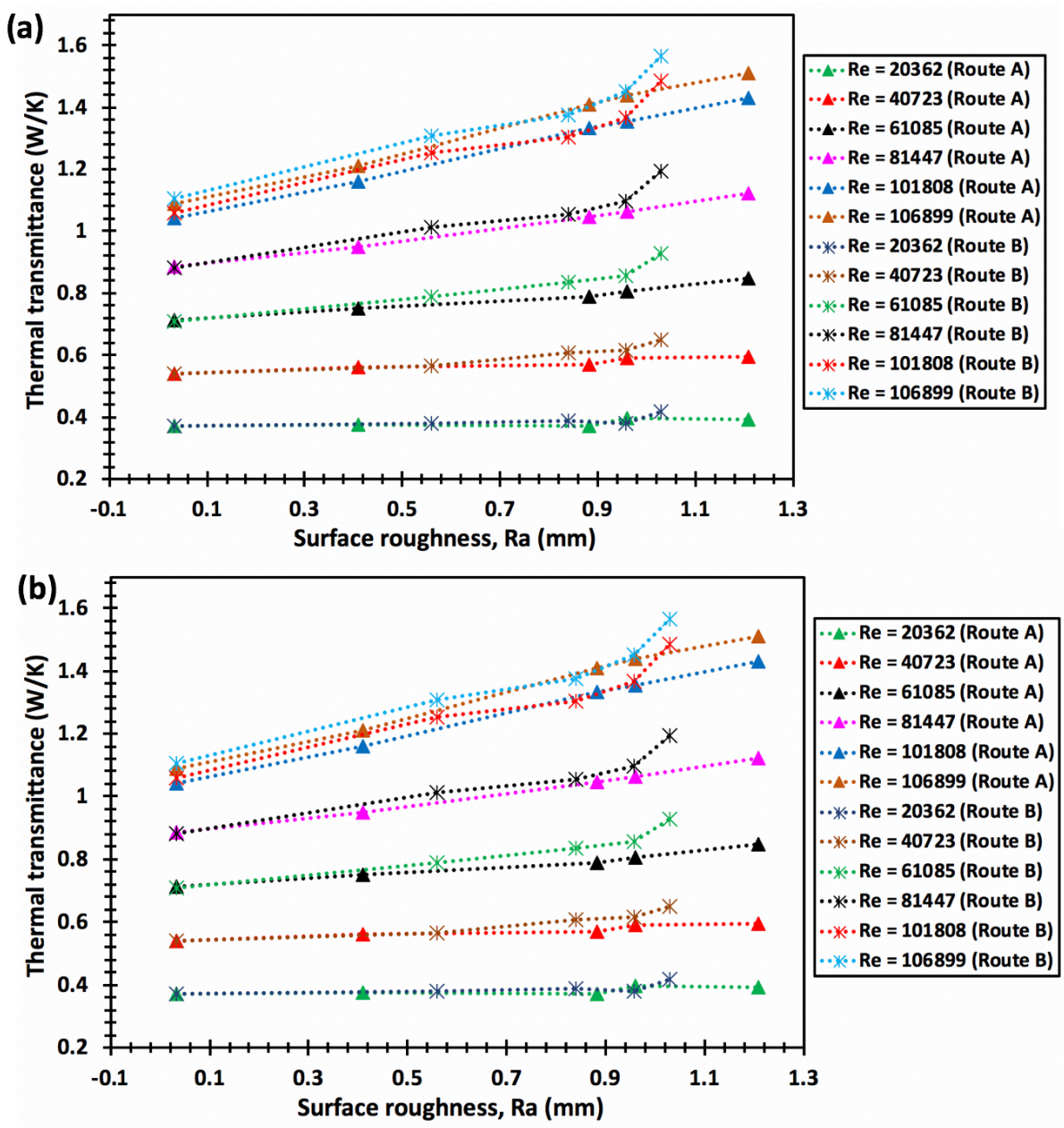

Figure 132: Two plots showing the experimental result of heat transfer performace of porous sheets (produced by route A and route B) with varrying porosity and surface roughness tested on a flat heating system, (a) thermal transmittance versus surface roughness of porous sheets and (b) dimensionless thermal transmittnce versus surface roughness of copper samples.

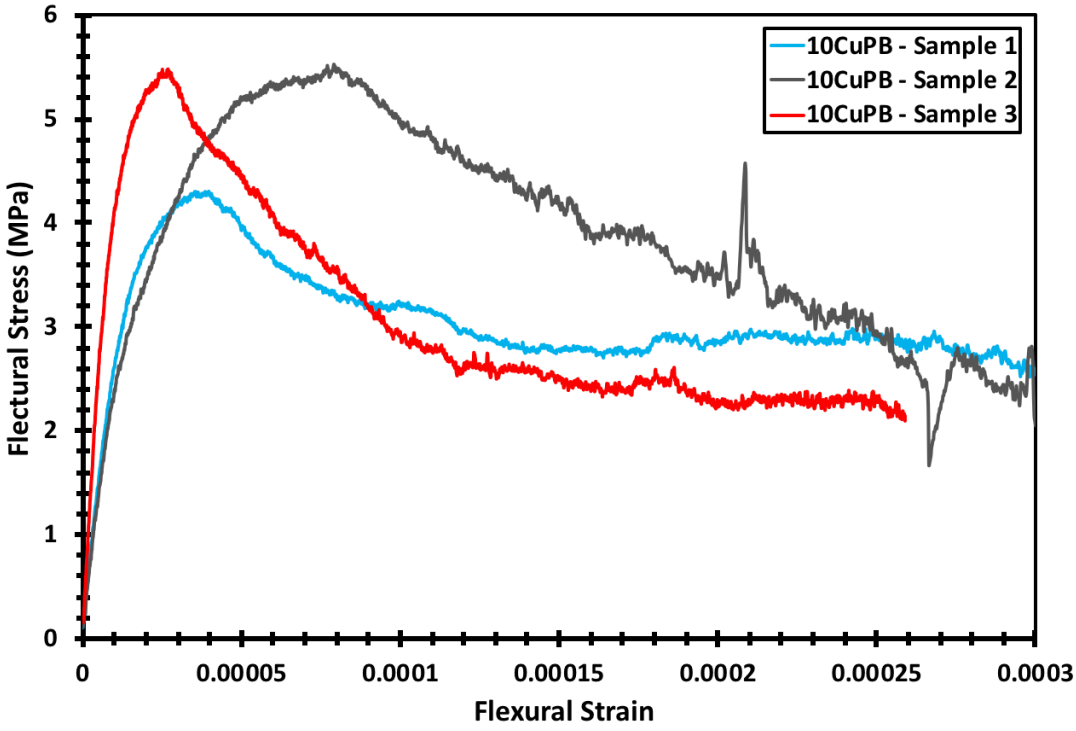

Figure 133: Example stress - strain curves of 10CuPB, obtained by 3 – point bending test.

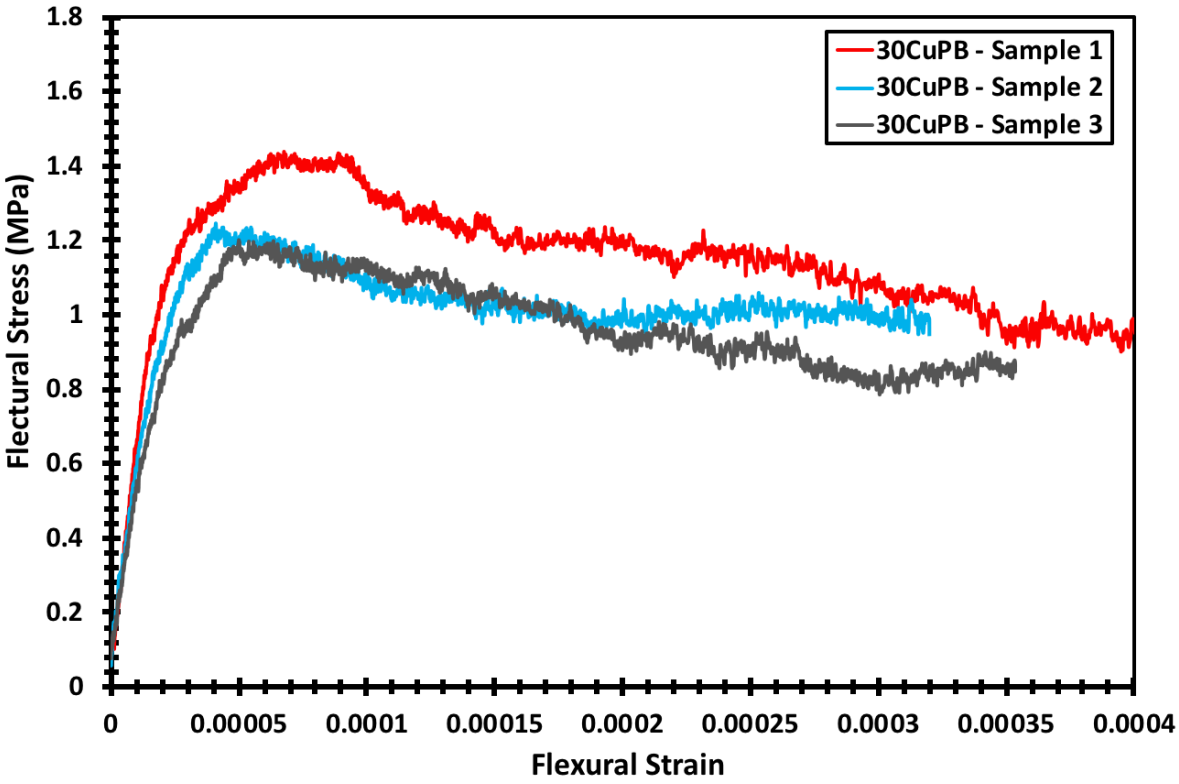

Figure 134: Example stress - strain curves of 30CuPB obtained by 3 – point bending test.

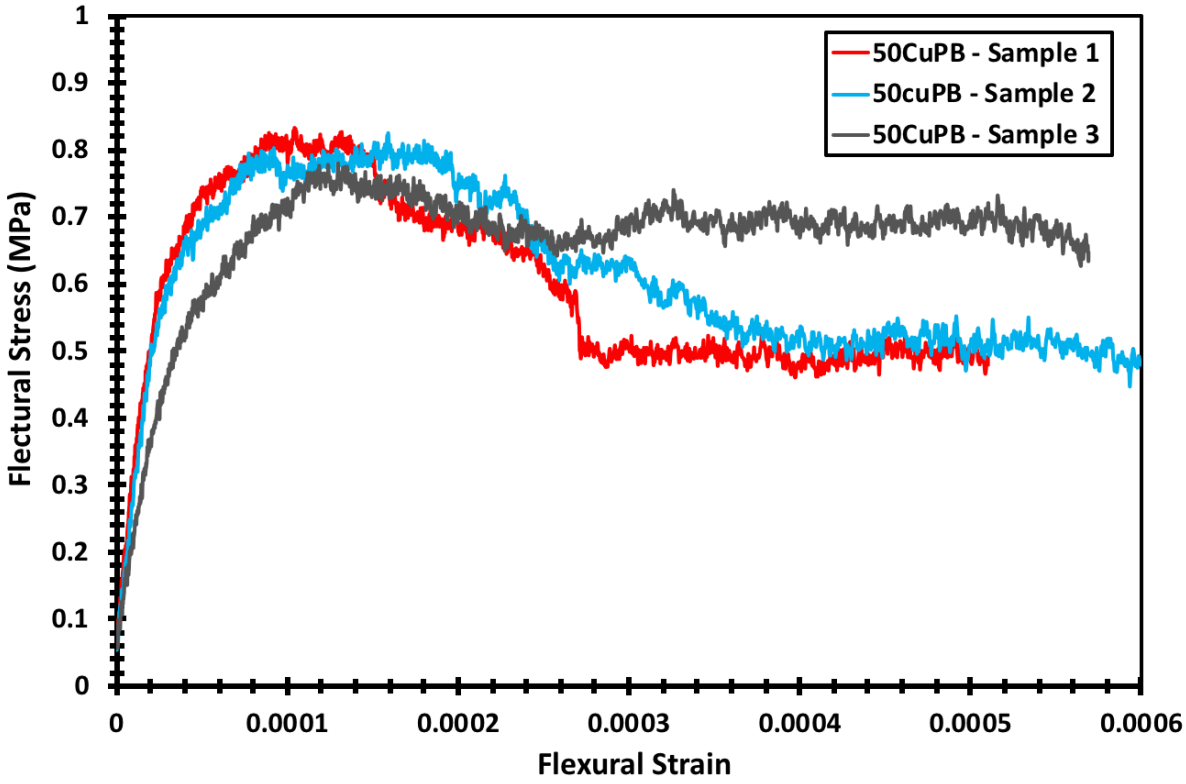

Figure 135: Example stress - strain curves of 50CuPB obtained by 3 – point bending test.